INTERESTING ELECTRONIC AND DYNAMIC PROPERTIES OF QUANTUM DOT QUANTUM WELLS AND OTHER SEMICONDUCTOR NANOCRYSTAL HETEROSTRUCTURES

A Dissertation
Presented to
The Academic Faculty

By

Alexander W. Schill

In Partial Fulfillment
Of the Requirements for the Degree
Doctor of Philosophy in Chemistry

Georgia Institute of Technology

August 2006

INTERESTING ELECTRONIC AND DYNAMIC PROPERTIES OF QUANTUM DOT QUANTUM WELLS AND OTHER SEMICONDUCTOR NANOCRYSTAL HETEROSTRUCTURES

Approved by:

Dr. Mostafa A. El-Sayed, Advisor
School of Chemistry and Biochemistry
Georgia Institute of Technology

Dr. Thomas M. Orlando
School of Chemistry and Biochemistry
Georgia Institute of Technology

Dr. Robert L. Whetten
School of Chemistry and Biochemistry
Georgia Institute of Technology

Dr. Z. John Zhang
School of Chemistry and Biochemistry
Georgia Institute of Technology

Dr. Phillip N. First
School of Physics
Georgia Institute of Technology

Date Approved: May 10, 2006

Education is what survives when what has been learned has been forgotten.
-B. F. Skinner, *New Scientist, May 21, 1964*

ACKNOWLEDGEMENTS

I would like to acknowledge all those who have supported and assisted me during my time as a graduate student. I thank my family, Mom, Dad, Jessica, Mom-Mom and Grandma Celeste for their infinite love and support through the years.

I would like to thank members of the Laser Dynamics Laboratory, a remarkable group of people from whom I have learned so much. I thank Dr. Stephan Link for teaching me the ways of femtosecond spectroscopy. I thank Dr. Christy Landes for guiding my choice of a research topic and for helpful discussion along the way. I thank Dr. David Hathcock for being my "big brother" in the lab and always being there for advice. I thank Dr. Wei Qian for his assistance with the laser systems in our laboratory – it was tough being the only "laser jock" before he joined the group. I would also like to acknowledge other member of the Laser Dynamics Laboratory with whom I have worked and shared science with over the years, Dr. Laurie Sanii, Dr. Susan Eustis, Qusai Darugar, Wenyu Huang, Dr. Xiaohua Huang, Prashant Jain and Chris Tabor. I wish them all the best of luck in their future endeavors.

I must show deepest of all my appreciation to Professor Mostafa A. El-Sayed for so many things. The wisdom and experience I have gained from him is immeasurable and has made me a better scientist and stronger person. I will miss having his guidance but I know that the lessons he's bestowed on me will last a lifetime.

Special thanks to Chris Gaddis from the Department of Materials Science and Engineering for the synthesis of CdS/CdSe/CdS colloidal quantum wells and Ag capped CdS nanocrystals. His synthetic abilities outshine mine, but I've managed to teach him a

thing or two about spectroscopy and experimentation. Together we did some good science and I hope for the best of his success in the future.

I must also thank some personal friends I have made along the way. First of all I'd like to acknowledge Dr. Sachidanand Kalaver for his continued friendship. Sachin was the first person I met when I came to Atlanta as my roommate in the Graduate Living Center and we have been close friends ever since. I'd also like to acknowledge the life-long friends I have made in Dr. Josh Aronson and Mr. Karl Huettinger with whom I have shared some great times while here at Georgia Tech.

TABLE OF CONTENTS

ACKNOWLEDGEMENTS……..……...…….....iv

LIST OF TABLES……..……..……viii

LIST OF FIGURES..……...…ix

LIST OF SCHEMES…..…….…xvii

SUMMARY……...….xviii

CHAPTER 1: INTRODUCTION……....1

1.1. Semiconductor Nanocrystals and Heterostructures…….……1

1.2. CdS/HgS/CdS Quantum Dot Quantum Wells…….3

1.3. CdS/CdSe/CdS Colloidal Quantum Wells……37

References……..…….47

CHAPTER 2: EXPERIMENTALTECHNIQUES…….…...……50

References……..74

CHAPTER 3:
SYNTHESIS OF QUANTUM DOT QUANTUM WELL NANOCRYSTALS……...75

References……..85

CHAPTER 4:
PROBE WAVELENGTH DEPENDENT HOT ELECTRON RELAXATION
IN PVP CAPPED CdS/HgS/CdS QUANTUM DOT QUANTUM WELL
NANOCRYSTALS……...86

References…….……..111

CHAPTER 5:
DEEP-TRAP STIMULATED EMISSION DYNAMICS IN QUANTUM DOT
QUANTUM WELL NANOCRYSTALS…….....113

References…….…….……122

CHAPTER 6:
ULTRAFAST ELECTRONIC RELAXATION IN CdS/HgS CORE/SHELL AND CdS/HgS/CdS QUANTUM DOT QUANTUM WELL NANOCRYSTAL HETEROSTRUCTURES: THE INFLUENCE OF SURFACE TRAPPING…….124

References……..…….……..……..137

CHAPTER 7:
SIZE LIMITING EFFECTS ON THE PREPARATION OF VERY SMALL QUANTUM DOT QUANTUM WELL NANOCRYSTALS……..……...139

References…….……145

CHAPTER 8:
PREPARATION OF QUANTUM DOT QUANTUM WELLS OF DIFFERENT COMPOSITIONS…….147

References…….160

CHAPTER 9:
ULTRAFAST ELECTRONIC RELAXATION AND ELECTRON LOCALIZATION IN CdS/CdSe/CdS COLLOIDAL QUANTUM WELL NANOCRYSTALS…….161

References……182

CHAPTER 10:
ORDER OF MAGNITUDE ENHANCMENT OF LUMINESCENCE IN SILVER CAPPED CdS QUANTUM DOTS……..184

References…….200

APPENDIX 1: LABVIEW PROGRAM DOCUMENTATION…….……203

APPENDIX 2: EXPONENTIAL DATA FITTING DOCUMENTATION……241

LIST OF TABLES

Table 1.1 – Parameters used in the theoretical calculations of the electronic structure of CdS/HgS/CdS nanocrystals using the effective mass approximation……..8

Table 4.1. Wavelength dependent kinetic decay parameters determined from fitting the experimental data traces obtained using 398 nm excitation. The data were fit to a two exponential decay function. Time constants for the fast (T1) and slow (T2) decay components are shown along with the percent relative amplitudes of each…….....97

LIST OF FIGURES

Figure 1.1 – Results of the determination of free Cd and Hg ions in solution during the course of chemically growing a monolayer of HgS on the surface of CdS nanocrystals…….6

Figure 1.2 – Ground state absorption spectra of (a) CdS, (b) CdS/HgS, (c) CdS/HgS/CdS, (d) and (e) CdS/HgS/CdS plus increasing amounts of CdS (thicker outer layer)……....10

Figure 1.3 – Development of the absorption spectrum of CdS nanocrystals during the addition of Hg^{2+} in 2×10^{-5} M increments (a_1 through b_2). Inset: CdS nanocrystals plus 8×10^{-5} M Hg^{2+} after times indicated along with an intentionally prepared CdS/HgS alloy colloid……..11

Figure 1.4 – Emission spectra of HgS nanocrystals capped with different amounts of CdS……..12

Figure 1.5 – Emission spectra of CdS nanocrystals as a function of added Hg^{2+}…….13

Figure 1.6 – Emission spectra of CdS/HgS/CdS (d and da) and CdS/HgS/$(CdS)_3$ (e and ea) before and after fluorescence activation……...14

Figure 1.7 – Luminescence decay of CdS nanocrystals monitored at 500 nm as a function of added Hg^{2+}……...15

Figure 1.8 – Luminescence decay of CdS nanocrystals with islands of HgS as a function of methyl viologen concentration. Excitation was carried out at 300 nm (CdS core) and monitoring of the emission at 650 nm……..16

Figure 1.9 – Luminescence decay of CdS nanocrystals with islands of HgS as a function of methyl viologen concentration. Excitation was carried out at 600 nm (HgS islands) and monitoring of the emission at 650 nm……..16

Figure 1.10 – Luminescence decay of CdS/HgS/CdS nanocrystals as a function of temperature……..17

Figure 1.11 – Ground state absorption spectra of (a) CdS, (b) CdS/HgS, (c) CdS/HgS/CdS and fluorescence line narrowing (FLN) and hole burning (HB) spectra of CdS/HgS/CdS……....19

Figure 1.12 – Single dot luminescence from CdS nanocrystals. Lower left: time profile of the integrated emission at 0.5 kW/cm^2 excitation density. Upper left: time profile of the integrated emission at 5.3 kW/cm^2 excitation density. Right: time averaged single dot emission spectra of CdS nanocrystals as a function of increasing excitation density……...20

Figure 1.13 – Single dot luminescence from CdS/HgS/CdS nanocrystals. Left: time profile of the integrated emission at three different excitation densities. Right: time averaged single dot emission spectra of CdS/HgS/CdS nanocrystals……....22

Figure 1.14 – Ground state absorption spectra of (a) CdS, (b) CdS/HgS, (c) CdS/HgS/CdS and their corresponding transient bleach spectra (a_1, b_1, c_1)……....25

Figure 1.15 – (a) homogeneous absorption and emission spectra of CdS/HgS/CdS nanocrystals as determined from experimental and calculated transient hole burning (HB, b and c) and fluorescence line narrowing (FLN, d) spectra of CdS/HgS/CdS nanocrystals……...27

Figure 1.16 – Picosecond transient hole burning spectra of (A) CdS and (B) CdS/HgS/CdS nanocrystals at different probe delay times……..29

Figure 1.17 – First order relaxation times and rise times (inset) of the transient bleach in CdS/HgS/CdS nanocrystals as a function of monitoring energy……...30

Figure 1.18 – Sub-picosecond transient hole burning (HB) spectra of CdS/HgS/CdS nanocrystals at different probe delay times. Dashed lines indicate the position of vibronic side peaks at frequency shifts of 250 cm^{-1} and 300 cm^{-1}…….31

Figure 1.19 – Pump probe trace of excited CdS/HgS/CdS obtained using a 30 fs, 635 nm pump pulse and a 10 fs, 650 nm probe pulse. Inset: Fourier analysis of the oscillatory component of the signal…….33

Figure 1.20 – Pump probe traces of excited CdS/HgS/CdS obtained using 160 fs, 620 nm pump pulses and 10 fs probe pulses with wavelengths shorter (580 – 610 nm) and longer (660 – 680 nm) than the pump wavelength. The decay time at 580 – 610 nm and rise time at 660 – 680 nm is 400 fs……...34

Figure 1.21 – Pump probe transient absorption traces of excited CdS/HgS/CdS obtained using 100 fs pump pulses of 400 nm and 650 nm wavelength. Samples were monitored at different wavelengths corresponding to transient bleach and stimulated emission……....35

Figure 1.22 – Pump probe transient absorption traces of excited CdS/HgS/CdS nanocrystals monitoring at 4500 nm following 100 fs excitation at 266 nm, 400 nm, 580 nm and 650 nm……...36

Figure 1.23 – Absorption and emission spectra of CdS/CdSe/CdS colloidal quantum wells made from 2.7 nm, 3.7 nm and 5.0 nm CdS templates with CdSe layer thickness between 1 and 7 monolayers…….40

Figure 1.24 – Transmission electron microscopy (TEM) images of CdS/CdSe/CdS colloidal quantum wells. (Right panel) electron diffraction pattern of CdS/CdSe/CdS with indices labeled to indicate a wurtzite crystal structure……..42

Figure 1.25 – Steady state absorption and emission spectra of CdS/CdSe/CdS colloidal quantum wells of varying layer thickness. Inset: quantum yield and peak position as a function of layer thickness…….....43

Figure 1.26 – Luminescence intensity (top panel), peak position (bottom squares) and FWHM (bottom circles) of CdS/CdSe/CdS colloidal quantum wells as a function of temperature from 300 K to 75 K…….....44

Figure 1.27 – Luminescence lifetimes of CdS/CdSe/CdS colloidal quantum wells of thickness 1-4 monolayers as a function of temperature from 300 K to 75 K…..45

Figure 1.28 – Lifetimes of radiative (circles) and non-radiative (triangles) recombination obtained from the analysis of the luminescence lifetime data for CdS/CdSe/CdS nanocrystals…….46

Figure 2.1 – Diagram of the amplified Ti:sapphire laser system used for pump-probe transient absorption and optical rotation experiments……...54

Figure 2.2 – General diagram of the optical layout of the pump-probe transient absorption system……....55

Figure 2.3 – Comparison of the transient bleach spectrum of CdSe nanocrystals obtained using active and post correction techniques. See text for details (Chirp Free Transient Absorption Spectroscopy)……..59

Figure 2.4 – General diagram of the optical layout of the pump-probe transient optical rotation experiment……64

Figure 2.5 – Ultrafast optical Kerr response of Coumarin 420 in methanol collected using the transient optical rotation setup……...…67

Figure 2.6 – Ultrafast optical Kerr response of PVP capped CdS nanocrystals collected using the transient optical rotation setup……67

Figure 2.7 – Luminescence spectra of Tris(2,2'-bipyridyl)dichlororuthenium(III) in water at different times with respect to the pulse laser……..70

Figure 2.8 – Kinetic traces extracted from the series of collected luminescence spectra at different monitoring wavelengths for Tris(2,2'-bipyridyl)dichlororuthenium(III) in water……..71

Figure 3.1 – Evolution of the absorption spectrum of CdS upon continued addition of Hg^{2+} in aqueous solution…….....83

Figure 3.2 – Absorption spectra taken during two preparations of PVP capped CdS/HgS/CdS on consecutive days (labeled Day 1 and Day 2)……....84

Figure 4.1. Absorption spectra collected during the preparation of PVP-CdS/HgS/CdS nanocrystals……...92

Figure 4.2. Pump-probe kinetic traces of excited PVP-CdS/HgS/CdS nanocrystals obtained following excitation with a 100 fs pulse of 398 nm light. Probe wavelengths indicated on the figure……....94

Figure 4.3. Pump-probe kinetic traces of excited PVP-Cd(Hg)S alloy nanocrystals obtained following excitation with a 100 fs pulse of 398 nm light. Probe wavelengths indicated on the figure……....94

Figures 4.4A and 4.4B. Pump-probe kinetic traces of excited PVP-CdS/HgS/CdS nanocrystals obtained following excitation with 100 fs pulses of 398 (A) and 520 (B) nm light. The traces shown are chirp-adjusted best-fit curves to the experimental data……..96

Figure 4.5A and 4.5B. Rise times of the transient signal at various probe wavelengths for PVP-CdS/HgS/CdS nanocrystals following excitation with 100 fs pulses of 398 (A) and 520 (B) nm light. Rise times were determined from the best-fit curves to the experimental data using the 10-90% method. The uncertainty in these times is ±50 fs and indicated by the error bars…….....99

Figure 4.6. The fit of the absorption spectra of PVP-CdS/HgS/CdS nanoparticles to two Gaussian bands as indicated in the figure and described in the text. The band at higher energy is proposed to be the absorption of pure CdS while the low energy band is proposed to be the absorption of pure HgS. Note: a third Gaussian (not shown) was used to fit the high energy side (below 425 nm) but was not included in the subsequent analysis……....101

Figure 4.7. Percentage of the HgS wavefunction contribution to states corresponding to probe wavelengths as determined from the ratio of the pure HgS to pure CdS from simulated absorption bands…….....102

Figures 4.8A and 4.8B. Probe wavelength dependent decay times for the fast (A) and slow (B) components of the bleach recovery following excitation at 398 nm. The results were obtained by fitting the experimental kinetics traces to a two exponential decay using a nonlinear least squares fitting routine. The fast component has been assigned to rapid electronic nonradiative relaxation while the slow component has been assigned to a thermal relaxation process……....109

Figure 5.1. Ground state absorption (red) and spontaneous emission (blue) spectra of CdS/HgS/CdS nanocrystals…….....118

Figure 5.2. Sub-picosecond pump-probe kinetic traces for PVP capped CdS/HgS/CdS nanocrystals obtained using a 500 nm, 100 fs excitation pulse. Monitoring wavelengths are indicated on the figure. Traces shown are best-fit curves to the experimental data that allow for clearer visualization of the rise and decay profiles……...119

Figure 5.3. Rise times of the transient bleach and stimulated emission from excited CdS/HgS/CdS nanocrystals as a function of probe wavelength. The excitation wavelength used for the measurement was 500 nm……....120

Figure 6.1A and 6.1B. Ground state absorption spectra taken during the preparation of CdS/HgS (A) and CdS/HgS/CdS (B) nanocrystals……..129

Figure 6.2. Sub-picosecond pump-probe transient bleach traces for excited CdS/HgS nanocrystals obtained using 400 nm excitation. Probe wavelengths indicated on the figure……130

Figure 6.3. Plot of wavelength dependent maximum dT (differential transmission) intensity for excited CdS/HgS and CdS/HgS/CdS nanocrystals……...131

Figure 6.4. Sub-picosecond pump-probe transient bleach traces for excited CdS/HgS and CdS/HgS/CdS nanocrystals obtained using 400 nm excitation and 500 nm probe wavelength……....132

Figure 6.5. Sub-picosecond pump-probe transient bleach traces for excited CdS/HgS and CdS/HgS/CdS nanocrystals obtained using 400 nm excitation and 550 nm probe wavelength……....132

Figure 6.6. Sub-picosecond pump-probe transient bleach traces for excited CdS/HgS and CdS/HgS/CdS nanocrystals obtained using 400 nm excitation and 600 nm probe wavelength……134

Figure 6.7. Difference in decay lifetime ($\Delta\tau = \tau_{core/well/shell} - \tau_{core/well}$) as a function of probe wavelength for CdS/HgS core/well and CdS/HgS/CdS core/well/shell nanocrystals……136

Figure 7.1. – Absorption spectra collected during the preparation of 4 nm CdS/HgS/CdS quantum dot quantum well nanocrystals……142

Figure 7.2. – Luminescence emission and excitation spectra of the CdS/HgS/CdS nanocrystals. Excitation and emission wavelengths are indicated on the figure…….....143

Figure 7.3. – Absorption, luminescence emission and excitation spectra of Cd(Hg)S alloy nanocrystals of the same chemical composition as the CdS/HgS/CdS quantum dot quantum well nanocrystals……..…144

Figure 8.1. Evolution of the absorption spectrum of ZnS nanocrystals with the addition of Hg^{2+} during the attempted preparation of ZnS/HgS/ZnS nanocrystals…….154

Figure 8.2. Absorption spectra collected during the preparation of ZnS/HgS/ZnS nanocrystals……..154

Figure 8.3. Absorption spectra collected during the preparation of 4 nm CdS/CdSe/CdS nanocrystals……....155

Figure 8.4. Absorption spectra collected during the preparation of larger (5 nm) CdS/CdSe/CdS nanocrystals……....156

Figure 8.5. Absorption, luminescence and luminescence excitation spectra of CdS/CdSe/CdS nanocrystals……...157

Figure 8.6. Luminescence decay of CdS/CdSe/CdS nanocrystals……..…158

Figure 8.7. Absorption spectra collected during the preparation of CdS/CuS/CdS nanocrystals……..159

Figure 9.1. Absorption spectra collected during the preparation of CdS/CdSe/CdS colloidal quantum wells…….....168

Figure 9.2. TEM images of CdS/CdSe/CdS colloidal quantum wells: (A) Lower magnification image shows the uniformity in size of the 5-6 nm nanocrystals, (B) Atomic resolution image of a single CdS/CdSe/CdS crystal, (C) Fourier transform of a single nanocrystal showing a wurtzite crystal structure, (D) Atomic resolution image of a rare nanocrystal containing a dislocation……...168

Figure 9.3. Ground state absorption and steady-state photoluminescence spectra of CdS/CdSe/CdS nanocrystals. The emission peak is occurs at 610nm and the quantum yield was estimated to be 21% compared to Rhodamine B under identical collection conditions……...171

Figure 9.4. Transient differential absorption traces monitored at 610 nm for CdS/CdSe/CdS nanocrystals with exciton densities (# e-h pairs) of 0.10 (orange crosses), 0.31 (red circles), 0.99 (black triangles), 1.97 (green diamonds) and 4.94 (blue squares). The traces shown are non-linear least squares fits to the experimental data for visual clarity of the kinetics and correct adjustment of "time zero"……...171

Figure 9.5. Transient differential absorption traces monitored at 450 nm (1P electron state) and 610 nm (1S electron state) for CdS/CdSe/CdS nanocrystals following excitation at 400 nm……...173

Figure 9.6. Intensity of the negative differential absorbance (-dA) of CdS/CdSe/CdS colloidal quantum wells as a function of exciton density (# electron-hole pairs per particle)……...173

Figure 9.7. Amplitude fraction of the fast rise time (see text for details) of CdS/CdSe/CdS colloidal quantum wells as a function of exciton density (# electron-hole pairs per particle)……...175

Figure 9.8. Apparent rise times of the slow (filled squares) and fast (open circles) components of the rise time at 610 nm in CdS/CdSe/CdS colloidal quantum wells excited with a 100 fs, 500 nm laser pulse…….....177

Figure 9.9. Transient differential absorption monitored at 610 nm for CdS/CdSe/CdS nanocrystals with excitation at 500 nm, 4.94 e-h pairs (closed circles) and 570 nm, 0.99 e-h pairs (open squares)……..177

Figure 9.10. Energy level diagrams used for interpretation of the experimental data. Top panel shows the expected relaxation pathways when 500 nm excitation is used. The bottom panel shows the expected relaxation pathways when 570 nm excitation is used. All energy levels and shown to scale……....179

Figure 10.1. Photoluminescence of as-synthesized oleic acid capped CdS crystallites compared to the PL of water-soluble mercaptoacetic acid capped crystals. The ligand exchange results in a large decrease in band edge luminescence while trap emission intensity is unchanged……...188

Figure 10.2. Luminescence intensity monitored during the growth of an Ag monolayer on water soluble, mercaptoacetic acid capped CdS quantum dots (3.9 nm average diameter). Emission was monitored near the peak of trap emission. The enhancement rate decreases nearly exponentially, reaching a plateau after 20 minutes. Inset: luminescence intensity at the peak of deep trap emission monitored as a function of time with the excitation shutter opened and closed repeatedly to demonstrate that silver growth and the associated enhancement is not dependent upon illumination……....190

Figure 10.3. Luminescence intensity monitored as a function of time. Three $AgNO_3$ injections of 7.5 μL each were introduced at different times that caused an exponentially decreasing enhancement rate to occur. The magnitude of the emission intensity increase dropped from 2.5x to 1.3x to 1.1x with successive Ag^+ additions……....191

Figure 10.4. Steady-state luminescence of water soluble, mercaptoacetic acid capped CdS nanocrystals after aging in darkness for several time periods…….193

Figure 10.5. High resolution TEM shows CdS crystallites after growth of an Ag monolayer. The Fourier transform shows a diffraction ring that corresponds to the (100) planes of wurtzite CdS…….193

Figure 10.6. Luminescence lifetime data collected for Ag capped and mercaptoacetic acid capped CdS crystallites are plotted. Multi-exponential behavior is observed for both samples. The data shows that the fast component of the Ag capped sample is 2.3 times slower than that of the MAA capped sample…...195

LIST OF SCHEMES

Scheme 4.1. Graphical representation of the relaxation model used for the interpretation of experimental data. Blue and green arrows represent excitation at 398 nm and 520 nm, respectively. Black arrows indicate the intra-band relaxation from higher excited states of which the relaxation rate is proportional to the rise times given in Figures 4A and 4B……...105

Scheme 5.1. Energy state diagram used for interpretation of the experimental results. An excited state produced by a 500 nm 100 fs pulse relaxes into intrinsic nanocrystal states and also an ensemble of deep trap states below the band gap energy. Stimulated emission from the deep traps has been observed and has an energy dependent relaxation signature (see text)…….....121

SUMMARY

Some interesting electronic and dynamic properties of semiconductor nanocrystal heterostructures have been investigated using various spectroscopic methods. Semiconductor nanocrystal heterostructures were prepared using colloidal synthesis techniques. Ultrafast transient absorption spectroscopy was used to monitor the relaxation of hot electrons in CdS/HgS/CdS quantum dot quantum wells. Careful analysis of the hot electron relaxation in CdS/HgS/CdS quantum dot quantum wells reveals an energy dependent relaxation mechanism involving electronic states of varying CdS and HgS composition. The composition of the electronic states, combined with the layered structure of the nanocrystal permits the assignment of CdS localized and HgS localized excited states. The dynamic effect of surface passivation is then shown to have the strongest influence on excited states that are localized in the HgS layer.

New quantum dot quantum well heterostructures of different sizes and compositions were also prepared and studied. The dynamic properties of CdS/CdSe/CdS colloidal quantum wells suggest simultaneous relaxation of excited electrons within the CdS core and CdSe shell on the sub-picosecond time scale. Despite the very different electronic structure of CdS/CdSe/CdS compared to CdS/HgS/CdS, the time scales of the relaxation and electron localization were very similar.

Enhancement of trap luminescence was observed when CdS quantum dots were coated with silver. The mechanism of the enhancement was investigated using time-resolved spectroscopic techniques.

CHAPTER 1

INTRODUCTION

1.1 Semiconductor Nanocrystals and Heterostructures

The properties of materials in the nanometer size regime have attracted a great deal of attention in recent years due to the enormous potential of nanomaterials to applications in optical and electrical technology. The unique properties of semiconductors of nanometer size arise from the effects of quantum confinement. For semiconductors, the characteristic length scale is the mean distance between the electron and hole known as the exciton Bohr radius.

$$a_b = \frac{\hbar^2 \varepsilon}{e^2}\left(\frac{1}{m_e} + \frac{1}{m_h}\right) \qquad (1.1)$$

where ε is the dielectric constant and m_e and m_h are the electron and hole effective masses, respectively. When the size of the material becomes comparable to the exciton Bohr radius, quantum confinement effects dominate the electronic properties of the semiconductor. For example, absorption and emission energies can be tuned continuously by simply changing the size. Absorption cross-sections, luminescence quantum yields and excited state lifetimes also vary dramatically as a function of size in the nanometer regime.

The interesting properties of quantum dots and semiconductor clusters have been thoroughly outlined in a number of review articles [1, 2], and recent interest in the field of semiconductor nanocrystals has focused on fabrication of systems with increasing

heterogeneity and functionality. The implementation of semiconductor heterostructures in the bulk phase has led to numerous everyday technological innovations such as the light-emitting diode (LED) and semiconductor diode laser. Molecular beam and atomic layer epitaxy have become increasingly advanced and are now capable of growing ultra-thin quantum wells of II-IV semiconductors [3]. Such ultra-thin wells are small enough in length-scale to benefit from the effects of quantum confinement, but the method of preparing such materials are difficult and costly. Colloidal approaches are often much cheaper and easier to implement, which is why colloidal semiconductor materials have received so much attention in recent years. The challenge has been to prepare high quality nanocrystals of narrow size distribution and specific structure and function.

One of the most successful discoveries in the field of semiconductor nanocrystal heterostructures was in the growth of a ZnS shell on the surface of CdSe nanocrystals [4]. Through capping CdSe with ZnS, a higher band-gap material, the luminescence quantum yield and photo-stability of the nanocrystals increased dramatically. The luminescence quantum yield increased by a factor of 6 and the lifetime became shorter by a factor of 10 [4], suggesting that capping with ZnS accelerates the rate of radiative recombination. Capping with ZnS passivates the surface traps, which are known to quench excitonic luminescence in colloidal semiconductors. The influence of the surface on the properties of semiconductor nanocrystals was predicted early on in the study of nanocrystals [5] and recent reports have further quantified the surface effects [6]. It was shown that relaxation rates in different size and shape CdSe nanocrystals were proportional to the surface electron density based on quantum mechanical calculations that predicted the radial charge distribution in rod and dot samples of CdSe. The calculations also show that

excited states can couple strongly to surface traps and that trapping can occur from states other than the band-gap.

The CdS/ZnS nanocrystal is a two-layer structure, and efforts to prepare more complex materials of 3 or more layers have been continuing in efforts to reduce the effect of surface trapping. One of the most complex and highest quality semiconductor nanocrystals materials prepared has the structure CdSe/CdS/$Zn_{0.5}Cd_{0.5}S$/ZnS and has shown luminescence efficiency as high as 85% [7]. While recent advances in synthesis techniques have led to powerful discoveries in the area of semiconductor nanocrystal heterostructures, much of the early interest in the area sprang from the first 3-layered colloidal heterostructure, the CdS/HgS/CdS quantum dot quantum well.

1.2 CdS/HgS/CdS Quantum Dot Quantum Wells

Colloidal nanocrystal heterostructures became a topic of increased interest after the growth of CdS islands on ZnS colloids was demonstrated in 1984 [8] by a surface cation exchange of Cd^{2+} ions for Zn^{2+} ions. This technique was also used to grow Ag_2S on the surface of nanometer-sized CdS colloids [9]. In 1993, the same type of colloidal chemistry led to the growth of HgS on CdS [10]. This was the first step towards the preparation of the first quantum dot quantum well, which was demonstrated by the same group later that year [11]. This new structure consisted of a nanometer-sized core of CdS surrounded by a single monolayer of HgS and then capped with an outer shell of CdS. The monolayer of HgS represents a highly confined quantum well which is buried inside

a material that is itself a quantum confined material. The difference in band-gap energy between the CdS (2.5 eV) and HgS (0.5 eV) defines the structure of this material as a Type I semiconductor heterostructure and the characteristics of the HgS layer suggest that it could act as a highly confined quantum well. For this reason the CdS/HgS/CdS system was named a quantum dot quantum well and quickly became the focus of numerous experiments regarding its preparation, composition, structure, electronic properties, photophysical properties and excited state dynamics.

Synthesis and Composition

The synthesis of quantum dot quantum wells begins with the preparation of a population of CdS nanocrystal colloids that have a stable structure and relatively narrow size distribution. The simplest way to prepare CdS colloids in this manner is through the polyphosphate method [12]. Aqueous cadmium salt is sulfidized with H_2S gas using sodium polyphosphate as a stabilizer. This procedure yields suspensions of CdS nanocrystals around 5 nm in diameter with a size distribution of 12-15%.

The preparation of the first quantum dot quantum well benefited greatly from the work of Weller and Henglein using surface exchange chemistry to easily grow heterostructures of colloidal materials [8, 9]. The success of this method derives from the exploitation of solubility differences between the materials being used to prepare the heterostructures. If the difference in solubility product is high enough, there is a strong driving force for the exchange of the atoms at the interface between a surface and a solution containing the exchanging ions. For example, consider the surface of a

nanometer-sized CdS colloid dispersed in a solution containing Hg^{2+} ions. The solubility product of HgS (5×10^{-54}) is twenty-seven orders of magnitude smaller than the solubility product of CdS (1×10^{-27}). This gives a free energy for the reaction of CdS with Hg^{2+} (Equation 1.2) of –150 kJ/mol.

$$CdS \rightarrow Cd^{2+}(aq.) + S^{2-}(aq.)$$

$$Hg^{2+}(aq.) + S^{2-}(aq.) \rightarrow HgS$$

$$CdS + Hg^{2+}(aq.) \rightarrow HgS + Cd^{2+}(aq.)$$

$$\Delta G_1 = 154 \text{ kJ/mol}$$

$$\Delta G_2 = -304 \text{ kJ/mol}$$

$$\Delta G_{total} = -150 \text{ kJ/mol}$$

Equation 1.2 – Chemical reactions and free energies determined from the solubility products of CdS and HgS.

The net effect of this circumstance is that the outermost layer of CdS will be displaced by a monolayer of HgS through exchange of Hg^{2+} ions for Cd^{2+} ions. Another beneficial consequence of this chemistry is the fact that the colloidal solution now contains a concentration of Cd^{2+} almost exactly equivalent to one monolayer of CdS; which can be deposited on the surface of the HgS well by the addition of sulfur ion, S^{2-}. The resulting structure is a Type I semiconductor heterostructure with a nanometer sized core, sub-nanometer sized well and sub-nanometer thick outer layer. The ion exchange

reaction has been monitored during the course of the preparation electrochemically and using ICP-MS [13]. Free Cd^{2+} and Hg^{2+} concentrations were monitored in the reaction

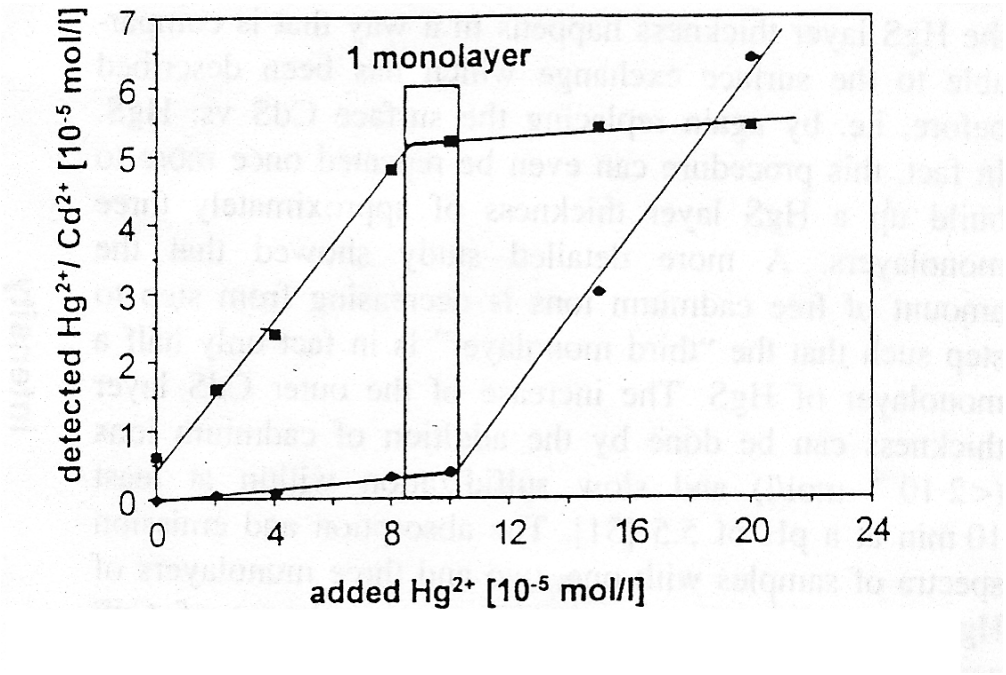

Figure 1.1 – Results of the determination of free Cd and Hg ions in solution during the course of chemically growing a monolayer of HgS on the surface of CdS nanocrystals.

Initially the concentration of Cd^{2+} increases while the concentration of Hg^{2+} remains around zero. This indicates release of surface cadmium ions into solution and replacement with mercury ions. This trend continues up to a concentration of Hg^{2+} equivalent to one monolayer on the surface of the average sized CdS colloid. After this point, the concentration of Hg^{2+} begins to increase dramatically while the Cd^{2+} concentration remains constant. This indicates that mercury ions are no longer replacing cadmium at the surface and simply remain in solution. This would be expected if the

surface of the colloids were now saturated with HgS; the additional Hg^{2+} have no ions to displace. At this point there is a concentration of cadmium ions in solution great enough to form nearly one monolayer of CdS on the surface of the HgS well. This is accomplished by simply adding sulfide (S^{2-}) solution in a slow drop-by-drop manner to avoid nucleation of small CdS seeds due to rapidly generated high local concentrations of sulfide. The capping of these particles with CdS is not only useful for defining their structure; it also serves to stabilize the particles from mixed binary phase formation (alloy formation) [13].

Structure

The first CdS/HgS/CdS quantum dot quantum well was assumed spherical and had a total radius of 4 nm: 2.3 nm core CdS, 0.3 nm HgS well, and 1.4 nm CdS shell [11]. From high-resolution transmission electron microscopy (HRTEM) it was determined that the predominant (> 60%) shape of the nanocrystals is actually tetrahedral with a cubic zinc-blend crystal lattice structure [15]. Colloidally precipitated HgS nanocrystals have the same cubic crystallinity [10]. Isolated samples of the particles CdS, CdS/HgS and CdS/HgS/CdS also show the same crystallinity, supporting the idea that the monolayer well of HgS forms epitaxialy as predicted [14]. X-ray diffraction and HRTEM results have also ruled out the possibility of a mixed binary phase of CdS and HgS [10, 13].

Electronic Structure Calculations

Electronic structure calculations for CdS/HgS/CdS have been carried out to determine the ground and excited state wavefunctions, wavefunction probability densities, theoretical band-gap energies and electronic absorption spectra [13, 14, 16, 17]. Schooss and co-workers did the most extensive theoretical work in 1994 using an effective mass model and incorporating Coulomb interaction potentials between the charge carriers [16]. The parameters used and the resulting values are shown in Table 1.1.

Table 1.1 – Parameters used in the theoretical calculations of the electronic structure of CdS/HgS/CdS nanocrystals using the effective mass approximation.

	m_e	m_h	E_g	E_{cb}	E_{vb}
CdS	0.2	0.7	2.5 eV	-3.8 eV	-6.3 eV
HgS	0.036	0.044	0.5 eV	-5.0 eV	-5.5 eV

m_e effective mass of the electron
m_h effective mass of the hole
E_g band gap energy
E_{cb} conduction band energy relative to the vacuum level
E_{vb} valence band energy relative to the vacuum level

The ground state wavefunctions and probability density functions predict that both charge carriers have the highest probability of presence in the HgS well. The probability increase with increasing well layer thickness and the hole is more highly localized than the electron. The calculations also accounted for variations in outer CdS shell thickness, and predict a 'leaking' of wavefunction density into the shell as the shell becomes thicker.

The effective mass model was found to give satisfying fits to experimental electronic absorption and emission data, but tight binding calculations should theoretically be better suited for calculating electronic structure in quantum wells of only one monolayer thickness – as is the case with CdS/HgS/CdS. Bryant and co-workers carried out calculations using the tight-binding approach in 2001 [17]. The results matched the experimental electronic absorption spectra well, although it is difficult to determine if the results are more accurate than those gathered from the effective mass approach.

Steady State Absorption and Emission Spectroscopy

The ground state absorption spectrum of CdS/HgS/CdS quantum dot quantum well nanocrystals is shown in Figure 1.2 taken from [11]. The individual spectra show the evolution of CdS/HgS/CdS throughout the course of the synthesis. The starting spectrum is that of CdS, followed by a spectrum of CdS/HgS and so on. The addition of Hg^{2+} ions to a colloidal suspension of CdS nanocrystals leads to a red shift of the absorption spectrum, as shown in Figure 1.3 [13]. The figure also shows the absorption

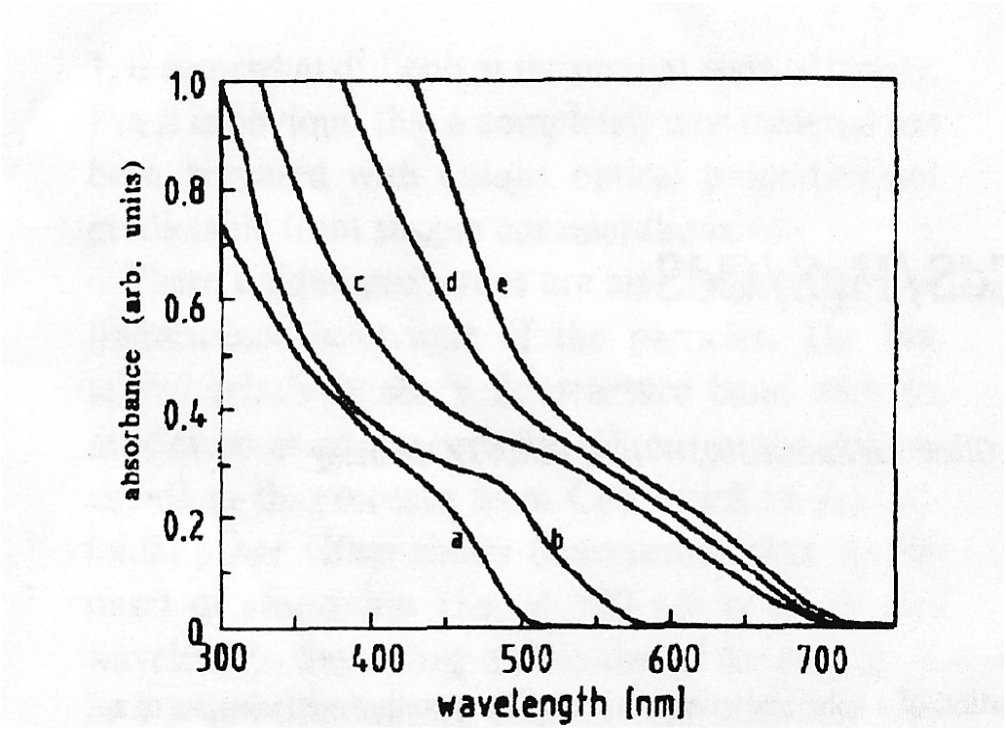

Figure 1.2 – Ground state absorption spectra of (a) CdS, (b) CdS/HgS, (c) CdS/HgS/CdS, (d) and (e) CdS/HgS/CdS plus increasing amounts of CdS (thicker outer layer)

spectrum of a mixed binary phase of Cd(Hg)S nanocrystals for comparison. From the difference in the spectra there is indication that the quantum dot quantum well nanocrystals should be layered in structure and not simply a mixed binary phase. More experimental evidence of this has been gathered and will be discussed more in a later section. The addition of Hg^{2+} and capping with CdS leads to an increase in the extinction coefficient of the particles, as would be predicted by an increase in size and therefore number of electrons in the nanocrystal [18].

The emission spectrum of CdS/HgS/CdS quantum dot quantum well nanocrystals is different from the emission spectrum of its individual parts, as investigated by

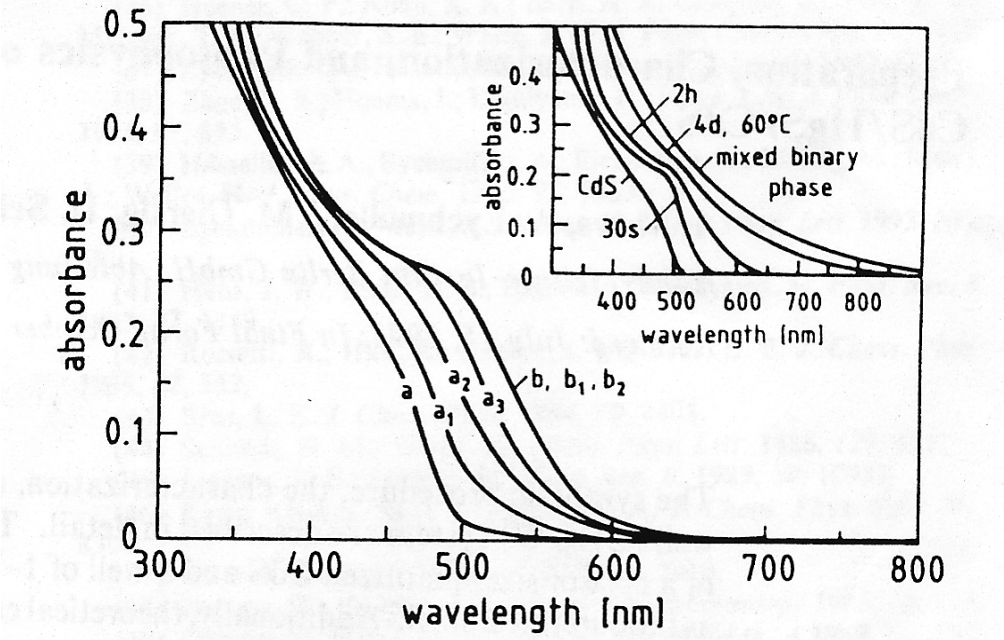

Figure 1.3 – Development of the absorption spectrum of CdS nanocrystals during the addition of Hg^{2+} in 2×10^{-5} M increments (a_1 through b_2). Inset: CdS nanocrystals plus 8×10^{-5} M Hg^{2+} after times indicated along with an intentionally prepared CdS/HgS alloy colloid

Haesselbarth and co-workers in 1993 [10]. They investigated the luminescence of mixed CdS/HgS colloids of different compositions. Colloidal HgS does not luminesce strongly on its own, but when capped with increasing amounts of CdS, a broad emission band centered around 950 nm become apparent Figure 1.4 [10] that does not shift with increasing amounts of CdS. The absence of spectral diffusion indicates that the composition of the particles is not changing, but rather the CdS capping is removing surface trapping sites that contribute to non-radiative relaxation pathways and quench the luminescence – this idea is know as fluorescence activation and may be used to enhance luminescence in semiconductor nanocrystals. The results in Figure 1.4 [10] imply the

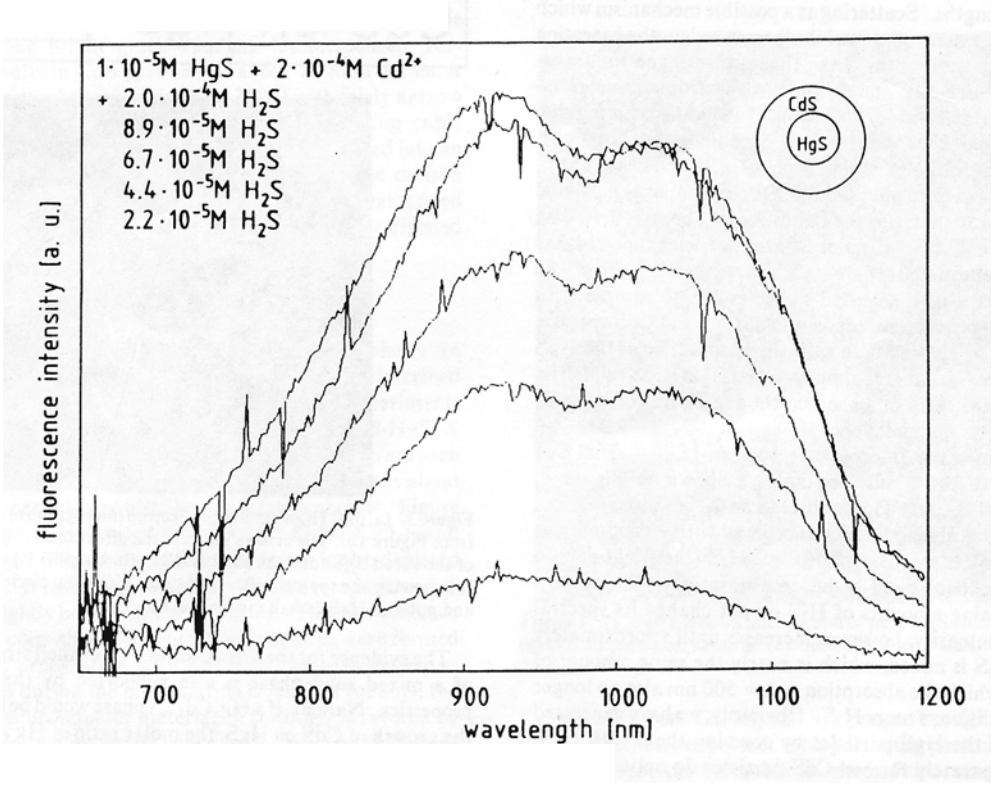

Figure 1.4 – Emission spectra of HgS nanocrystals capped with different amounts of CdS.

formation of a CdS shell over the HgS core particle. The formation of HgS islands on CdS was also characterized through fluorescence spectroscopy in Figure 1.5 [10]. With increasing addition of Hg^{2+} to the suspension of CdS, the excitonic emission of CdS decreases while a new, broader emission band grows in at longer wavelengths. The new emission band is interpreted as emission from the size-quantized islands of HgS on the surface of CdS [10].

The emission spectrum of CdS/HgS/CdS quantum dot quantum well nanocrystals is shown in Figure 1.6 [11]. The fluorescence intensity of the colloidal sample depends on the number of layers of CdS used to cap the HgS well – more CdS layers produce an

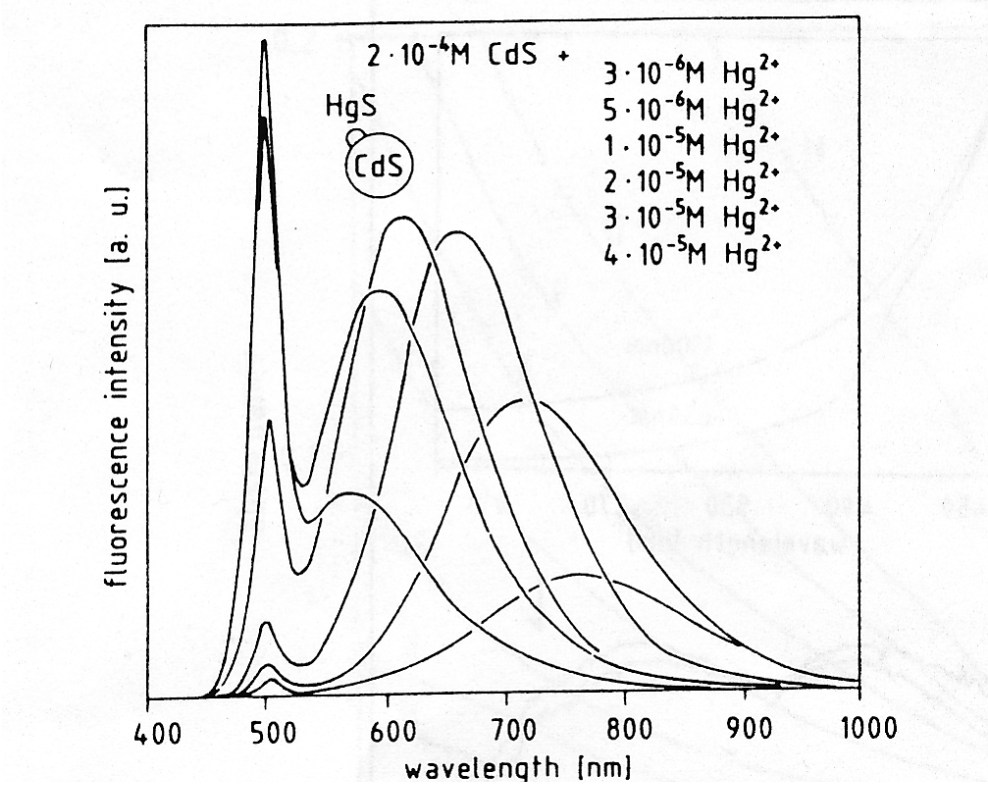

Figure 1.5 – Emission spectra of CdS nanocrystals as a function of added Hg^{2+}.

increase in fluorescence intensity [13]. The quantum yields for luminescence also decrease as a function of HgS well layer thickness.

Time-Resolved Luminescence Spectroscopy

The time dependence of luminescence from HgS islands on the surface of CdS nanocrystals was the first investigation of luminescence decay in CdS/HgS mixed

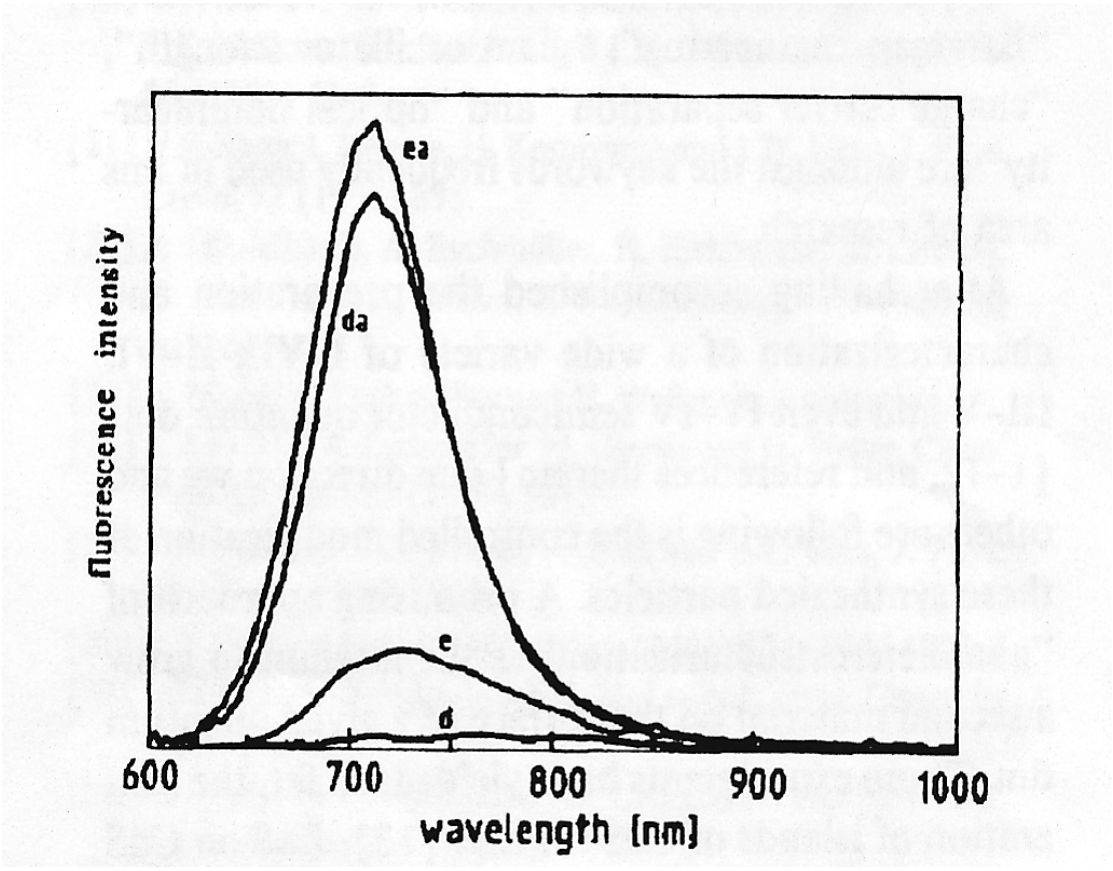

Figure 1.6 – Emission spectra of CdS/HgS/CdS (d and da) and CdS/HgS/$(CdS)_3$ (e and ea) before and after fluorescence activation.

nanoparticles [10]. The addition of Hg^{2+} ions to a suspension of CdS nanocrystals led to the quenching of the CdS excitonic emission intensity at 500 nm, but did not affect the luminescence lifetime as shown in Figure 1.7. With the loss of excitonic emission at 500 nm comes the growth of an emission band at longer wavelengths due to HgS island emission. The emission from CdS/HgS island composites was characterized using methyl viologen as an electron scavenger [10]. Methyl viologen was observed to dynamically quench the excitonic luminescence from the CdS core after excitation at 300 nm (Figure 1.8). Dynamic quenching refers to the process of decreasing the radiative lifetime without affecting the initial luminescence intensity. This kind of result is

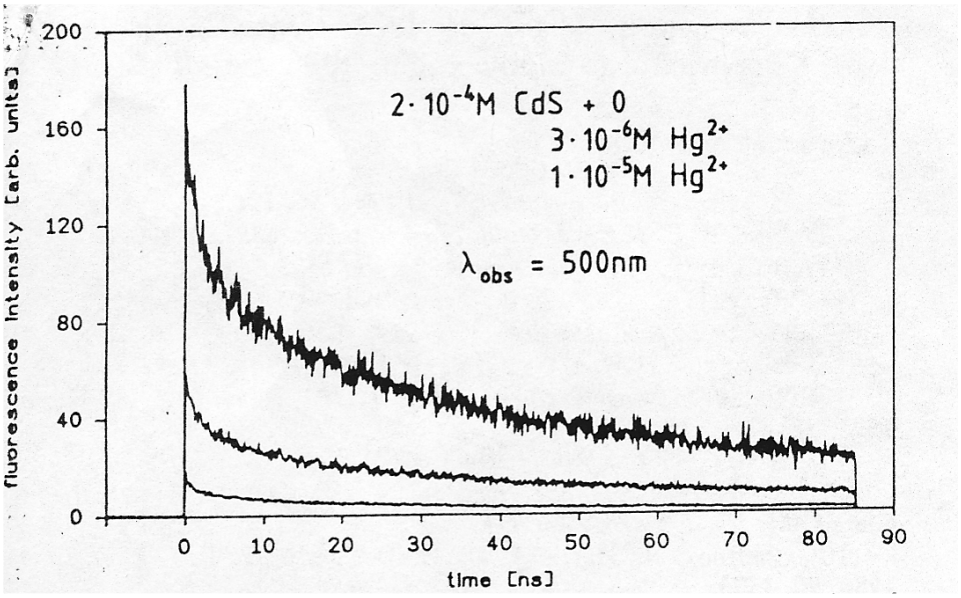

Figure 1.7 – Luminescence decay of CdS nanocrystals monitored at 500 nm as a function of added Hg^{2+}.

consistent with a quenching mechanism in which the quenching process kinetically competes with the electron-hole radiative recombination. Luminescence from the HgS islands at 650 nm behaves differently however, with the initial intensity and lifetime decreasing with the addition of methyl viologen (Figure 1.9). Together these results suggest that the methyl viologen scavenges electrons from the CdS surface through electron transfer before they can reach the HgS islands to give HgS luminescence. This mechanism explains both the dynamic quenching of the CdS luminescence and the reduced signal intensity and lifetime of the HgS island luminescence.

The time dependence of the luminescence decay for excited CdS/HgS/CdS nanocrystals is shown in Figure 1.10 and follows a two exponential decay at all temperatures [13]. The fast component of the decay remains constant at all temperatures while the slow component becomes much lower in amplitude at low temperatures. The

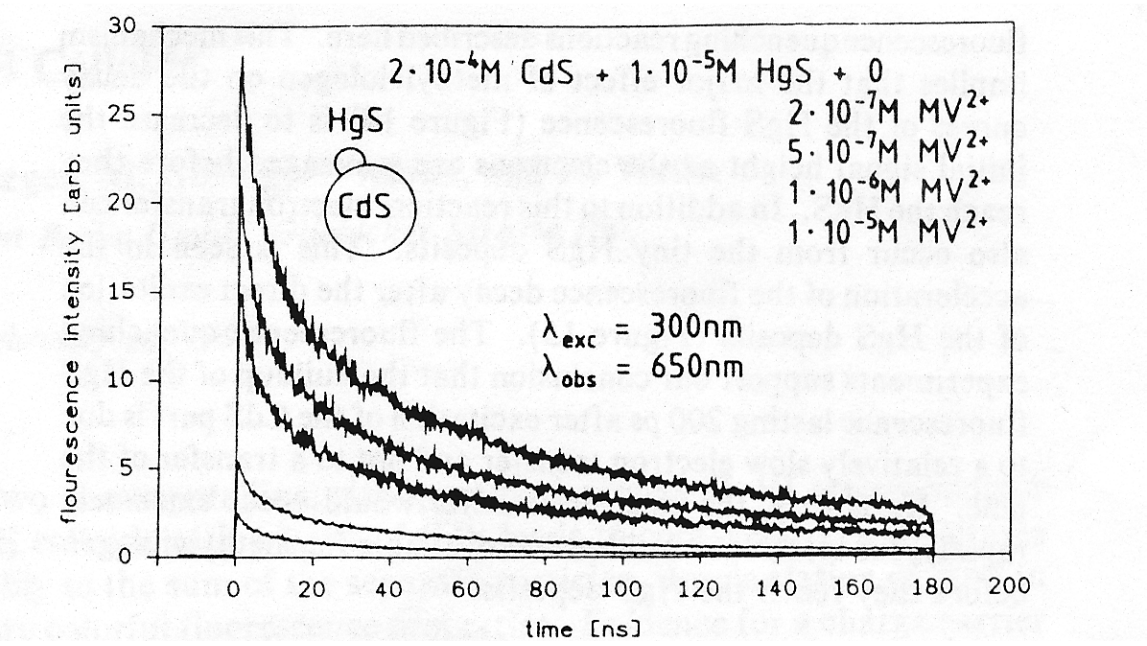

Figure 1.8 – Luminescence decay of CdS nanocrystals with islands of HgS as a function of methyl viologen concentration. Excitation was carried out at 300 nm (CdS core) and monitoring of the emission at 650 nm.

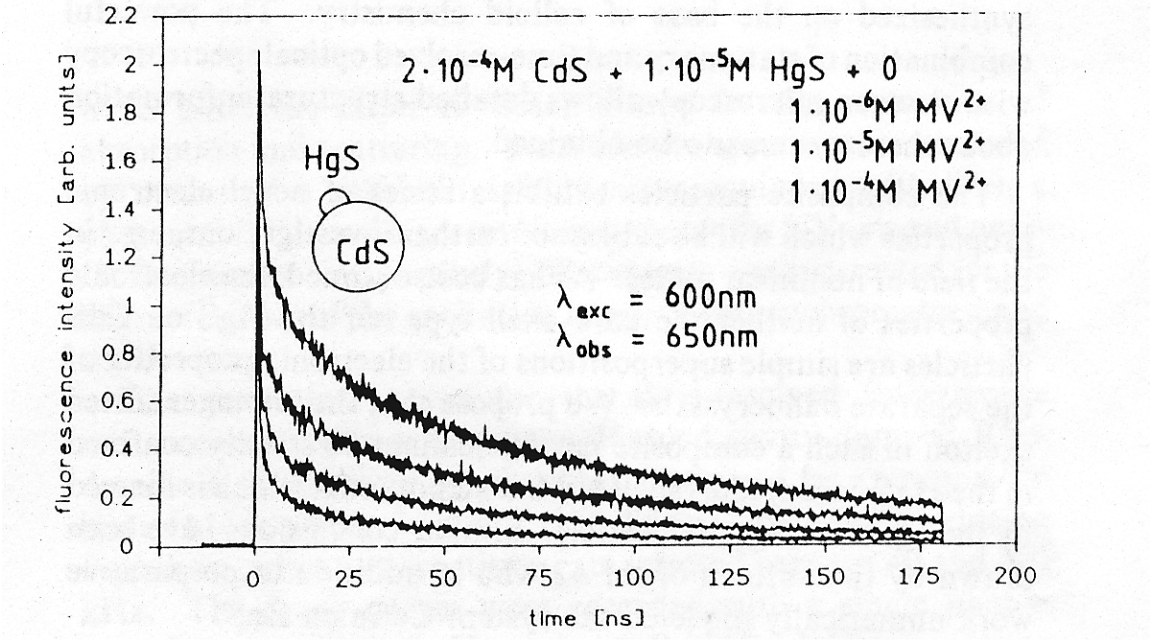

Figure 1.9 – Luminescence decay of CdS nanocrystals with islands of HgS as a function of methyl viologen concentration. Excitation was carried out at 600 nm (HgS islands) and monitoring of the emission at 650 nm.

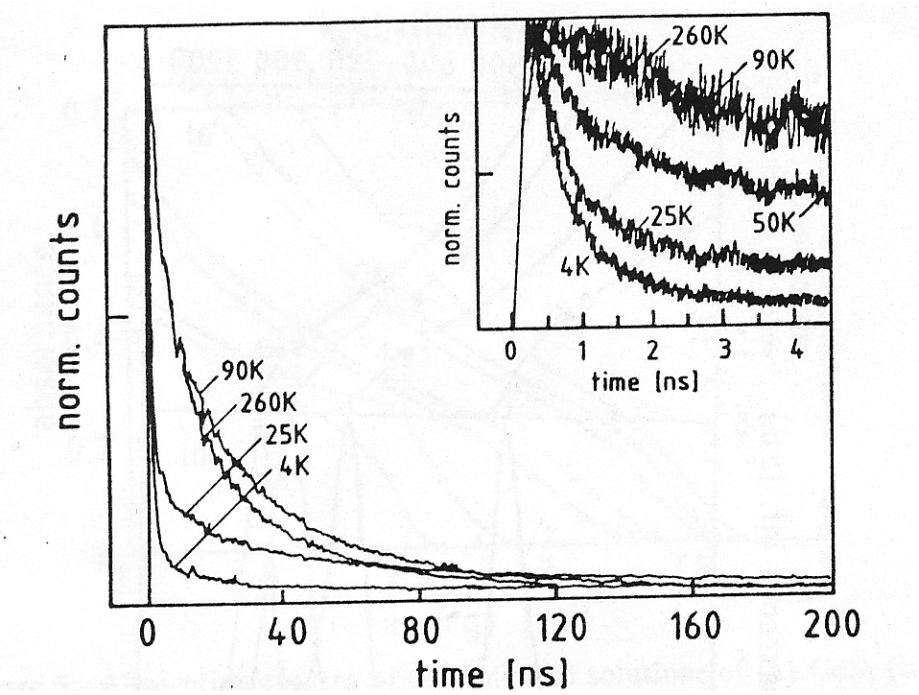

Figure 1.10 – Luminescence decay of CdS/HgS/CdS nanocrystals as a function of temperature.

single wavelength decay kinetics at longer emission wavelengths is slower, with radiative lifetimes at 20 K of several microseconds. In most semiconductor nanocrystals, slow luminescence decay kinetics is attributed to radiative relaxation from surface trap states in which the overlap between the electron and hole wavefunction may be reduced. However, since the radiative recombination in CdS/HgS/CdS most likely occurs in the isolated HgS well, the time-resolved luminescence results for this system bring this model under some scrutiny. Mews proposed the importance of the exchange interaction between electrons and holes in suggesting a model for the time-resolved luminescence results for CdS/HgS/CdS quantum dot quantum wells [14]. The exchange interaction splits the lowest excited state into several energy levels, the lowest of which is optically

passive according to the selection rules for radiative electronic transitions. The low oscillator strength of these low energy transitions leads to the slow kinetics observed.

Fluorescence Line Narrowing Spectroscopy

Size-selective spectroscopy techniques such as fluorescence line narrowing spectroscopy (FLN) are powerful methods for overcoming the inhomogeneous broadening of electronic transitions in semiconductor nanocrystals. The principle of fluorescence line narrowing spectroscopy is to selectively excite a small fraction of the nanocrystal sample population and observe the emission spectrum with high resolution. Selection is carried out by exciting the sample at the very edge of the absorption onset, thereby selecting only the largest of the nanocrystals in the sample. If carried out at low temperature, this procedure should give intrinsic, sharp emission spectra that aren't washed out by rapid non-radiative relaxation and inhomogeneous broadening effects. The FLN spectrum of CdS/HgS/CdS quantum dot quantum well nanocrystals (Figure 1.11) shows a vibronic progression of 285 cm^{-1} [14, 15]. This type of vibrational mode is associated with the phonon modes in the semiconductor crystal lattice and arises in the FLN spectrum through coupling of the electronic transitions to longitudinal optical (LO) phonons. The LO phonon modes of bulk CdS and HgS are 300 cm^{-1} and 250 cm^{-1} respectively. The observed progression of 285 cm^{-1} is therefore closer to the LO phonon mode of CdS, suggesting that radiative transitions from the lowest excited state couple to a ground state that is predominately CdS in structure. This result has been supported by a number of other spectroscopic measurements.

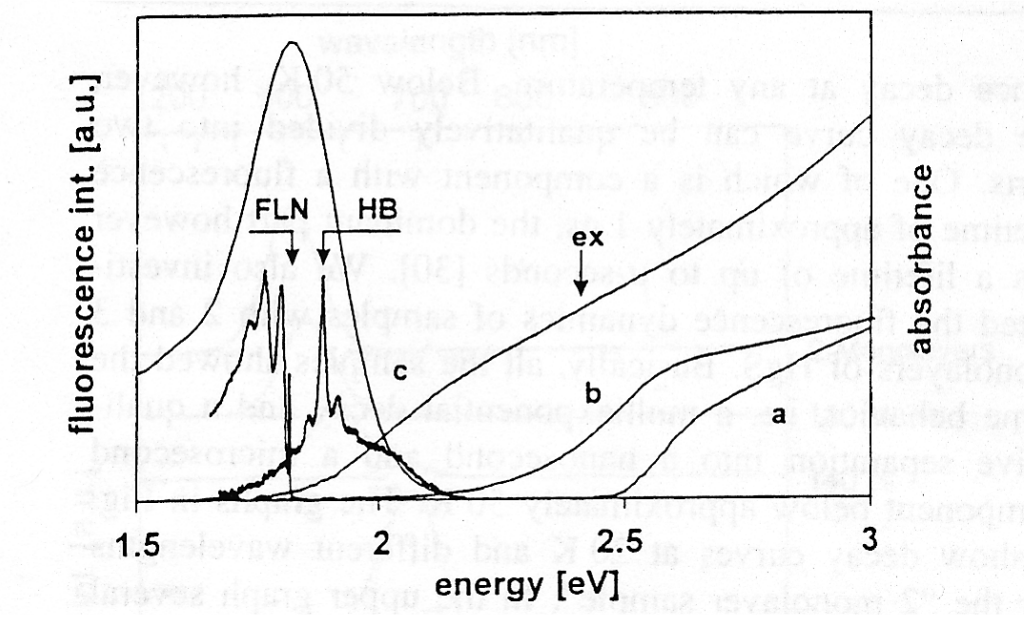

Figure 1.11 – Ground state absorption spectra of (a) CdS, (b) CdS/HgS, (c) CdS/HgS/CdS and fluorescence line narrowing (FLN) and hole burning (HB) spectra of CdS/HgS/CdS.

Single-Dot Spectroscopy

Koberling, Mews and Basche performed an extensive single-dot spectroscopy study in which they investigated the spectral and temporal evolution of the single dot luminescence from CdS and CdS/HgS/CdS nanocrystals as a function of excitation power [19]. Their results help to corroborate the idea that emission from quantum dot quantum well nanocrystals comes from the isolated HgS well layer of the structure.

The spectral and temporal profile of the single-dot emission from CdS nanocrystals is shown in Figure 1.12 [19]. At lower excitation powers (300 W/cm^2) the emission spectrum consists of a single line that is fairly narrow and featureless. The integrated emission intensity as a function of time is also constant, with no indication of

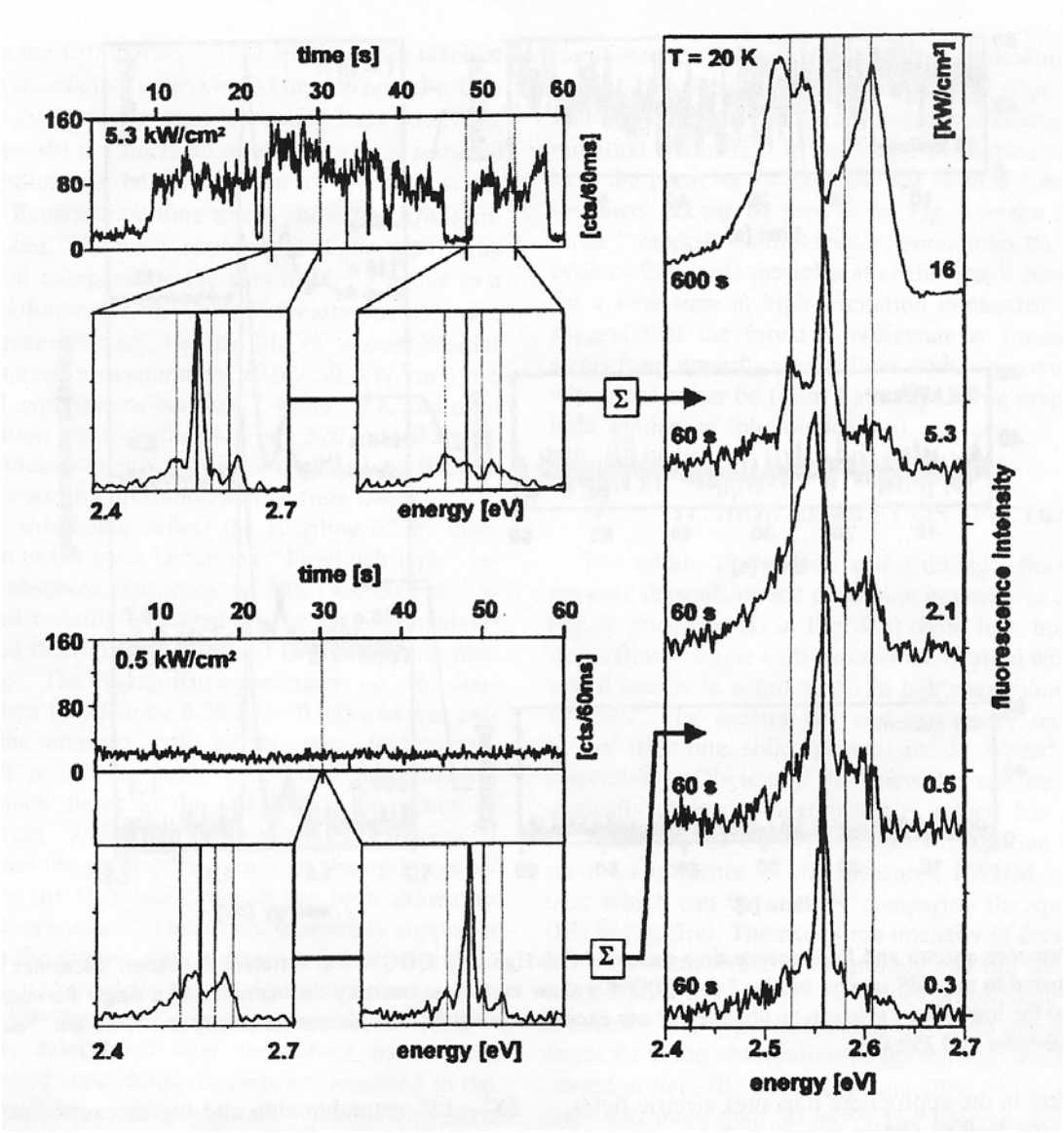

Figure 1.12 – Single dot luminescence from CdS nanocrystals. Lower left: time profile of the integrated emission at 0.5 kW/cm^2 excitation density. Upper left: time profile of the integrated emission at 5.3 kW/cm^2 excitation density. Right: time averaged single dot emission spectra of CdS nanocrystals as a function of increasing excitation density.

blinking phenomena. At higher laser powers (2-16 kW/cm^2), new lines begin to appear in the spectrum and blinking starts to become apparent in the temporal profile.

Some of the proposed origins of the new spectral lines and blinking in the time profile include bi-exciton effects and surface trap induced Stark effects. Wind and co-

workers [20] have studied luminescence from single CdSe nanocrystals at high laser intensity and identified a number of optically active transitions coming from bi-exciton states with transition energies very close to that of the 1S-1S lowest excited state transition. Also in CdSe, Empedocles and Bawendi [21] observed spectral shifts up to 75 meV that was attributed to Stark effects induced by charge carriers trapped in surface states. Similar shifts are seen in CdS nanocrystals, and it seems reasonable to assume that the surface Stark effect plays a large role in the explanation of the observed single-dot spectral.

In contrast to CdS, quantum dot quantum well CdS/HgS/CdS nanocrystals Figure 1.13 [19] show no fluctuations in their single-dot spectra as a function of excitation power. Blinking is also not observed in the time profile although some fluctuations are apparent at the highest power. As mentioned before, a good deal of evidence suggests that emission from CdS/HgS/CdS quantum dot quantum well nanocrystals comes from the HgS well. Since the HgS well is imbedded with in the particle, surface trapping effects should have a minimal influence on the emission spectrum. If the power-dependent multiple lines seen in CdS single-dot spectra can be attributed to surface trap induced Stark effects, it seems reasonable to suggest that such effects are not involved for CdS/HgS/CdS, since power-dependent mulitplets are not observed.

An additional line in the single dot emission spectrum of CdS/HgS/CdS is observed, however its position and relative intensity does not shift with changing laser intensity. The line is shifted 285 cm^{-1} lower in energy from the main emission peak. The same vibronic progression was observed in fluorescence line narrowing experiments (FLN) and was attributed to the coupling of the electronic transition to LO phonons of

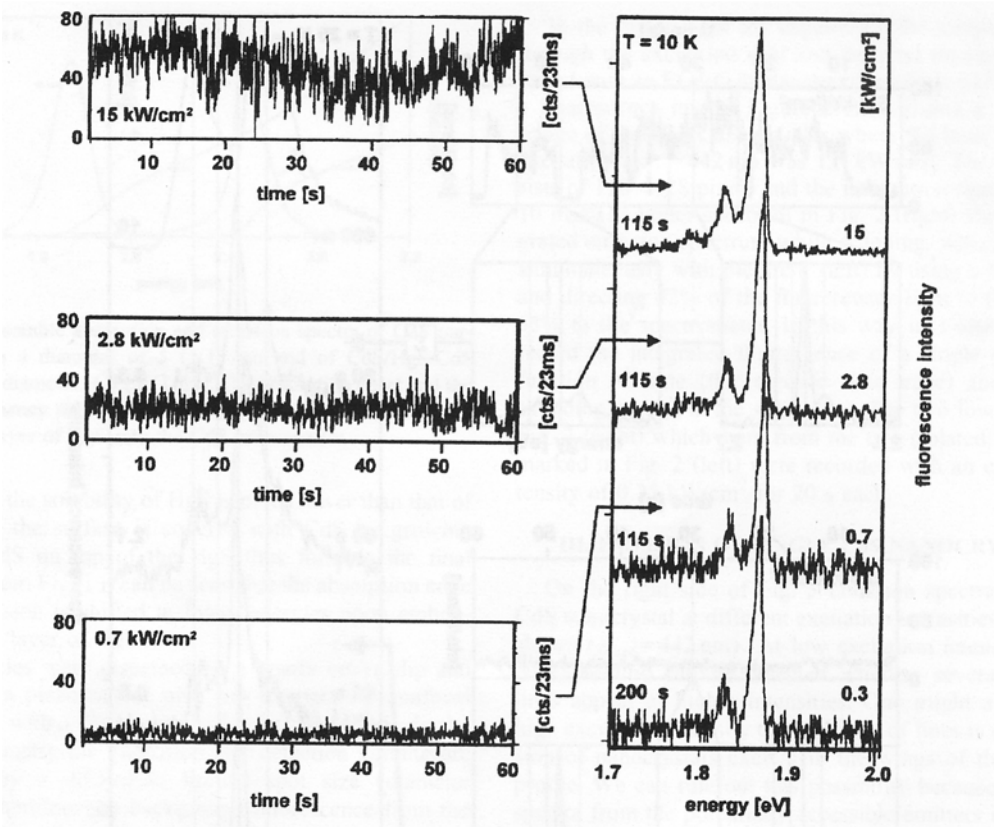

Figure 1.13 – Single dot luminescence from CdS/HgS/CdS nanocrystals. Left: time profile of the integrated emission at three different excitation densities. Right: time averaged single dot emission spectra of CdS/HgS/CdS nanocrystals as a function of

CdS (bulk LO phonon mode 300 cm^{-1}). This again indicates that the ground state is most likely delocalized over the entire nanocrystal and having high CdS character [19].

Transient Photobleaching Spectroscopy

High-intensity laser pulses have been used to induce transient photobleaching in CdS and CdS/HgS/CdS quantum dot quantum well nanocrystals [18]. Transient photobleaching is the process by which a medium becomes partially transparent for a

brief (fs-ns) time following excitation with an intense laser pulse. The mechanism behind transient photobleaching in semiconductor nanocrystals remains the subject of some debate, with the two most common mechanisms being the state-filing model and the screening effect model.

The state-filling model assumes that, at the time of laser excitation, all charge carriers are in their lowest energy state and there is no net charge in either the valence or conduction bands of the semiconductor nanoparticle. Laser excitation produces an electron-hole pair with the electron occupying one of the levels in the conduction band and the hole similarly occupying a level in the valence band. During the time these charge carriers remain in these states, as determined by the appropriate relaxation rates, the transition involving those two states will be unavailable – the states are considered 'filled' as implied by the name of the model. The state-filling model seems appropriate for conditions of low excitation density: one or two electron-hole pairs per particle. However, under conditions of high excitation density (10 or more e-h pairs per particle), the screening effect model may be more influential.

The screening effect model of transient photobleaching assumes that the surface plays the greatest role in the excited state dynamics of semiconductor nanocrystals. It relies on charge carriers becoming trapped at the surface of the crystal and thereby inducing strong internal fields that effectively decrease the oscillator strength of the 1S-1S excitonic transitions [18]. The decreased oscillator strength leads to a temporary reduction in the absorption cross-section and ultimately leads to bleaching of the 1S-1S transitions. For high excitation densities one would imagine that Auger ionization and exciton-exciton repulsion would cause a number of charge carriers to access surface trap

states that may not be energetically available at low excitation density. Additionally, it seems unlikely that the screening effect produced by only one or two electron-hole pairs per particle would be sufficient to have a profound effect on the oscillator strength of the excitonic transition. For most general experimental conditions it is important to consider both mechanisms for interpretation of transient photobleaching processes.

Regardless of the mechanism involved in the bleaching process, the bleach spectrum should closely resemble the homogeneously broadened 1S-1S absorption spectrum. Bleach spectra of CdS, CdS/HgS and CdS/HgS/CdS nanocrystals are shown in Figure 1.14. For CdS nanocrystals, the bleach spectrum is centered on 470 nm, which corresponds nicely with the predicted 1S-1S transition energy from the ground state absorption spectrum [18]. For CdS/HgS/CdS, the bleach is centered on 650 nm with no bleach at 470 nm. All bleach spectra are symmetric broad Gaussian bands. The bleach spectrum of CdS/HgS/CdS also corresponds nicely with the expected 1S-1S excitonic transition of the particle as predicted from the ground state absorption spectrum. The fact that bleach at shorter wavelengths from CdS nanocrystals is not observed in the CdS/HgS/CdS spectrum implies that the electronic structure of CdS/HgS/CdS may be treated as a whole entity and not simply as a sum of CdS and HgS parts. Had bleach from CdS been observed in the transient photobleaching spectrum of CdS/HgS/CdS it would indicate that CdS and HgS were close contact, separated systems in which the electron transfer from one to another occurs on a nanosecond timescale. While the wavefunctions may indeed be combinations of CdS and HgS wavefunctions, the results of this study suggest that the contribution from the HgS well is to add a perturbation to the electronic structure of the system.

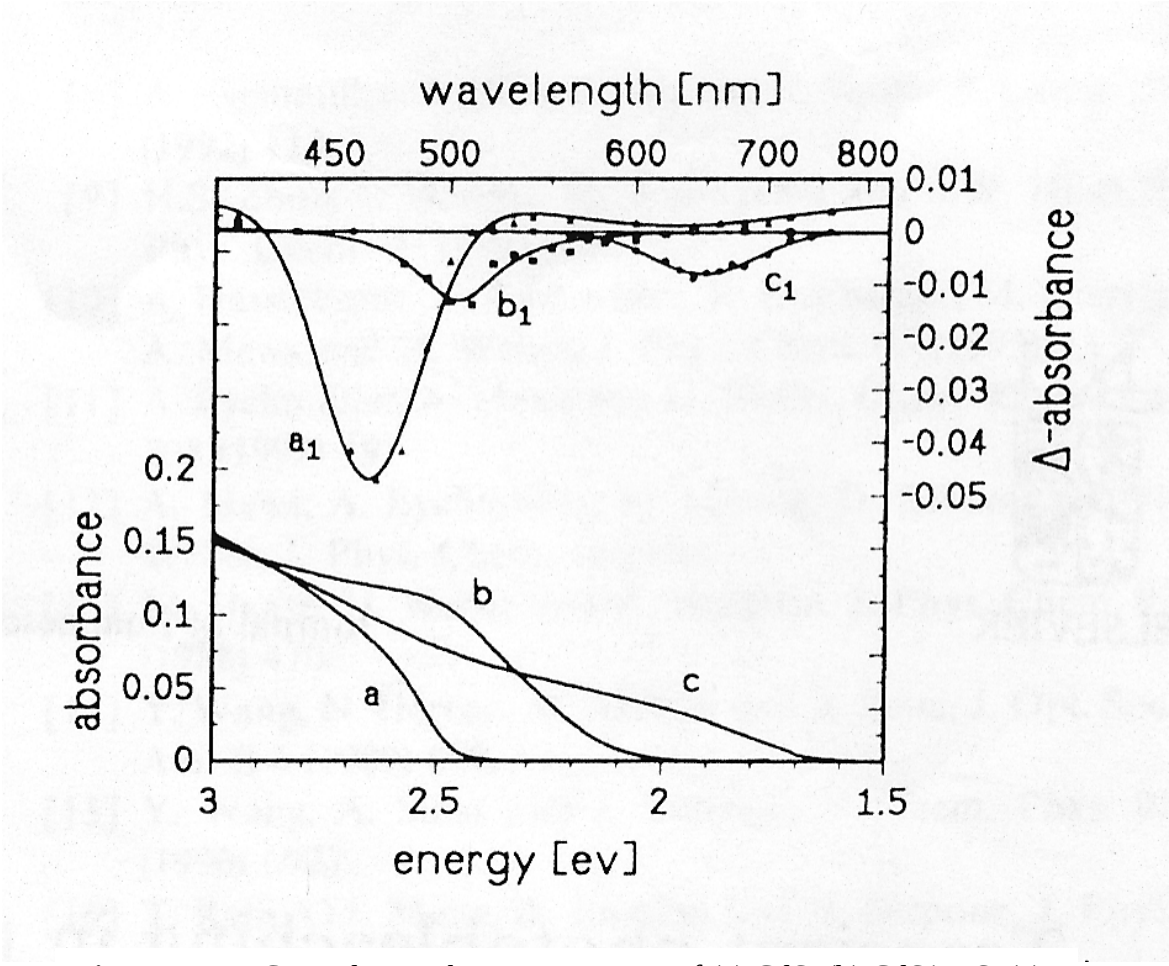

Figure 1.14 – Ground state absorption spectra of (a) CdS, (b) CdS/HgS, (c) CdS/HgS/CdS and their corresponding transient bleach spectra (a_1, b_1, c_1).

Transient Hole Burning Spectroscopy

Another size-selective spectroscopy technique that has been used to study semiconductor nanocrystals is transient hole burning spectroscopy (HB). The principles of transient hole burning spectroscopy are very similar to fluorescence line narrowing: narrow optical excitation of a small fraction of the sample size distribution to reduce homogeneous broadening effects. In transient HB spectroscopy, the sample is excited with a narrow bandwidth nanosecond laser pulse very close to the absorption onset and

probed with a broadband light source to obtain transient absorption spectra. As for FLN, HB spectroscopy is done at cryogenic temperatures.

The transient HB spectrum of CdS/HgS/CdS nanocrystals is shown in Figure 1.15 [14]. The change in absorption is negative indicating ground state depletion or 'bleach' and the bleach profile should follow the structure of the lowest 1S-1S excitonic transition. On top of a broad bleach band there is also a sharp peak at the excitation frequency with low intensity side bands at higher and lower energy. The side bands are split from the main peak by 250 cm^{-1}, almost identical to the bulk LO phonon of HgS (253 cm^{-1}).

From the experimental HB spectra recorded for different excitation wavelengths, a calculated homogeneous ground state absorption spectrum was calculated [14, 22] and shown in Figure 1.15. Since absorption reveals feature of the excited state electronic and vibrational structure, it was concluded that the 250 cm^{-1} vibronic progression was characteristic of an HgS well localized excited state in CdS/HgS/CdS. A homogenous linewidth of 50 cm^{-1} was extracted from the calculated spectrum, which is quite broad compared to the linewidth for molecules. The explanation given for this was the rapid dephasing of the excited state to large amplitude, low energy acoustic vibrational mode of the nanocrystal, but further investigation is needed to fully confirm this interpretation [14].

Picosecond Hole Burning Spectroscopy

R. Little and co-workers used picosecond hole burning spectroscopy to investigate the ultrafast relaxation of the excited state in CdS core and CdS/HgS/CdS

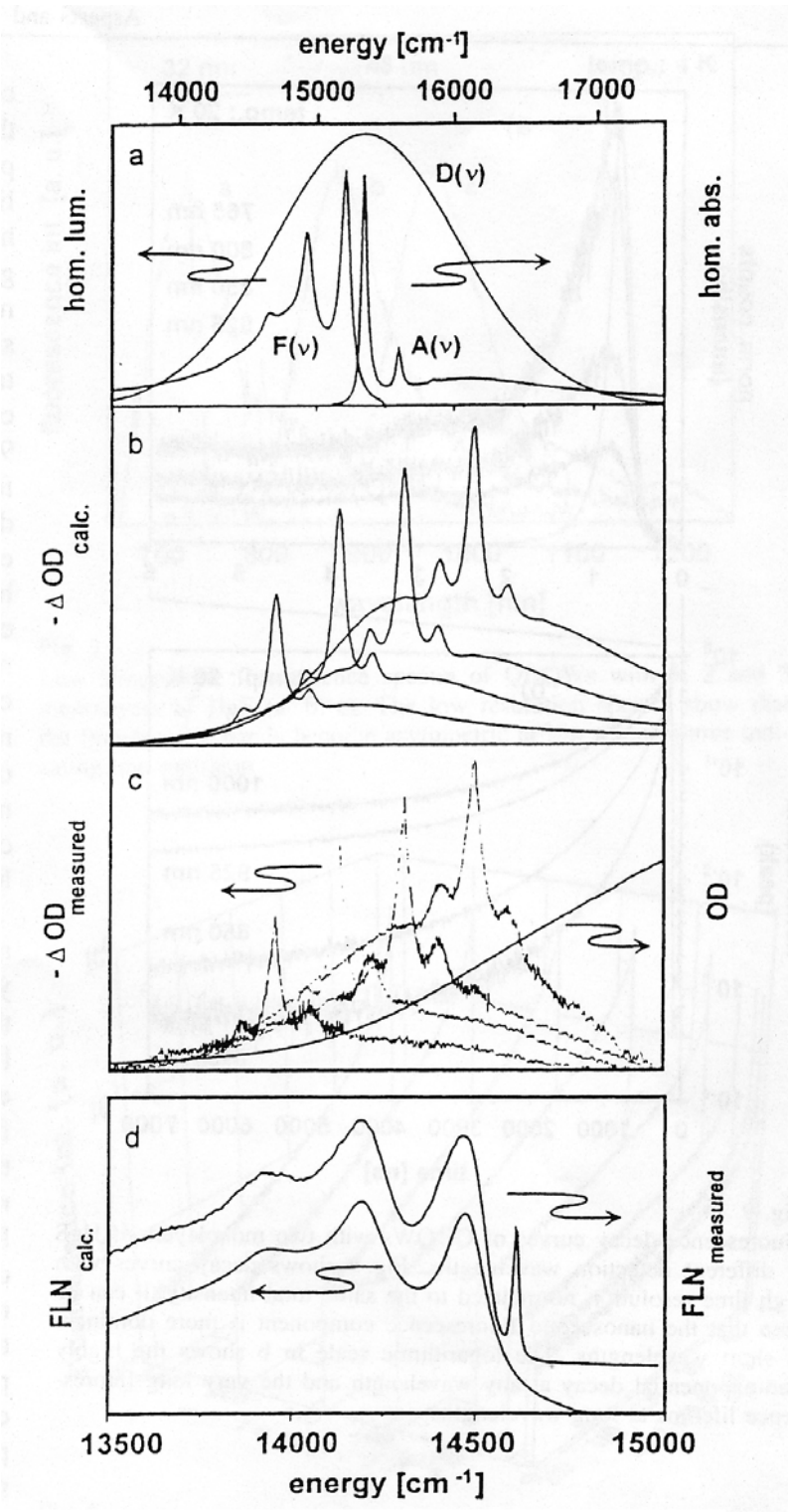

Figure 1.15 – (a) homogeneous absorption and emission spectra of CdS/HgS/CdS nanocrystals as determined from experimental and calculated transient hole burning (HB, b and c) and fluorescence line narrowing (FLN, d) spectra of CdS/HgS/CdS nanocrystals.

quantum dot quantum well nanocrystals [23]. HB spectra were recorded using femtosecond laser excitation at 400 nm and a broadband white light continuum probe. Optical holes burned in the spectrum of CdS particles did not shift as a function of time and remained centered at 475 nm over the timescale of 0-20 ps (Figure 1.16) [23]. The optical hole spectrum for CdS/HgS/CdS diffuses as a function of time in the first 2 picoseconds of the relaxation. Time constants for the fast and slow components of the transient bleach decay at different probe wavelengths were determined as well as the rise times (Figure 1.17) [23]. The wavelength dependent time constants follow two distinct functions: a steeply sloped function between 1.8 and 2.1 eV and a less steep, almost constant slope above 2.1 eV. The intersection of these two curves corresponds very well to the minimum of the second derivative ground state absorption spectrum and was assigned as an energy corresponding to a dark electronic transition or 'dark state'.

Sub-picosecond Hole Burning Spectroscopy

Yeh and co-workers investigated the evolution of spectra holes in CdS/HgS/CdS on the sub-picosecond time scale [22]. Hole burning spectra were collected using a 40 cm^{-1} bandwidth, 400 fs pump pulse and a 10 fs broadband probe pulse and the results are shown in Figure 1.18 [22]. Within the duration of the pump pulse, the hole-burning spectrum shows vibronic sidebands that are split from the main peak by 300 cm^{-1}. After the 400 fs pump, the energy splitting becomes 250 cm^{-1}, the same splitting observed in nanosecond hole burning experiments. This result suggests that the excited state evolves from an initially delocalized CdS state to a localized HgS state within the HgS well

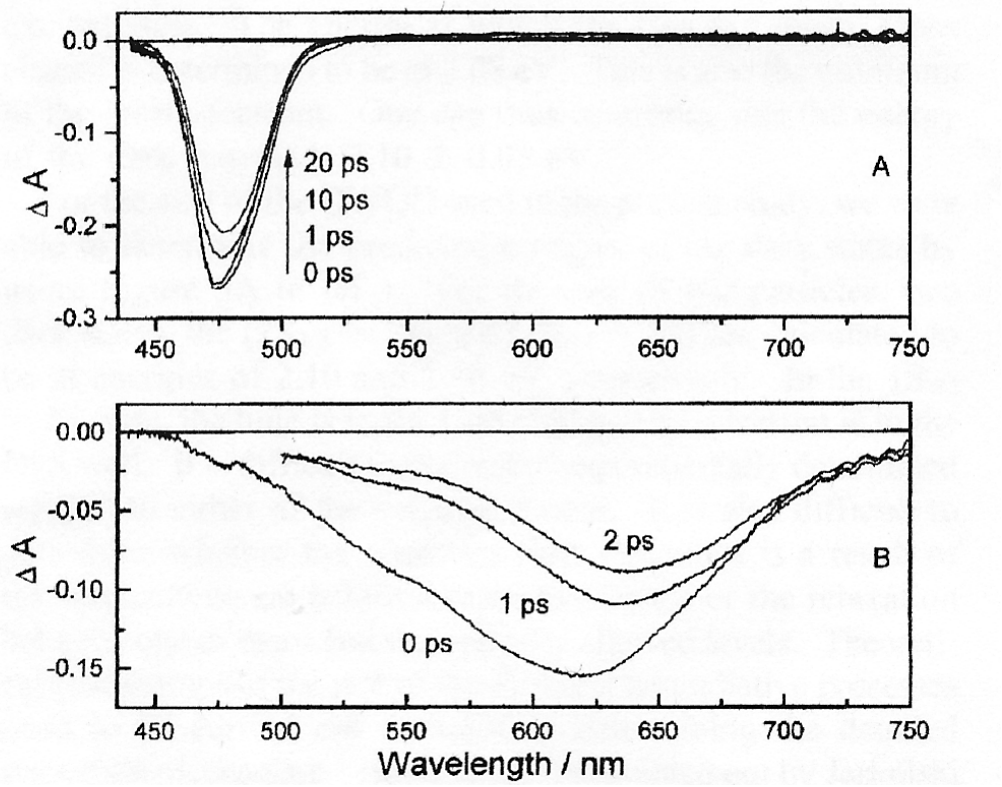

Figure 1.16 – Picosecond transient hole burning spectra of (A) CdS and (B) CdS/HgS/CdS nanocrystals at different probe delay times.

within a few hundred femtoseconds. This result is supported by pump-probe single wavelength kinetics experiments carried out by the same group of researchers [22].

Single wavelength pump-probe spectroscopy was performed using a 30 fs, 635 nm pump pulse and a 10 fs broadband probe pulse spectrally filtered at 650 nm. The results of the experiment are shown in Figure 1.19 [22]. The time profile of the transient bleach at 650 nm shows evidence of coherent oscillations in the differential transmission signal. A Fourier analysis of this oscillatory signal reveals an oscillation frequency of 300 cm^{-1}. This is the same frequency extracted from the HB spectra on this fast time scale and again suggests that the initial excited state is a delocalized CdS state.

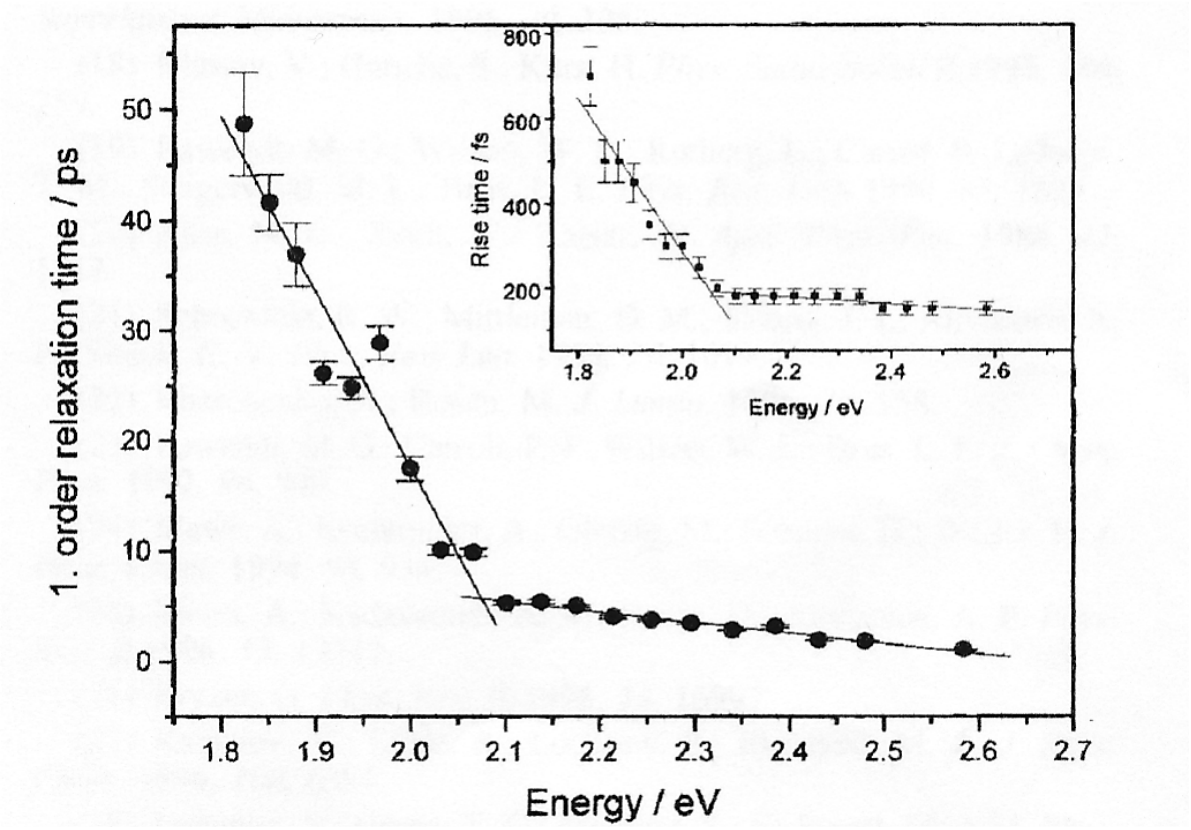

Figure 1.17 – First order relaxation times and rise times (inset) of the transient bleach in CdS/HgS/CdS nanocrystals as a function of monitoring energy.

Further pump-probe studies were carried out using a 120 fs, 620 nm pump pulse with probe pulses at longer (660-680 nm) and shorter wavelengths (580-610 nm). The experimental results are shown in Figure 1.20 [22]. For wavelengths to the red of pump, the transient bleach signal rises with a time constant of 400 fs, while for wavelengths to the blue of the pump; the bleach signal rises instantaneously and decays with a fast time constant of 400 fs. These results were interpreted to suggest the delocalized CdS initial state migrates to the HgS well within 400 fs.

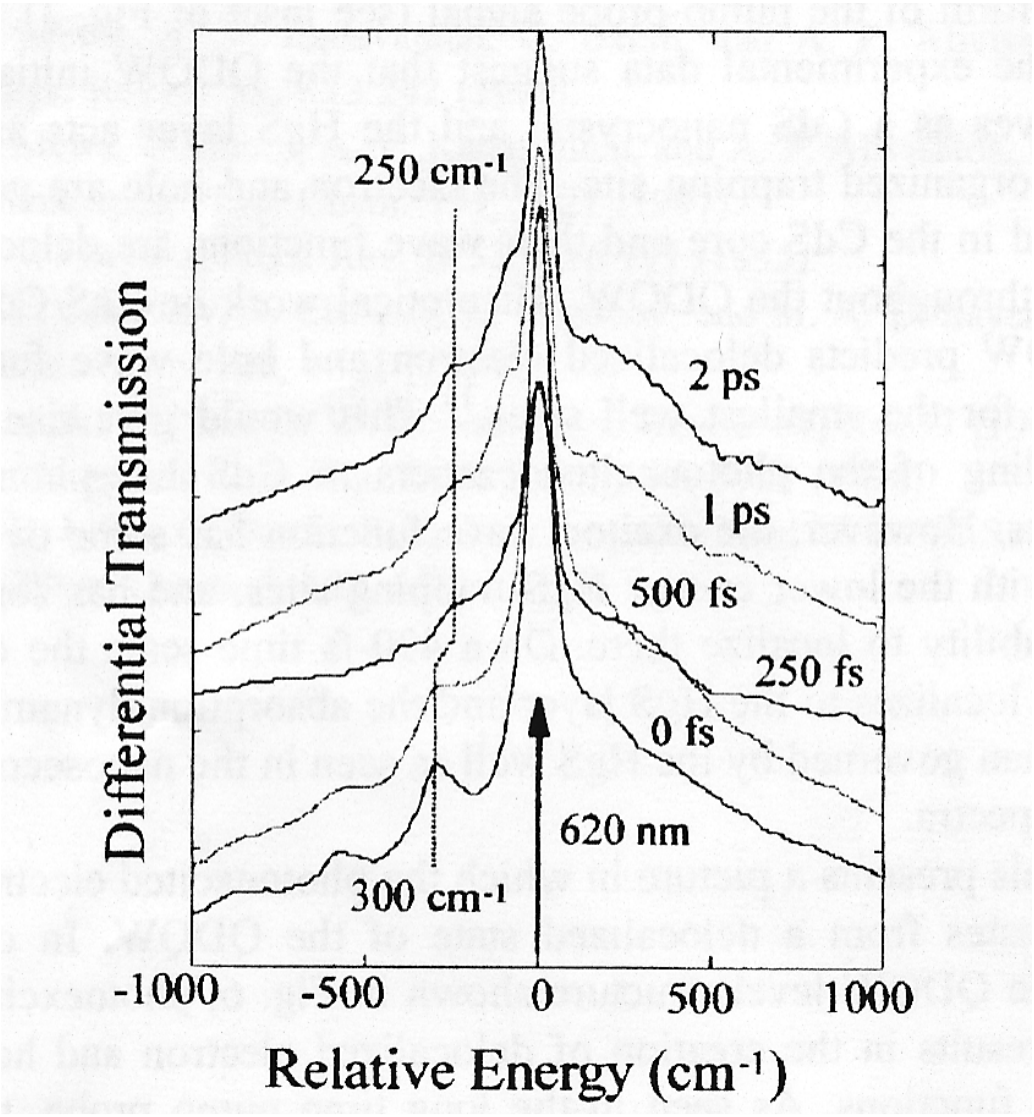

Figure 1.18 – Sub-picosecond transient hole burning (HB) spectra of CdS/HgS/CdS nanocrystals at different probe delay times. Dashed lines indicate the position of vibronic side peaks at frequency shifts of 250 cm^{-1} and 300 cm^{-1}.

Electron and hole localization times

Braun and co-workers [24] used sub-picosecond transient absorption spectroscopy to determine the localization times of the electron and hole in excited CdS/HgS/CdS nanocrystals. Pump-probe transient absorption measurements were done using different pump and probe wavelengths. Figure 1.21 [24] shows the rise and early decay portions of the transient signals obtained with 400 nm (a) and 650 nm (b) excitation. The probe wavelengths used were 470 nm, 525 nm, 560 nm, 625 nm and 760 nm. Using 400 nm excitation the rise time of the transient bleach signals at 470 nm, 525 nm, 560 nm and 625 nm was between 200 and 300 fs while the stimulated emission signal at 760 nm had a rise time of 1.5 ps. Using 650 nm excitation, the rise times of the bleach and stimulated emission signals were faster than the instrument response and assigned an upper limit of 50 fs. These results suggest that 400 nm and 650 nm excitation produce different excited state configurations that relax to the ground state with different kinetic parameters.

It has been suggested that 400 nm excitation of CdS/HgS/CdS nanocrystals produces an excited state that is predominately CdS in character. This supposition is supported by the work of Yeh and co-workers discussed previously [22]. The initially produced CdS excited state then relaxes to an HgS localized excited state within few hundred femtoseconds. This is evidenced by the 200-300 fs rise times of the transient bleach observed using 400 nm excitation. The long rise time of the stimulated emission at 760 nm comes from the fact that stimulated emission requires both charge carriers in the lowest excited state, whereas bleaching only requires one of the carriers to fill a particular state to bleach the transition. The rise of the stimulated emission signal

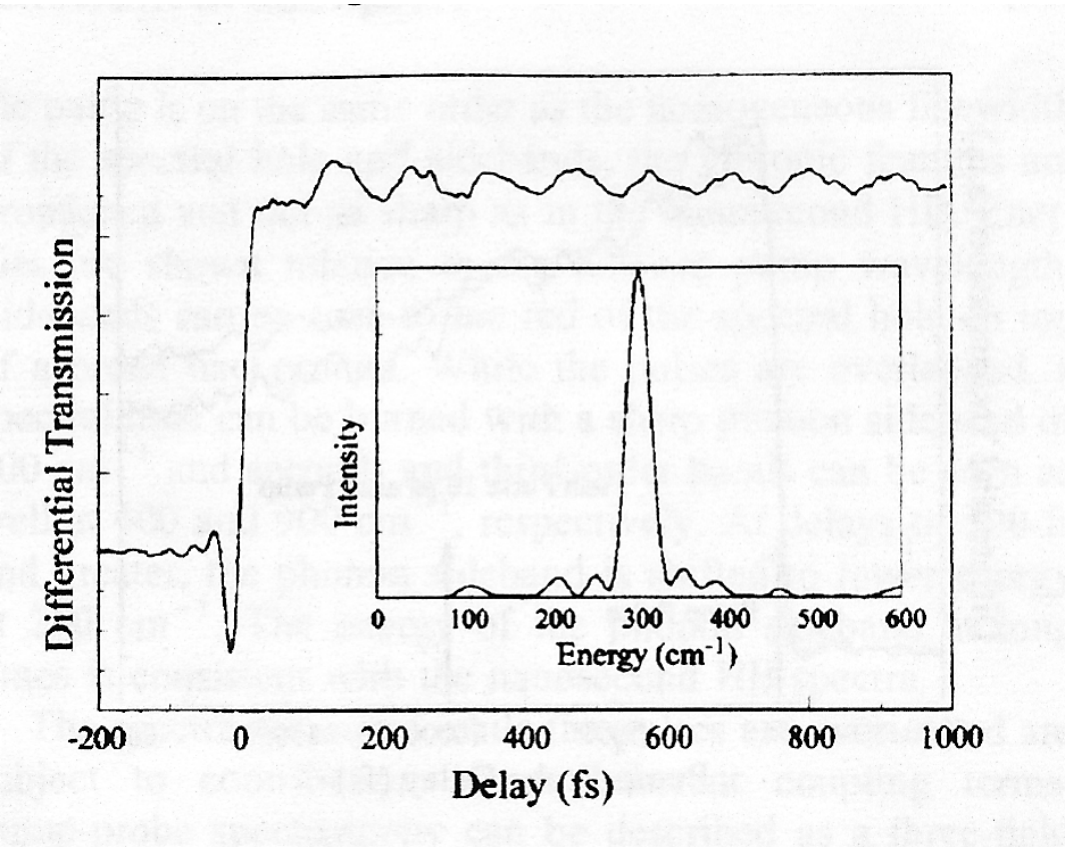

Figure 1.19 – Pump probe trace of excited CdS/HgS/CdS obtained using a 30 fs, 635 nm pump pulse and a 10 fs, 650 nm probe pulse. Inset: Fourier analysis of the oscillatory component of the signal.

given the evidence supporting the assignment of the lowest excited state in CdS/HgS/CdS to a localized HgS wavefunction, the rise time of the stimulated emission using 400 nm excitation is indicative of the carrier localization time of the slowest charge carrier (i.e. the time required to transfer charge from CdS to HgS). The assignment of which charge carrier localizes the slowest requires more state-specific evidence about the localization time of at least one of the carriers.

Intraband transient absorption in semiconductors and semiconductor nanocrystals appears in the near to mid infrared, typically between 1000 nm and 2000 nm for the electron and 3000 nm to 5000 nm for the hole. Theoretical calculations on the

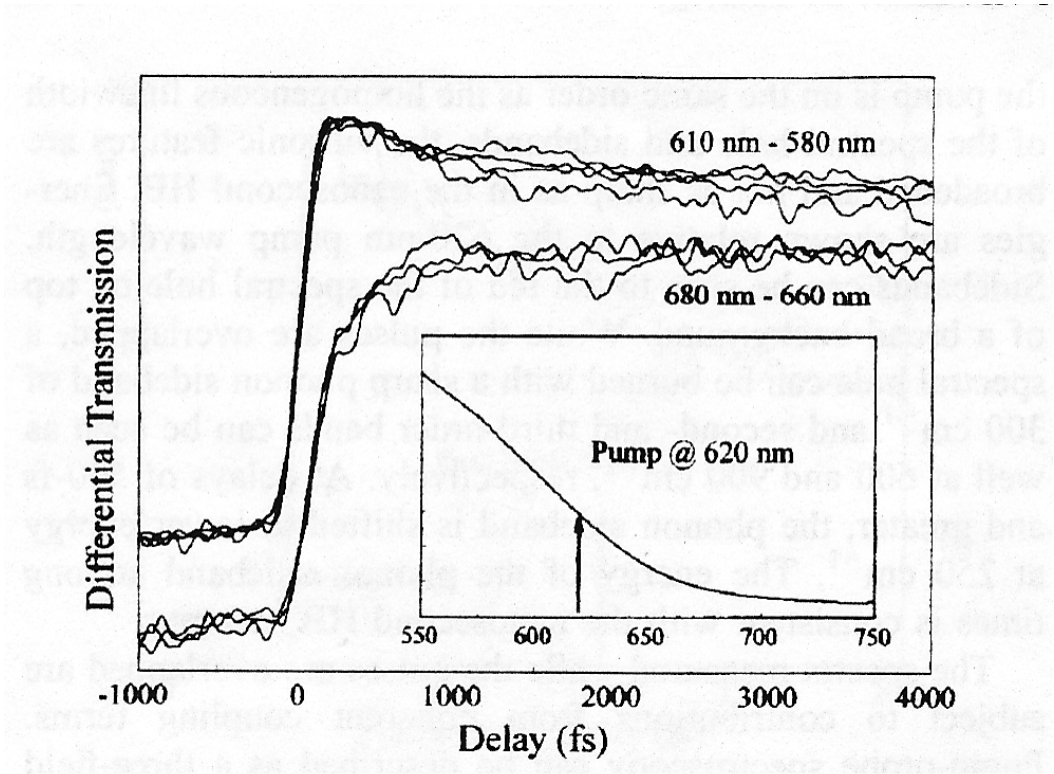

Figure 1.20 – Pump probe traces of excited CdS/HgS/CdS obtained using 160 fs, 620 nm pump pulses and 10 fs probe pulses with wavelengths shorter (580 – 610 nm) and longer (660 – 680 nm) than the pump wavelength. The decay time at 580 – 610 nm and rise time at 660 – 680 nm is 400 fs.

CdS/HgS/CdS system found an intraband transition energy for the hole of 0.28 eV, equivalent to 4400 nm. Pump probe transient absorption spectroscopy measurements were done using 4700 nm as a probe wavelength to determine the localization time of the hole. The results are shown in Figure 1.22 [24]. The rise time of the transient absorption signal at 4700 nm was measured for excitation wavelengths of (a) 266 nm, (b) 400 nm, (c) 580 nm, (d) 650 nm. In all cases the rise times are much faster than 1.5 ps, suggesting that the hole is the faster charge carrier and that the electron localizes to the HgS localized lowest excited state in 1.5 ps. Braun and co-workers [24] interpreted this by considering the fact that the electron must migrate between Cd and Hg metal ions in the

conduction band while the hole migrate between S ions in the valence band. Since the hole transfer process is a charge resonance process between similar sulfur ions it should be faster that transfer between two dissimilar ions such as Cd and Hg.

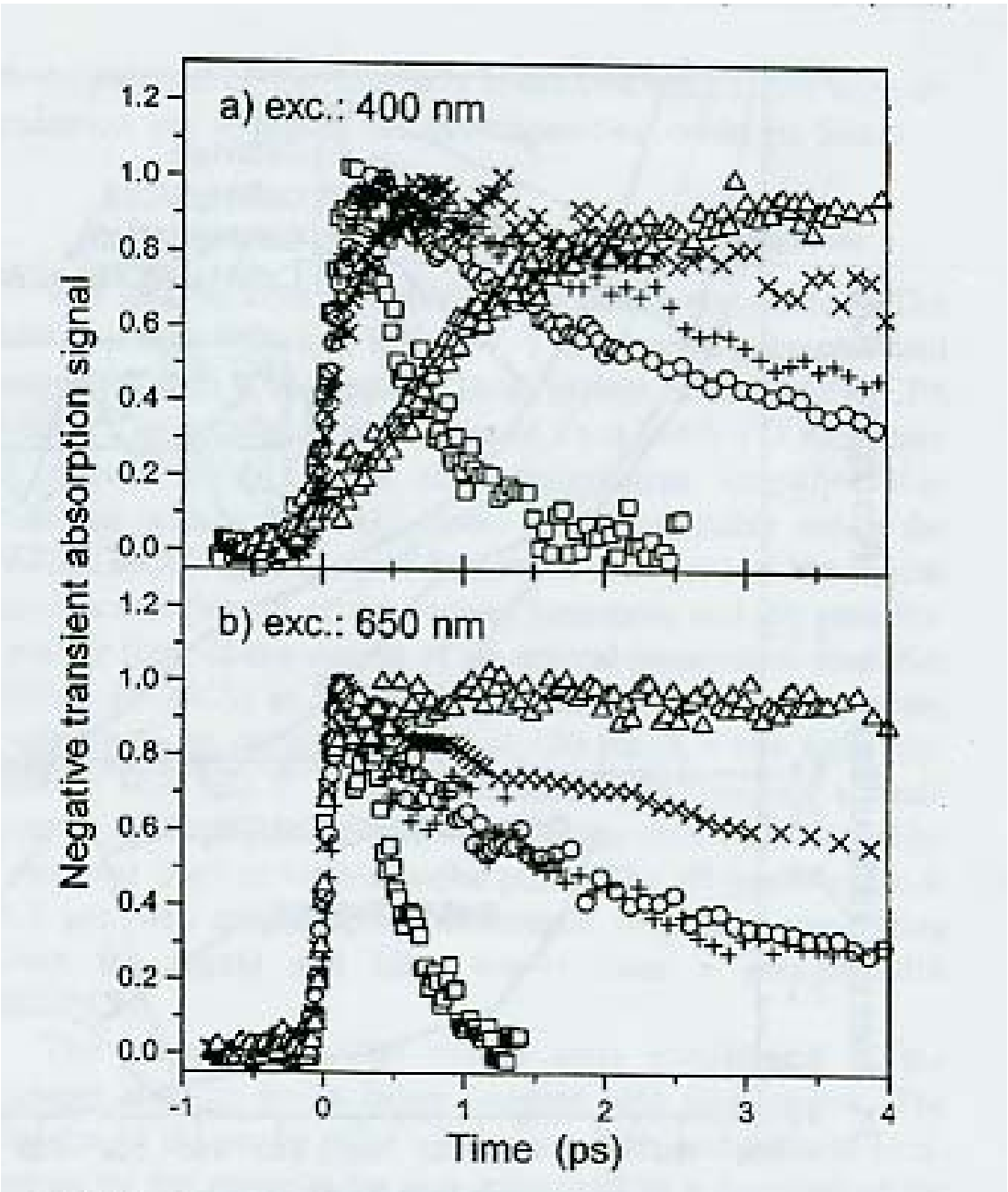

Figure 1.21 – Pump probe transient absorption traces of excited CdS/HgS/CdS obtained using 100 fs pump pulses of 400 nm and 650 nm wavelength. Samples were monitored at different wavelengths corresponding to transient bleach and stimulated emission.

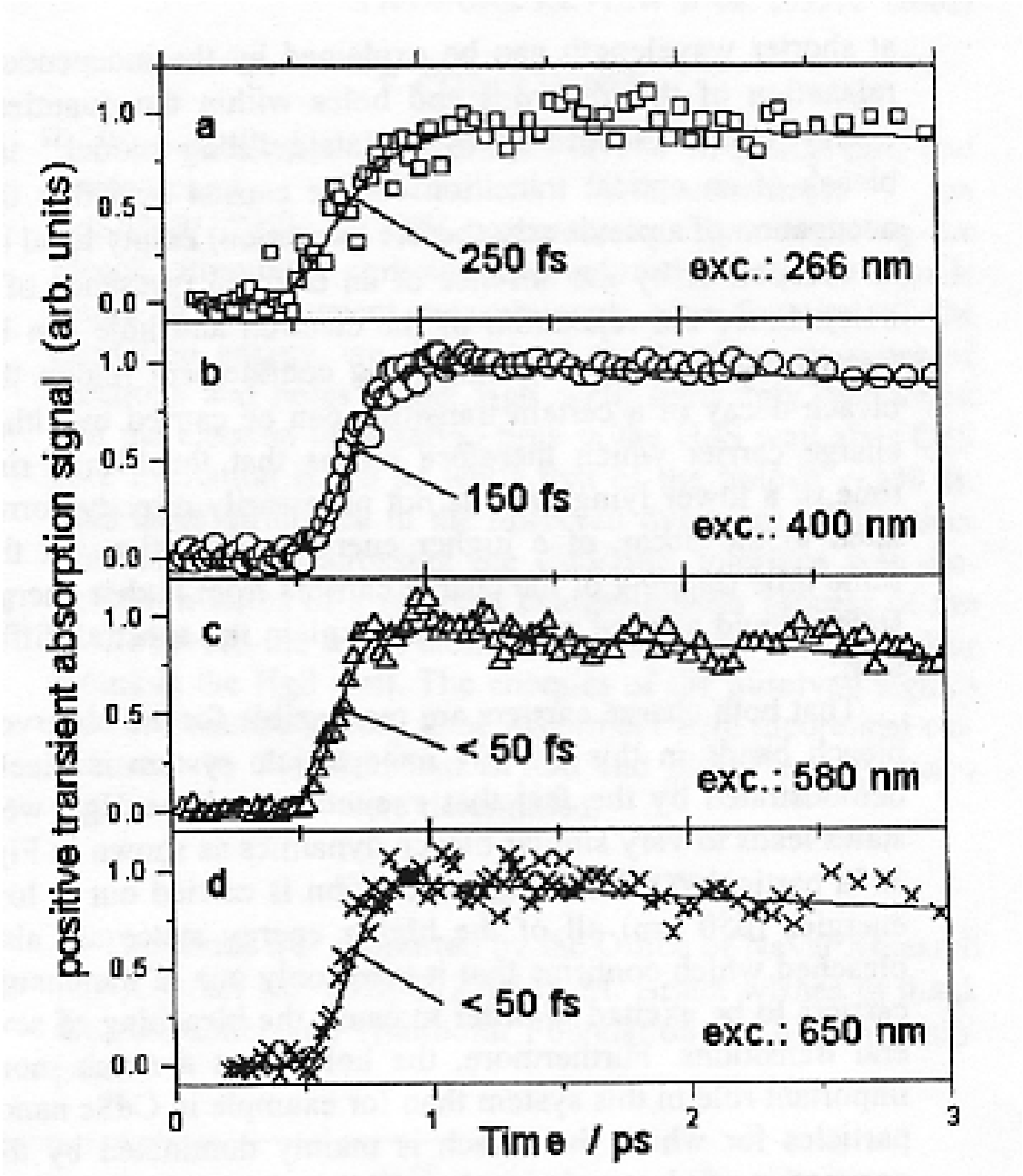

Figure 1.22 – Pump probe transient absorption traces of excited CdS/HgS/CdS nanocrystals monitoring at 4500 nm following 100 fs excitation at 266 nm, 400 nm, 580 nm and 650 nm.

1.3 CdS/CdSe/CdS Colloidal Quantum Wells

Continuing research in the area of semiconductor nanocrystal heterostructures has focused on the preparation and characterization of new systems with different structure and composition. The goal of this process is to prepare nanocrystals with increasing performance capabilities, i.e. higher luminescence quantum yields and longer photo-stability lifetimes, for use in the next generation of optical and electronic components. A major advancement in the field of semiconductor nanocrystal heterostructures has been the application of the SILAR (Selective Ion Layer Adsorption and Reaction) method to the growth of increasingly complex nanostructures. The SILAR method has been used for many years in the thin film industry but has just recently been applied to the preparation of colloidal systems. The best characterized of these new SILAR formed structures consists of a CdS core, a CdSe well of variable thickness and a CdS outer shell of variable thickness which is commonly referred to as a CdS/CdSe/CdS colloidal quantum well.

Synthesis and Composition

Synthesis of CdS/CdSe/CdS follows the same route as preparation of CdS/HgS/CdS nanocrystals. First, a stable core of CdS nanocrystals with a narrow size distribution is produced. The most effective way to stable and high quality CdS nanocrystals is through a high temperature organometallic reaction using CdO and elemental sulfur as precursors [25]. Cadmium oxide is heated in a fatty acid solvent to

300°C until the CdS dissociates to form Cd^{2+} ions. Elemental sulfur is dissolved in octadecene and rapidly injected into the hot reaction mixture. Small CdS crystals nucleate rapidly and homogeneously with the injection and then continue to grow in size as the mixture is continuously heated. The fatty acid solvent serves to stabilized the particles from aggregation by acting as a capping material. The size of the nanocrystals can be monitored by UV-VIS absorption spectroscopy. Once the desired size is reached that reaction mixture is cooled to arrest the growth process. Washing with methanol to remove any precursors that may be left over after the reaction purifies the nanocrystal samples. Cadmium sulfide nanocrystals prepared in this manor may be dispersed in many organic solvents and are stable for extended periods of time.

Growth of the CdSe shell on the outside of a CdS core is done by the SILAR method. Unlike in the case of CdS/HgS/CdS, the introduction of a CdSe layer onto CdS colloids cannot be accomplished by surface ion exchange. Instead, the growth of the CdSe layer proceeds by repeatedly injecting calculated quantities of Cd^{2+} and Se^{2-} precursors into the CdS core mixture that correspond to fractions of a monolayer until the desired shell thickness is reached [26]. Cadmium oxide is again used as the Cd^{2+} precursor and is dissolved in oleic acid. Elemental Se is used as the source of Se^{2-} and is dissolved in trioctylphosphine (TOP) in the form of the TOP-Se complex. The key aspect of the SILRAR method in colloidal synthesis is injection of the precursors in alternating fashion. First, Cd^{2+} is introduced into the hot reaction mixture of CdS nanocrystals. The Cd^{2+} ions migrate to the surface of the nanocrystals and remain in close contact do to electrostatic interaction with the partially charged surface. The selenium precursor is then injected which selectively reacts with the cadmium ions on the

surface of the nanocrystals to form a partial shell of CdSe. The process is repeated in alternating fashion until 1-7 monolayers [26] of CdSe are built upon the surface of the CdS core crystals. Absorption and emission spectra of samples with different core sizes and CdSe layer thickness are shown in Figure 1.23 [26]. As expected, increasing the thickness of the CdSe shell leads to a red shift of the absorption onset and peak of the emission. The quality of the samples prepared by this method can be shown by the TEM images in Figure 1.24 [26]. Template CdS cores and 3, 5 and 7 layer CdS/CdSe/CdS colloidal quantum wells all have narrow distribution in size and appear spherical in shape. The electron diffraction pattern shown also indicates the crystallinity of these particles, which have a wurtzite crystal structure as indicated by the indices of the diffraction rings.

Luminescence Studies

Colloidal quantum wells of CdS/CdSe/CdS have shown promising luminescence properties. Quantum yields as high as 40% are obtained with the right combination of CdS core size and CdSe layer thickness. The luminescence properties of CdS/CdSe/CdS have been studied using steady state and time-resolved techniques.

As shown in Figure 1.25 [27], the luminescence quantum yield for CdS/CdSe/CdS reaches a maximum at a layer thickness of 2 monolayers (0.14 nm). With increasing layer thickness the quantum yield drops from the maximum at 40% to approximately 10% at a layer thickness of 5 monolayers (0.35 nm).

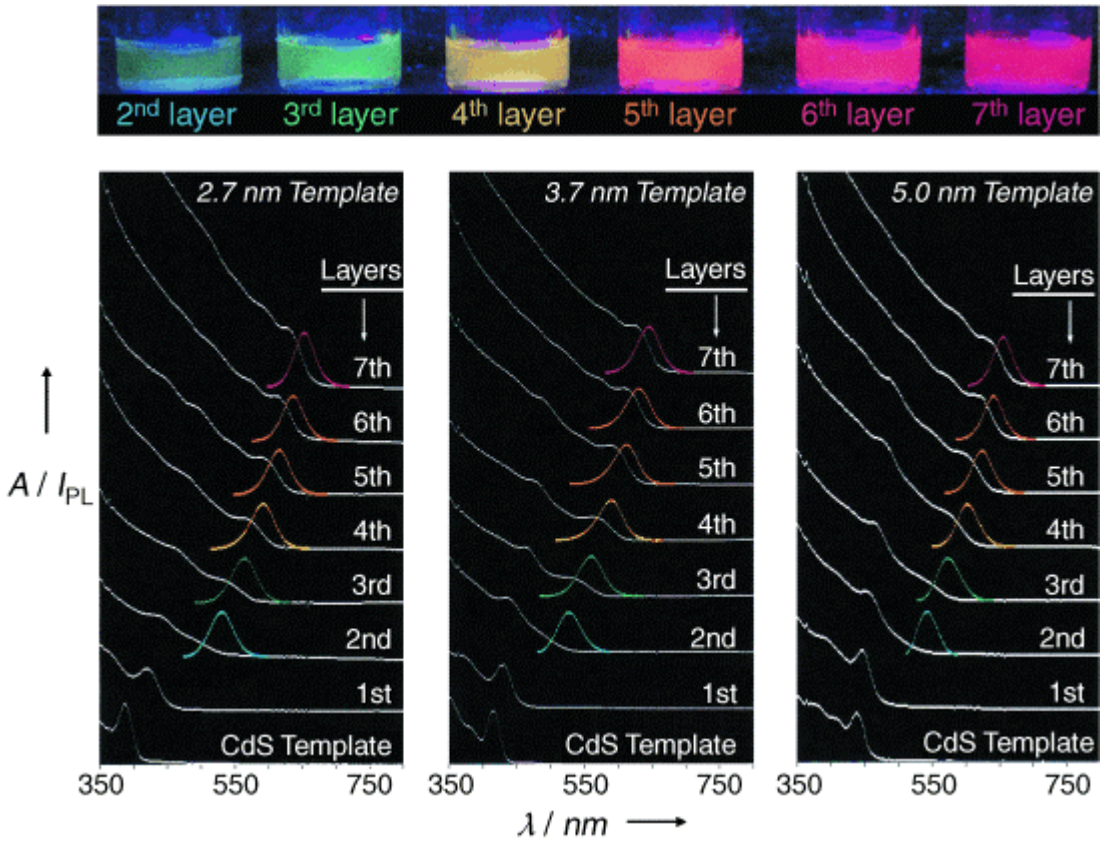

Figure 1.23 – Absorption and emission spectra of CdS/CdSe/CdS colloidal quantum wells made from 2.7 nm, 3.7 nm and 5.0 nm CdS templates with CdSe layer thickness between 1 and 7 monolayers.

As in many colloidal semiconductors, the luminescence peak position, intensity and bandwidth changes as a function of temperature for CdS/CdSe/CdS nanocrystals. Temperature dependent results are shown in Figure 1.26 [27] for samples of CdS/CdSe/CdS with 3-ML thick CdSe well. As expected, luminescence intensity increases with decreasing temperature due to inhibition of non-radiative sources of relaxation. Peak position shifts to higher energy at lower temperature due to compression of the nanocrystal lattice as predicted by the Varshni formula (solid fit in Figure 1.26a)

$$E(T) = E(0) - \beta T^2 \Big/ (T + \gamma) \qquad (1.2)$$

where $E(T)$ is the temperature dependent energy gap, $E(0)$ is the energy gap at 0 K, β is the slope of E(T) vs. T in the limit $T \to \infty$, and γ is the Debye temperature of the material.

The decrease in size of the crystals at low temperature raises the band-gap energy due to quantum confinement effects. Similarly, the linewidth of the emission peak becomes narrower with the decreasing effects of homogeneous broadening at low temperature as determined from the fit of the data in Figure 1.26b to the expression

$$\Gamma = \Gamma_0 + \Gamma_{LO}\left[e^{(\hbar\omega/kT)} - 1\right]^{-1} \qquad (1.3)$$

where Γ_0 is the temperature independent linewidth, Γ_{LO} is the LO phonon scattering strength and $\hbar\omega$ is the LO phonon energy.

Lower temperatures also have effect on the luminescence lifetime and, analysis of the temperature-dependent lifetime data gives clues into the rates of radiative and non-radiative relaxation mechanisms. The effect of temperature on the luminescence lifetime of CdS/CdSe/CdS nanocrystals with CdSe layer thickness between 1 and 4 monolayers is shown in Figure 1.27 [28]. It is interesting that temperature has a minimal effect on the lifetime of the 4-monolayer sample. All other samples show a continuous decrease in lifetime as the temperature is decreased. Such behavior, coupled with an increase in luminescence intensity at low temperature reflects a two-fold change in the properties of the excited state: enhancement of the radiative rate and quenching of non-radiative

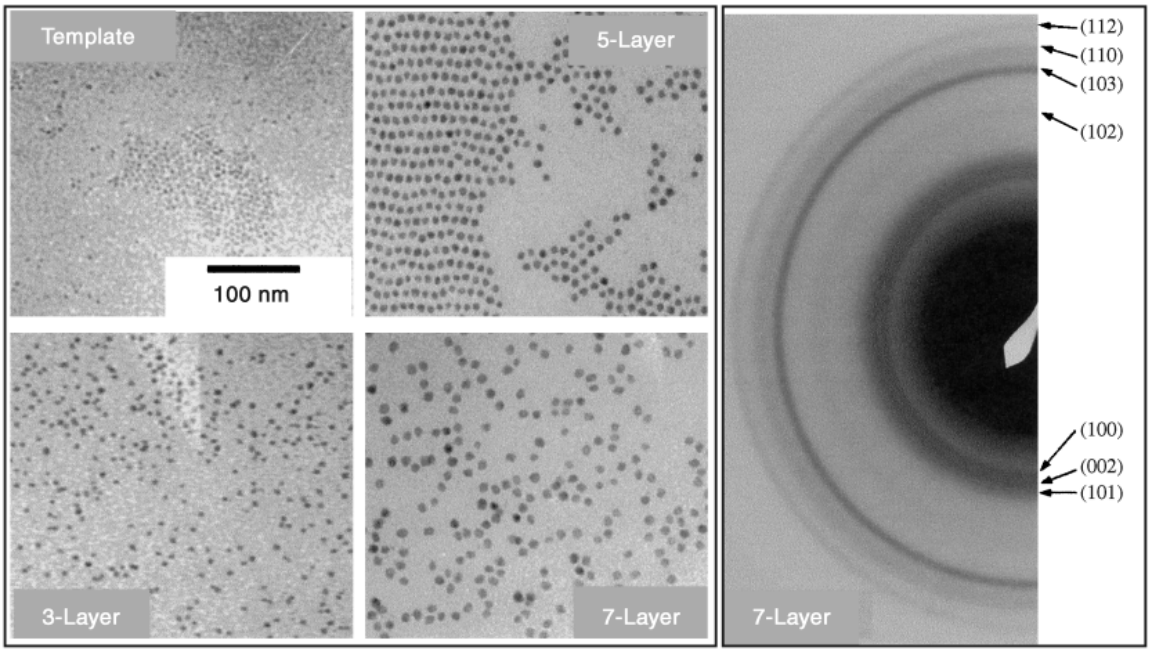

Figure 1.24 – Transmission electron microscopy (TEM) images of CdS/CdSe/CdS colloidal quantum wells. (Right panel) electron diffraction pattern of CdS/CdSe/CdS with indices labeled to indicate a wurtzite crystal structure.

relaxation pathways. The contributions from both of these changes are quantified in Figure 1.28 [28]. With decreasing temperature from 300 K to 200 K, enhancement of the radiative recombination rate is the dominant contribution to the accelerated luminescence lifetimes. Below 200 K, quenching of the non-radiative relaxation becomes more important and is responsible for the decreasing rate of change in the luminescence lifetime at low temperature. Enhancement of the radiative recombination rate continues to reduce the luminescence lifetime, while quenching of non-radiative processes acts to increase the lifetime. The two effects nearly cancel one another at lower temperatures.

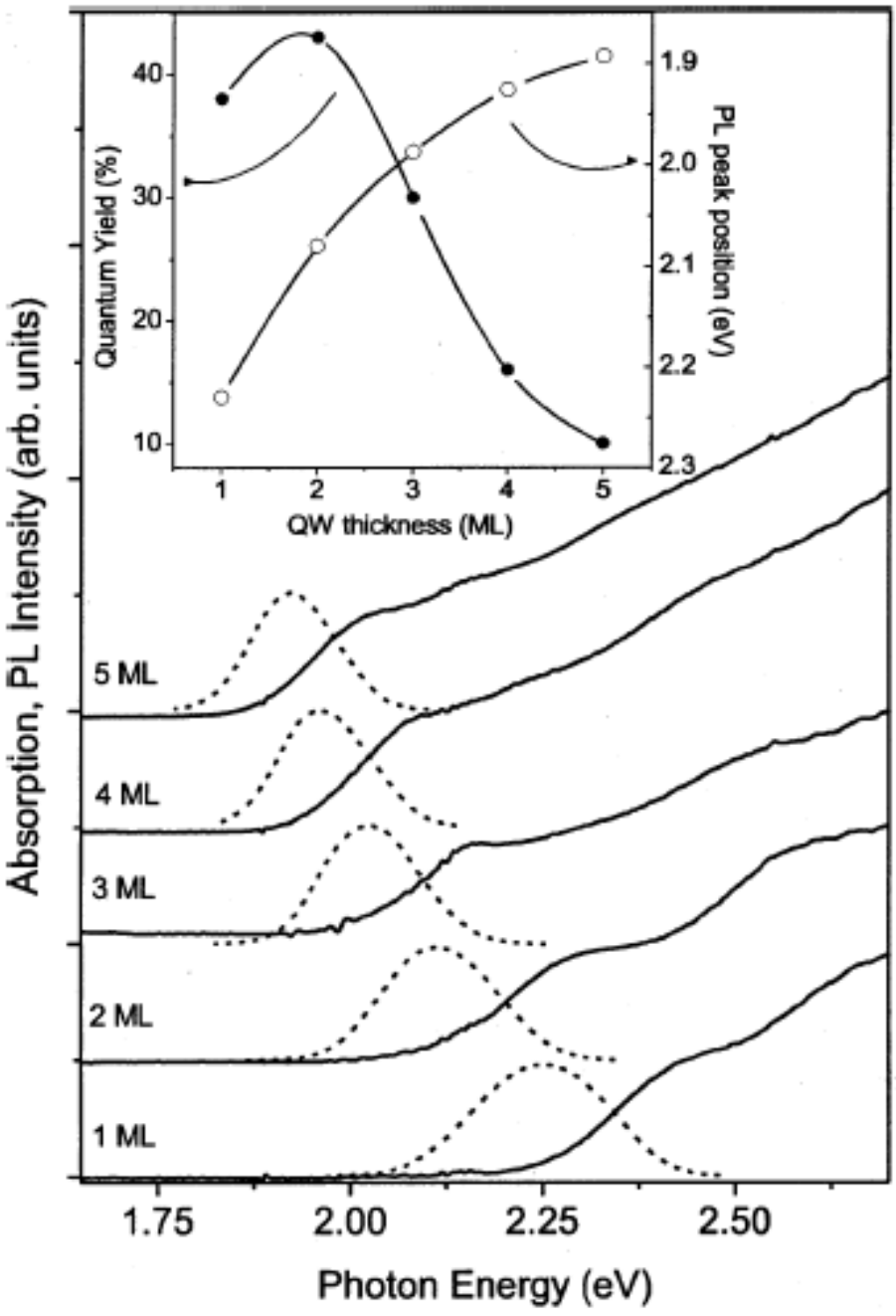

Figure 1.25 – Steady state absorption and emission spectra of CdS/CdSe/CdS colloidal quantum wells of varying layer thickness. Inset: quantum yield and peak position as a function of layer thickness.

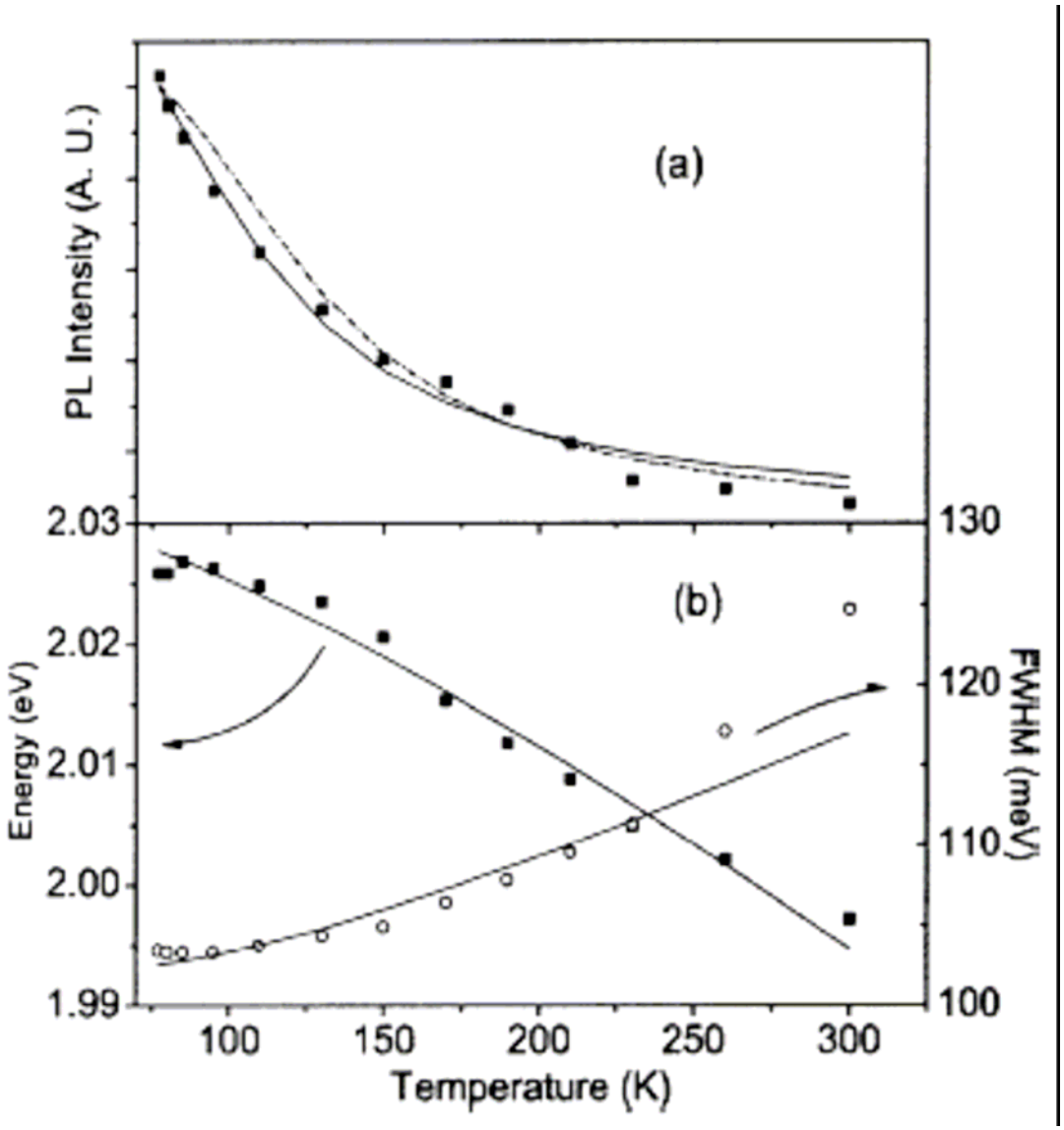

Figure 1.26 – Luminescence intensity (top panel), peak position (bottom squares) and FWHM (bottom circles) of CdS/CdSe/CdS colloidal quantum wells as a function of temperature from 300 K to 75 K.

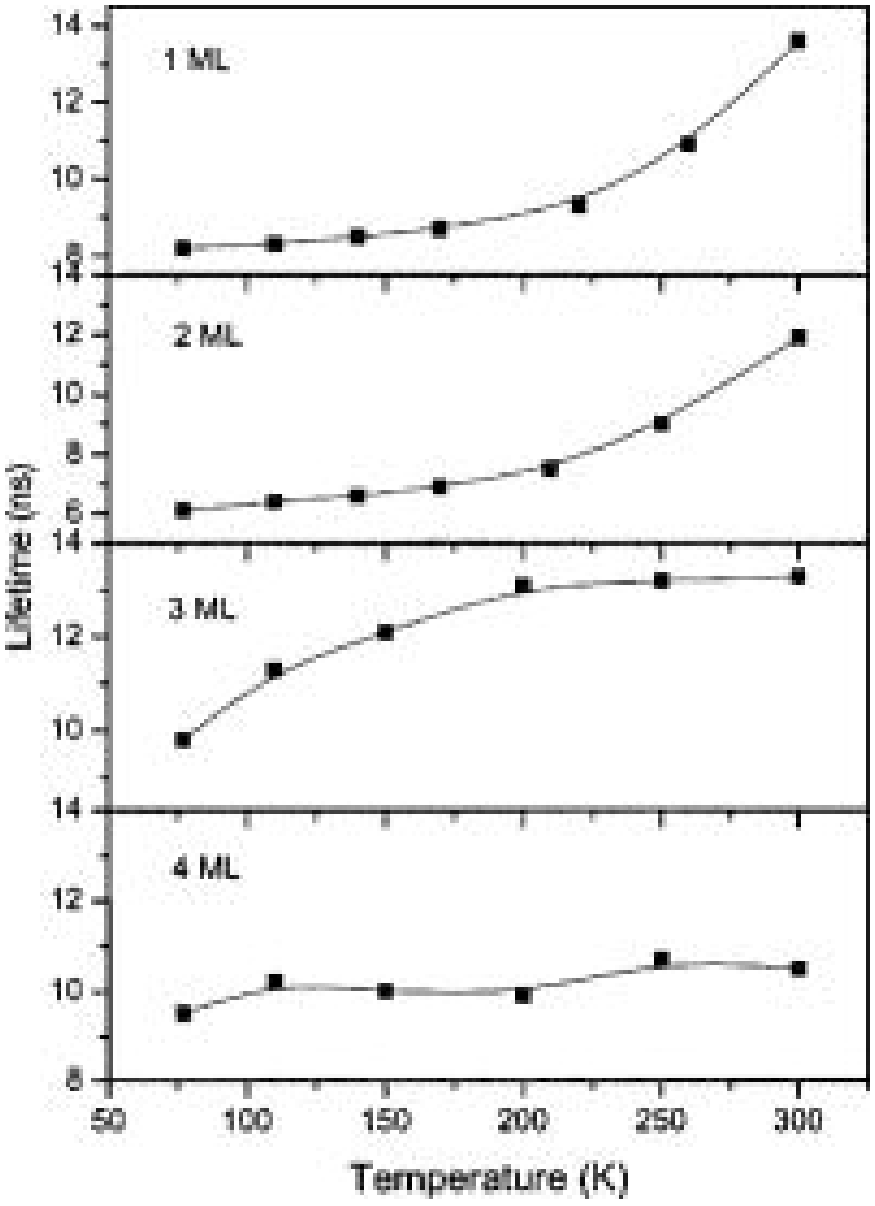

Figure 1.27 – Luminescence lifetimes of CdS/CdSe/CdS colloidal quantum wells of thickness 1-4 monolayers as a function of temperature from 300 K to 75 K.

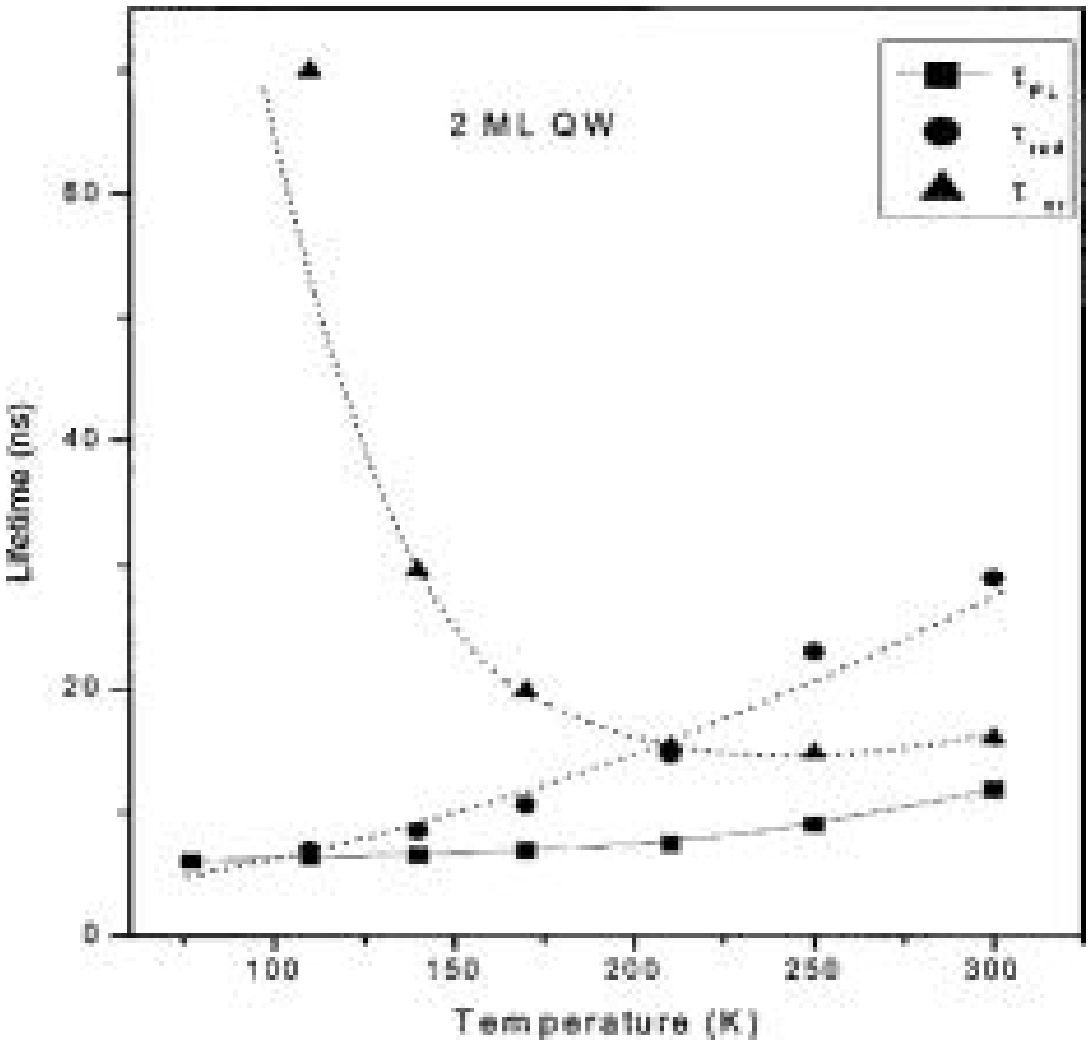

Figure 1.28 – Lifetimes of radiative (circles) and non-radiative (triangles) recombination obtained from the analysis of the luminescence lifetime data for CdS/CdSe/CdS nanocrystals.

References

1. Alivisatos, A. P. *J. Phys. Chem.*, **1996**. 100, 13226-13239.
2. Alivisatos, A. P. *Science*, **1996**. 271, 933-937.
3. I. Hernandez-Calderon, M. Garcia-Rocha, P. Diaz-Arencibia. *Phys. Stat. Sol.*, **2004**. 241, 3, 558-563.
4. M. A. Hines, P. Guyot-Sionnest. *J. Phys. Chem.*, **1996**. 100, 468-471.
5. Y. Wang, N. Herron. *J. Phys. Chem.*, **1991**. 95, 525-532.
6. Q. Darugar, C. Landes, S. Link, A. Schill, M. A. El-Sayed. *Chemical Physics Letters*, **2003**. 373, 284-291.
7. R. Xie, U. Kolb, J. Li, T. Basche, A. Mews. *Journal of the American Chemical Society*, **2005**. 127, 20, 7480-7488.
8. H. Weller, U. Koch, M. Gutierrez, A. Henglein. *Ber. Bunsenges. Phys. Chem.*, **1984**. 88, 649.
9. L. Spanhel, H. Weller, A. Fojtik, A. Henglein. *Ber. Bunsenges. Phys. Chem.*, **1987**. 91, 88.
10. A. Haesselbarth, A. Eychmueller, R. Eichberger, M. Giersig, A. Mews, H. Weller. *Journal of Physical Chemistry*, **1993**. 97, 5333-5340.
11. A. Eychmueller, A. Mews, H. Weller. *Chemical Physics Letters*, **1993**. 208, 1, 59-61.
12. L. Spanhel, M. Haase, H. Weller, A. Henglein. *Journal of the American Chemical Society*, **1987**. 109, 5649.

13. A. Mews, A. Eychmueller, M. Giersig, D. Schooss, H. Weller. *Journal of Physical Chemistry,* **1994**. 98, 934-941.

14. A. Eychmueller, A. Mews. *Ber. Bunsenges. Phys. Chem.*, **1998**. 102, 1343-1357.

15. A. Mews, A. V. Kadavanich, U. Banin, A. P. Alivisatos. *Physical Review B*, **1996**. 53, 20, 13242-13244.

16. D. Schooss, A. Eychmueller, A. Mews, H. Weller. *Physical Review B*, **1994**. 49, 24, 17072-17078.

17. G. W. Bryant, W. Jaskolski. *Phys. Stat. Sol.*, **2001**. 224, 3, 751-755.

18. A. Eychmueller, A. Mews, H. Weller. *Journal of Luminescence*, **1994**. 58, 223-226.

19. F. Koberling, A. Mews, Thomas Basche. *Physical Review B*, **1999**. 60, 3, 1921-1927.

20. O. Wind, F. Gindele, U. Woggon, C. Klingshirn. *Journal of Crystal Growth*, **1996**. 159, 867,

21. S. A. Empedocles, M. G. Bawendi. *Science*, **1997**. 278, 2114,

22. A. Yeh, G. Cerullo, U. Banin, A. Mews, A. P. Alivisatos, C. V. Shank. *Physical Review B*, **1999**. 59, 7, 4973-4977.

23. R. B. Little, C. Burda, S. Link, S. Logunov, M. A. El-Sayed. *Journal of Physical Chemistry A*, **1998**. 102, 33, 6581-6584.

24. M. Braun, S. Link, C. Burda, M. A. El-Sayed. *Physical Review B*, **2002**. 66, 20, 205312-205317.

25. Peng, Z. Adam and Xiaogang Peng. *Journal of the American Chemical Society*, **2001**. 123, 1, 183-184.

26. Battaglia, David, Jack J. Li, Yunjun Wang, and Xiaogang Peng. *Angewandte Chemie, International Edition*, **2003**. 42, 41, 5035-5039.

27. Xu, Jianfeng, David Battaglia, Xiaogang Peng, and Min Xiao. *Journal of the Optical Society of America B: Optical Physics*, **2005**. 22, 5, 1112-1116.

28. Xu, Jianfeng, Min Xiao, David Battaglia, and Xiaogang Peng. *Applied Physics Letters*, **2005**. 87, 4, 043107/1-043107/3.

CHAPTER 2

EXPERIMENTAL TECHNIQUES

The use of time-resolved experimental techniques is a valuable tool for the investigation of dynamic properties of molecules, clusters, nanocrystals, macromolecular structures and solids. The wide range of time scales for dynamic and kinetic events in photophysics and photochemistry demand the use of a variety of time-resolved spectroscopic techniques of inherently different time resolutions. Events that occur on the sub-picosecond to picosecond time scale include electronic excitation, electron transfer, vibrational motion, transition state dissociation, non-radiative relaxation and rotational/translational motion of small molecules. These events can be probed using the ultrashort light pulses provided by today's state-of-the-art ultrafast lasers and suitable detection schemes. Events that occur on the sub-nanosecond to microsecond time scale include diffusion controlled chemical reactions, radiative relaxation (fluorescence and phosphorescence) and rotational/translational motion of large molecules. Such events can be probed using nanosecond or slower laser pulses and can often be detected using modern electronic devices.

The events of primary interest to the investigation of semiconductor nanocrystals are those that occur on the sub-picosecond to picosecond time scale, and the techniques used for such studies will be of primary emphasis. These techniques include sub-picosecond pump-probe transient absorption spectroscopy and sub-picosecond pump-probe transient optical rotation. For the investigation of time-dependent events on the nanosecond and longer time scale, nanosecond gated luminescence spectroscopy and

microsecond transient absorption spectroscopy are powerful techniques for the study of photo-induced events in molecules, nanocrystals and macromolecular structures.

Sub-Picosecond Pump-Probe Transient Absorption Spectroscopy

Principles

To observe ultrafast events occurring on the sub-picosecond to picosecond time scale, it is necessary to use the optical/mechanical techniques of pump-probe spectroscopy. Pump-probe techniques use two ultrashort light pulses from a mode-locked ultrafast laser, typically with pulse durations of less than 200 fs. One of the pulses, designated the 'pump' pulse, is used to induce a transient state in the sample of interest. This transient state could arise from any single or multi-photon interaction that changes the optical characteristics of the sample. For transient absorption spectroscopy, the transient state of the sample is induced by single photon electronic excitation of the sample from its ground state to an excited state. The excited state of the sample is then probed using the second 'probe' pulse that interrogates the same portion of the sample as the 'pump' pulse. Both pump and probe pulses are typically of the same pulse duration but usually have widely different pulse energies. Probe pulses are much lower in pulse energy since they are used simply to monitor the transient optical characteristics of the sample following the pump pulse. For transient absorption the change in the transmission (dT) of the probe pulse is the experimental signal of interest. Negative changes in the transmission ($dT < 0$) correspond to transient absorption while positive changes ($dT > 0$)

correspond to transient ground state depletion or 'bleach'. Under the appropriate conditions a positive dT can also indicate stimulated emission from the sample, a phenomenon of interest in the development of semiconductor nanocrystal lasers. It is clear that, for the transient changes to be observed, the pump and probe pulses must not only overlap one another in space but also in time. This condition is met by carefully controlling the distance traveled by each pulse through the optical setup and is adjusted by the use of an optical delay line. One or both pulses is passed down a mechanical delay line equipped with a suitable retroreflecting optic, the position of which must be adjustable in increments that are appropriate for the time resolution of the experiment. This increment is determined simply from the speed of light and the time resolution desired, for example: 1 fs = 0.3 μm, 100 fs = 30 μm, 1 ps = 300 μm, etc. Regardless of the resolution of the delay line, the response time of the instrument is determined by the pulsewidth of the laser; known as the instrument response time or IRF.

While the basic principles of pump-probe transient absorption spectroscopy are relatively straightforward, each laboratory employs its own special techniques to achieve the best results. The specifics of the experimental setup used in our laboratory are as follows.

Apparatus

Pump and Probe Pulses

Our laboratory uses an amplified Ti:sapphire laser system (Clark MXR, CPA-1000®) capable of producing 100 fs pulses at 795 nm with pulse energies of 800 μJ and a repetition rate of 1 kHz (Figure 2.1). The fundamental pulse is split into pump and probe pulses using a 95/5 beamsplitter that reflects 95% of the fundamental energy and sends it to the OPA/Harmonic Generator while the remaining 5% is transmitted and sent to white light continuum generation. Pump pulses are generated from an optical parametric amplifier (Light Conversion/Quantronix TOPAS®) or second and third harmonic generator to give wavelengths of 265 nm, 394 nm and 480-650 nm of suitable energy for sample excitation. Broadband probe pulses from a white light continuum are generated by focusing 5% of the fundamental into a high quality sapphire window (1 inch round, 2 mm thickness). Pump pulses are directed down an optical delay line having a step resolution of 6.3 μm (21 fs); probe pulses are kept on a fixed-length optical path. The pump beam is chopped at a frequency of 500 Hz using a synchronized optical chopper (HMS Light Beam Chopper 221®) for lock-in detection of pump-induced signals. See Figure 2.2 for a layout of the pump probe transient absorption system. Pump and probe pulses are overlapped in the sample with beam diameters of approximately 250 μm for the pump and 100 μm for the probe. Pump energies at the sample are kept at or below 2 μJ and probe pulse energies are typically less than 100 nJ. After transmission through the

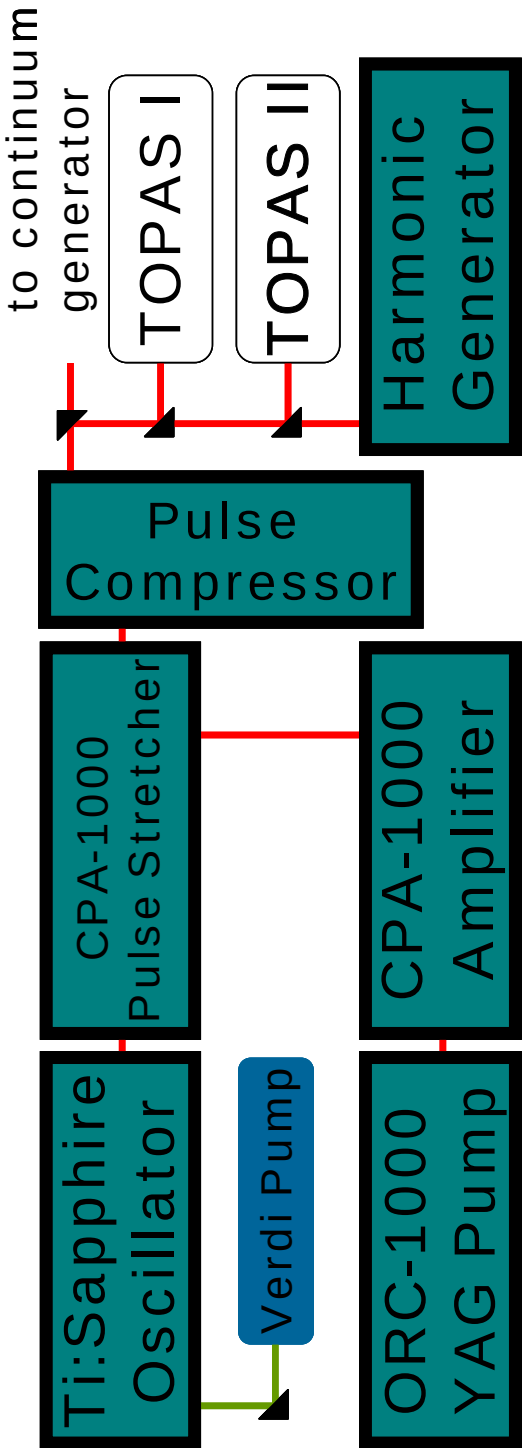

Figure 2.1 – Diagram of the amplified Ti:sapphire laser system used for pump-probe transient absorption and optical rotation experiments.

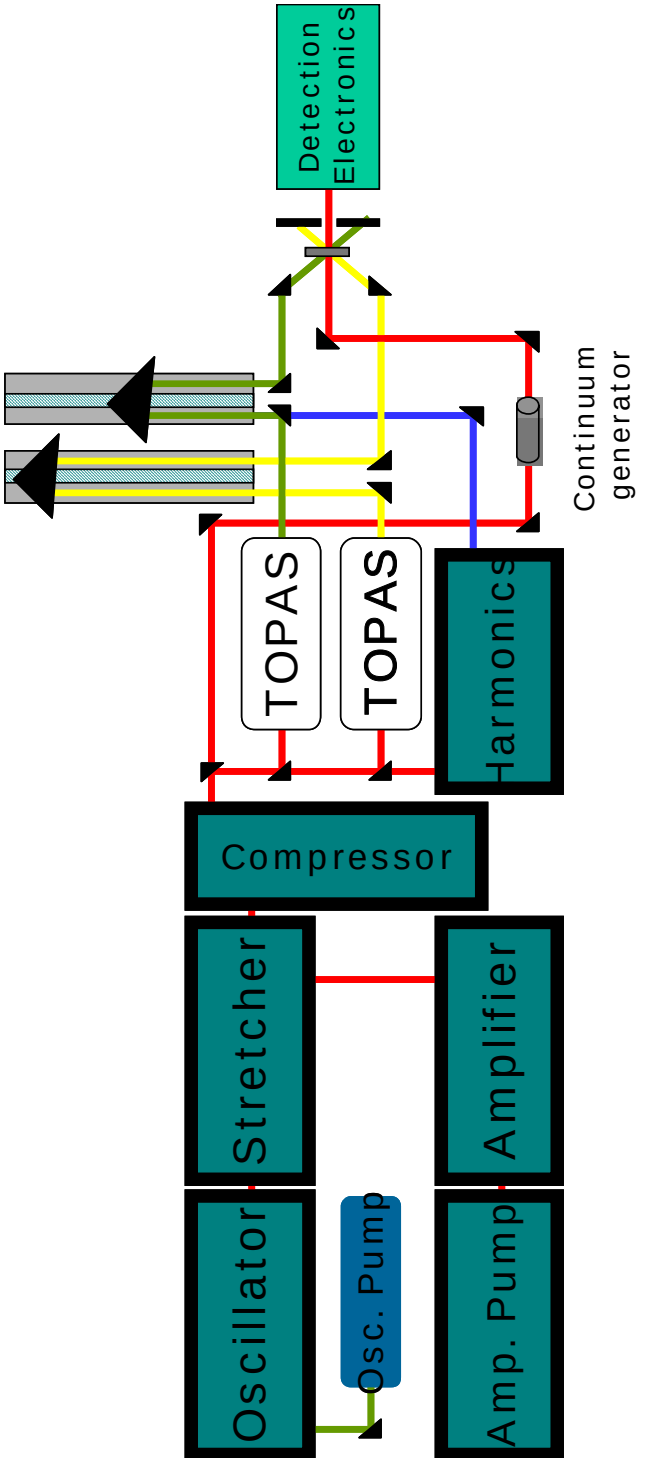

Figure 2.2 – General diagram of the optical layout of the pump-probe transient absorption system.

sample, the white light probe is filtered using an near IR cut-off filter to eliminate any high energy 795 nm fundamental from entering the detection system.

Detection

Our laboratory employs the technique of single channel lock-in detection for the extraction of transient signals. The transmitted white light probe is launched onto the end of a multimode optical fiber and sent to the input port of a scanning monochromator (Acton Research Corporation, SpectraPro 275®). Single wavelengths are selected and sent to a high-speed silicon PIN amplified photodiode (Thorlabs). The response of the photodiode is integrated using a boxcar integrator (Stanford Research, SR 280®). The resulting waveform is a square wave with a 1 kHz frequency and voltage that corresponds to the integrated signal of the photodiode response and is proportional to the intensity of transmitted probe light.

When pump-induced changes in the transmission of the probe light occur, the waveform becomes a 500 Hz square wave with peak-to-trough amplitude proportional to change in transmission of the sample, dT. This waveform can be sent directly to a lock-in amplifier (Stanford Research, SR 530®) but our experience has shown that additional treatment of the signal is needed to get reliable and reproducible data traces.

One of the challenges of using a white light continuum probe is long-term intensity fluctuation over the course of data accumulation. This can lead to dT vs. time decay traces that are not reproducible and make it impossible to identify the correct transient behavior. We have found that the best way to account for these fluctuations is

to use the boxcar averager to do an online division of the signal waveform by the online *average* of the signal waveform:

$$I = \frac{V(t)}{V_{avg}(t)} \qquad (2.1)$$

This technique effectively normalizes the signal waveform such that changes in the intensity of the white light probe do not affect the intensity of the dT signal. Some experimenters use a reference beam to accomplish the same goal but our experience has shown that this method can lead to a compounding fluctuation effect when both sample and reference beam intensities fluctuate in opposite direction (i.e. sample beam increase while reference decreases), leading to even less reproducibility and false kinetic traces. After online treatment of the waveform using the boxcar integrator, it is sent to the lock-in amplifier for phase-sensitive extraction of the transient signal. The lock-in amplifier is interfaced with a personal computer by a general-purpose interface bus (GPIB, National Instruments) where the output from the lock-in is matched with corresponding position of the delay line for the display and acquisition of time-dependent transient absorption traces.

Chirp-Free Transient Absorption Spectroscopy

One of the challenges of transient absorption spectroscopy on the ultrafast time scale is the distortion of transient absorption spectral intensity due to chirp in the light pulse also known as group velocity dispersion (GVD). While the amount of chirp in the

laser pulse can be adjusted using optical techniques, it is often necessary to employ special experimental techniques to eliminate the effects of chirp from transient spectra. A common method is to collect a large number of transient spectra (greater than 30 typically) from a spectrograph/CCD camera based detection system at small delay increments from one another and apply a chirp correction function to obtain chirp corrected transient absorption spectra (post correction). This method is not only time consuming but can also introduce inaccuracies if not performed correctly. An alternative to this approach is to correct for chirp *while* the data is being collected (active correction). As the monochromator scans the wavelengths of the spectrum, the delay line moves to adjust the time delay and therefore compensate for the chirp of the pulse. This method is desirable for immediate interpretation of experimental results and for the enhanced sensitivity gained from using single-wavelength lock-in detection instead of a spectrograph/CCD camera arrangement. A comparison of the two chirp correction techniques is shown in Figure 2.3 for the transient bleach spectrum of CdSe nanocrystals suspended in toluene. The active corrected spectrum matches the post corrected spectrum very well, and was obtained from one spectrum rather than sixty.

Automation and Data Acquisition

The detailed documentation of the LabVIEW programs written for automation and data acquisition are available in Appendix 1. In general, these programs were designed to control and coordinate the various components of the ultrafast system. The duties performed include moving the position of the delay line in user-defined steps,

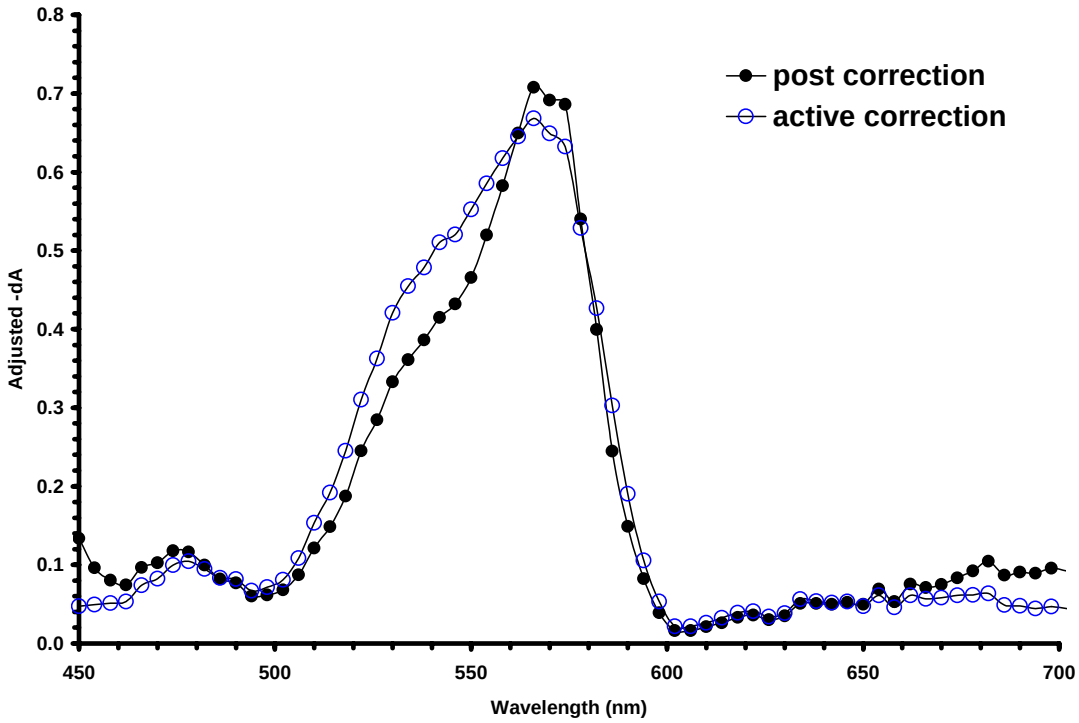

Figure 2.3 – Comparison of the transient bleach spectrum of CdSe nanocrystals obtained using active and post correction techniques. See text for details (Chirp Free Transient Absorption Spectroscopy).

moving the wavelength of the monochromator, and collecting the signal from the lock-in amplifier. The programs also manipulate the signal and position of the delay line into dT vs. time data, scan the delay line to acquire transient absorption decay traces, average multiple accumulations and save the average and individual traces to the hard drive of the computer.

Sub-Picosecond Pump-Probe Transient Optical Rotation

Principles

To observe ultrafast optical rotation events occurring on the sub-picosecond to picosecond time scale, it is necessary to use the optical/mechanical techniques of pump-probe spectroscopy. Pump-probe techniques use two ultrashort light pulses from a mode-locked ultrafast laser, typically with pulse durations of less than 200 fs. One of the pulses, designated the 'pump' pulse, is used to induce a transient state in the sample of interest. This transient state could arise from any single or multi-photon interaction that changes the optical characteristics of the sample.

In sub-picosecond transient optical rotation, the probe pulse interrogates the transient change in refractive index of the photoexcited sample. The transient change in refractive index can arise from a number of linear and non-linear optical processes. These changes in refractive index give rise to changes in polarization of the probe pulse; in essence the sample becomes temporarily birefringent. The change in polarization can be analyzed using polarization optics and detected in much the same way as pump-probe transient absorption.

Transient Birefringent Phenomena: Kerr rotation and Faraday rotation

Two optically induced transient birefringent phenomena are Kerr rotation and Faraday rotation. Kerr rotation arises from the response of a material to intense electric

fields. Faraday rotation is a resonance-enhanced process that arises from the circular birefringence induced by a spin polarized cross section of material.

Kerr rotation

Linearly polarized pump pulses of high energy are used to measure the third order nonlinear optical response of the sample, also known as the Kerr response. Under the influence of an intense electric field, all materials have a tendency to become temporarily birefringent for the duration of the applied field. This tendency is given by the Kerr coefficient of the material, which is particularly high in many nitro-substituted benzene molecules in liquid phase [1]. As indicated, the Kerr effect is a nonlinear process that follows as the square of the electric field intensity:

$$\Delta n = K\lambda E^2 \qquad (2.2)$$

where Δn is the difference in refractive index, K is the Kerr constant, λ is the wavelength and E is the electric field intensity. The intense electric field present in the duration of a high-energy sub-picosecond laser pulse is suitable for inducing a Kerr response. If a linearly polarized probe pulse interrogates the same sample volume as the high-energy pump pulse, the polarization of the probe will rotate to an extent determined by the Kerr response of the sample and the overlap distance of the pump and probe pulses. Sub-picosecond pump-probe optical rotation can be used to investigate the Kerr response of

nanocrystal and nanocrystal assemblies, which have been suggested as having large cross-sections for non-linear optical processes.

Faraday Rotation

Circularly polarized pump pulses in electronic resonance with a material will generate a spin-polarized population of excited states within the pump volume of the sample. The net local magnetization associated with this excited spin population induces a circular birefringence in the sample with a duration that is determined by the spin-polarization relaxation time. Spin polarizations relax on a much longer time scale than electronic relaxation and, in the case of semiconductors, can exist long after electron-hole recombination has occurred. If a linearly polarized probe pulse interrogates the same sample volume as the magnetization-inducing pump pulse, the polarization of the probe will rotate to an extent determined by the Faraday response of the sample and the overlap distance of the pump and probe pulses. Spin relaxation kinetics can reveal the nature of the environment experience by excited electrons in semiconductor nanocrystals.

Apparatus

Pump and Probe Pulses

Our laboratory uses an amplified Ti:sapphire laser system (Clark MXR, CPA-1000®) capable of producing 100 fs pulses at 795 nm with pulse energies of 800 μJ and a

repetition rate of 1 kHz (Figure 2.1). The fundamental pulse is split into pump and probe pulses using a 95/5 beamsplitter that reflects 95% of the fundamental energy and sends it to the OPA/Harmonic Generator while the remaining 5% is transmitted and sent to white light continuum generation. Pump pulses are generated from an optical parametric amplifier (Light Conversion/Quantronix TOPAS®) or second and third harmonic generator to give wavelengths of 265 nm, 394 nm and 480-650 nm of suitable energy for sample excitation. For transient optical rotation measurements, the 394 nm second harmonic is split into pump and probe pulses using a 1 cm thick fused silica beamsplitter. Most of the beam intensity is transmitted and the approximate transmission/reflection ratio for the beamsplitter is 70%/30%. Pump pulses are directed down an optical delay line having a step resolution of 6.3 μm (21 fs); probe pulses from the front face of the beamsplitter passed down a fixed-length optical path. Pump pulse energies and adjusted using a set of reflective neutral density filters. Both pump and probe beams are polarized using calcite Glan-Taylor polarizing prisms. For all experiments probe pulses remain linearly polarized, while pump pulses may either be linearly or circularly polarized, depending on whether Kerr rotation or Faraday rotation are being measured. For Faraday rotation experiments involving spin dynamics, an electromagnet (GMW Model 3470 driven by a Sorensen DCM 60-10 power supply) is used to generate a transverse magnetic field. The magnetic field strength is quantified using a digital teslameter (Group3 DTM-133). See Figure 2.4 for a layout of the optical rotation setup.

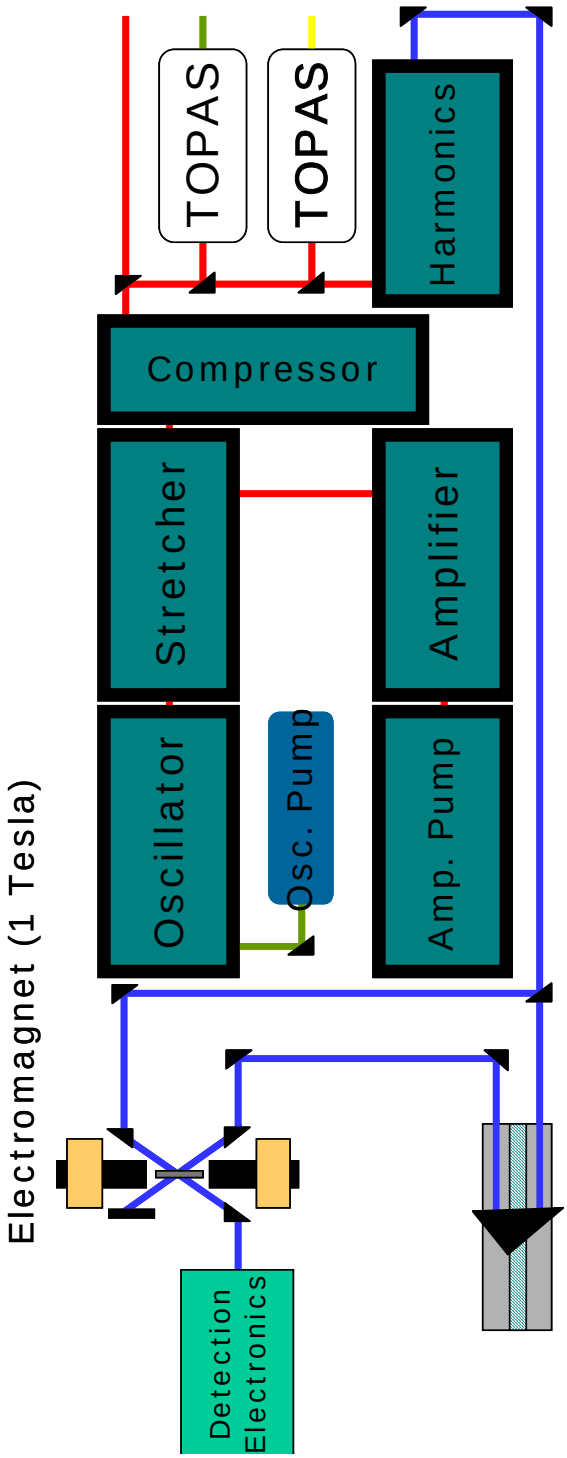

Figure 2.4 – General diagram of the optical layout of the pump-probe transient optical rotation experiment.

Detection System

The probe beam is focused and passed through the sample in a polarization analyzer arrangement. The sample is set between crossed Glan-Taylor polarizers that have been adjusted for maximum extinction of the probe beam after the sample. Residual probe light not extinguished by the analyzer is detected using a high-sensitivity, slow response silicon PIN photodiode coupled into a low-noise, high-gain preamplifier (Stanford Research, SR 560®). The amplified photodiode response (~1 kHz square waveform) is input directly into the lock-in amplifier for phase-sensitive detection of the optical signal. In the absence of the pump-induced birefringence of the sample, the voltage detected by the lock-in is small and high gain settings and integration times are needed to quantify the signal. Application of the pump causes a strong increase in the intensity of probe light that passes the analyzer and is detected by the detection electronics. The increase in intensity is typically one to two orders of magnitude higher than background and this leads to high signal to noise ratios for measurements of this type. As in transient absorption measurements, the lock-in amplifier is interfaced with a personal computer by a general-purpose interface bus (GPIB, National Instruments) where the output from the lock-in is matched with corresponding position of the delay line for the display and acquisition of time-dependent transient optical rotation traces.

Examples

Examples of optical rotation data taken using our optical rotation setup are shown in Figures 2.5 and 2.6. Figure 2.5 shows the optical Kerr response of Coumarin 420 in methanol while Figure 2.6 is the optical Kerr response of PVP capped CdS nanocrystals.

Automation and Data Acquisition

The detailed documentation of the LabVIEW programs written for automation and data acquisition are available in Appendix 1. In general, these programs were designed to control and coordinate the various components of the ultrafast system. The duties performed include moving the position of the delay line in user-defined steps, moving the wavelength of the monochromator, and collecting the signal from the lock-in amplifier. The programs also manipulate the signal and position of the delay line into dT vs. time data, scan the delay line to acquire decay traces, average multiple accumulations and save the average and individual traces to the hard drive of the computer.

Nanosecond Gated Luminescence Spectroscopy

Principles

Gated CCD (charge coupled device) cameras have become powerful tools for various fields of spectroscopy, microscopy and high-speed imaging. In particular, CCD

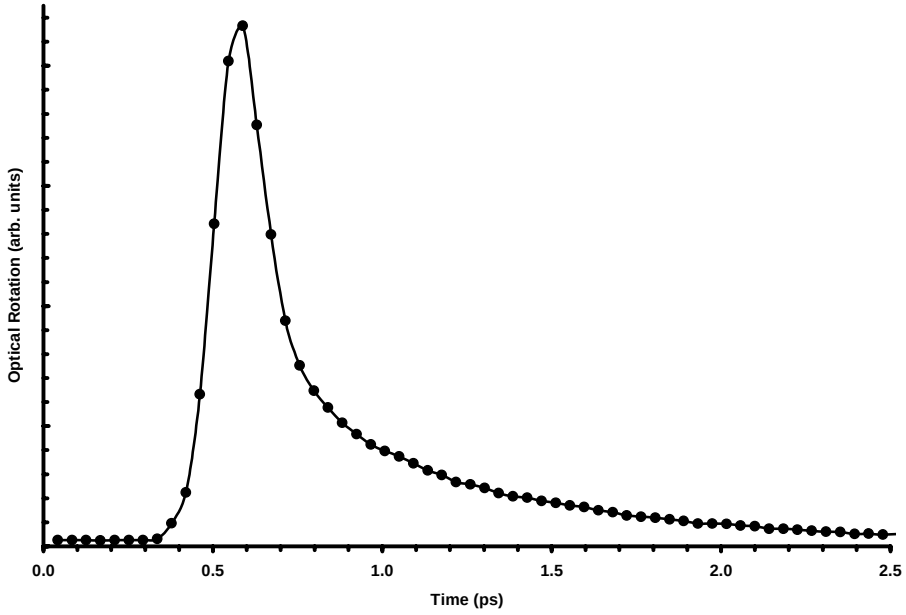

Figure 2.5 – Ultrafast optical Kerr response of Coumarin 420 in methanol collected using the transient optical rotation setup.

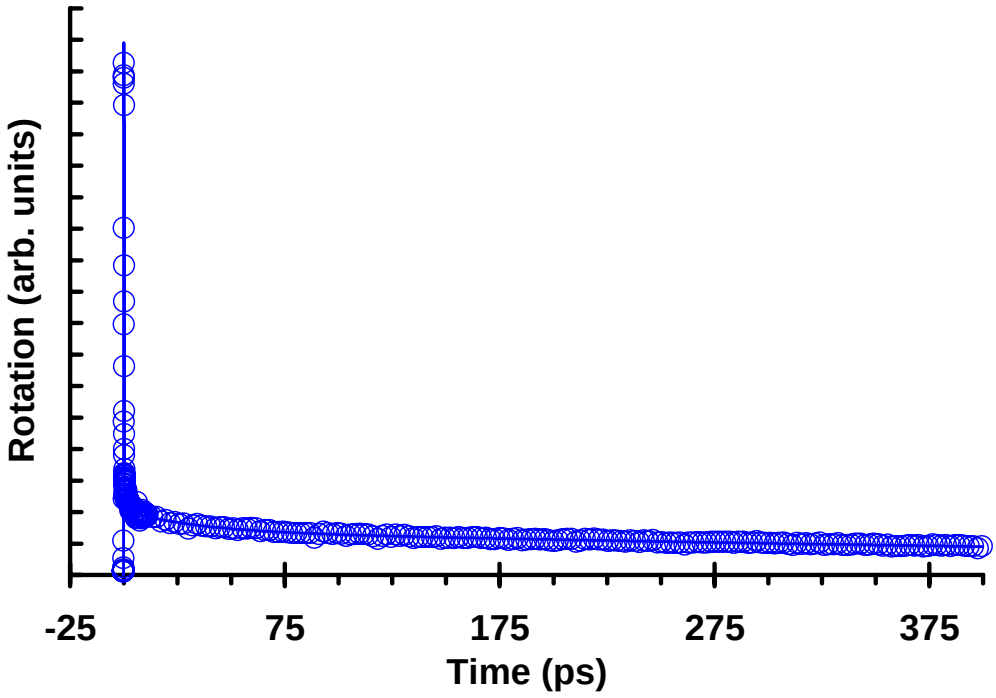

Figure 2.6 – Ultrafast optical Kerr response of PVP capped CdS nanocrystals collected using the transient optical rotation setup.

cameras have enhanced the techniques of luminescence spectroscopy to allow the user to obtain snapshots of entire emission spectra with time resolutions of only a few nanoseconds. This is a powerful approach to understanding the dynamic luminescent characteristics of molecules and nanoparticles. While the technology behind gated CCD spectroscopy is quite sophisticated, the principles of the measurement are very straightforward.

In nanosecond-gated spectroscopy, a synchronization pulse from a nanosecond laser is used to trigger the electronic gating of the camera intensifier. Luminescence from the sample is incident on the array of the camera and detected by the CCD only during the application of the gate pulse. The gate pulse can be adjusted in time to obtain time-dependent information about the sample luminescence.

Apparatus

Excitation pulses (8 ns FWHM, 0.5 mJ) are provided by a nanosecond optical parametric amplifier (Spectra-Physics, MOPO Series®) pumped by the third harmonic output from a Nd:YAG laser (Spectra Physics, Quanta-Ray Series®). Excitation of the sample is carried out in a 90° geometry. Emission from the sample is collected onto the input slit of a monochromator/spectrograph (Acton Research Corporation, SpectraPro 275®). Appropriate cut-off optical glass filters are used to eliminate scattered laser light. The emission spectrum is dispersed onto a 512 x 512 array air-cooled CCD camera (Roper Scientific, PI-MAX®) operating in gated mode. Gate pulses are synchronized and delayed with respect to the Q-switch pulse of the Nd:YAG laser using a built-in pulse

timing generator (PTG, Roper Scientific). Gate widths between 2 ns and 50 ns are used, depending on the time resolution of the decay. The WinSpec software package (Princeton Instruments) is used for camera control and data acquisition.

Examples

Examples of the data obtainable using nanosecond gated luminescence spectroscopy are shown in Figures 2.7 and 2.8. Figure 2.7 shows the transient luminescence spectra of Tris(2,2'-bipyridyl)dichlororuthenium(III) in water at different times with respect to the pulse laser. Figure 2.8 shows the kinetic traces extracted from the series of collected luminescence spectra at different monitoring wavelengths for Tris(2,2'-bipyridyl)dichlororuthenium(III) in water.

Microsecond Transient Absorption

Principles

The dynamic behavior of large macromolecules often occurs on time scales longer than the nanosecond. For these relatively long time scales transient absorption measurements no longer require pump-probe techniques and can be done using all electronic components. The signal of interest remains the same for both pump-probe and

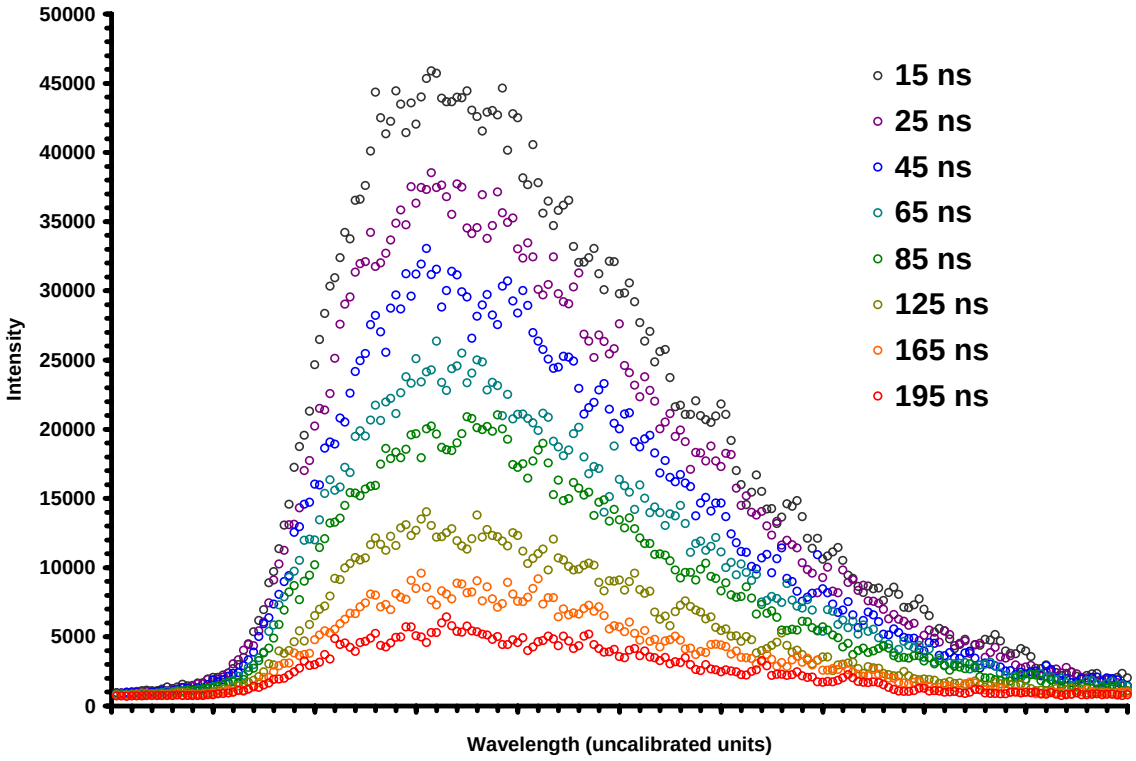

Figure 2.7 – Luminescence spectra of Tris(2,2'-bipyridyl)dichlororuthenium(III) in water at different times with respect to the pulse laser.

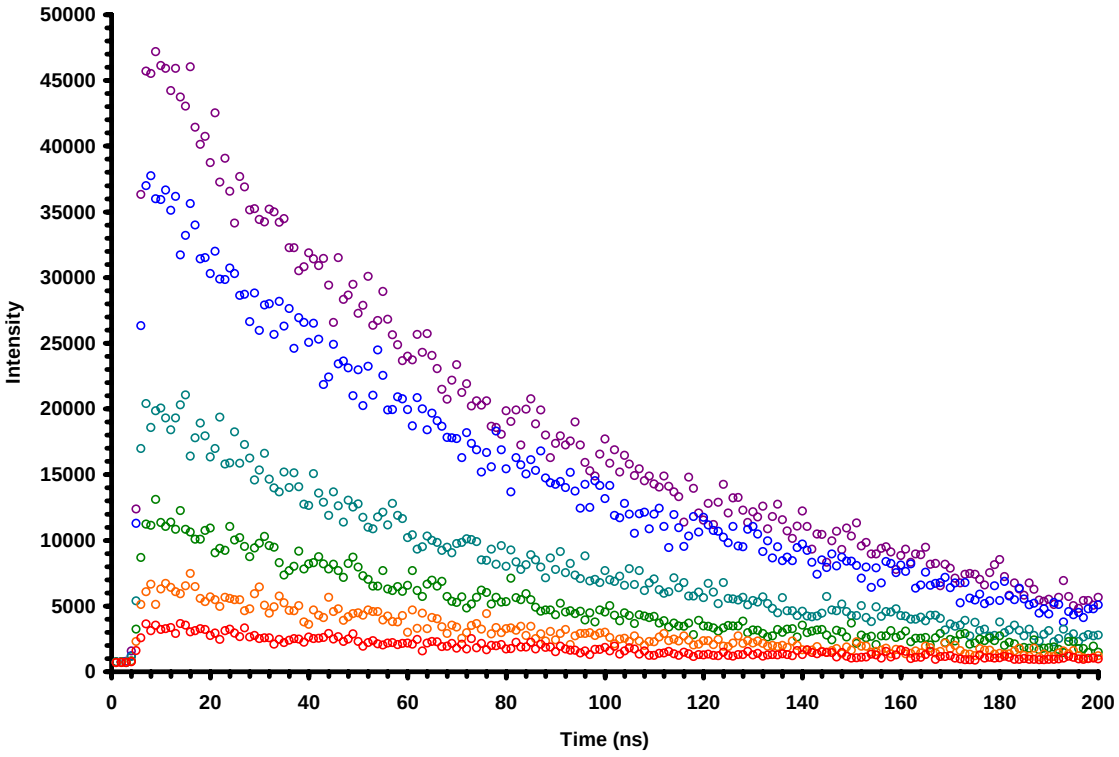

Figure 2.8 – Kinetic traces extracted from the series of collected luminescence spectra at different monitoring wavelengths for Tris(2,2'-bipyridyl)dichlororuthenium(III) in water.

traditional transient absorption: the change in transmission of the sample following pulsed optical excitation.

Apparatus

Excitation pulses (8 ns FWHM, 1 – 50 mJ) are provide by a pulsed ns Nd:YAG laser (Spectra-Physics, Quanta-Ray Series®). The second (532 nm) or third (355 nm) harmonic of the YAG fundamental wavelength is used for excitation of the sample. There are two different optical layouts used for microsecond transient absorption measurements, one that accommodates large sample volumes (3 mL or greater) and one that accommodates very small sample volumes (less than 1 mL).

For large sample volumes a side-on 90° excitation geometry is used to use the maximum pulse energy from the nanosecond laser. Monitoring light is provided by a 200 W continuous Xenon arc lamp (Photon Technologies Incorporated) that is focused, heat-filtered through and 10 cm water cell, spectrally filtered using narrow-band interference filters and made to pass through the sample cell within the excitation volume of the pump laser. Transmitted light is collected and dispersed directly onto the photocathode of a red-sensitive, high-sensitivity photomultiplier (PMT) tube (Hamamatsu) operated at a voltage of 200-700 V. Current from the PMT is passed through a variable resistor that is adjustable between 50 Ω and 50 kΩ, depending on the time resolution and sensitivity needed for the measurement. The output from the resistor is DC coupled at 1 MΩ into a 500 MHz digital oscilloscope (LeCroy) for digitization of the time-dependent voltage from the detection system. Transient absorption decay traces are averaged typically for

1000 scans and time/voltage data is saved to 3.5” floppy discs for transfer to a PC for data analysis.

Small sample volumes require only a fraction of the total excitation energy of the pulsed laser and monitoring beam. The output from a 200 W Xenon arc lamp is passed through a low-resolution, micrometer-driven monochromator whose monochromatic output is coupled onto the end of a multimode optical fiber. The end of the fiber is mounted to the top of a vertically arranged optical layout the collects and focuses the output from the fiber to a 2 mm^2 spot at the sample position. Excitation is also done in the vertical geometry and the advantage of this setup is the accommodation of non-freestanding films or collections of small crystals that would not remain suspended in a horizontal sample arrangement. Thin samples with pathlengths less than 1 mm are used and the transmitted light is collected and coupled onto the end of another multimode optical fiber which is used to direct the monitoring light to the detection electronics. Output from the fiber is collected and dispersed directly onto the photocathode of a red-sensitive, high-sensitivity photomultiplier (PMT) tube (Hamamatsu) operated at a voltage of 200-700 V. Current from the PMT is passed through a variable resistor that is adjustable between 50 Ω and 50 kΩ, depending on the time resolution and sensitivity needed for the measurement. The output from the resistor is DC coupled at 1 MΩ into a 500 MHz digital oscilloscope (LeCroy) for digitization of the time-dependent voltage from the detection system. Transient absorption decay traces are averaged typically for 1000 scans and time/voltage data is saved to 3.5” floppy discs for transfer to a PC for data analysis.

References

1. Rulliere, Claude, *Femtosecond Laser Pulses: Principles and Experiments*. 1998, Berlin: Springer.

CHAPTER 3

SYNTHESIS OF QUANTUM DOT QUANTUM WELL NANOCRYSTALS

A modified synthesis technique for preparing CdS/HgS/CdS quantum dot quantum well nanocrystals has been developed that yields more consistent samples of higher stability than previous methods. The use of PVP as a stabilizing material instead of the usual alkanethiol capping ligand approach makes preparation more convenient and the resulting nanocrystal samples are stable indefinitely when stored in a concentrated PVP matrix.

Introduction

Colloidal preparation of nanocrystals has been used for years to prepare quantum-confined materials. Much of the early work in this area centered on the preparation of CdS and ZnS quantum dots [1-4]. These materials can be readily prepared by sulfidation of inorganic salts in aqueous or alcoholic solvents at room temperature. High temperature and coordinating solvent conditions are not necessary to achieve samples with reasonable (10% standard deviation) size distributions and good crystallinity. The other advantage of using aqueous, room temperature methods is the ease with which ionic exchange chemistry can occur, leading to new materials of different compositions. The growth of CdS on ZnS and islands of HgS on CdS demonstrated the use of this technique [1, 3, 5, 6]. In 1993 the principles of this technique were extended to the preparation of one of the first multi-layered nanocrystals, CdS/HgS/CdS [7]. For the first time, a size-

quantized material was imbedded within a larger size-quantized material: a quantum well within a quantum dot – or quantum dot quantum well, as it became known.

Principles

The synthesis of quantum dot quantum wells begins with the preparation of a population of CdS nanocrystal colloids that have a stable structure and relatively narrow size distribution. The simplest way to prepare CdS colloids in this manner is through the polyphosphate method [5]. Aqueous cadmium salt is sulfidized with H_2S gas using sodium polyphosphate as a stabilizer. This procedure yields suspensions of CdS nanocrystals around 5 nm in diameter with a size distribution of 12-15%.

The preparation of the first quantum dot quantum well benefited greatly from the work of Weller and Henglein using surface exchange chemistry to easily grow heterostructures of colloidal materials [1, 2]. The success of this method derives from the exploitation of solubility differences between the materials being used to prepare the heterostructures. If the difference in solubility product is high enough, there is a strong driving force for the exchange of the atoms at the interface between a surface and a solution containing the exchanging ions. For example, consider the surface of a nanometer-sized CdS colloid dispersed in a solution containing Hg^{2+} ions. The solubility product of HgS (5×10^{-54}) is twenty-seven orders of magnitude smaller than the solubility product of CdS (1×10^{-27}). This gives a free energy for the reaction

$$CdS \rightarrow Cd^{2+}(aq.) + S^{2-}(aq.)$$
$$Hg^{2+}(aq.) + S^{2-}(aq.) \rightarrow HgS \qquad (3.1)$$
$$CdS + Hg^{2+}(aq.) \rightarrow HgS + Cd^{2+}(aq.)$$

of –150 kJ/mol. The net effect of this circumstance is that the outermost layer of CdS will be displaced by a monolayer of HgS through exchange of Hg^{2+} ions for Cd^{2+} ions. Another beneficial consequence of this chemistry is the fact that the colloidal solution now contains a concentration of Cd^{2+} almost exactly equivalent to one monolayer of CdS; which can be deposited on the surface of the HgS well by the addition of sulfur ion, S^{2-}. The resulting structure is a Type I semiconductor heterostructure with a nanometer sized core, sub-nanometer sized well and sub-nanometer thick outer layer. The ion exchange reaction has been monitored during the course of the preparation electrochemically and using ICP-MS [6]. Free Cd^{2+} and Hg^{2+} concentrations were monitored in the reaction solution as a function of added Hg^{2+}. Initially the concentration of Cd^{2+} increases while the concentration of Hg^{2+} remains around zero. This indicates release of surface cadmium ions into solution and replacement with mercury ions. This trend continues up to a concentration of Hg^{2+} equivalent to one monolayer on the surface of the average sized CdS colloid. After this point, the concentration of Hg^{2+} begins to increase dramatically while the Cd^{2+} concentration remains constant. This indicates that mercury ions are no longer replacing cadmium at the surface and simply remain in solution. This would be expected if the surface of the colloids were now saturated with HgS; the additional Hg^{2+} have no ions to displace. At this point there is a concentration of

cadmium ions in solution great enough to form nearly one monolayer of CdS on the surface of the HgS well. This is accomplished by simply adding sulfide (S^{2-}) solution in a slow drop-by-drop manner to avoid nucleation of small CdS seeds due to rapidly generated high local concentrations of sulfide. The capping of these particles with CdS is not only useful for defining their structure; it also serves to stabilize the particles from mixed binary phase formation (alloy formation) [6].

Polyphosphate Synthesis of CdS/HgS/CdS

This was the first procedure used by Eychmueller and co-workers to prepare the CdS/HgS/CdS quantum dot quantum well system. The procedure consists of preparing nanometer sized CdS in basic solution using polyphosphate as a capping material. After preparation of the CdS seeds a surface ion exchange reaction is carried out to replace the outer layer of CdS with a layer of HgS. Finally, CdS is redeposited on top of the HgS monolayer to complete the quantum well structure.

CdS seed nanoparticles are prepared by sulfidation of cadmium chloride salt using hydrogen sulfide gas. One hundred milliliters (100 mL) of deionized water in a 250 mL three-neck round-bottomed flask is purged with nitrogen for 30 minutes. Afterwards, 0.2 mL each of 0.1 M cadmium (II) chloride (aq.) and 0.1 M sodium polyphosphate (aq.) are added to the reaction solution and vigorously stirred. The solution is purged for several minutes until the pH reaches a minimum (usually around pH 4) and then the pH is adjusted to pH 9.5 using NaOH. One milliliter (1 mL) of hydrogen sulfide gas is injected into the reaction vessel under vigorous magnetic stirring. Within seconds the reaction

mixture becomes yellow as an indication of the formation of CdS nanocrystals. After 15 minutes of crystal growth the mixture is purged with nitrogen for 30 minutes before removing a 3 mL sample and the pH is adjusted to pH 7.

A monolayer of HgS is deposited on the outer surface of the CdS seeds through an ion-exchange reaction. Two hundred fifty microliters (250 μL) of 0.1 M mercury (II) chloride is rapidly injected into the reaction mixture under vigorous stirring. The solution immediately turns red in color as an indication that the surface chemistry has taken place and CdS/HgS particles are present. A 3 mL sample of the CdS/HgS solution is extracted followed by the final slow sulfidation step to give CdS/HgS/CdS.

One hundred milliliters (100 mL) of deionized water is sealed in a 125 mL Erlenmeyer flask into which 1 mL of hydrogen sulfide gas is injected. The flask is shaken vigorously for 1 minute and 30 mL of this solution is transferred to volumetric addition funnel fitted to the top of the three-neck reaction flask. The sulfide solution is slowly dripped at a rate of 1-2 drops/second into the rapidly swirling reaction solution. Within a few minutes the solution becomes darker in color and eventually becomes dark reddish brown after all 30 mL of sulfide have been added. The final solution is purged with nitrogen for 30 minutes, adjusted to pH 7 and stored tightly sealed in the dark until it is used in experiments.

Ligand Exchange

The nanocrystals capped with polyphosphate tend to aggregate at high concentrations and after storage longer than a period of a few days. In order to make

these particles more stable it is necessary to exchange the capping ligand. This is done through a two-step dialysis procedure.

One hundred microliters (100 μL) of mercaptoacetic acid is added to 12 mL of deionized water. The pH of this solution is adjusted to pH 10.5 by dropwise addition of tetrabutylammonium hydroxide. Three milliliters (3 mL) of this solution is then added to the finished reaction mixture and well stirred. Two liters (2 L) of deionized water containing 0.5 mL mercaptoacetic acid in a large flask is adjusted to pH 10.5 using tetrabutylammonium hydroxide and gently stirred using a magnetic stir bar. The sample solution is transferred in 30-40 mL portions to dialysis tubes and immersed in the 2 L dialysis solution for at least 6 hours. The sample tubes are then carefully removed and immersed in another 2 L solutions, prepared the same as the first, for another 6 hours. This dialysis procedure serves to replace the capping polyphosphate ligands with mercaptoacetic acid and remover sodium ions from the solution and replace them with tetrabutylammonium ions. The crystals capped in this manner are stable for a few months and can be kept at high concentration.

PVP Synthesis of CdS/HgS/CdS

An alternate synthesis route has been developed that generates more stable and consistent samples of CdS/HgS/CdS than the traditional technique. The preparation is carried out in alcoholic solvent using PVP (polyvinylpyrrolidone) as a capping material. The CdS seeds generated under these growth conditions are slightly smaller (4 nm rather than 5 nm) but the remainder of the synthesis procedure remains the same.

CdS seed nanoparticles are prepared by sulfidation of cadmium chloride salt using hydrogen sulfide gas. One hundred milliliters (100 mL) of methanol in a 250 mL three-neck round-bottomed flask is purged with nitrogen for 30 minutes. Afterwards, 0.5 mL each of 0.1 M cadmium (II) chloride (aq.) and 10% PVP in methanol are added to the reaction solution and vigorously stirred. The solution is purged for another 10 min and then sealed. One milliliter (1 mL) of hydrogen sulfide gas is injected into the reaction vessel under vigorous magnetic stirring. Within seconds the reaction mixture becomes yellow as an indication of the formation of CdS nanocrystals. After 15 minutes of crystal growth the mixture is purged with nitrogen for 30 minutes before removing a 3 mL sample and continuing to the next step in the synthesis.

A monolayer of HgS is deposited on the outer surface of the CdS seeds through an ion-exchange reaction. Two hundred fifty microliters (250 μL) of 0.1 M mercury (II) chloride is rapidly injected into the reaction mixture under vigorous stirring. The solution immediately turns red in color as an indication that the surface chemistry has taken place and CdS/HgS particles are present. A 3 mL sample of the CdS/HgS solution is extracted followed by the final slow sulfidation step to give CdS/HgS/CdS.

One hundred milliliters (100 mL) of methanol is sealed in a 125 mL Erlenmeyer flask into which 1 mL of hydrogen sulfide gas is injected. The flask is shaken vigorously for 1 minute and 30 mL of this solution is transferred to volumetric addition funnel fitted to the top of the three-neck reaction flask. The sulfide solution is slowly dripped at a rate of 1-2 drops/second into the rapidly swirling reaction solution. Within a few minutes the solution becomes darker in color and eventually becomes dark reddish brown after all 30

mL of sulfide have been added. The final solution is purged with nitrogen for 30 minutes and stored tightly sealed in the dark until it is used in experiments.

Results

The evolution of the absorption spectrum of CdS nanocrystals following the addition of Hg^{2+} ions is shown in Figure 3.1. As mentioned before, the effect of adding Hg^{2+} is to exchange the outer layer of CdS for a layer of HgS. When equivalent concentrations of less than one monolayer HgS are used, the small patches of HgS that form on the surface of CdS are enough to alter the absorption spectrum in a detectable way. As seen in Figure 3.1, the effect of added Hg^{2+} is to shift the absorption to longer wavelengths and the development of a slight tail in the absorption that extends to nearly 650 nm. Complete monolayer formation is achieved when the absorption band stops migrating and begins to sharpen slightly around 500 nm as shown in the final spectrum. Continued addition of Hg^{2+} beyond the point of monolayer formation results in broadening of the absorption in the long wavelength tail of the spectrum.

The complete spectra of PVP capped CdS/HgS/CdS are shown in Figure 3.2. The two spectra shown are the results of two preparations carried out on different days. The spectra in red are that of the PVP capped CdS core nanocrystals that are approximately 4 nm in diameter as determined from the position of the absorption onset. One monolayer addition of HgS results in the green spectra of CdS/HgS. Finally, a monolayer capping of CdS completes the particle and leads to the spectra shown in blue of PVP capped CdS/HgS/CdS. Notice that there are only slight differences between the spectra taken on

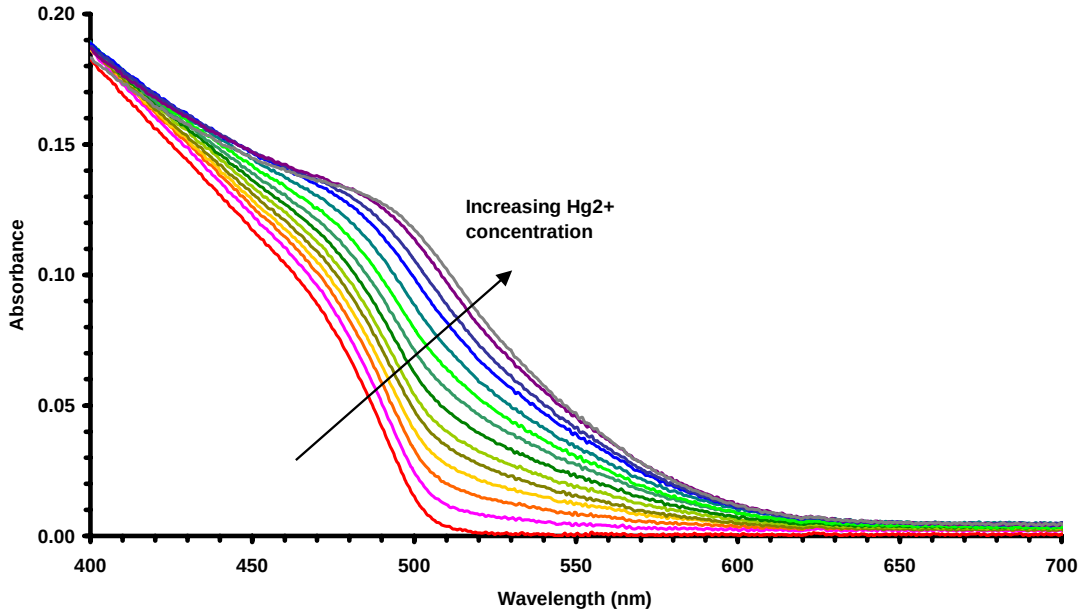

Figure 3.1 – Evolution of the absorption spectrum of CdS upon continued addition of Hg^{2+} in aqueous solution.

different days. Such was not the case with the polyphosphate synthesis technique in which different results were obtained for every synthesis, regardless of the rigorous attention to detail applied to reagent preparation and synthesis execution.

Conclusion

The principles behind the preparation of CdS/HgS/CdS nanocrystals are quite simple, but in practice it is difficult to make consistent samples from day to day that are stable for extended periods of time. A solution to this difficulty was found by developing a modified synthesis technique using PVP as a capping material instead of

polyphosphate. The resulting crystals can be prepared nearly identical from day to day and are stable at room temperature for several months even at concentrations of 0.1 M.

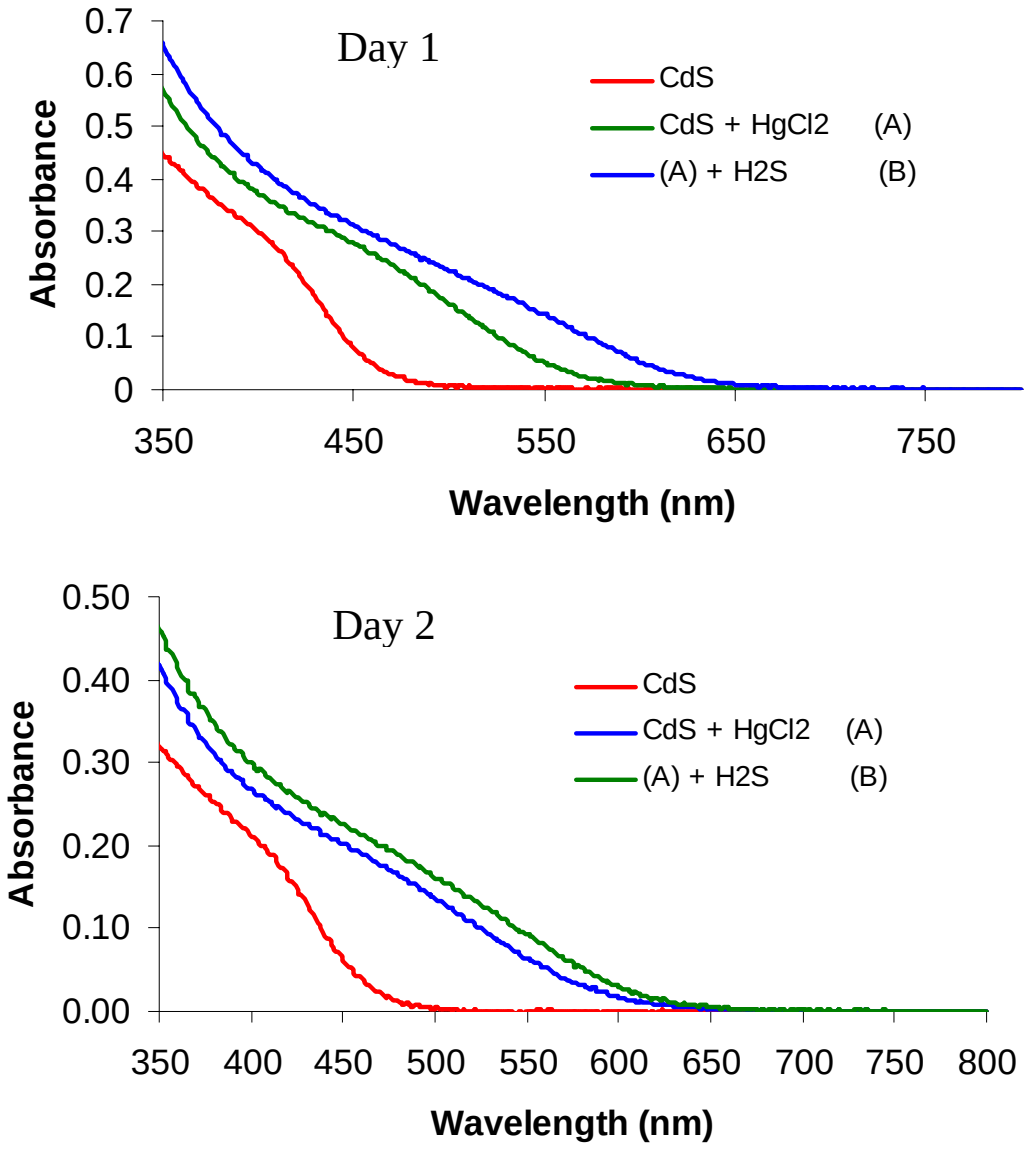

Figure 3.2 – Absorption spectra taken during two preparations of PVP capped CdS/HgS/CdS on consecutive days (labeled Day 1 and Day 2).

References

1. H. Weller, U. Koch, M. Gutierrez, A. Henglein. *Ber. Bunsenges. Phys. Chem.*, **1984**. 88, 649.
2. L. Spanhel, H. Weller, A. Fojtik, A. Henglein. *Ber. Bunsenges. Phys. Chem.*, **1987**. 91, 88.
3. Henglein, Arnim. *Topics in Current Chemistry*, **1988**. 143, 115, 131.
4. Katsikas, L., A. Eychmueller, M. Giersig, and H. Weller. *Chemical Physics Letters*, **1990**. 172, 3-4, 201-4.
5. Eychmueller, A., A. Haesselbarth, and H. Weller. *Journal of Luminescence*, **1992**. 53, 1-6, 113-5.
6. Haesselbarth, A., A. Eychmueller, R. Eichberger, M. Giersig, A. Mews, and H. Weller. *Journal of Physical Chemistry*, **1993**. 97, 20, 5333-40.
7. Eychmueller, A., A. Mews, and H. Weller. *Chemical Physics Letters*, **1993**. 208, 1-2, 59-62.

CHAPTER 4

PROBE WAVELENGTH DEPENDENT HOT ELECTRON DYNAMICS IN PVP CAPPED CdS/HgS/CdS QUANTUM DOT QUANTUM WELL NANOCRYSTALS

Sub-picosecond pump-probe transient absorption spectroscopy has been used to examine the probe wavelength dependent kinetics of PVP capped CdS/HgS/CdS quantum dot quantum well nanoparticles. Using 398 nm and 520 nm excitations, the relaxation of the excited hot electrons above the band gap state is characterized by both rapid electronic nonradiative relaxation and slower thermal relaxation processes. The wavelength dependence of both the fast rise and fast decay of the transient bleach is discussed in terms of electron-phonon relaxation processes involving mixed CdS/HgS states at short probe wavelengths or pure HgS states at long probe wavelengths. The slow decay of the transient bleach is discussed in terms of a thermal phonon-phonon relaxation process leading to the dissipation of heat from the hot nanoparticle lattice to the surrounding medium.

Introduction

The interest in nanocrystalline semiconductor heterostructures was first demonstrated by the preparation of mixed ZnS/CdS and CdS/HgS colloids [1, 2]. This was then followed by the preparation of the first quantum well within a quantum dot in the form CdS/HgS/CdS [3]. This new type of nanocrystalline heterostructure became known as the Quantum Dot Quantum Well (QDQW) and has since been the subject of numerous spectroscopic and photophysical studies. Experiments concerning the QDQW

crystal structure [4], luminescence properties [5], picosecond relaxation [6], magnetic properties [7] and charge-carrier localization times [8] have been conducted in the past decade following its discovery.

The characteristic property of the QDQW is that it is formed of two or more semiconductor materials with large differences in band-gap energy. In the case of CdS/HgS/CdS, the core material, CdS, has a band gap energy of 2.42 eV while HgS, the well material, has a band gap energy of 0.5 eV. This band gap energy difference, combined with the layered structure of the particle, generates within the crystal a region of high local confinement within the HgS well. The behavior of excited charge carriers in such an environment has been the focus of most research being done on the QDQW system.

The sizes of CdS/HgS/CdS nanocrystals are between 5 and 6 nm in diameter. In this size regime, quantum confinement effects dominate the electronic structure and therefore the optical absorption spectrum of the particles immersed in solution. The absorption spectrum of these particles extends throughout the entire visible region from 700 to 400 nm and into the UV (Figure 4.1). The absorption spectrum shares many of the characteristics of the CdS spectrum, but with additional absorption due to new transitions arising from the perturbation by the HgS well monolayer. From theoretical studies of the CdS/HgS/CdS system, it is known that higher excited states are characterized by electronic wavefunctions that are more CdS in character, while lower excited states have more HgS character [9-11]. It is therefore possible to think about the excitation of the CdS/HgS/CdS system in terms of core excitation (producing an excited state with mostly CdS character) versus much lower energy well excitation (producing an excited state with predominately HgS character). Using fluorescence line narrowing spectroscopy, it

has been demonstrated that the emission from colloidal CdS/HgS/CdS has a vibronic signature associated with the LO phonon mode of bulk HgS [5],[12]. This serves as experimental confirmation of what the theory has predicted, that the lowest excited state of CdS/HgS/CdS is dominated by an HgS electronic structure. From this we can establish a model for the excited state relaxation of the CdS/HgS/CdS system in terms of core excitation versus well excitation and in terms of hot electron relaxation from core-dominated excited states to well-dominated states near the band gap.

This model has been used previously to interpret measurements of ultrafast relaxation processes in QDQW nanocrystals [13],[8]. Time-resolved pump-probe studies have revealed the behavior of transient signals resulting from electronic excitation of CdS/HgS/CdS nanocrystals. A rapid spectral diffusion from higher energy, CdS dominated bleached absorption to lower energy, HgS dominated bleached absorption occurs within the first 5 picoseconds of the relaxation. In addition to transient bleaching behavior, the rise and decay of stimulated emission from excited CdS/HgS/CdS was also investigated. Under the premise of the proposed model, the time evolution of the stimulated emission signal yields parameters associated with the migration of charge carriers into their respective lowest excited states. It is not necessarily expected that the electron and hole relax to their lowest excited states at the same rate, but the rise time of the stimulated emission signal indicates the time it takes for the slowest of the carriers to relax. In order to further investigate this phenomenon, Braun et. al. [8] also monitored the kinetic behavior of transient signals that are only associated with hole relaxation. In particular, they used transient IR excited state absorption spectroscopy at 4700 nm to probe the evolution of the hole relaxation independently from that of the electron. This study demonstrated that the transient signal associated with the hole shows up within 50-

120 fs while the stimulated emission signal rises in 1.5 ps. It was therefore suggested that the electron is the slower of the two migrating charge carriers [8].

The focus of the present work is to further characterize the excited hot electron relaxation of CdS/HgS/CdS nanoparticles following the introduction of PVP as a capping material. The probe wavelength dependent relaxation kinetics are to be examined under different excitation conditions and in terms of the extent of mixing between the core CdS and well HgS states involved in the relaxation processes observed.

Experimental

PVP-CdS/HgS/CdS nanocrystals were prepared using a modified version of the synthesis technique that has traditionally been used [3]. The synthesis may be separated into three parts: (1) growing the CdS core, (2) exchanging the outermost Cd atoms for Hg to form the HgS well monolayer, (3) Capping the well with a monolayer of CdS.

The core of CdS was synthesized in methanol using PVP (mw 50,000 Da) as a capping material. For the source of Cd^{2+}, a 0.1 M solution of $CdCl_2$ was prepared in deionized water. A 0.2 mL portion of the Cd^{2+} solution was added to 100 mL of methanol in a 250 mL three-neck reaction flask. A 0.2 mL portion of 10% PVP in methanol was also added to the reaction flask and the mixture was purged with argon gas for 30 minutes under vigorous stirring. Afterwards, 1.0 mL of H_2S gas was rapidly injected into the sealed reaction vessel while the mixture continued to stir rapidly. After 10 minutes, a bright greenish-yellow solution had evolved, indicating the growth of CdS nanocrystals. This solution was then purged with argon for an additional 30 minutes to

remove any excess H_2S gas that may have remained. A 3 mL sample of the CdS colloidal suspension was taken for analysis followed by a rapid injection of 0.1 mL of 0.1 M $HgCl_2$ in deionized water. After 5-10 seconds of vigorous stirring after the injection of Hg^{2+} a 3 mL sample of the CdS/HgS colloid was removed and the remaining reaction mixture was treated with a drop-wise addition of 30 mL of a 1 mL H_2S/100 mL methanol solution. The slow addition of S^{2-} is necessary to avoid the generation of high local concentrations of Cd^{2+} and S^{2-}, which could result in the formation of new CdS seeds. The slow addition process should take at least 20 minutes and a completed synthesis is indicated by a deep reddish-brown color of the reaction solution. After the addition of S^{2-} in the last step is complete, the reaction mixture was again purged with argon to remove any excess dissolved gas. The approximately 120 mL of CdS/HgS/CdS colloidal suspension was then transferred to a 250 mL round-bottomed flask and 1 gram of PVP added to the solution. The additional PVP ensures complete protection of the nanocrystals and also facilitates the preparation of a dry film of the QDQW sample. The 120 mL sample was concentrated to about 10 mL using a rotary evaporator and the final samples were stored in vials in the dark. Samples taken during the course of the preparation were transferred to a 1 cm glass cuvette and characterized using UV-VIS spectroscopy.

Alloy nanocrystals of Cd(Hg)S were also prepared for comparison to the layered CdS/HgS/CdS quantum dot quantum well system. Portions of 10% PVP (0.2 mL), 0.1 M $CdCl_2$ (0.2 mL) and 0.1 M $HgCl_2$ (0.1 mL) were added to 100 mL of methanol in a 250 ml three neck flask. The solution was bubbled with nitrogen for thirty minutes. Hydrogen sulfide gas (1.0 mL) was rapidly injected into the mixture under vigorous stirring. The resulting nanocrystals were red in color and did not share the same

absorption as the quantum dot quantum well layered nanocrystals. For sub-picosecond pump-probe spectroscopy, the concentrated samples were filtered through a 0.1 micron syringe filter and placed into cylindrical glass cuvettes with a pathlength of 2 mm. Under low excitation energies (<800 nJ), the samples could be studied without rotation of the sample cell. At higher pump powers however, the cells should be rotated to avoid local photobleaching. For all experiments the pump pulse produced less than one electron-hole pair per particle.

Sub-picosecond pump-probe transient spectroscopy was carried out using an amplified Ti:Sapphire laser system and a traditional slow-scan pump-probe optical setup. The amplified Ti:Sapphire laser (Clark-MXR CPA-1000) has an output of 0.8 mJ, 100 fs pulses at a fundamental wavelength of 795 nm. A small fraction of the beam (4%) was split and sent to a white-light continuum generator while the remaining 96% was used for harmonic generation (398 and 265 nm) and the pumping of two OPAs (Quantronix TOPAS). Pump beams from either the harmonic generator or OPA were passed down a delay line and overlapped with the white light continuum beam within the sample. The spot sizes were approximately 250 micron for the pump beam and 100 micron for probe. Single wavelength kinetics were monitored using a monochromator/photodiode arrangement coupled to a boxcar integrator and a lock-in amplifier. The pump beam was chopped at 492 Hz (f/2) and used as the reference frequency for the lock-in.

Results

Absorption spectra taken during the course of CdS/HgS/CdS preparation are shown in Figure 4.1. The CdS nanocrystals show an excitonic transition at about 400 nm

(3.1 eV), indicating an approximate size of 4 nm in diameter [14]. Following the addition

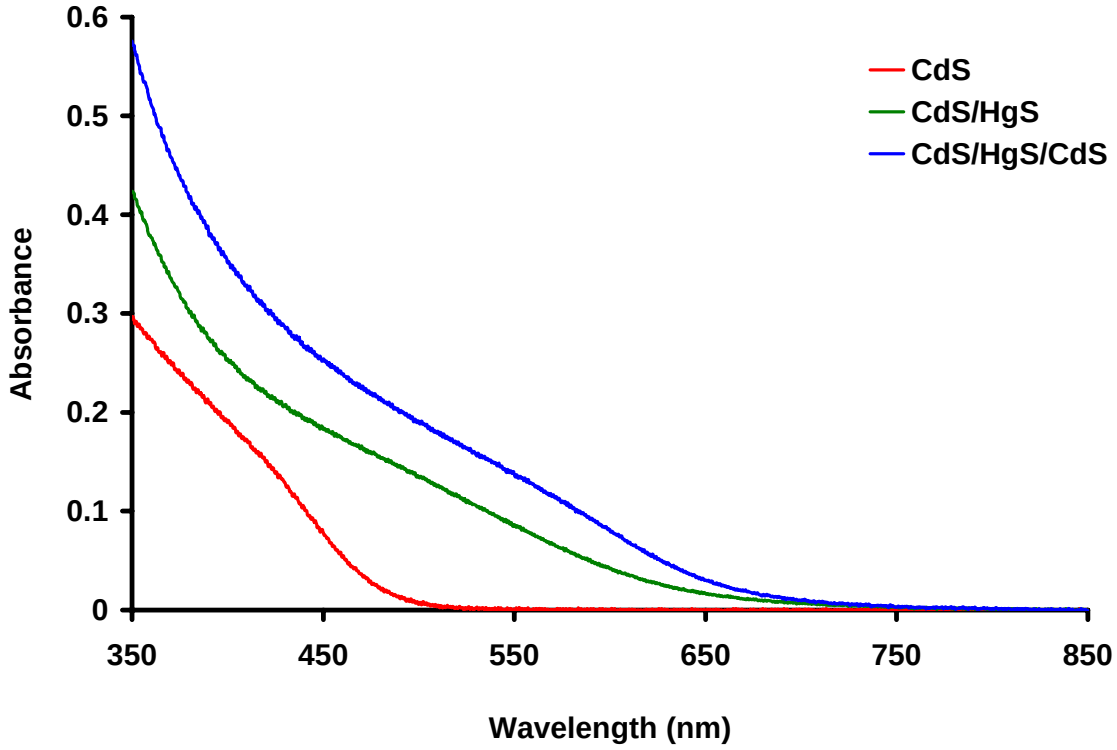

Figure 4.1. Absorption spectra collected during the preparation of PVP-CdS/HgS/CdS nanocrystals.

of the HgS well layer the spectrum red shifts to about 500 nm, and the overall extinction increases over the entire spectrum. The final addition of the CdS outer layer again shifts the absorption spectrum slightly to about 560 nm, and the extinction again increases slightly. The final CdS/HgS/CdS particles are about 5 nm in diameter, assuming a layer thickness of 0.5 nm for both the HgS well and CdS outer layer and considering that the outermost layer of the CdS core was displaced by a monolayer of HgS.

Figure 4.2 shows the pump-probe kinetic traces of excited PVP-CdS/HgS/CdS nanocrystals obtained using 398 nm excitation and monitored at different wavelengths. The probe wavelengths selected cover the entire range of the ground state bleach and demonstrate the differences in the bleach relaxation behavior for different transitions. As can be seen in the figure, transitions at higher energy relax much faster than lower energy transitions. This behavior is contrasted by the results in Figure 4.3 for the pump-probe kinetic traces of the Cd(Hg)S alloy nanocrystals. In this case all of the kinetic traces at each of the wavelengths probed look nearly identical within experimental error – no wavelength dependence of the relaxation dynamics appears.

Rise times of the kinetic traces in Figure 4.2 were obtained from a fit using a non-linear least squares fitting routine. The fitting function used consisted of a multiple exponential rise and decay numerically convoluted with a 150 fs FWHM Gaussian instrument response function (Appendix 2). In order to obtain acceptable fits of the rise portion of the traces, the fitting procedure was limited to the data points within the first three picoseconds of the signal. The best-fit curves are shown in Figure 4.4A. From these fit functions, the rise times were determined using the 10-90% of maximum signal methodology. The reported rise times are therefore the times taken for the signal to rise from 10% to 90% of its maximum intensity. These times are plotted as a function of

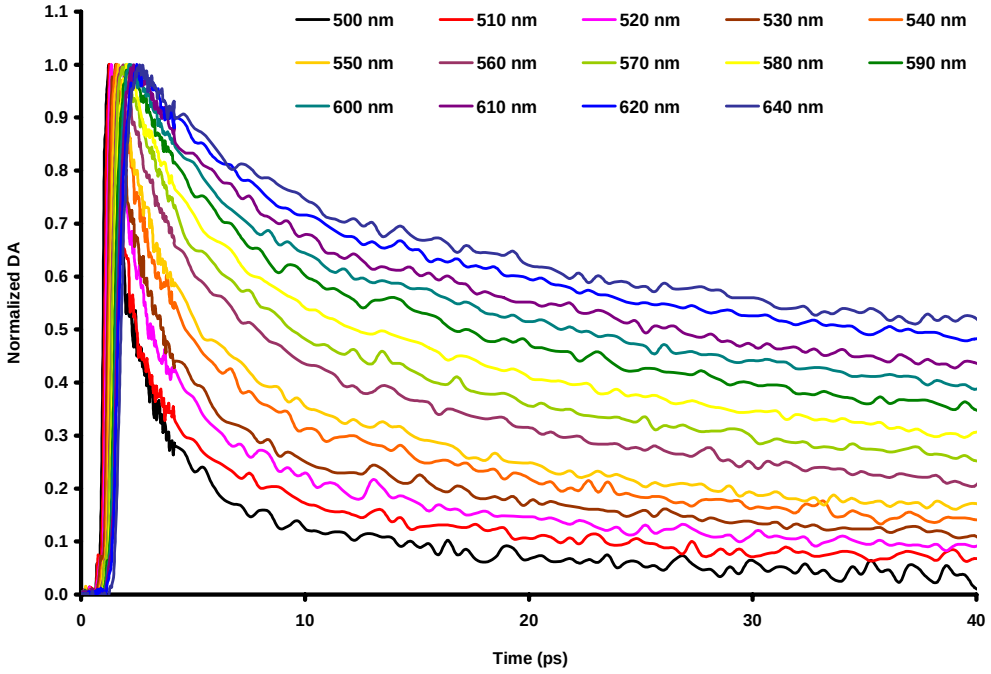

Figure 4.2. Pump-probe kinetic traces of excited PVP-CdS/HgS/CdS nanocrystals obtained following excitation with a 100 fs pulse of 398 nm light. Probe wavelengths indicated on the figure.

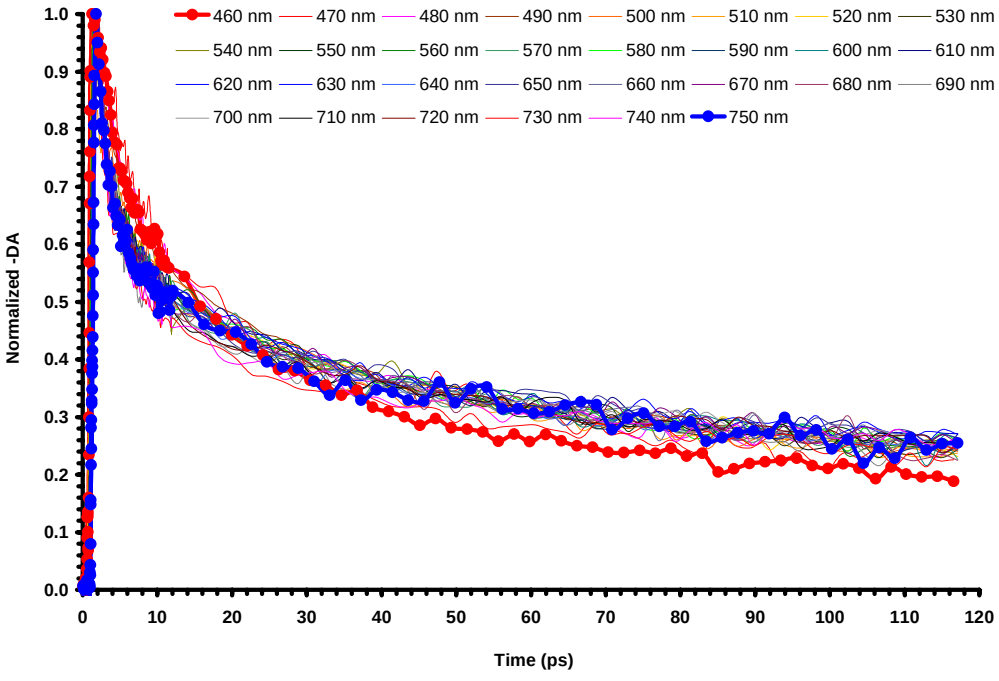

Figure 4.3. Pump-probe kinetic traces of excited PVP-Cd(Hg)S alloy nanocrystals obtained following excitation with a 100 fs pulse of 398 nm light. Probe wavelengths indicated on the figure.

probe wavelength in Figure 4.5A. The decay portion of the traces shown in Figure 4.2 were fit to a two exponential decay function and the parameters of the fit are summarized in Table 4.1.

Figure 4.2B shows the pump-probe kinetic traces recorded for excited PVP-CdS/HgS/CdS nanocrystals following excitation at 520 nm. For comparison and rise time calculations, the experimental data were again fit using a non-linear least squares fitting routine. The best-fit curves are plotted in Figure 4.4B. The rise times in Figure 4.4B were again determined using the 10-90% methodology and plotted as a function of probe wavelength in Figure 4.5B.

Discussion

Wavelength Dependent Rise Times

Excitation of colloidal PVP-CdS/HgS/CdS at 398 nm generates hot excited electrons high above the band gap energy level. Relaxation from this initial state was monitored using pump-probe transient absorption spectroscopy at different probe wavelengths. Bleaching of ground state absorptions in semiconductor nanocrystals can be attributed to state-filling by either the electron, the hole or by both carriers. However, it has been shown that the observed time dependent bleach in the visible region is attributed to the relaxation of the electron [15]. Excited states in the CdS/HgS/CdS system can be modeled as a mixing of pure CdS states with pure HgS states. The wavefunctions for higher excited states of CdS/HgS/CdS can be considered as having more CdS character, while the opposite is true for the lower excited states, those having

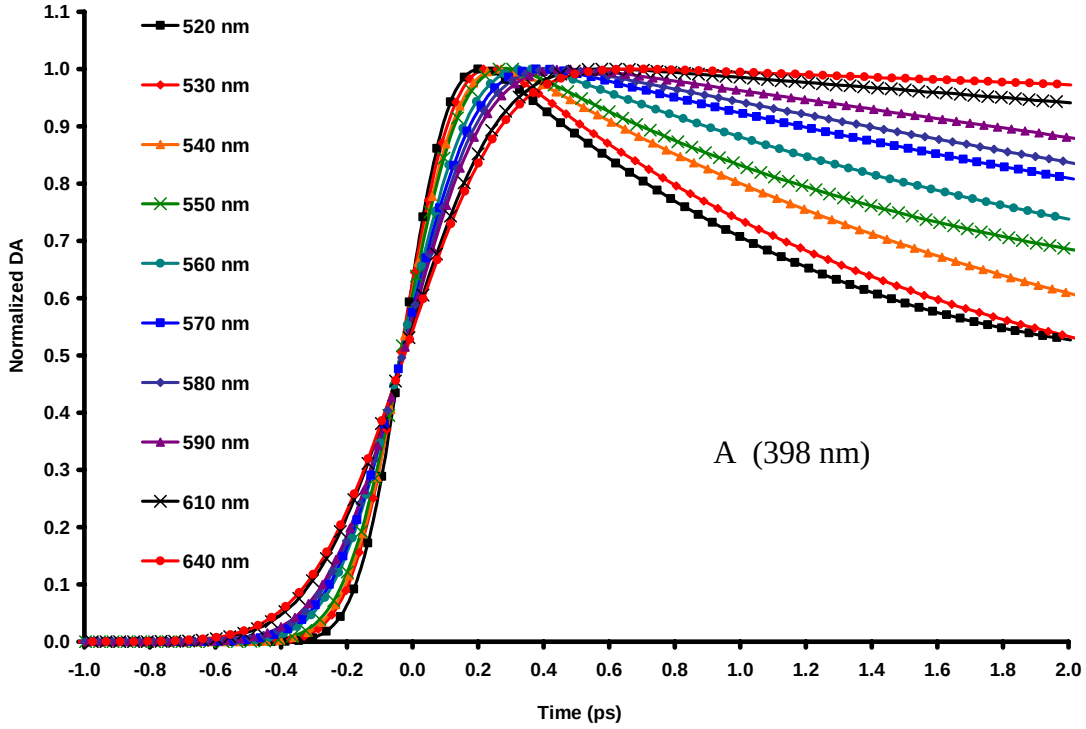

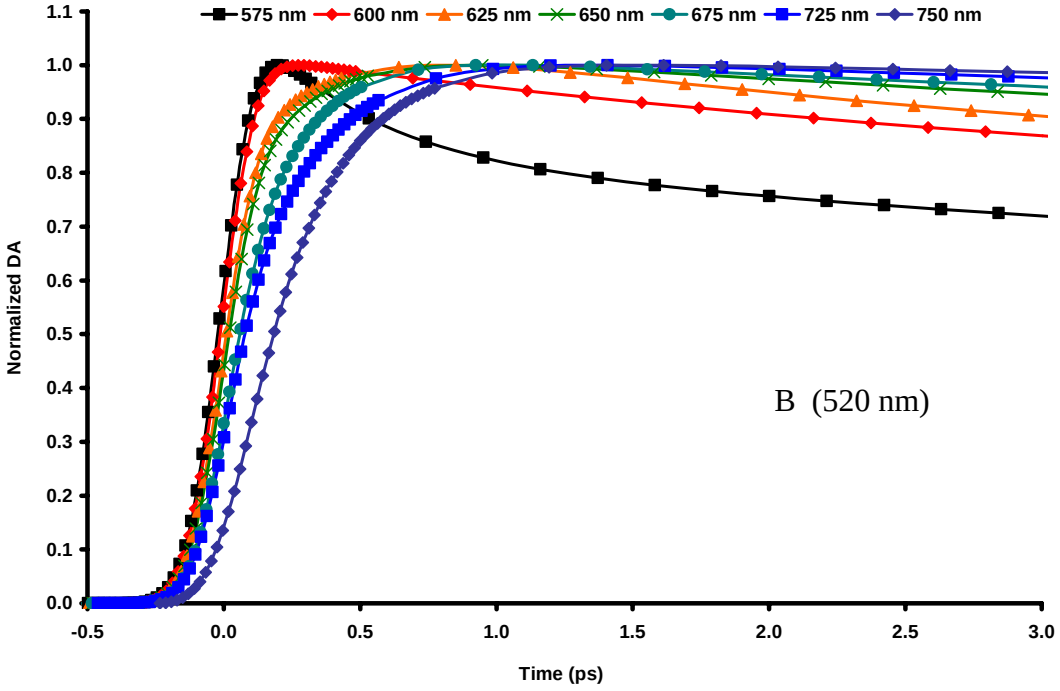

Figures 4.4A and 4.4B. Pump-probe kinetic traces of excited PVP-CdS/HgS/CdS nanocrystals obtained following excitation with 100 fs pulses of 398 (A) and 520 (B) nm light. The traces shown are chirp-adjusted best-fit curves to the experimental data.

Table 4.1. Wavelength dependent kinetic decay parameters determined from fitting the experimental data traces obtained using 398 nm excitation. The data were fit to a two exponential decay function. Time constants for the fast (T1) and slow (T2) decay components are shown along with the percent relative amplitudes of each.

Probe Wavelength (nm)	T1 (ps)	% T1	T2 (ps)	% T2
500	0.8	64	7	36
510	1.0	65	16	35
520	1.5	80	24	20
530	1.8	69	34	31
540	2.2	63	36	38
550	2.5	58	40	42
560	3.2	55	47	45
570	3.6	50	56	50
580	4.2	47	64	53
590	4.4	41	69	59
600	4.7	39	77	61
610	5.1	36	85	64
620	6.0	29	95	71
630	5.9	33	107	67
640	6.0	30	115	70
650	6.0	27	115	73
660	6.0	22	119	78
670	6.0	28	121	72
680	6.0	26	128	74
690	6.0	26	134	74
700	6.0	28	140	72
710	6.0	23	158	77
720	6.0	33	160	67

more HgS character. Intermediate states are composed of a mixture of pure CdS and HgS states. The probe wavelength dependence of the pump-probe kinetics in PVP-CdS/HgS/CdS due to excited state relaxation is expected to reflect the nature of the wavefunctions of these states.

Figure 4.6 shows the results of fitting the ground state absorption spectrum of PVP-CdS/HgS/CdS to a sum of two Gaussian absorption bands. Non-linear least squares techniques were employed to obtain the best fit to the experimental spectrum. Assuming that the bandwidth is either homogenous or that inhomogeneous broadening affects both absorption bands in the same manner, the same bandwidth (4000 cm^{-1}) was used for the fit of both Gaussians and only the height and center wavelength (wavenumber) were left as adjustable parameters. As indicated in the figure, the two bands have been designated pure HgS and pure CdS. Using these two Gaussian functions one can quantitatively predict the fraction or percentage of the absorption due to pure HgS (pure CdS) states at every excitation and probe wavelength used in this study.

$$\%HgS = 100\% \times \frac{A_{HgS}(\lambda)}{A_{HgS}(\lambda) + A_{CdS}(\lambda)} \qquad (4.1)$$

The results of this calculation are shown in Figure 4.7. On the figure are indicated representative wavelengths of interest and their corresponding %HgS absorption intensity values. Above 493 nm, the mixed wavefunction is predominately HgS in character and eventually becomes pure (>98%) HgS above 627 nm.

Rise times of bleached absorptions from 500-720 nm are plotted in Figure 4.5. Figure 4.5A shows the wavelength dependence of the bleach following 398 nm excitation while Figure 4.5B shows the same dependence under 520 nm excitation conditions. In

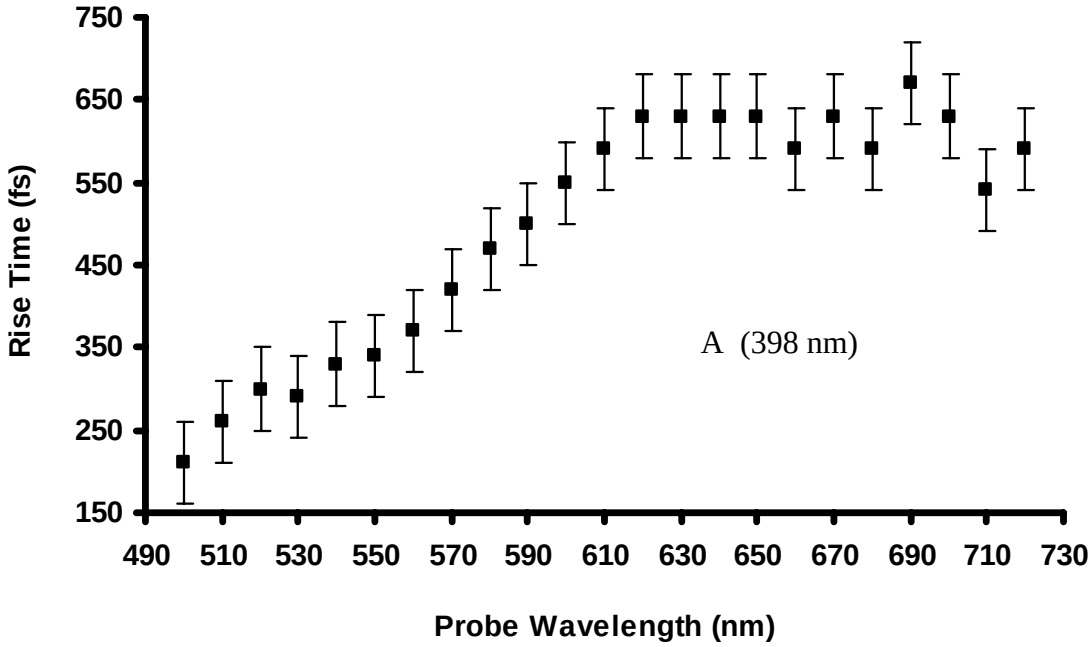

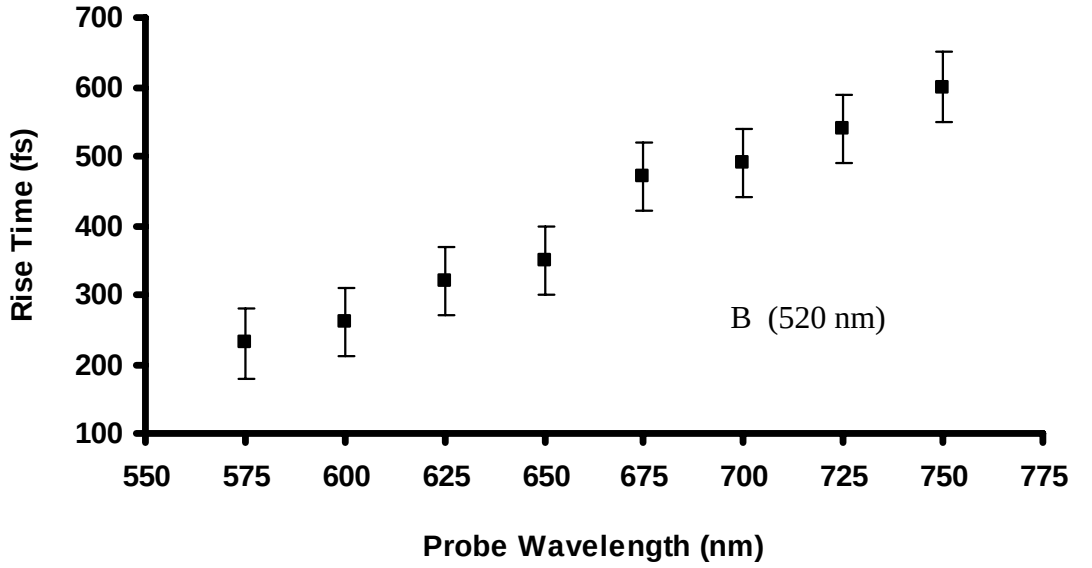

Figure 4.5A and 4.5B. Rise times of the transient signal at various probe wavelengths for PVP-CdS/HgS/CdS nanocrystals following excitation with 100 fs pulses of 398 (A) and 520 (B) nm light. Rise times were determined from the best-fit curves to the experimental data using the 10-90% method. The uncertainty in these times is ±50 fs and indicated by the error bars.

Figure 4.5A, there is a steady increase in the rise times between 500 nm and 620 nm, followed by a constant between 620 nm and 720 nm. Since bleached absorptions in this region are associated with electron relaxation, the rise time of the bleach is proportional to the relaxation time of the electron from the higher excited state at 398 nm (3.1 eV) to a particular state monitored at a longer wavelength (lower energy). The higher energy absorptions involve states whose wavefunctions are more similar to that of the initially prepared state and have mostly CdS character. The states monitored using probe wavelengths between 500 nm and 620 nm are mixtures of CdS and HgS states, as predicted from the two-absorption band fit function. The states monitored at wavelengths longer than 620 nm are those of the HgS well. This qualitative picture is represented graphically in Scheme 4.1.

Following excitation at 520 nm, the rise times of the bleach increase steadily across the entire spectrum of bleached absorptions (Figure 4.5B). In contrast to the wavelength dependence for 398 nm excitation, there isn't any sign of leveling off to a constant rise time for the bleach resulting from 520 nm excitation.

A qualitative explanation of this is that the prepared state at 520 nm is a CdS/HgS mixed state. Its relaxation to other mixed states or pure HgS states must always be described using cross terms involving states in the two materials.

The above qualitative explanation can be formulated quantum mechanically as follows. Assume that the wavefunctions of any excited state in CdS/HgS/CdS nanoparticles can be written as a linear combination of CdS and HgS wavefunctions

$$\psi_\lambda = \alpha_\lambda^{CdS}\psi^{CdS} + (1-\alpha_\lambda^{CdS})\psi^{HgS} \qquad (4.2)$$

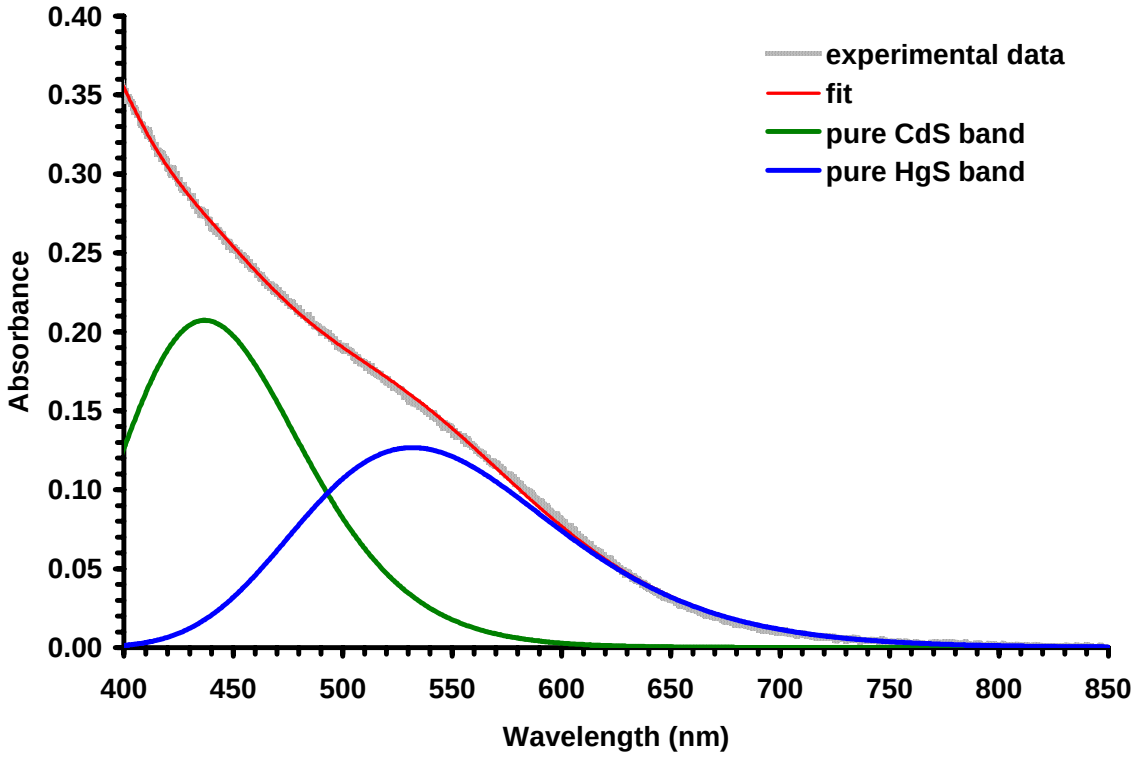

Figure 4.6. The fit of the absorption spectra of PVP-CdS/HgS/CdS nanoparticles to two Gaussian bands as indicated in the figure and described in the text. The band at higher energy is proposed to be the absorption of pure CdS while the low energy band is proposed to be the absorption of pure HgS. Note: a third Gaussian (not shown) was used to fit the high energy side (below 425 nm) but was not included in the subsequent analysis

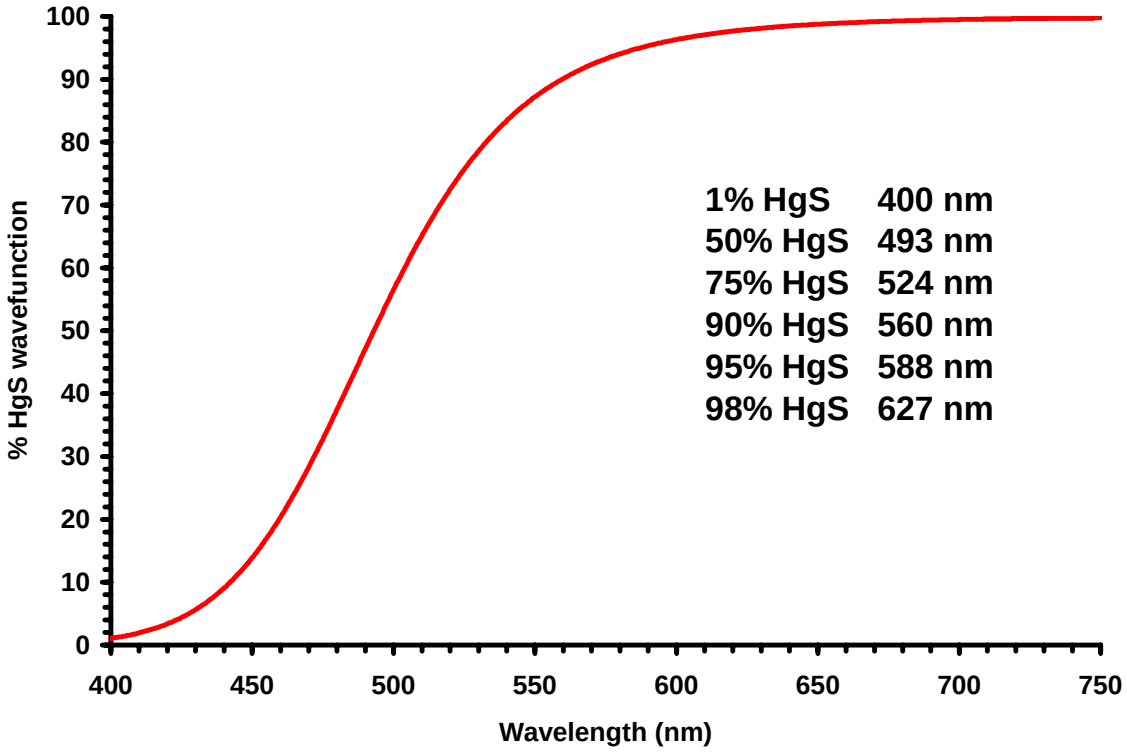

Figure 4.7. Percentage of the HgS wavefunction contribution to states corresponding to probe wavelengths as determined from the ratio of the pure HgS to pure CdS from simulated absorption bands.

where ψ^{CdS} and ψ^{HgS} are the wavefunctions for pure CdS and pure HgS, respectively. The wavelength dependent coefficient α_λ determines the fraction of CdS character within the mixed CdS/HgS wavefunction for a state monitored at wavelength λ. Pure CdS states would therefore have α_λ equal to 1 while pure HgS would have α_λ equal to 0. Mixed states would then of course have α_λ between 0 and 1. Given this expression for the wavefunctions of the CdS/HgS/CdS system, another expression can be written for the relaxation rate between an initial state, $\psi_{\lambda pump}$ and a final state $\psi_{\lambda probe}$ using Fermi's Golden Rule,

$$\omega_{\psi_{\lambda_{pump}},\psi_{\lambda_{probe}}} = \frac{1}{\tau^{rise}_{\lambda_{probe}}} = \left|\left\langle \psi_{\lambda_{pump}} H \psi_{\lambda_{probe}} \right\rangle\right|^2 \frac{\rho_{\lambda_{probe}}}{\hbar} \qquad (4.3)$$

where the initial state is labeled with the subscript λ_{pump} and the final state carries the subscript λ_{probe}, H is the perturbing Hamiltonian responsible for coupling and relaxation between the two states and ρ is the density of the final state. This expression describes the dynamics of relaxation from the initial state generated by optical excitation at λ_{pump} to the state monitored by the probe wavelength λ_{probe}. This will be used to interpret the results obtained for the wavelength dependent transient bleach rise times with λ_{pump}= 398 nm and λ_{pump}= 520 nm.

With 398 nm excitation, the initial state is made up almost entirely of pure CdS wavefunctions while the initial state prepared by 520 nm excitation is a mixed state consisting of contributions of pure CdS and pure HgS wavefunctions. The relaxation from the initial state at 398 nm to a bleach monitored at 500 nm involves relaxation from

a state that is entirely CdS in character to one that is mixed CdS/HgS in character. Equation 4.3 can be rewritten as

$$\omega_{398\rightarrow 500nm} = \frac{1}{\tau^{rise}_{500nm}} = \left|\left\langle \psi_{398nm} H \psi_{500nm} \right\rangle\right|^2 \frac{\rho_{500nm}}{\hbar} \qquad (4.4)$$

for the relaxation rate from the initial state at 398 nm to the first bleached absorption at 500 nm. However, from Equation 4.2 it can be supposed that the wavefunction ψ_{500nm} is mixed in character, having a value of α_λ between 0 and 1. As the probe wavelength increases, the fraction of HgS in the mixed state increases, α_λ becomes closer to zero, the matrix element in Equation 4.3 becomes smaller and the result is an increase in rise time across the wavelength range 500-620 nm. Above 620 nm, the states composing the bleached absorptions are entirely HgS in character, α_λ equals zero and the relaxation times from the initial state and corresponding rise times remain constant. We can rewrite the expression for the relaxation rate as,

$$\omega_{398\rightarrow >620nm} = \frac{1}{\tau^{rise}_{>620nm}} = \left|\left\langle \psi_{398nm} H \psi_{>620nm} \right\rangle\right|^2 \frac{\rho_{>620nm}}{\hbar} \qquad (4.5)$$

this time writing for a bleached absorption at a wavelength greater than 620 nm. Since the bleach above 620 nm involves states that are entirely HgS in character, in other words $\psi_{>620nm}$ equals ψ^{HgS}, and the initial state at 398 nm is pure CdS in character, the expression in Equation 4.5 can be written more simply as

$$\omega_{398\rightarrow >620nm} = \left|\left\langle \psi^{CdS} H \psi^{HgS} \right\rangle\right|^2 \frac{\rho_{HgS}}{\hbar} = \omega_{\psi_{CdS},\psi_{HgS}} \qquad (4.6)$$

The constant rise time across the region 620-720 nm (~610 fs) therefore reflects the intrinsic relaxation time from a pure CdS state to a pure HgS state in PVP-CdS/HgS/CdS

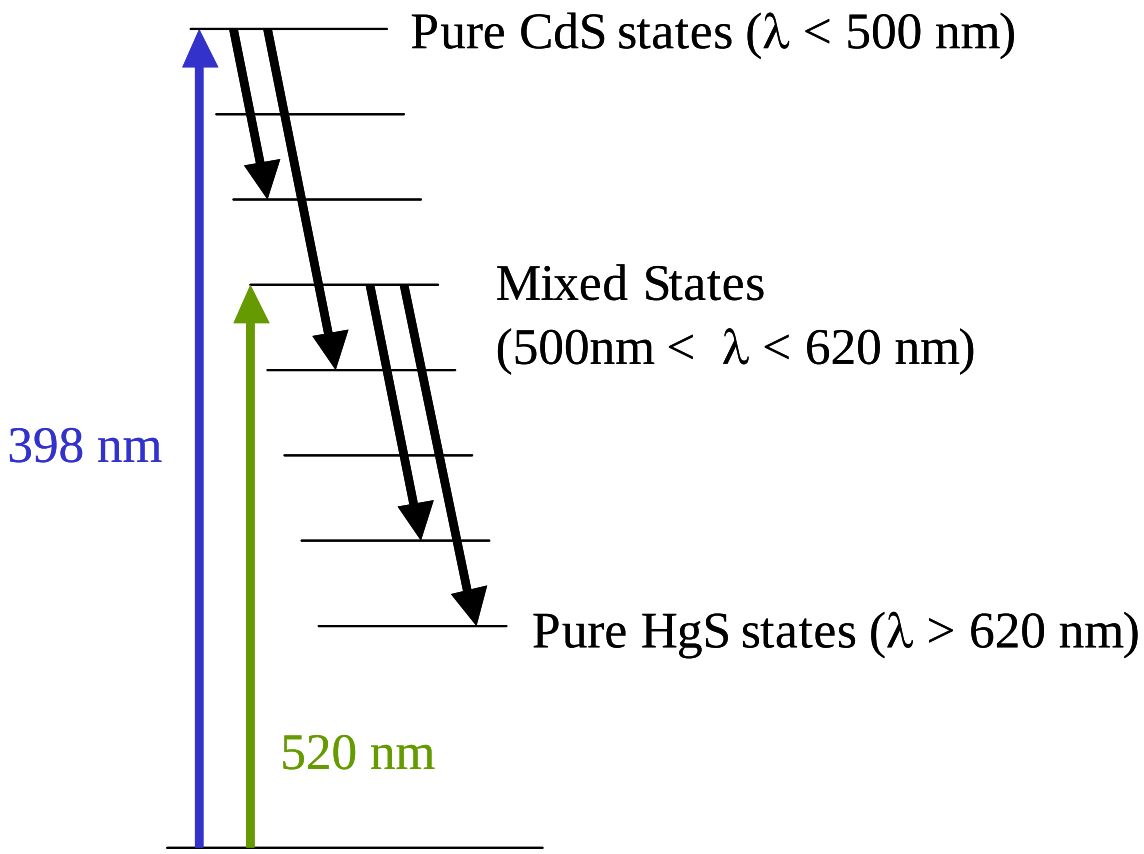

Scheme 4.1. Graphical representation of the relaxation model used for the interpretation of experimental data. Blue and green arrows represent excitation at 398 nm and 520 nm, respectively. Black arrows indicate the intra-band relaxation from higher excited states of which the relaxation rate is proportional to the rise times given in Figures 4A and 4B.

nanocrystals, i.e. the electronic interfacial crossing time between the two materials. The crossing time of 0.61 ps determined in the present work may be compared with the value of 1.5 ps determined from the rise time of the stimulated emission when excited at 400 nm in mercaptoacetic acid capped CdS/HgS/CdS quantum dot quantum wells of 6 nm in size [8]. The difference between these two values arises most likely from differences in the size of particles and the experimental methods used rather than a significant effect of capping material or solvent.

The relaxation from the initial state prepared with 520 nm excitation involves relaxation from a mixed CdS/HgS state to another mixed state (bleach at 575 nm to 620 nm) and eventually to a purely HgS state (bleach above 620 nm). In this case the initial state is a mixed state of constant coefficients while the final state is either a mixed state of probe wavelength dependent coefficients or a pure HgS state. From the gradual increase in the rise times from 200 fs to 600 fs, it can be suggested that one of the factors involved in the relaxation from the 520 nm initial state is the decrease in the CdS character of the states composing the bleached absorptions from 575 nm to 750 nm. Even though the 520 nm initial state is a mixed state, it probably has a larger fraction of CdS than HgS and will relax more rapidly into mixed states that also have larger fractions of CdS character. As the probe wavelength increases from 575 nm to 750 nm, the fraction of CdS character steadily drops off to zero. Under this argument it might be expected that a leveling off of the rise time should still be observed. However, given that within the bandwidth of the laser pulses used (~ 4 nm), a coherent ensemble of initial mixed states with slightly different CdS and HgS compositions is produced that will each relax in slightly different ways. In addition, inhomogeneous broadening also affects the

mixed states monitored for particles of different sizes. Thus, when the excited initial state itself is a mixed state, the resolution of the monitored state becomes more difficult.

Wavelength Dependent Decay Times

For wavelength dependent decay measurements, excitation was carried out at 398 nm. The probe wavelength dependent decay times are shown in Figure 4.8. The decay traces for the bleached transitions at different probe wavelengths were fit to a two exponential decay function and the two components are plotted separately in Figures 4.8A and 4.8B. The fast component follows the same functional dependence as the rise times, increasing over the range 500-620 nm and then leveling off over the range 620-720 nm. On the other hand, the second, slow decay component increases consistently over the whole spectrum of the bleached absorptions. This suggests that the two decay times are attributed to different relaxation pathways within the CdS/HgS/CdS system.

Since the probe wavelength dependent function for the fast time constant is very similar to that of the rise times, a similar argument for the relaxation mechanism can be made for this decay as was made for the rise. As a result of the analysis of the rise times, it was established that the mechanism behind the relaxation of excited CdS/HgS/CdS could be evaluated in terms of the relationship between the initial and final states. The two absorption band fit and wavelength dependent rise time functions identified regions of the bleach spectrum that are associated with states that were either mixed CdS/HgS or pure HgS in character.

Using the mixed wavefunction formalism of Equation 4.1, the fast component decay rate of a particular bleached absorption at a monitoring wavelength λ can be expressed as

$$\left(\frac{1}{\tau}\right)_\lambda = \alpha_\lambda^{CdS}\,\frac{1}{\tau_{CdS}} + \left(1-\alpha_\lambda^{CdS}\right)\frac{1}{\tau_{HgS}} \qquad (4.7)$$

assuming that the decay rate will be a wavelength dependent function of the decay rates of pure CdS states and pure HgS states. For bleached absorptions above 620 nm, the decaying state is pure HgS, α_λ equals 0. For bleached absorptions below 620 nm, the decaying state is a mixture whose composition (determined by the α_λ value) is wavelength dependent. The observed wavelength dependence of the fast decay component suggests that the excited electron decays faster in states with more CdS character. In other words, $\tau_{CdS} < \tau_{HgS}$ in Equation 4.7. The idea that excited electrons relax faster in CdS than in HgS is understandable considering that there is many more Cd atoms than Hg atoms in these CdS/HgS/CdS nanoparticles. The number of phonons, defects, surface states and the density of the hole states are all much larger in the CdS system than in the protected HgS well. Therefore, any of the proposed electronic nonradiative relaxation mechanisms, whether by electron-phonon coupling, by defects or surface states [16], or by electron-hole coupling [17], would predict that electrons in CdS would relax faster than electrons in the HgS well.

The long decay component must be explained in a different way. In this case, the probe wavelength dependence does not level off to a constant value, but instead increases steadily over the entire spectrum of bleached absorptions. Also, these decay times are much larger than those of the first time constants, indicating a different type of

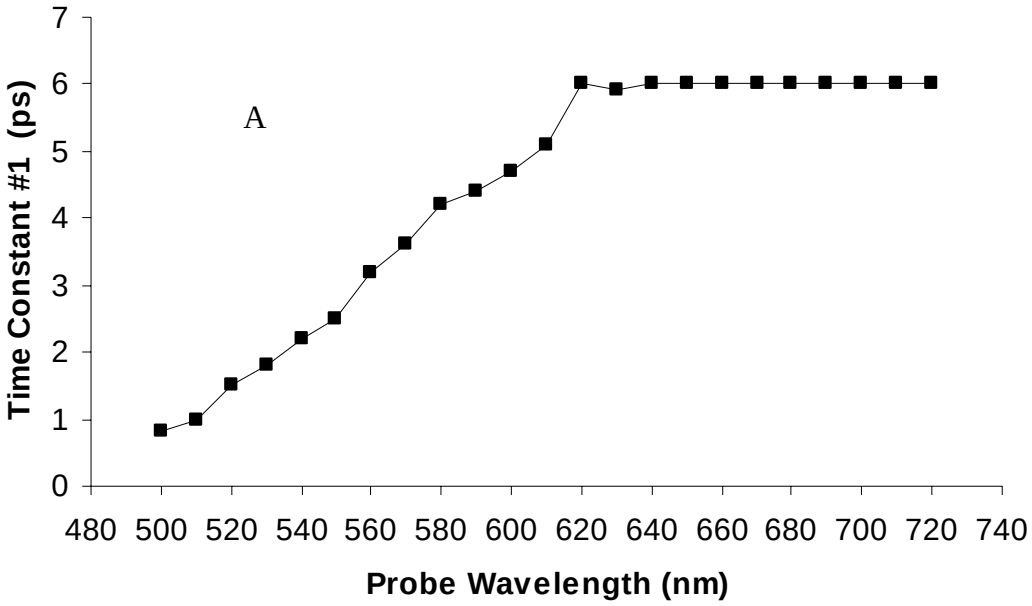

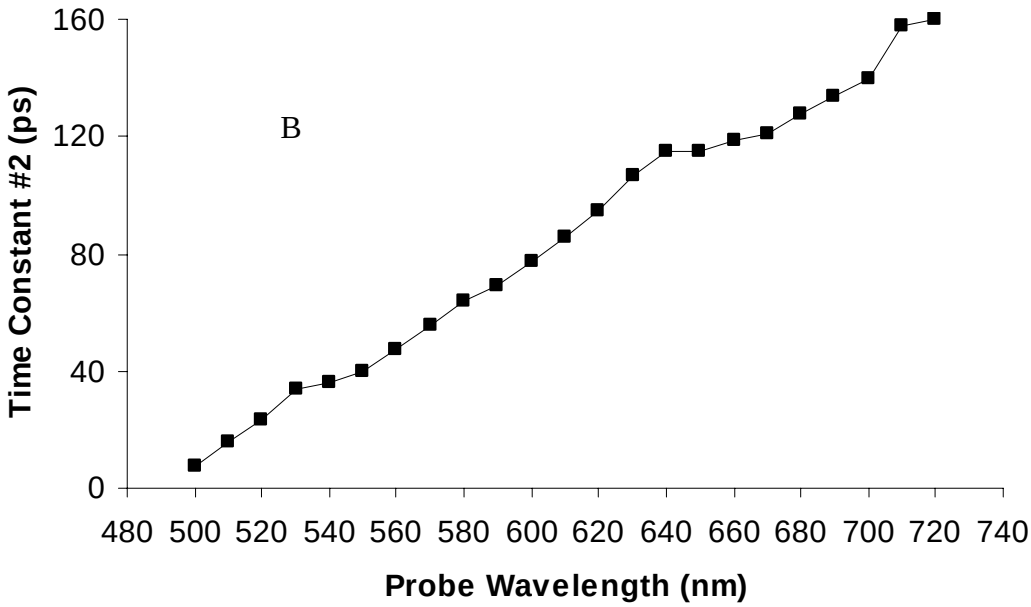

Figures 4.8A and 4.8B. Probe wavelength dependent decay times for the fast (A) and slow (B) components of the bleach recovery following excitation at 398 nm. The results were obtained by fitting the experimental kinetics traces to a two exponential decay using a nonlinear least squares fitting routine. The fast component has been assigned to rapid electronic nonradiative relaxation while the slow component has been assigned to a thermal relaxation process.

non-radiative relaxation mechanism. Electronic nonradiative relaxation occurs on a faster time scale, so it is most probable that the relaxation process involved for the slow component is not electronic, but rather involves cooling of the hot lattice by heating the surrounding medium. Hot electrons generated by the excitation pulse dissipate energy as heat to the phonons of the lattice. The hot particle lattice must then dissipate heat to the surrounding bath: capping material and solvent. Since electronic relaxation is not involved, the electronic composition of the relaxing state is immaterial and the only parameter affecting the relaxation rate is the amount of heat to be dissipated and the coupling mechanism involved between the particle surface and the heat bath (surrounding medium). The rate-limiting step for relaxation by this mechanism is the cooling of the particle lattice by heat transfer to the surrounding bath. The rate of heat loss is directly proportional to the temperature difference between the two media and will occur faster for a hotter lattice resulting from the relaxation of a higher energy excited electron. Hot electrons in bleached states that are closer to the initial state are expected to produce more vibrational energy when they relax than lower energy states and are therefore responsible for more heating of the lattice. Thus assuming that the coupling between the nanoparticle and the surrounding medium is the same and that the type of relaxation is not rate determined by the heat conductivity of the medium, the observed functional dependence of the relaxation time on monitoring wavelength (excited electron energy) can be understood.

References

1. A. Haesselbarth, A. Eychmueller, R. Eichberger, M. Giersig, A. Mews, H. Weller. *Journal of Physical Chemistry*, **1993**. 97, 5333-5340.
2. Henglein, Arnim. *Topics in Current Chemistry*, **1988**. 143, 115, 131.
3. A. Eychmueller, A. Mews, H. Weller. *Chemical Physics Letters*, **1993**. 208, 1, 59-61.
4. A. Mews, A. Eychmueller, M. Giersig, D. Schooss, H. Weller. *Journal of Physical Chemistry*, **1994**. 98, 934-941.
5. A. Mews, A. V. Kadavanich, U. Banin, A. P. Alivisatos. *Physical Review B*, **1996**. 53, 20, 13242-13244.
6. V. F. Kamalov, R. B. Little, S. Logunov, M. A. El-Sayed. *Journal of Physical Chemistry*, **1996**. 100, 16, 6381-6384.
7. E. Lifshitz, H. Porteanu, A. Glozman, H. Weller, M. Pflughoeft, A. Eychmueller. *Journal of Physical Chemistry B*, **1999**. 103, 6870-6875.
8. M. Braun, S. Link, C. Burda, M. A. El-Sayed. *Physical Review B*, **2002**. 66, 20, 205312-205317.
9. D. Schooss, A. Eychmueller, A. Mews, H. Weller. *Physical Review B*, **1994**. 49, 24, 17072-17078.
10. G. W. Bryant, W. Jaskolski. *Phys. Stat. Sol.*, **2001**. 224, 3, 751-755.
11. J. Perez-Conde, A. K. Bhattacharjee. *Phys. Stat. Sol.*, **2002**. 229, 1, 485-488.
12. A. Eychmueller, A. Mews. *Ber. Bunsenges. Phys. Chem.*, **1998**. 102, 1343-1357.
13. M. Braun, C. Burda, M. Mohamed, M. A. El-Sayed. *Physical Review B*, **2001**. 64, 3, 35317.

14. T. Vossmeyer, L. Katsikas, M. Giersig, I. G. Popovic, K. Diesner, A. Chemseddine, A. Eychmueller, H. Weller. *Journal of Physical Chemistry*, **1994**. 98, 7665-7673.

15. Klimov, V. I. *Journal of Physical Chemistry B*, **2000**. 104, 6112-6123.

16. Darugar, Qusai, Christy Landes, Stephan Link, Alexander Schill, and M. A. El-Sayed. *Chemical Physics Letters*, **2003**. 373, 3,4, 284-291.

17. Efros, Al L., V. A. Kharchenko, and M. Rosen. *Solid State Communications*, **1995**. 93, 4, 281-4.

CHAPTER 5

DEEP-TRAP STIMULATED EMISSION DYNAMICS IN QUANTUM DOT QUANTUM WELL NANOCRYSTALS

The ultrafast stimulated emission dynamics of PVP capped CdS/HgS/CdS nanocrystals has been studied using sub-picosecond transient absorption spectroscopy. The rise time of the stimulated emission signal increases from 440 fs to almost 2 ps as the observation wavelength is moved to lower energy. This behavior suggests carrier relaxation into an ensemble of progressively lower energy, optically active deep trap states that give the observed stimulated emission.

Introduction

The potential for use of semiconductor nanocrystals in tunable laser applications has generated interest in understanding the characteristics of stimulated emission and optical gain in these systems [1-5]. Stimulated emission and optical gain has been observed in colloidal solution [6], densely packed thin films [7] and cylindrical microcavities [8]. Optical gain has even been observed at room temperature in these systems. Most of the studies to date have been conducted on homogeneous core nanocrystals or core/shell structures such as CdSe/ZnS or CdSe/CdS. The detailed stimulated emission dynamics of multi-layered structures such as the CdS/HgS/CdS quantum dot quantum well have not been explored. Stimulated emission from CdS/HgS/CdS has been observed in previous studies of the electron-hole migration

dynamics [9]. In this report we seek to expand upon the dynamics of stimulated emission from CdS/HgS/CdS nanocrystals. Our recent results suggest that stimulated emission from this system can be generated from an array of low energy deep trap states as indicated by the dynamics of stimulated emission as a function of monitoring energy.

Experimental

PVP-CdS/HgS/CdS nanocrystals were prepared using a modified version of the synthesis technique that has traditionally been used [10]. The synthesis may be separated into three parts: (1) growing the CdS core, (2) exchanging the outermost Cd atoms for Hg to form the HgS well monolayer, (3) capping the well with a monolayer of CdS.

The core of CdS was synthesized in methanol using PVP (mw 50,000 Da) as a capping material. For the source of Cd^{2+}, a 0.1 M solution of $CdCl_2$ was prepared in deionized water. A 0.2 mL portion of the Cd^{2+} solution was added to 100 mL of methanol in a 250 mL three-neck reaction flask. A 0.2 mL portion of 10% PVP in methanol was also added to the reaction flask and the mixture was purged with argon gas for 30 minutes under vigorous stirring. Afterwards, 1.0 mL of H_2S gas was rapidly injected into the sealed reaction vessel while the mixture continued to stir rapidly. After 10 minutes, a bright greenish-yellow solution had evolved, indicating the growth of CdS nanocrystals. This solution was then purged with argon for an additional 30 minutes to remove any excess H_2S gas that may have remained. A 3 mL sample of the CdS colloidal suspension was taken for analysis followed by a rapid injection of 0.1 mL of 0.1 M $HgCl_2$ in deionized water. After 5-10 seconds of vigorous stirring after the injection of

Hg^{2+} a 3 mL sample of the CdS/HgS colloid was removed and the remaining reaction mixture was treated with a drop-wise addition of 30 mL of a 1 mL H_2S/100 mL methanol solution. The slow addition of S^{2-} is necessary to avoid the generation of high local concentrations of Cd^{2+} and S^{2-}, which could result in the formation of new CdS seeds. The slow addition process should take at least 20 minutes and a completed synthesis is indicated by a deep reddish-brown color of the reaction solution. After the addition of S^{2-} in the last step is complete, the reaction mixture was again purged with argon to remove any excess dissolved gas. The approximately 120 mL of CdS/HgS/CdS colloidal suspension was then transferred to a 250 mL round-bottomed flask and 1 gram of PVP added to the solution. The additional PVP ensures complete protection of the nanocrystals and also facilitates the preparation of a dry film of the QDQW sample. The 120 mL sample was concentrated to about 10 mL using a rotary evaporator and the final samples were stored in vials in the dark. Samples taken during the course of the preparation were transferred to a 1 cm glass cuvette and characterized using UV-VIS spectroscopy.

Spontaneous emission from excited CdS/HgS/CdS nanocrystals was collected using gated luminescence emission spectroscopy. Pulses from a Q-Switched Nd:YAG laser (8 ns, 355 nm) were used to excite the sample, which was contained in a 1 cm glass cuvette. Emission from the sample was collected and dispersed through a spectrograph onto the array of an intensified gated CCD camera (Roper Scientific). This technique allows for observation of weak emission signals with the simultaneous elimination of scattering backgrounds. The CCD was gated with a width of 2 ns to observe the emission from the excited sample as a function of time. Spectra were collected at delay of 50 ns

following the laser pulse to ensure instantaneous scattering and stray laser light did not interfere with the spectrum.

For sub-picosecond pump-probe spectroscopy, the concentrated samples were filtered through a 0.1 micron syringe filter and placed into cylindrical glass cuvettes with a pathlength of 2 mm. Under low excitation energies (<800 nJ), the samples could be studied without rotation of the sample cell. At higher pump powers however, the cells should be rotated to avoid local photobleaching. For all experiments the pump pulse produced less than one electron-hole pair per particle.

Sub-picosecond pump-probe transient spectroscopy was carried out using an amplified Ti:Sapphire laser system and a traditional slow-scan pump-probe optical setup. The amplified Ti:Sapphire laser (Clark-MXR CPA-1000) has an output of 0.8 mJ, 100 fs pulses at a fundamental wavelength of 795 nm. A small fraction of the beam (4%) was split and sent to a white-light continuum generator while the remaining 96% was used for harmonic generation (398 and 265 nm) and the pumping of two OPAs (Quantronix TOPAS). Pump beams from either the harmonic generator or OPA were passed down a delay line and overlapped with the white light continuum beam within the sample. The spot sizes were approximately 250 micron for the pump beam and 100 micron for probe. Single wavelength kinetics were monitored using a monochromator/photodiode arrangement coupled to a boxcar integrator and a lock-in amplifier. The pump beam was chopped at 492 Hz (f/2) and used as the reference frequency for the lock-in.

Results and Discussion

Ground-state absorption and spontaneous emission spectra of CdS/HgS/CdS nanocrystals are shown in Figure 5.1. The emission from CdS/HgS/CdS peaks at around 600 nm (excitonic emission) and extends out to the near IR (deep trap emission).

Sub-picosecond pump-probe transient absorption spectroscopy was used to measure the kinetics of the transient bleach and stimulated emission in CdS/HgS/CdS quantum dot quantum well nanocrystals. The data traces are shown in Figure 5.2. The data shown was obtained using 500 nm excitation pulses and probe pulses of different wavelengths spectrally selected from the white light continuum pulse. One can see from the data traces that the transient signals rise very rapidly at shorter wavelengths (higher energy) and become slower at longer wavelengths (lower energy). In particular, data obtained at wavelengths longer that 690 nm is attributed to transient stimulated emission since this region of the spectrum overlaps with the region of spontaneous emission and there is negligible ground-state absorption at these wavelengths as well. Figure 5.3 shows the probe wavelength dependent rise times of the transient bleach and stimulated emission from excited CdS/HgS/CdS nanocrystals obtained from the data in Figure 5.2.

Deep trap emission from semiconductor nanocrystals is often attributed to impure composition, poor crystallinity, interfacial or surface defects or poorly passivated nanocrystal surfaces. Deep traps quench the overall spontaneous emission intensity and give rise to multi-exponential decays in luminescence lifetimes. The majority of emission from PVP capped CdS/HgS/CdS nanocrystals appears to be deep-trap, as evidenced by the broad, featureless emission band at longer wavelengths in the emission

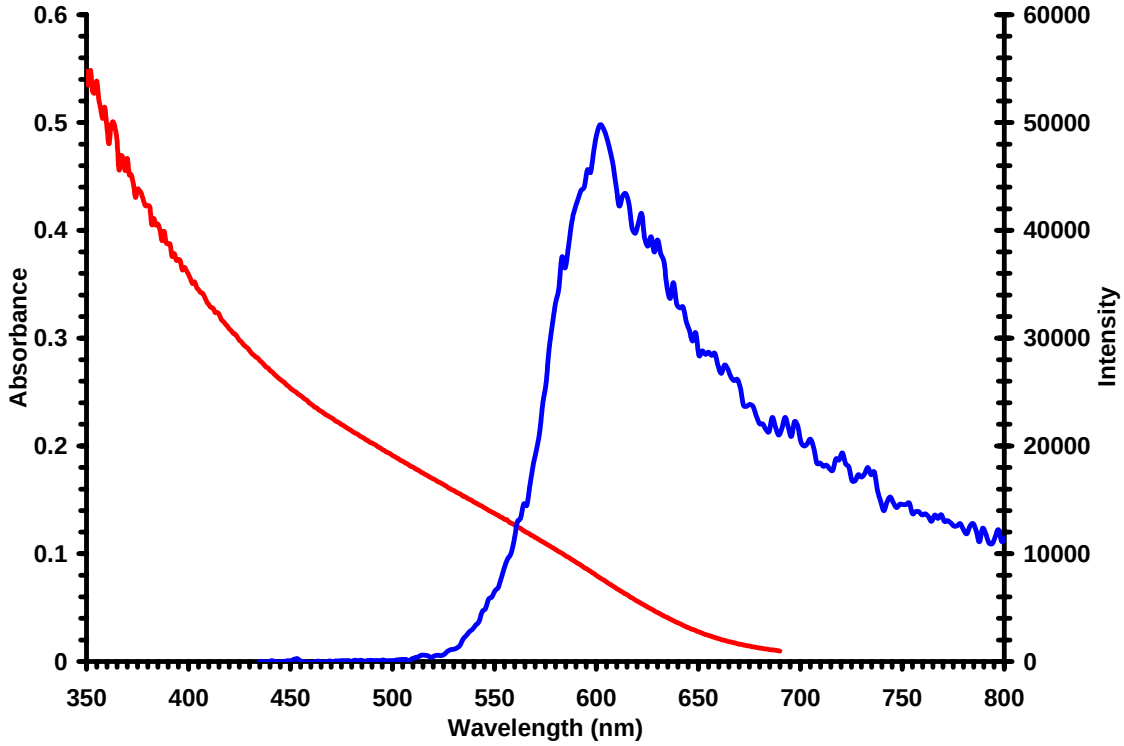

Figure 5.1. Ground state absorption (red) and spontaneous emission (blue) spectra of CdS/HgS/CdS nanocrystals.

spectrum in Figure 5.1. Thus the quantum yield for these nanocrystals is also quite low, estimated at best to be 10^{-3} based on simple inspection of the luminescence intensity.

It is peculiar therefore that stimulated emission is readily observable in these samples of CdS/HgS/CdS nanocrystals. Stimulated emission is identified using sub-picosecond pump-probe transient absorption spectroscopy. By probing in the region overlapping with both the spontaneous emission spectrum and negligible ground state absorption by the sample, the positive differential transmission (dT) observed in the pump-probe data can be attributed to transient stimulated emission of the excited sample.

The stimulated emission should come from radiative recombination of the lowest energy conduction band electron with a valence band hole to reach the ground state. If

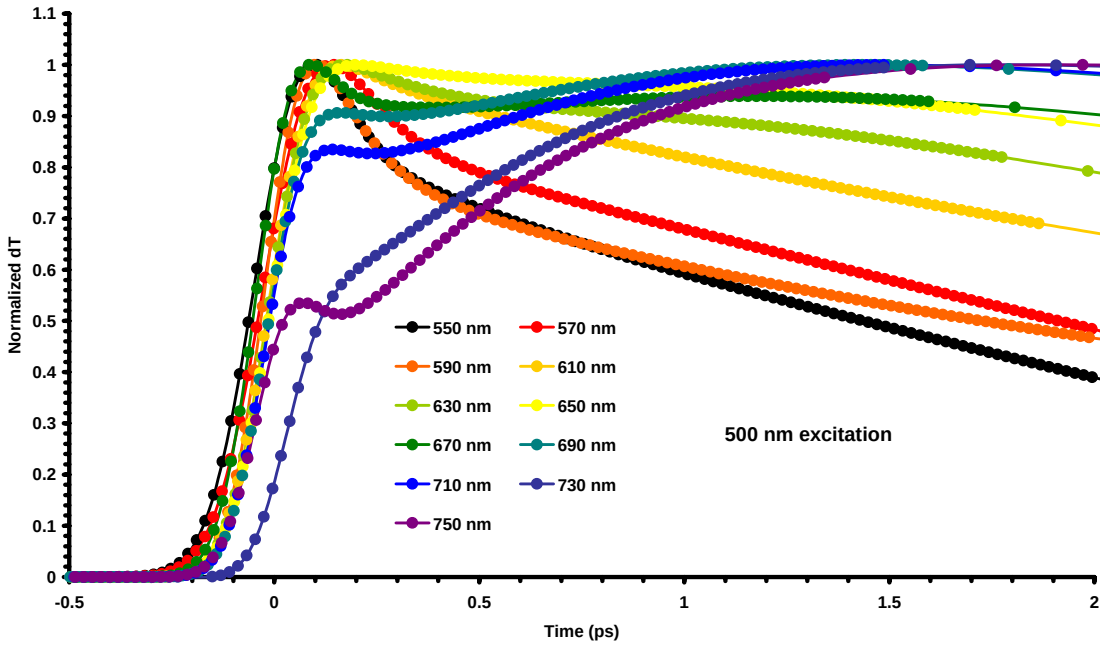

Figure 5.2. Sub-picosecond pump-probe kinetic traces for PVP capped CdS/HgS/CdS nanocrystals obtained using a 500 nm, 100 fs excitation pulse. Monitoring wavelengths are indicated on the figure. Traces shown are best-fit curves to the experimental data that allow for clearer visualization of the rise and decay profiles

deep trap states below the band gap are optically active, or can be stimulated to be optically active, emission from these low energy states is also possible. The results shown in Figures 5.3A and 5.3B suggest that the relaxation time from an upper excited state down to the deep trap states has an energy-gap dependence and becomes slower for lower energy deep trap states.

From the position of the ground state absorption onset and the variation in the rise times of the pump-probe signal, the onset of stimulated emission can be identified at around 690. The rise time at 690 nm is 440 fs and the rise time then increases in a roughly linear fashion as the probe wavelength is scanned to longer wavelengths. The rise time eventually reaches a maximum value of 1890 fs. As the stimulated emission

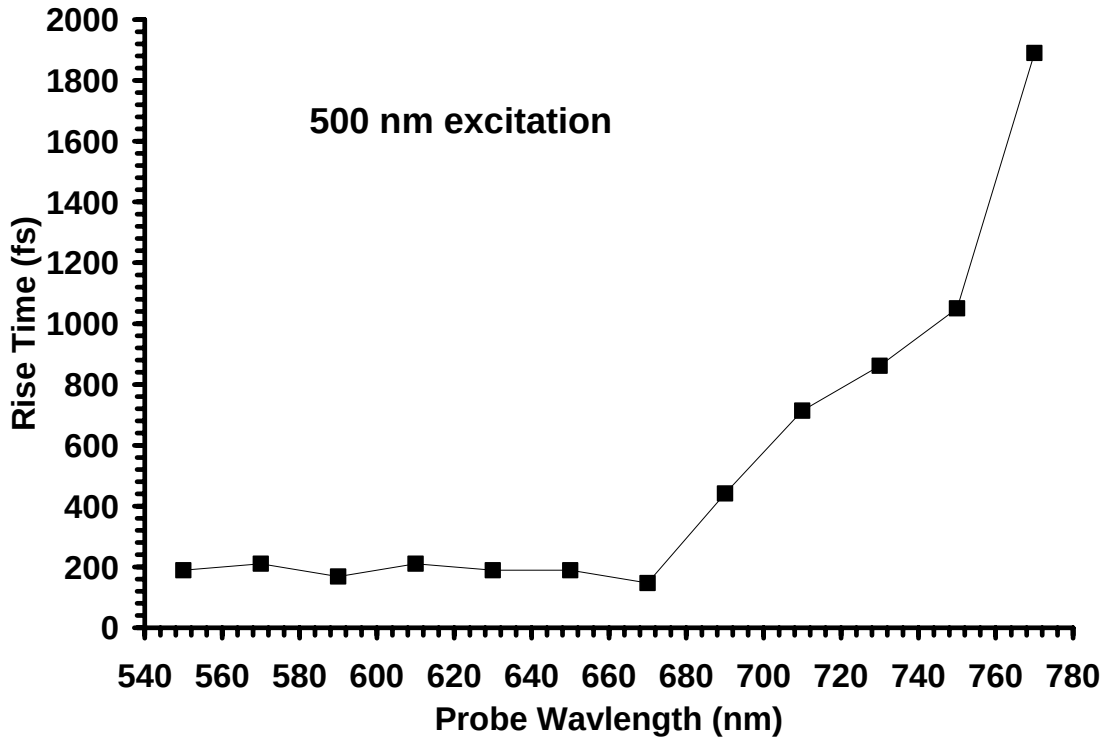

Figure 5.3. Rise times of the transient bleach and stimulated emission from excited CdS/HgS/CdS nanocrystals as a function of probe wavelength. The excitation wavelength used for the measurement was 500 nm.

band is scanned from 690 nm (1.797 eV) to 770 nm (1.610 eV), the stimulated emission rise time increases by over a factor of four. The energy gap between the highest optically active deep trap state at 690 nm and the lowest observed optically active deep trap state at 770 nm is 187 meV. Given a band spacing of 20 meV, typical of densely spaced conduction band states in semiconductor nanocrystals, it seems feasible that the stimulated emission comes from an ensemble of closely packed deep trap states below the excitonic band edge of the nanocrystal (Scheme 5.1). Using pump-probe spectroscopy, the relaxation into various states within this ensemble can be mapped by scanning the probe wavelength across the various stimulated emission wavelengths. The

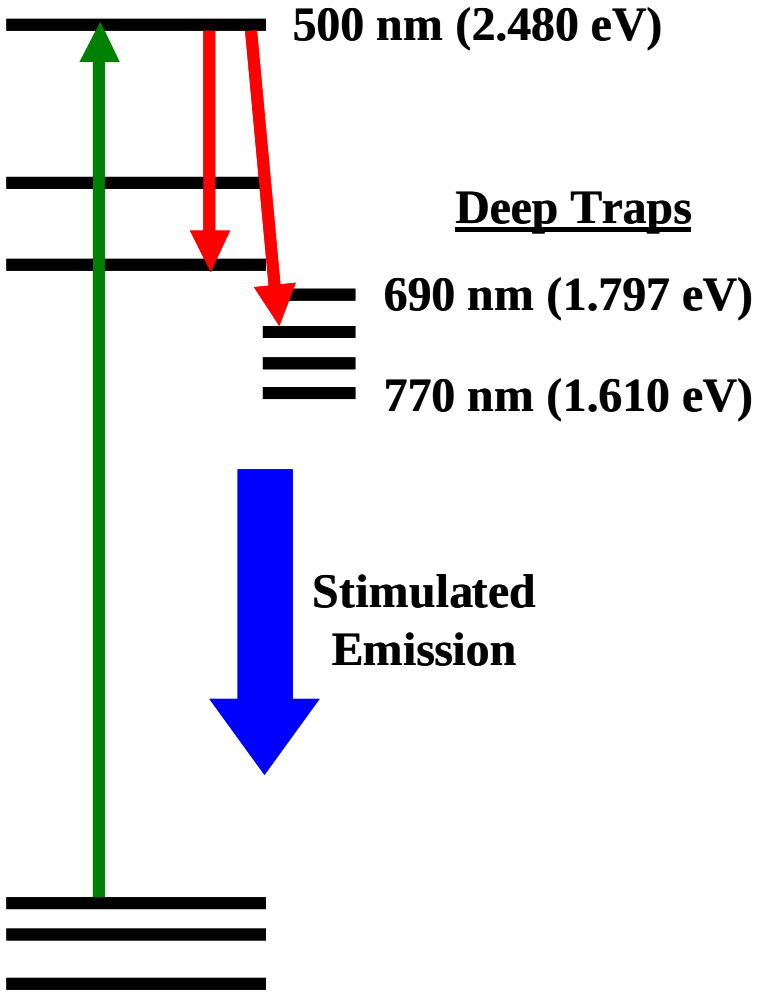

Scheme 5.1. Energy state diagram used for interpretation of the experimental results. An excited state produced by a 500 nm 100 fs pulse relaxes into intrinsic nanocrystal states and also an ensemble of deep trap states below the band gap energy. Stimulated emission from the deep traps has been observed and has an energy dependent relaxation signature (see text).

relaxation time becomes longer as lower energy emitting trap states are probed, presumably due to increasingly poorer coupling between the intrinsic nanocrystal states and the deep trap states. The specific nature of the deep trap wavefunctions in semiconductor nanocrystals is generally not well understood, so a detailed description of the interaction and coupling strength is at this point not available. Nevertheless, the role of deep trap emission in the dynamics of stimulated emission from semiconductor nanocrystals must be considered in the development of nanocrystal-based electro-optical materials.

References

1. V. S. Dneprovskii, V. I. Klimov, D. K. Okorokov, Y. V. Vandyshev. *Solid State Communications*, **1992**. 81, 227.
2. J. Butty, Y. Z. Hu, N. Peyghambarian, Y. H. Kao, J. D. Mackenzie. *Applied Physics Letters*, **1996**. 69, 3224.
3. H. Giessen, U. Woggon, B. Fluegel, G. Mohs, Y. Z. Hu, S. W. Koch, N. Peyghambarian. *Optics Letters*, **1996**. 21, 1043.
4. F. Gindele, R. Westphaeling, U. Woggon, L. Spanhel, V. Platschek. *Applied Physics Letters*, **1997**. 71, 2181.
5. V. I. Klimov, A. A. Mikhailovsky, S. Xu, A. Malko, J. A. Hollingsworth, C. A. Leatherdale, H. J. Eisler, M. G. Bawendi. *Science*, **2000**. 290, 314.
6. S. Link, M. A. El-Sayed. *Journal of Applied Physics*, **2002**. 92, 11, 6799-6803.

7. A. A. Mikhailovsky, A. V. Malko, J. A. Hollingsworth, M. G. Bawendi, V. I. Klimov. *Applied Physics Letters,* **2002**. 80, 2380.

8. M. Kazes, D. Y. Lewis, Y. Ebenstein, T. Mokari, U. Banin. *Advanced Materials*, **2002**. 14, 317.

9. M. Braun, S. Link, C. Burda, M. A. El-Sayed. *Physical Review B*, **2002**. 66, 20, 205312-205317.

10. A. Eychmueller, A. Mews, H. Weller. *Chemical Physics Letters*, **1993**. 208, 1, 59-61.

CHAPTER 6

ULTRAFAST ELECTRONIC RELAXATION IN CdS/HgS CORE/SHELL AND CdS/HgS/CdS QUANTUM DOT QUANTUM WELL NANOCRYSTAL HETEROSTRUCTURES: THE INFLUENCE OF SURFACE TRAPPING

The ultrafast electronic relaxation dynamics of CdS/HgS and CdS/HgS/CdS nanocrystals has been investigated using sub-picosecond pump-probe transient absorption spectroscopy. Stable colloids of the core/shell (CdS/HgS) and quantum dot quantum well (CdS/HgS/CdS) have been prepared using modified preparation techniques. The overall electronic relaxation proceeds through the same mechanism in both CdS/HgS and CdS/HgS/CdS nanocrystals, however the relaxation rates are much greater in CdS/HgS. These accelerated rates are discussed in terms of more rapid trapping of the excited electron to the unpassivated interface between HgS and the surroundings of the CdS/HgS nanocrystal compared to trapping to the more passivated interface between HgS and CdS in the CdS/HgS/CdS quantum dot quantum well.

Introduction

The investigation of semiconductor nanocrystal heterostructures has become a recent topic of interest [1-4], mainly for their potential uses in the next generation of semiconductor diode lasers or optoelectronic devices. The goal has been to identify and develop a chemically synthesized, colloidal nanocrystal system of high quality that can overcome the drawbacks of many semiconductor nanocrystals systems: poorly formed

surfaces that lead to undesired losses in quantum efficiency. Quantum wells grown within quantum dots may be a good solution, but before development the detailed mechanism of electronic relaxation and factors that affect it must be well understood. A number of groups have been successful at preparing systems with such layered structures. The first to be prepared was the CdS/HgS/CdS quantum dot quantum well [5]. Recently, high quality nanocrystals of CdS/CdSe/CdS have also been prepared [1] and characterized. The CdS/HgS/CdS system has been studied extensively using ultrafast transient absorption spectroscopy [2, 6-9] to investigate the relaxation of excited electrons and holes. Until modifications were made to the synthesis techniques for these CdS/HgS systems, the isolation of stable intermediate CdS/HgS core/shell structures had not been possible. Previously these structures were stable for only short periods of time and could not withstand extended exposure to high intensity lasers. The CdS/HgS particles capped with polyvinylpyrrolidone (PVP) are much more stable and can be studied under high laser intensity for extended periods. In this letter we will discuss the differences in the electronic relaxation dynamics of CdS/HgS core/shell and CdS/HgS/CdS quantum dot quantum well nanocrystals in terms of the influence of interface trapping on the rate of electronic relaxation.

Experimental

PVP capped CdS/HgS and CdS/HgS/CdS nanocrystals were prepared using a modified version of the synthesis technique that has traditionally been used [5]. The synthesis may be separated into three parts: (1) growing the CdS core, (2) exchanging the

outermost Cd atoms for Hg to form the HgS well monolayer to form CdS/HgS, (3) Capping the well with a monolayer of CdS to form CdS/HgS/CdS.

The core of CdS was synthesized in methanol using PVP (MW 50,000 Da) as a capping material. For the source of Cd^{2+}, a 0.1 M solution of $CdCl_2$ was prepared in deionized water. A 0.2 mL portion of the Cd^{2+} solution was added to 100 mL of methanol in a 250 mL three-neck reaction flask. A 0.2 mL portion of 10% PVP in methanol was also added to the reaction flask and the mixture was purged with argon gas for 30 minutes under vigorous stirring. Afterwards, 1.0 mL of H_2S gas was rapidly injected into the sealed reaction vessel while the mixture continued to stir rapidly. After 10 minutes, a bright greenish-yellow solution had evolved, indicating the growth of CdS nanocrystals. This solution was then purged with argon for an additional 30 minutes to remove any excess H_2S gas that may have remained. A 3 mL sample of the CdS colloidal suspension was taken for analysis followed by a rapid injection of 0.1 mL of 0.1 M $HgCl_2$ in deionized water. The preparation is stopped at this point for the CdS/HgS core/shell particles.

After 5-10 seconds of vigorous stirring after the injection of Hg^{2+} a 3 mL sample of the CdS/HgS colloid was removed and the remaining reaction mixture was treated with a drop-wise addition of 30 mL of a 1 mL H_2S/100 mL methanol solution. The slow addition of S^{2-} is necessary to avoid the generation of high local concentrations of Cd^{2+} and S^{2-}, which could result in the formation of new CdS seeds. The slow addition process should take at least 20 minutes and a completed synthesis is indicated by a deep reddish-brown color of the reaction solution. After the addition of S^{2-} in the last step is complete, the reaction mixture was again purged with argon to remove any excess dissolved gas.

The approximately 100-120 mL of CdS/HgS or CdS/HgS/CdS colloidal suspension was then transferred to a 250 mL round-bottomed flask and 1 gram of PVP added to the solution. The additional PVP ensures complete protection of the nanocrystals and also facilitates the preparation of a dry film of the QDQW sample. The 120 mL sample was concentrated to about 10 mL using a rotary evaporator and the final samples were stored in vials in the dark. Samples taken during the course of the preparation were transferred to a 1 cm glass cuvette and characterized using UV-VIS spectroscopy.

For sub-picosecond pump-probe spectroscopy, the concentrated samples were filtered through a 0.1 micron syringe filter and placed into cylindrical glass cuvettes with a pathlength of 2 mm. Under low excitation energies (<800 nJ), the samples could be studied without rotation of the sample cell. At higher pump powers however, the cells should be rotated to avoid local photobleaching. For all experiments the pump pulse produced less than one electron-hole pair per particle.

Sub-picosecond pump-probe transient spectroscopy was carried out using an amplified Ti:Sapphire laser system and a traditional slow-scan pump-probe optical setup. The amplified Ti:Sapphire laser (Clark-MXR CPA-1000) has an output of 0.8 mJ, 100 fs pulses at a fundamental wavelength of 795 nm. A small fraction of the beam (4%) was split and sent to a white-light continuum generator while the remaining 96% was used for harmonic generation (398 and 265 nm) and the pumping of two OPAs (Quantronix TOPAS). Pump beams from either the harmonic generator or OPA were passed down a delay line and overlapped with the white light continuum beam within the sample. The spot sizes were approximately 250 micron for the pump beam and 100 micron for probe.

Single wavelength kinetics were monitored using a monochromator/photodiode arrangement coupled to a boxcar integrator and a lock-in amplifier. The pump beam was chopped at 492 Hz (f/2) and used as the reference frequency for the lock-in.

Results and Discussion

The ground-state absorption spectra of the samples used in this study are shown in Figure 6.1. Figure 6.1A was taken during the preparation of CdS/HgS nanocrystals and Figure 6.1B was taken during the preparation of CdS/HgS/CdS nanocrystals. The CdS nanocrystal cores are identical for both samples, approximately 5 nm in diameter as determined from the position of the absorption onset [10]. Introducing a layer of HgS shifts the spectrum to longer wavelengths, even though the diameter of the nanocrystals does not change with the surface exchange technique. This is indicative of the perturbation caused by the addition of the small band-gap HgS well layer to the nanocrystal. For the sample of CdS/HgS/CdS, addition of sulfide at the final step cause a further shifting of the absorption to lower energy, mostly due to an increase in the size of the nanocrystal and reduction of the confinement of the exciton.

The results from the sub-picosecond pump-probe transient absorption measurements are shown in Figure 6.2. The data shown was collected for excited CdS/HgS core/shell nanocrystals using 400 nm excitation pulses and probe pulse of different wavelengths and has been normalized at the maximum of the dT (differential transmission, T_{pump}-$T_{no\ pump}$) signal. As observed previously [2], the decay of the transient bleach becomes slower as the probe wavelength is scanned to lower energies.

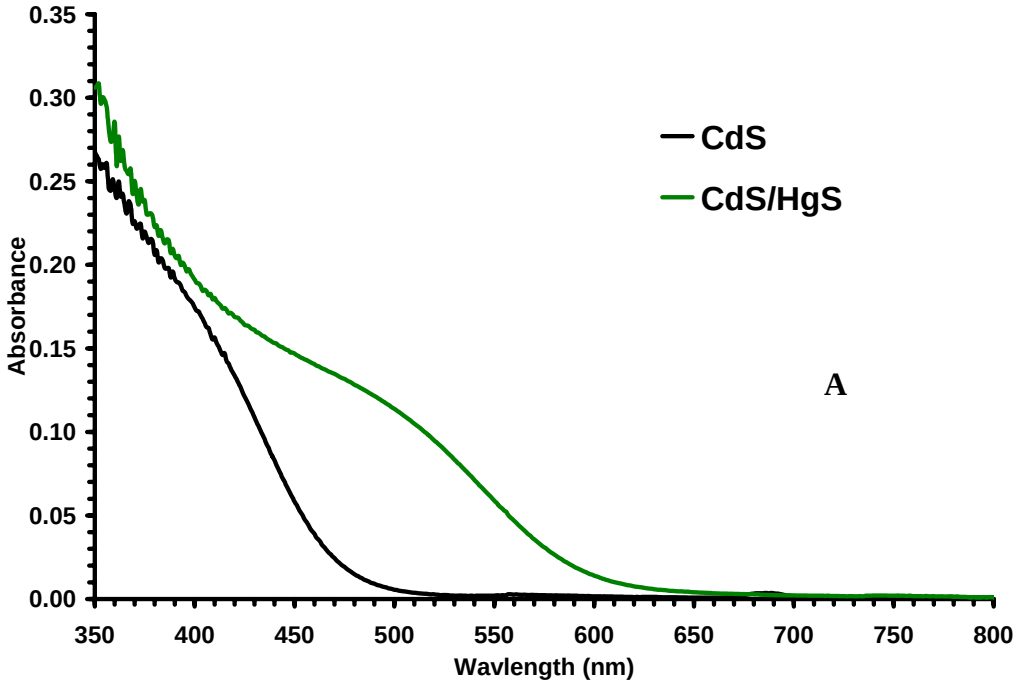

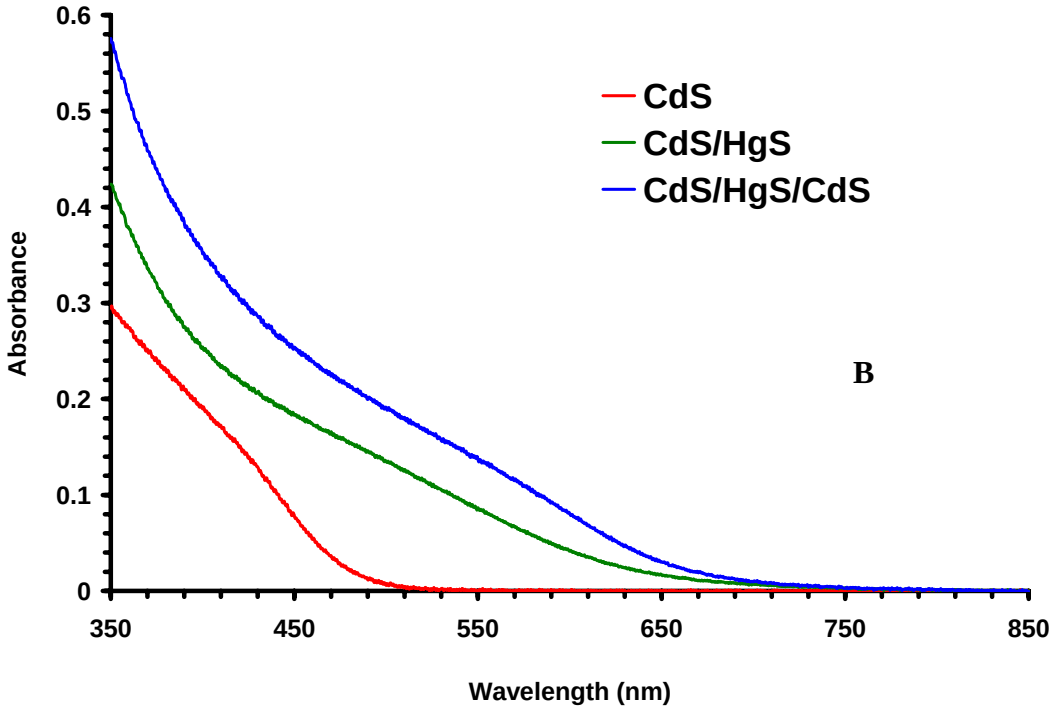

Figure 6.1A and 6.1B. Ground state absorption spectra taken during the preparation of CdS/HgS (A) and CdS/HgS/CdS (B) nanocrystals.

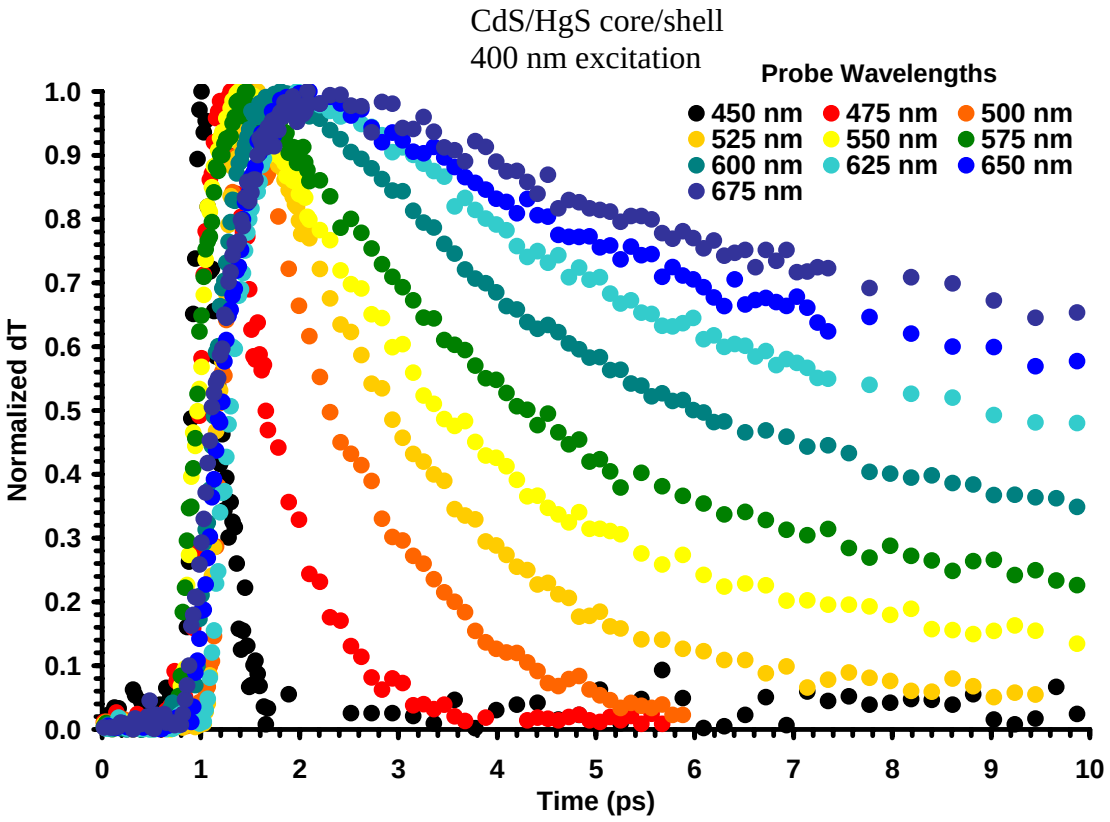

Figure 6.2. Sub-picosecond pump-probe transient bleach traces for excited CdS/HgS nanocrystals obtained using 400 nm excitation. Probe wavelengths indicated on the figure.

This is characteristic of the migration of a hot electron energy distribution from its initial position in the energy spectrum (400 nm, 3.1 eV) to lower energies and eventually to radiative and non-radiative recombination with the hole. To understand how the electron distribution relaxes, the intensity of the transient bleach can be observed at different monitoring wavelengths to sample the population of hot electrons at different energies during the relaxation. This "distribution function" can be seen for both CdS/HgS core/shell and CdS/HgS/CdS quantum dot quantum well nanocrystals in Figure 6.3. For both samples the maximum intensity of the electron population appears around

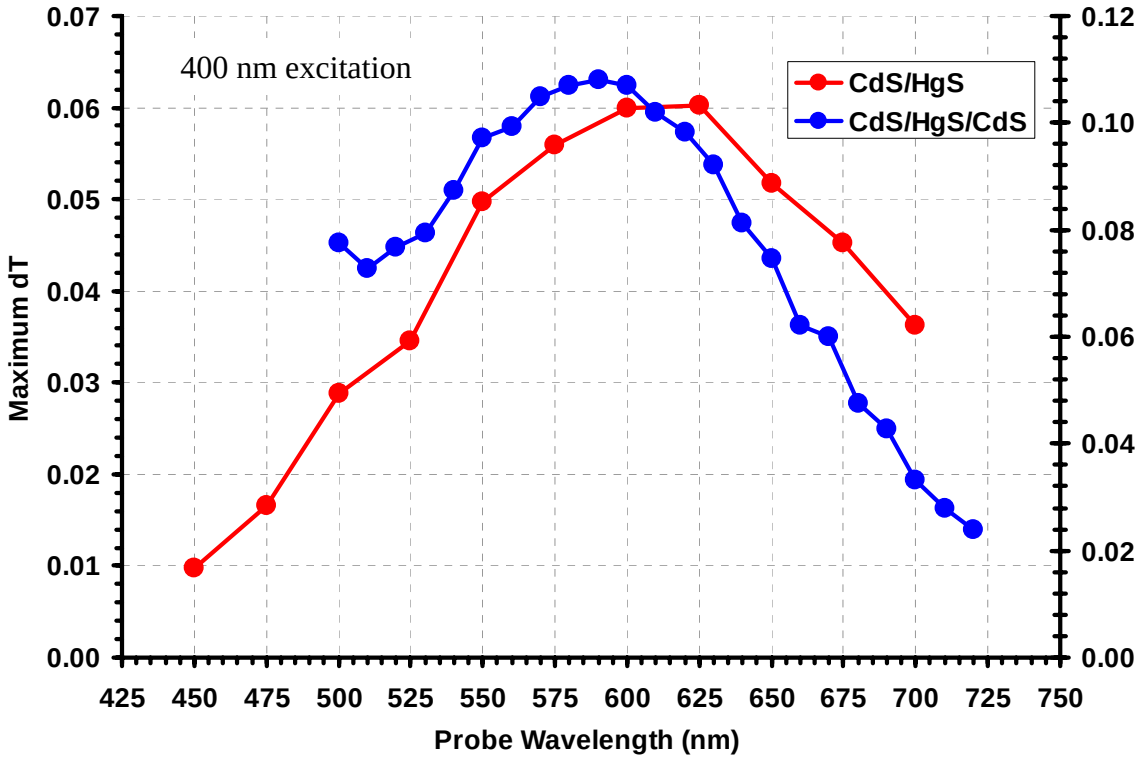

Figure 6.3. Plot of wavelength dependent maximum dT (differential transmission) intensity for excited CdS/HgS and CdS/HgS/CdS nanocrystals.

600 nm, thus indicating that the relaxation process is nearly identical in both samples. The exposure of the surface in the core/shell sample does not affect the overall relaxation mechanism, but the relaxation rates may be different.

Figures 6.4 through 6.6 highlight the change in the relaxation rate for CdS/HgS core/shell nanocrystals. The decay profile of the excited samples CdS/HgS and CdS/HgS/CdS are shown in each figure. The same experimental conditions were used for both samples. It can be seen that, for each monitoring wavelength 500-650 nm, the relaxation time for the core/shell sample is accelerated with respect to the full quantum dot quantum well. Trapping to defects at interfaces is expected to be a large contribution

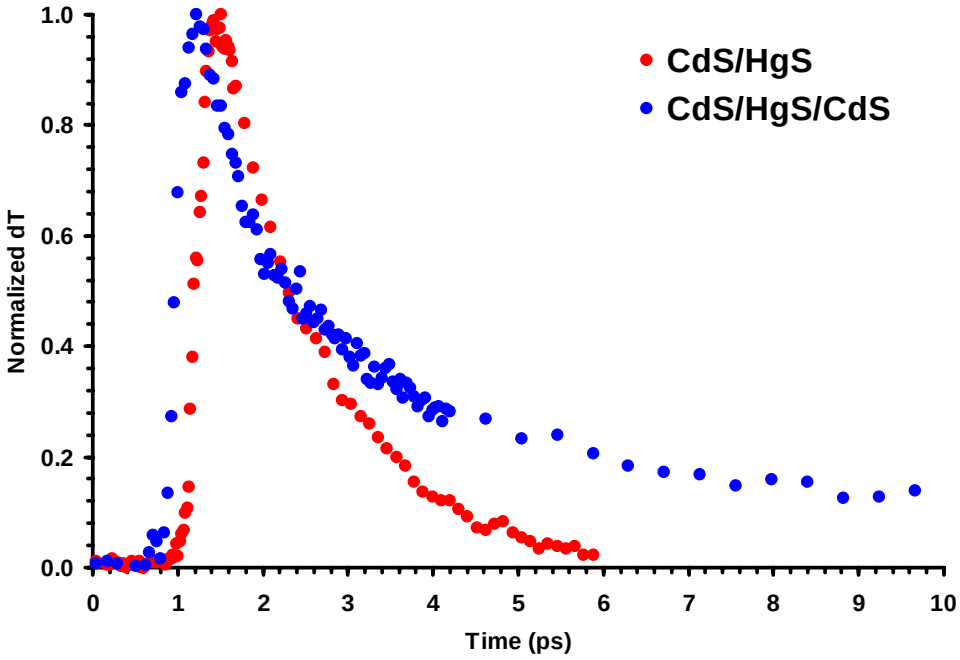

Figure 6.4. Sub-picosecond pump-probe transient bleach traces for excited CdS/HgS and CdS/HgS/CdS nanocrystals obtained using 400 nm excitation and 500 nm probe wavelength.

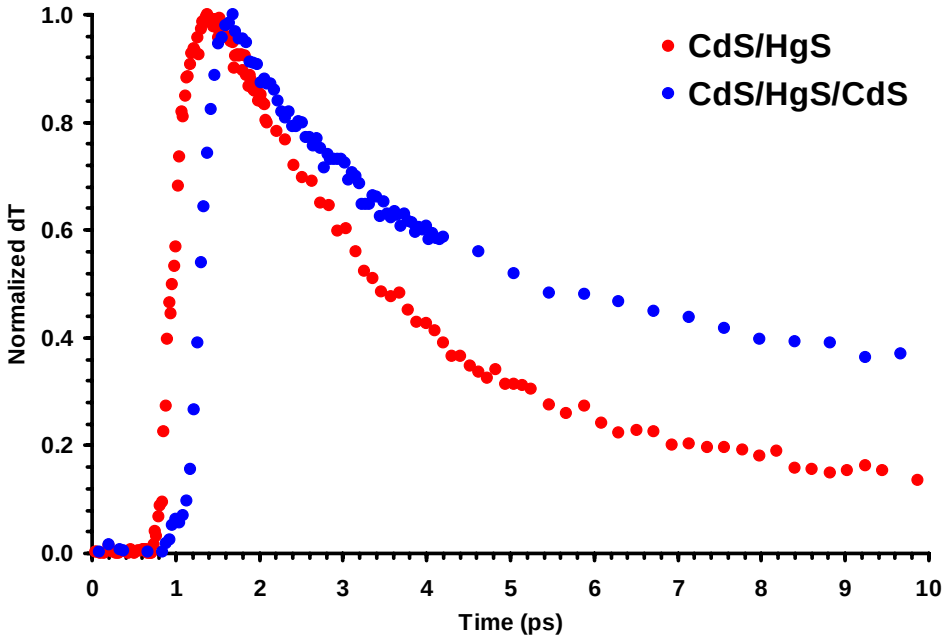

Figure 6.5. Sub-picosecond pump-probe transient bleach traces for excited CdS/HgS and CdS/HgS/CdS nanocrystals obtained using 400 nm excitation and 550 nm probe wavelength.

to the relaxation in semiconductor nanocrystals. It has also been shown that excited electrons in CdS/HgS/CdS localize to the HgS layer in less than 1 ps [2, 7], which may be fast enough to compete with the rate of trapping. The rate of trapping can be expressed as follows

$$k_{trap} = \left| \left\langle \psi_{nc} H \psi_{trap} \right\rangle \right|^2 \frac{N_{trap}}{4\pi r^2 \hbar} \qquad (6.1)$$

where ψ_{nc} is the intrinsic nanocrystal state wavefunction, ψ_{trap} is the trap state wavefunction, H is the Hamiltonian describing coupling between intrinsic nanocrystal states and trap states, N_{trap} is the number of trap states at the surface/interface. The value of N_{trap} will depend on the extent of surface passivation – surfaces with better passivation are expected to have fewer traps than unpassivated surfaces. As shown in a previous report, passivation of CdSe nanocrystal surfaces using ZnS eliminates trap sites and promotes strong luminescence from the band-edge [11]. Similarly, the CdS/HgS core/shell will have more trap sites than CdS/HgS/CdS, since an additional outer monolayer of CdS serves to passivate trap sites on the HgS surface. Fewer traps at the HgS surface for the CdS/HgS/CdS quantum dot quantum well explains the slower relaxation rate we observe, as given by Equation 6.1. Trap density at the surface (right hand side of Equation 6.1) is only half of the picture, to completely understand the trapping rate in these nanocrystal heterostructures; we must also consider the coupling between intrinsic nanocrystal states and trap states (left hand side of Equation 6.1).

The coupling between nanocrystal and surface states depends on the energy structure. Specifically, the coupling strength will depend on how well the intrinsic nanocrystal wavefunctions overlap with trap state wavefunctions localized at the

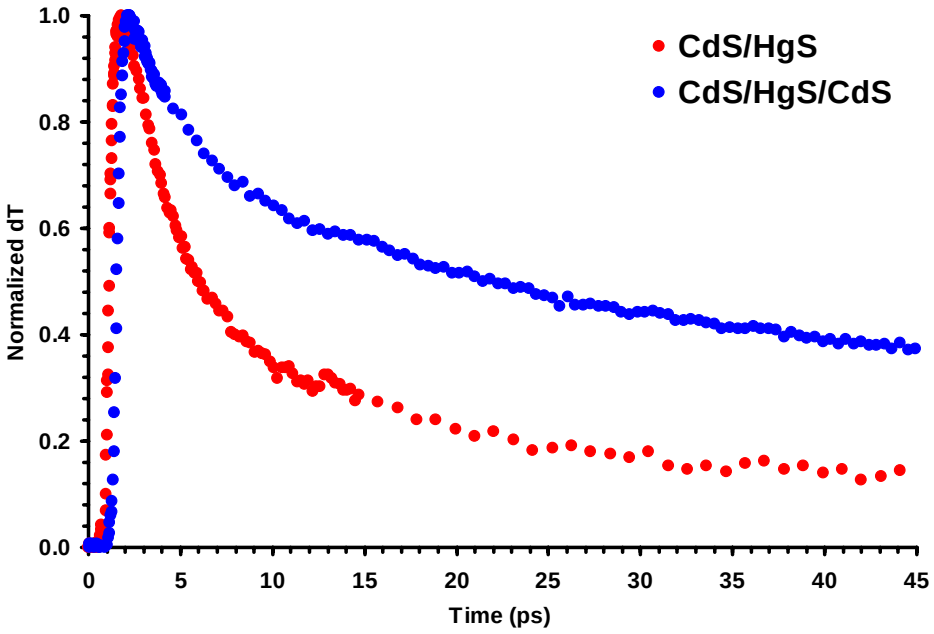

Figure 6.6. Sub-picosecond pump-probe transient bleach traces for excited CdS/HgS and CdS/HgS/CdS nanocrystals obtained using 400 nm excitation and 600 nm probe wavelength.

surface/interface. The surface/interface of interest in CdS/HgS core/shell and CdS/HgS/CdS quantum dot quantum well nanocrystals is the outer surface of the HgS layer. In the case of CdS/HgS, this boundary is between HgS and the surrounding medium (solvent, stabilizer molecules) while in the CdS/HgS/CdS quantum dot quantum well, this boundary is between HgS and the outer monolayer of CdS. As was already examined, the number of traps N_{trap} at the boundary for CdS/HgS core/shell is higher than the number of traps at the boundary for CdS/HgS/CdS, leading to the faster decay rate. In a previous study [2], we demonstrated that excited electrons in CdS/HgS/CdS relax through mixed electronic states with varying compositions of CdS and HgS character. High energy excited states were found to have more CdS character, while lower energy excited states had more HgS character. Theoretical calculations of the

radial distribution functions (RDF) for CdS/HgS/CdS predict CdS states delocalized throughout the particle cross section and HgS states having most RDF amplitude within the thin HgS shell [12]. In principle, our previous results and theoretical predictions of the RDFs would suggest that lower energy excited states are localized within the HgS layer, while higher energy states are delocalized across the nanocrystal in CdS/HgS heterostructures. This could mean that lower energy excited states will couple more strongly to traps at the boundary than higher energy states. It may therefore be said that, for low energy excited states that are localized within the HgS layer, the *effect of passivation with CdS will be more important than for high energy states delocalized throughout the nanocrystal*.

This idea can be explored experimentally by comparing the relaxation times of core/shell and quantum dot quantum well nanocrystals under the same pump and probe conditions. Figure 6.7 shows a plot of the difference in decay lifetime ($\Delta\tau = \tau_{QDQW} - \tau_{core/shell}$) as a function of probe wavelength for CdS/HgS core/shell and CdS/HgS/CdS quantum dot quantum well nanocrystals. The difference in decay lifetime increases as the probe wavelength is moved to 500 nm to 600 nm, suggesting that the mechanism responsible for making the decay more rapid in the CdS/HgS core/shell nanocrystals has increasing influence as the energy states become lower (more HgS shell localized).

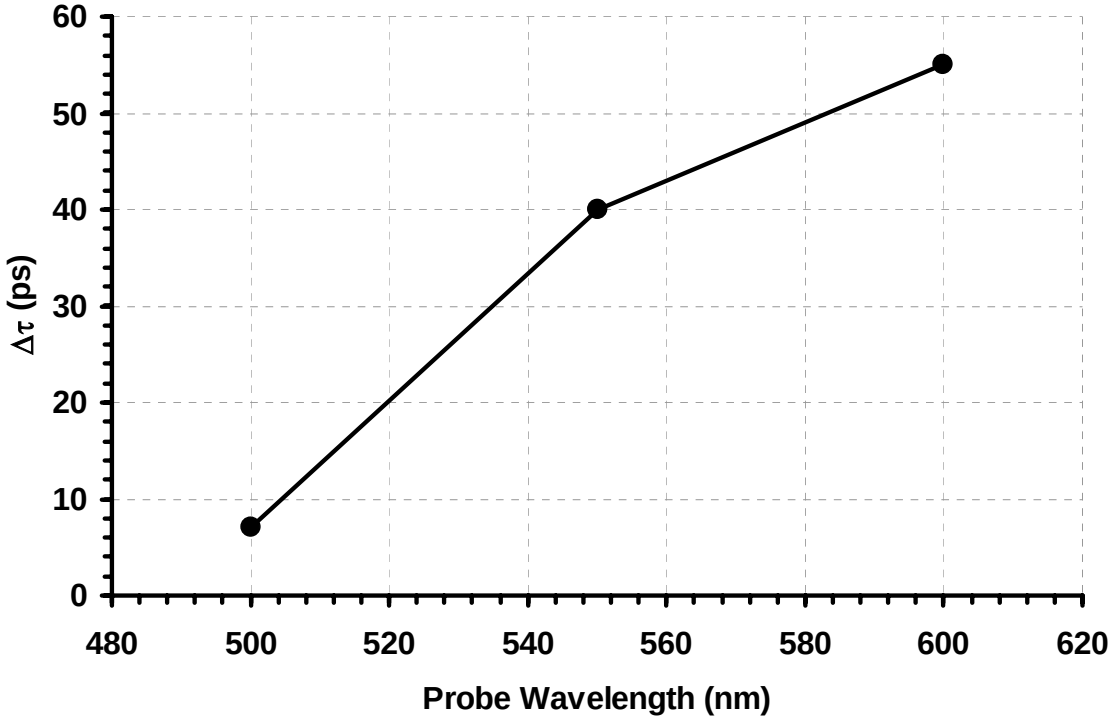

Figure 6.7. Difference in decay lifetime ($\Delta\tau = \tau_{core/well/shell} - \tau_{core/well}$) as a function of probe wavelength for CdS/HgS core/well and CdS/HgS/CdS core/well/shell nanocrystals.

References

1. D. Battaglia, J. Li, Y. Wang, X. Peng. *Angewante Chemie International Edition*, **2003**. 42, 5035-5039.
2. A. W. Schill, M. A. El-Sayed. *J. Phys. Chem. B*, **2004**. 108, 13619-13625.
3. J. Berezovsky, M. Ouyang, F. Meier, D. Awschalom, D. Battaglia, X. Peng. *Physical Review B*, **2005**. 71,
4. J. Xu, M. Xiao, D. Battaglia, X. Peng. *Applied Physics Letters*, **2005**. 87,
5. A. Eychmueller, A. Mews, H. Weller. *Chemical Physics Letters*, **1993**. 208, 1, 59-61.
6. V. F. Kamalov, R. B. Little, S. Logunov, M. A. El-Sayed. *Journal of Physical Chemistry*, **1996**. 100, 16, 6381-6384.
7. A. Yeh, G. Cerullo, U. Banin, A. Mews, A. P. Alivisatos, C. V. Shank. *Physical Review B*, **1999**. 59, 7, 4973-4977.
8. M. Braun, C. Burda, M. Mohamed, M. A. El-Sayed. *Physical Review B*, **2001**. 64, 3, 35317.
9. M. Braun, S. Link, C. Burda, M. A. El-Sayed. *Physical Review B*, **2002**. 66, 20, 205312-205317.
10. T. Vossmeyer, L. Katsikas, M. Giersig, I. G. Popovic, K. Diesner, A. Chemseddine, A. Eychmueller, H. Weller. *Journal of Physical Chemistry*, **1994**. 98, 7665-7673.
11. M. A. Hines, P. Guyot-Sionnest. *J. Phys. Chem.*, **1996**. 100, 468-471.

12. D. Schooss, A. Eychmueller, A. Mews, H. Weller. *Physical Review B*, **1994**. 49, 24, 17072-17078.

CHAPTER 7

SIZE LIMITING EFFECTS ON THE PREPARATION OF VERY SMALL QUANTUM DOT QUANTUM WELL NANOCRYSTALS

Efforts to prepare CdS/HgS/CdS quantum dot quantum wells of smaller size have been undertaken in order to investigate the changes in the behavior of the material when confinement is not limited to within the HgS well. The results indicate that layered structures of CdS/HgS/CdS are indistinguishable from the CdS/HgS mixed binary phase nanocrystal. The observation suggests that, for very small sizes where the number of surface atoms takes up a large fraction of the total number of atoms, layered structures can anneal to mixed binary phase and the effects of confinement in the HgS well will not be observed.

Introduction

The first quantum dot quantum well nanocrystals were prepared in 1993 by Eychmueller and co-workers [1]. The system consisted of a 5 nm spherical core of CdS, a 0.5 nm shell of HgS and a 1-2 nm outer shell of CdS. This type of layered structure forms a Type I semiconductor heterostructure with an HgS layer sufficiently thin enough to act as a quantum well. It is for this reason that the structure was named a quantum dot quantum well and it represents a unique material in that carriers in such a system experience quantum confinement effect not only in the whole of the particle but also in the wells themselves. Numerous spectroscopic studies were carried out to investigate this

unique system, including single particle [2], picosecond dynamics [3, 4] and luminescence relaxation [5] studies.

Recently some effort has been directed at modifying the size, shape and composition of quantum dot quantum well nanocrystals in order to understand the fundamental effects of quantum confinement on charge carries in these systems. Recent results suggest that the formation of layered nanocrystal structures such as the CdS/HgS/CdS quantum dot quantum well through the surface exchange technique introduced by Spanhel and Henglein [6] becomes difficult at small nanocrystal sizes, presumably due to diffusion of surface atoms into the core of the particles to from mixed binary phase alloy nanocrystals.

Experimental

Colloidal CdS seeds were prepared using the method of Rossetti et. al. [7] using polyvinylpyrrolidone (PVP, MW = 50,000) as a capping material. Fifty milliliters (50 mL) of nitrogen-saturated methanol was kept in a 250 mL three neck flask and stirred using a magnetic stirrer. To the solvent was added 0.5 mL of 0.1 M $CdCl_2$ (aq.) and 0.5 mL of 10% PVP under vigorous stirring. The reaction solution was then cooled to –77 °C in a dry ice/isopropanol bath. Half a milliliter (0.5 mL) of 0.1 M Na_2S (aq.) was then added to the reaction solution to form 3 nm diameter CdS seed nanocrystals. A 3 mL sample of the CdS colloid was removed for confirmation of nanocrystal formation by UV absorption spectroscopy. Still at –77 °C, the rapidly stirring CdS seed colloidal solution was treated with a 220 μL portion of 0.1 M $HgCl_2$ (aq.) to form a HgS monolayer on the

surface of the CdS particles. A 3 mL sample of this CdS/HgS core/shell colloid was quickly removed followed by a dropwise addition of a 220 μL/25 mL Na_2S in methanol to the reaction mixture. The slow drop-by-drop addition of the Na_2S solution discourages the nucleation of small CdS crystallites and ensures epitaxial formation of a CdS layer on the surface of the CdS/HgS core/shell nanocrystals. The final particle is expected to have a diameter of about 4 nm, over 3 nm smaller than that of the CdS/HgS/CdS quantum dot quantum well nanocrystals prepared using room temperature, polyphosphate synthesis.

Alloy nanocrystals of the same chemical composition as the CdS/HgS/CdS quantum dot quantum well were prepared by simultaneously reacting 0.5 mL of 0.1 M $CdCl_2$ (aq.), 0.5 mL of 10% PVP and 220 μL of 0.1 M $HgCl_2$ (aq.) with 0.5 mL of 0.1 M Na_2S (aq.). The resulting nanocrystals would not be expected to spontaneously form a core/shell layered structure and therefore act as a control for distinguishing properties of the quantum dot quantum well that arise from its layered structure.

Results and Discussion

The absorption spectra taken during the preparation of very small CdS/HgS/CdS quantum dot quantum well nanocrystals are shown in Figure 7.1. Spectrum A (red) shows the absorption spectrum of 3 nm CdS core nanocrystals, whose size was determined from the band-gap absorption size relationship determined by Vossmeyer and Weller [8]. Spectrum B (orange) shows the absorption spectrum of the colloid after adding a portion of Hg^{2+} sufficient to form a monolayer of HgS on the surface of the CdS core. Spectrum C (green) shows the absorption spectrum obtained by slowly dropping

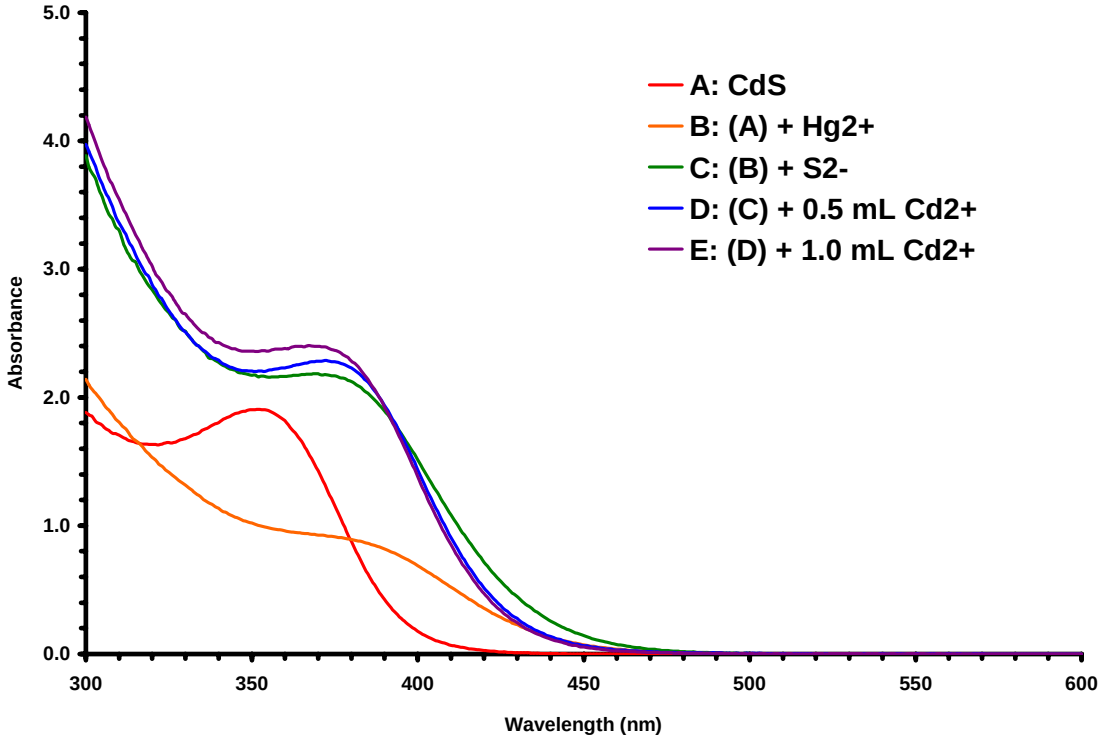

Figure 7.1. – Absorption spectra collected during the preparation of 4 nm CdS/HgS/CdS quantum dot quantum well nanocrystals.

S^{2-} into the colloidal solution to from an outer layer of CdS on the surface of the core/shell particle. The remaining spectra D and E show the effect of adding additional Cd^{2+} ions to saturate the surface of the nanocrystals with Cd and possibly reduce surface mediated non-radiative relaxation. As expected, very little effect on the absorption spectrum is observed upon these additions of Cd^{2+}.

Figure 7.2 shows the photoluminescence emission and excitation spectra obtained from colloidal samples of the small CdS/HgS/CdS nanocrystals. As indicated on the figure, emission spectra were collected at two different excitation wavelengths and excitation spectra were collected for two different emission wavelengths to demonstrate

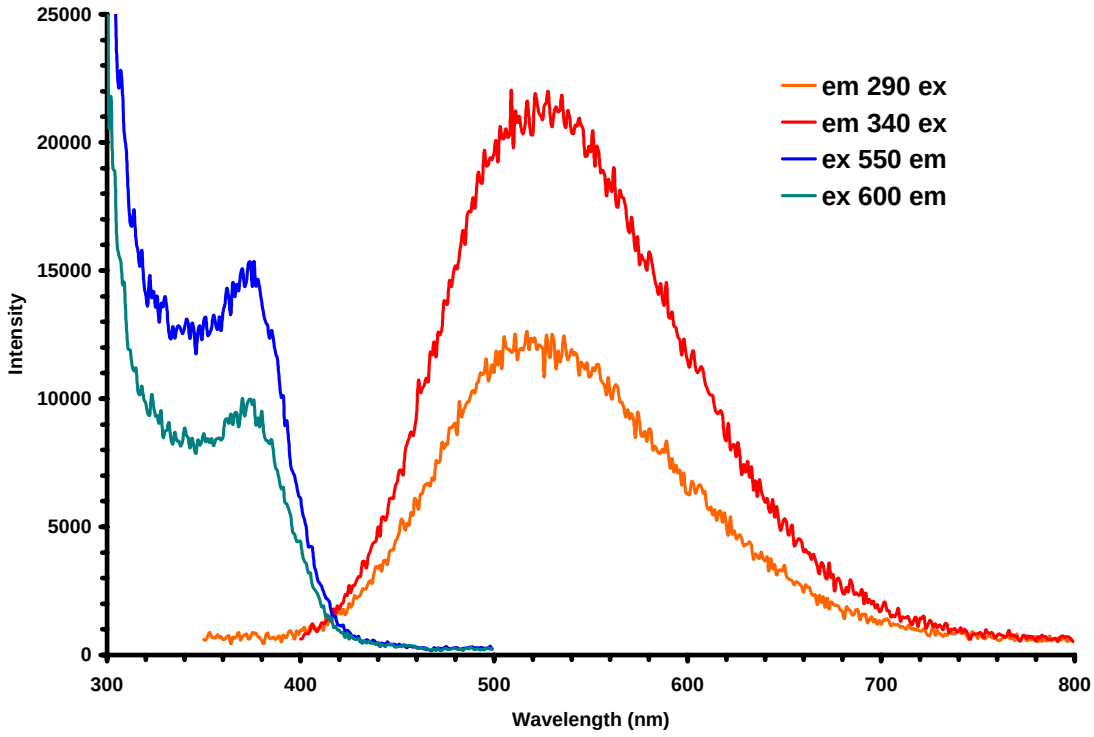

Figure 7.2. – Luminescence emission and excitation spectra of the CdS/HgS/CdS nanocrystals. Excitation and emission wavelengths are indicated on the figure.

the consistency of the luminescence across the spectrum. The excitation spectra are found to closely match the absorption spectrum, indicating that all relaxation processes for the nanocrystal are intrinsic and energy transfer and electron transfer processes are not responsible for the observed emission.

Figure 7.3 shows the absorption, luminescence excitation and luminescence emission spectra of the intentionally prepared Cd(Hg)S alloy of the same chemical composition as the CdS/HgS/CdS quantum dot quantum well. Both the position and shape of the spectral features are nearly identical to those of the layered particle given in Figures 7.1 and 7.2. This result suggests that the nanocrystal sample, which was intended

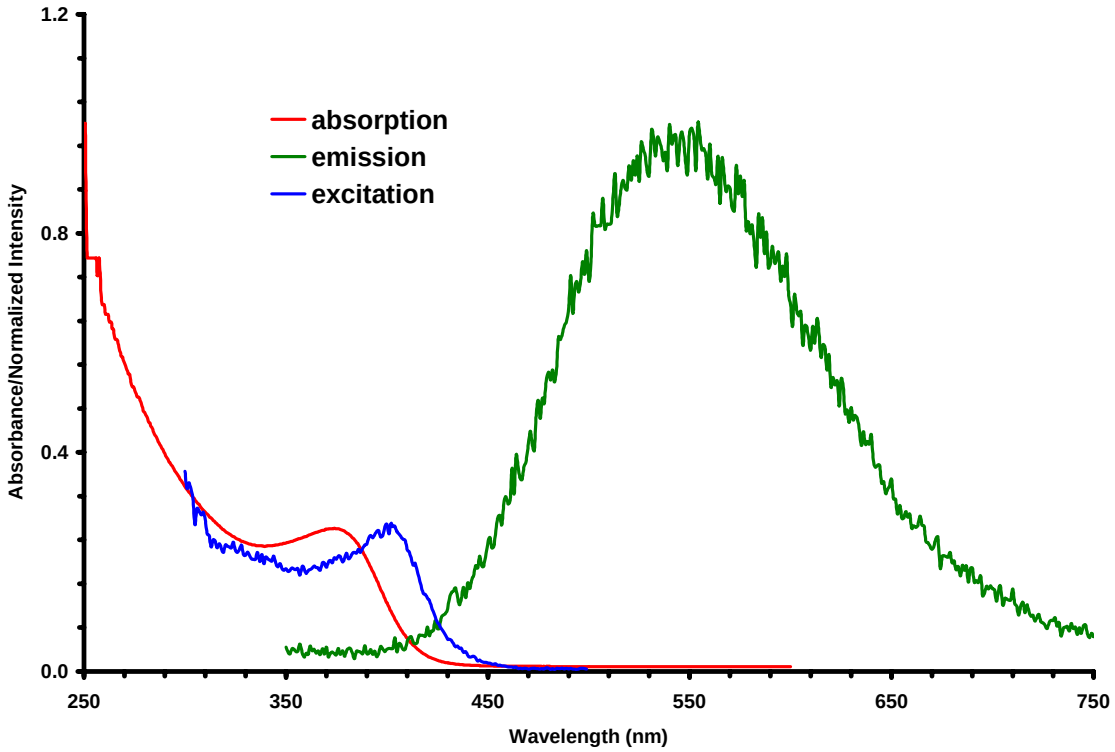

Figure 7.3. – Absorption, luminescence emission and excitation spectra of Cd(Hg)S alloy nanocrystals of the same chemical composition as the CdS/HgS/CdS quantum dot quantum well nanocrystals.

to be a layered quantum dot quantum well structure, may merely be an alloy of CdS and HgS.

Intentionally prepared mixed binary alloy colloids of CdS and HgS were prepared by Mews and co-workers early in their work on the CdS/HgS system [5]. The resulting absorption spectrum is much different than that of the quantum dot quantum well, lacking both the spectral shape and position of the layered nanoparticle spectrum. The particle sizes determined in their study were 6 nm in diameter, 2 nm larger than the size expected of the colloids prepared in this study. As the size of a nanocrystal is reduced, the surface atom/total atom ratio becomes increasingly large, eventually reaching a point where a

majority of the atoms making up the nanocrystal reside on the particle surface. It is reasonable to assume that, at such a small size, the atoms need only diffuse to a small extend to severely perturb the physical and electronic structure of the material. Enthalpic or entropic forces may also drive the formation of an alloyed structure over a layered one; forces that are sufficiently overcome in the 6 nm crystals by virtue of the enhanced structural stability of the large nanocrystals.

References

1. A. Eychmueller, A. Mews, H. Weller. *Chemical Physics Letters*, **1993**. 208, 1, 59-61.
2. F. Koberling, A. Mews, Thomas Basche. *Physical Review B,* **1999**. 60, 3, 1921-1927.
3. V. F. Kamalov, R. B. Little, S. Logunov, M. A. El-Sayed. *Journal of Physical Chemistry*, **1996**. 100, 16, 6381-6384.
4. A. Yeh, G. Cerullo, U. Banin, A. Mews, A. P. Alivisatos, C. V. Shank. *Physical Review B,* **1999**. 59, 7, 4973-4977.
5. A. Mews, A. Eychmueller, M. Giersig, D. Schooss, H. Weller. *Journal of Physical Chemistry*, **1994**. 98, 934-941.
6. L. Spanhel, H. Weller, A. Fojtik, A. Henglein. *Ber. Bunsenges. Phys. Chem.*, **1987**. 91, 88.
7. R. Rossetti, R. Hull, J. M. Gibson, L. E. Brus. *Journal of Chemical Physics*, **1985**. 82, 552,

8. T. Vossmeyer, L. Katsikas, M. Giersig, I. G. Popovic, K. Diesner, A. Chemseddine, A. Eychmueller, H. Weller. *Journal of Physical Chemistry*, **1994**. 98, 7665-7673.

CHAPTER 8

PREPARATION OF QUANTUM DOT QUANTUM WELL NANOCRYSTALS OF DIFFERENT COMPOSITIONS

Quantum dot quantum well nanocrystals of different composition have been attempted using the same surface exchange reaction method used for preparation of CdS/HgS/CdS. The surface exchange method for nanocrystals does not work in general and must depend largely on the lattice parameters and solubility products of the materials involved. Other methods of epitaxialy depositing thin layers on top of semiconductor nanocrystals must be introduced in order to fabricate systems of the desired composition and structure.

Introduction

The interesting results obtained from the CdS/HgS/CdS quantum dot quantum well system have raised questions about the behavior of other quantum dot quantum wells of different size, shape and composition. In particular, it would be interesting to understand the influence of different materials on the electronic structure and dynamics of these nanometer sized semiconductor heterostructures.

It has been demonstrated that the excited electron in CdS/HgS/CdS migrates from the CdS core of the particle to the HgS well ten times slower than the hole [3]. The reason for this is likely the conduction band energy offset between CdS and HgS and large differences in the wavefunction between Cd and Hg atoms leading to insufficient

overlap integrals and Franck-Condon factors to facilitate the electron transfer process. It would be interesting to see if the opposite was true and the hole migrates slower in a material in which the non-metal is different between the core and well semiconductor materials (i.e. CdS/CdSe/CdS or CdS/CdTe/CdS). In such a case the valence band offset would be larger and the overlap between S and Se or S and Te might determine the rate of the relaxation for the hole in these systems.

In the CdS/HgS/CdS system, it has been shown that the luminescence occurs from an HgS well localized lowest excited state [1, 2]. This may be due largely to the fact that the band-gap difference between CdS and HgS is very large (nearly 2 eV) and the HgS well is therefore very deep. It is not clear that well-layer localized emission would be observed for other systems of quantum dot quantum well nanocrystals in which the difference in band-gap energy is not as large as in CdS/HgS/CdS. It may be that in these instances the lowest excited state is delocalized or that all luminescence occurs from trap states associated with defects at interfaces and surfaces.

For such investigations, the synthesis and characterization of a number of quantum dot quantum well nanocrystal systems has been attempted. The preparation techniques and results for ZnS/HgS/ZnS, CdS/CdSe/CdS and CdS/CuS/CdS are presented and discussed.

Experimental

ZnS/HgS/ZnS Preparation

ZnS/HgS/ZnS nanocrystals were prepared in the same manner as CdS/HgS/CdS. The synthesis may be separated into three parts: (1) growing the ZnS core, (2) exchanging the outermost Zn atoms for Hg to form the HgS well monolayer, (3) Capping the well with a monolayer of ZnS.

The core of ZnS was synthesized in methanol using PVP (mw 50,000 Da) as a capping material. For the source of Zn^{2+}, a 0.1 M solution of $ZnCl_2$ was prepared in deionized water. A 0.2 mL portion of the Zn^{2+} solution was added to 100 mL of methanol in a 250 mL three-neck reaction flask. A 0.2 mL portion of 10% PVP in methanol was also added to the reaction flask and the mixture was purged with argon gas for 30 minutes under vigorous stirring. Afterwards, 1.0 mL of H_2S gas was rapidly injected into the sealed reaction vessel while the mixture continued to stir rapidly. After 10 minutes of nanocrystal growth, this solution was then purged with argon for an additional 30 minutes to remove any excess H_2S gas that may have remained. A 3 mL sample of the ZnS colloidal suspension was taken for analysis followed by a rapid injection of 0.1 mL of 0.1 M $HgCl_2$ in deionized water. After 5-10 seconds of vigorous stirring after the injection of Hg^{2+} a 3 mL sample of the CdS/HgS colloid was removed and the remaining reaction mixture was treated with a drop-wise addition of 30 mL of a 1 mL H_2S/100 mL methanol solution. The slow addition of S^{2-} is necessary to avoid the generation of high local concentrations of Cd^{2+} and S^{2-}, which could result in the

formation of new CdS seeds. The slow addition process should take at least 20 minutes. After the addition of S^{2-} in the last step is complete, the reaction mixture was again purged with argon to remove any excess dissolved gas. The approximately 120 mL of CdS/HgS/CdS colloidal suspension was then transferred to a 250 mL round-bottomed flask and 1 gram of PVP added to the solution. The additional PVP ensures complete protection of the nanocrystals and also facilitates the preparation of a dry film of the QDQW sample. The 120 mL sample was concentrated to about 10 mL using a rotary evaporator and the final samples were stored in vials in the dark. Samples taken during the course of the preparation were transferred to a 1 cm glass cuvette and characterized using UV-VIS spectroscopy.

CdS/CdSe/CdS Preparation

The core of CdS was synthesized in methanol using PVP (mw 50,000 Da) as a capping material. For the source of Cd^{2+}, a 0.1 M solution of $CdCl_2$ was prepared in deionized water. A 0.5 mL portion of the Cd^{2+} solution was added to 100 mL of methanol in a 250 mL three-neck reaction flask. A 0.5 mL portion of 10% PVP in methanol was also added to the reaction flask and the mixture was purged with argon gas for 30 minutes under vigorous stirring. Afterwards, 1.0 mL of H_2S gas was rapidly injected into the sealed reaction vessel while the mixture continued to stir rapidly. After 10 minutes of nanocrystal growth, this solution was then purged with argon for an additional 30 minutes to remove any excess H_2S gas that may have remained. A 3 mL

sample of the CdS colloidal suspension was taken for analysis followed by a rapid injection of 0.44 mL of 0.05 M NaHSe in deionized water. The NaHSe solution was produced by reacting H_2Se gas (generated from the reaction of Al_2Se_3 with 10% sulfuric acid) with 0.05 M NaOH in a sealed flask. After 5-10 seconds of vigorous stirring after the injection of NaHSe a 3 mL sample of the CdS/CdSe colloid was removed and the remaining reaction mixture was treated with a drop-wise addition of 30 mL of a 1 mL CdS/100 mL methanol solution. The slow addition of Cd^{2+} is necessary to avoid the generation of high local concentrations of Cd^{2+} and S^{2-}, which could result in the formation of new CdS seeds. The slow addition process should take at least 20 minutes. After the addition of Cd^{2+} in the last step is complete, the reaction mixture was again purged with argon to remove any excess dissolved gas. The approximately 120 mL of CdS/CdSe/CdS colloidal suspension was then transferred to a 250 mL round-bottomed flask and 1 gram of PVP added to the solution. The additional PVP ensures complete protection of the nanocrystals and also facilitates the preparation of a dry film of the QDQW sample. The 120 mL sample was concentrated to about 10 mL using a rotary evaporator and the final samples were stored in vials in the dark. Samples taken during the course of the preparation were transferred to a 1 cm glass cuvette and characterized using UV-VIS spectroscopy.

CdS/CuS/CdS Preparation

The core of CdS was synthesized in methanol using PVP (mw 50,000 Da) as a capping material. For the source of Cd^{2+}, a 0.1 M solution of $CdCl_2$ was prepared in

deionized water. A 0.5 mL portion of the Cd^{2+} solution was added to 100 mL of methanol in a 250 mL three-neck reaction flask. A 0.5 mL portion of 10% PVP in methanol was also added to the reaction flask and the mixture was purged with argon gas for 30 minutes under vigorous stirring. Afterwards, 1.0 mL of H_2S gas was rapidly injected into the sealed reaction vessel while the mixture continued to stir rapidly. After 10 minutes of nanocrystal growth, this solution was then purged with argon for an additional 30 minutes to remove any excess H_2S gas that may have remained. A 3 mL sample of the CdS colloidal suspension was taken for analysis followed by a rapid injection of 0.5 mL of 0.1 M $CuSO_4$ in deionized water. After 5-10 seconds of vigorous stirring after the injection of $CuSO_4$ a 3 mL sample of the CdS/CuS colloid was removed and the remaining reaction mixture was treated with a drop-wise addition of 30 mL of a 1 mL H_2S/100 mL methanol solution. The slow addition of Cd^{2+} is necessary to avoid the generation of high local concentrations of Cd^{2+} and S^{2-}, which could result in the formation of new CdS seeds. The slow addition process should take at least 20 minutes. After the addition of Cd^{2+} in the last step is complete, the reaction mixture was again purged with argon to remove any excess dissolved gas. The approximately 120 mL of CdS/CuS/CdS colloidal suspension was then transferred to a 250 mL round-bottomed flask and 1 gram of PVP added to the solution. The additional PVP ensures complete protection of the nanocrystals and also facilitates the preparation of a dry film of the QDQW sample. The 120 mL sample was concentrated to about 10 mL using a rotary evaporator and the final samples were stored in vials in the dark. Samples taken during the course of the preparation were transferred to a 1 cm glass cuvette and characterized using UV-VIS spectroscopy.

Results and Discussion

ZnS/HgS/ZnS

Figure 8.1 shows the evolution of the ground-state absorption spectrum of ZnS nanocrystals as a function of increasing Hg^{2+} concentration. The initial ZnS absorption band centered on 300 nm broadens and shifts as more Hg^{2+} is added. This is similar to the effect observed for CdS/HgS/CdS nanocrystals and is a promising indication that a ZnS/HgS core shell particle may be formed by this technique. Figure 8.2 shows the spectra obtained during the full-scale synthesis of ZnS/HgS/ZnS. In this case the spectrum shows no sign of a significant red shift following the addition of Hg^{2+}. The only red shift and broadening of the absorption is seen after the addition of sulfide to cap the particles with ZnS. Even so, the spectra are featureless and lack that structure desired based on the results seen for CdS/HgS/CdS quantum dot quantum wells.

CdS/CdSe/CdS

Figure 8.3 shows the absorption spectra collected during the preparation of small (4 nm) CdS/CdSe/CdS nanocrystals. As mentioned in the experimental section, performing the synthesis at lower temperature generates particles of smaller diameter and typically narrower size distribution. The spectrum in blue is typical of 3 nm core CdS nanocrystals prepared by the low temperature method. Upon addition of NaHSe there is only a slight red shift in the absorption as shown in the spectrum in green. The final

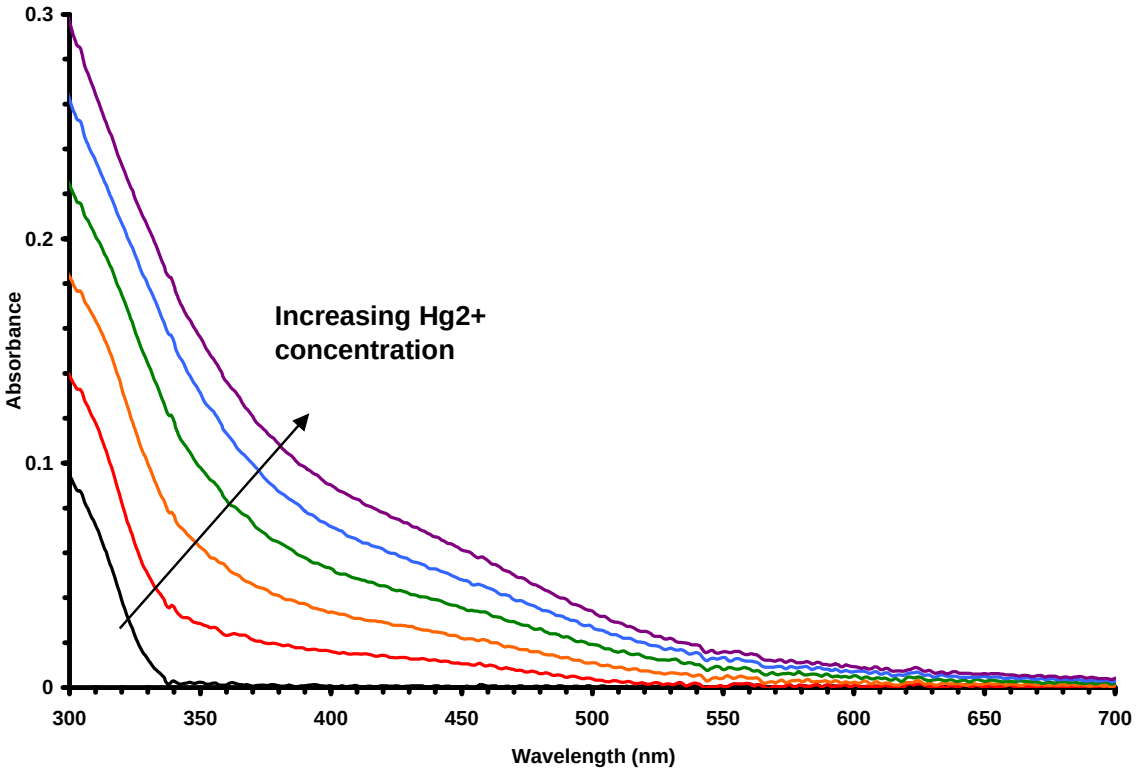

Figure 8.1. Evolution of the absorption spectrum of ZnS nanocrystals with the addition of Hg^{2+} during the attempted preparation of ZnS/HgS/ZnS nanocrystals.

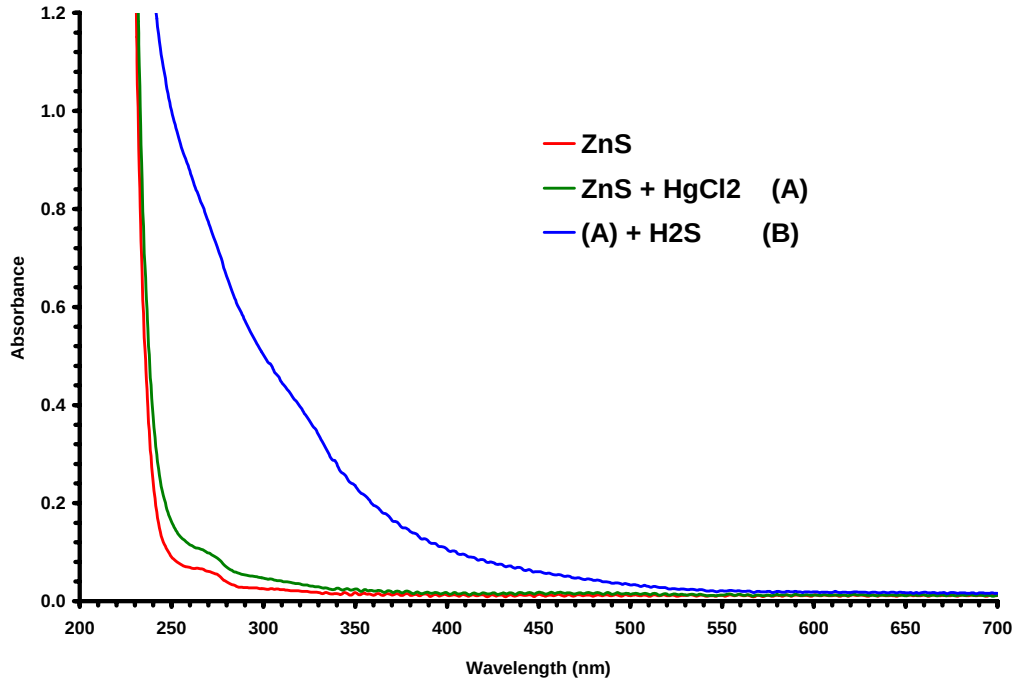

Figure 8.2. Absorption spectra collected during the preparation of ZnS/HgS/ZnS nanocrystals.

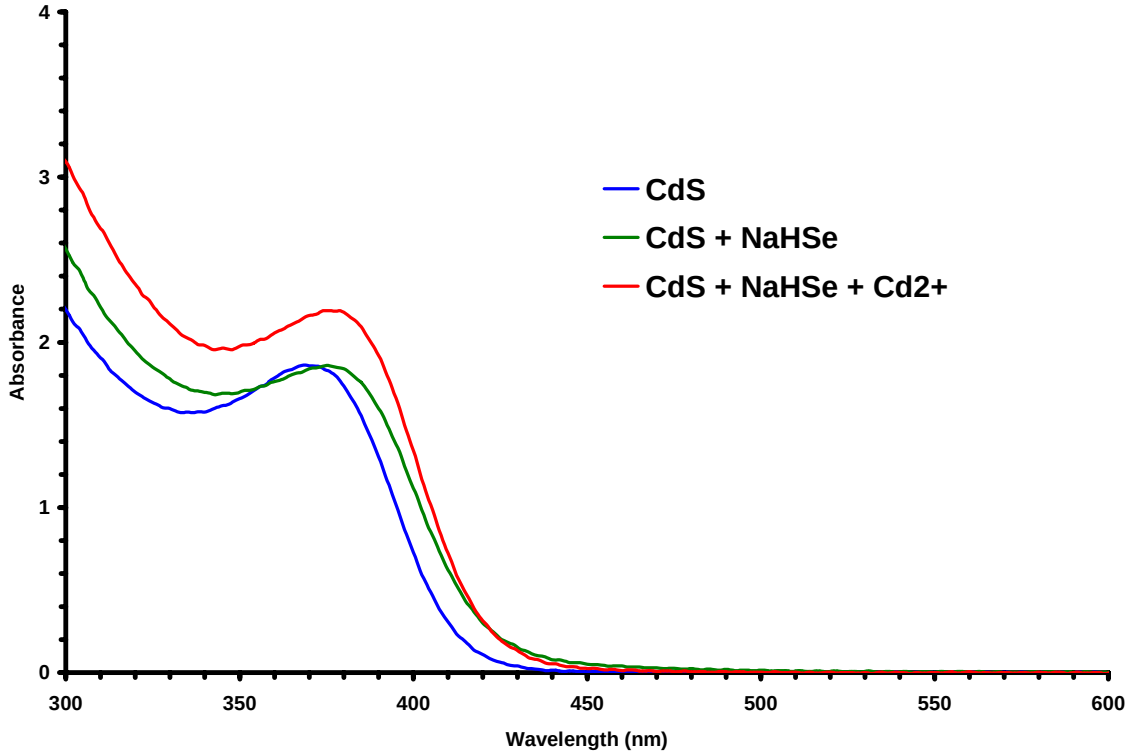

Figure 8.3. Absorption spectra collected during the preparation of 4 nm CdS/CdSe/CdS nanocrystals.

addition of Cd^{2+} yields the spectrum in red, which is assumed to be of CdS/CdSe/CdS nanocrystals. From the only slight shift in the absorption spectrum it is difficult to assign this structure based solely off of the optical data. A confident assignment of this product to the CdS/CdSe/CdS structure is not justified without the presence of other supporting data at this time.

Larger CdS/CdSe/CdS nanocrystals can be attempted by running the synthesis at a higher temperature. The nanocrystals prepared by this method are shown in Figure 8.4, again showing the evolution of the absorption spectrum during the course of the synthesis. The spectrum in green is of core CdS crystals and it is evident that the

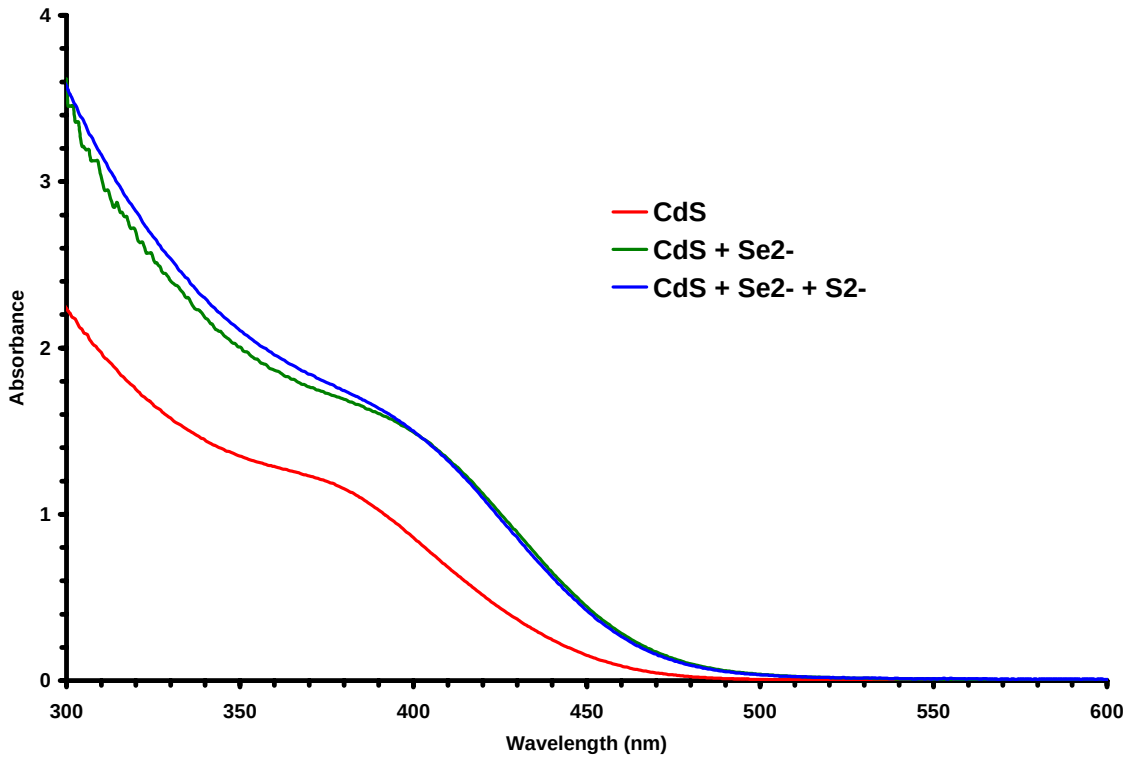

Figure 8.4. Absorption spectra collected during the preparation of larger (5 nm) CdS/CdSe/CdS nanocrystals.

spectrum is broader and the absorption onset longer than was the case for the small CdS crystallites. This is expected based on the temperature dependent growth condition and the quantum confinement effect. Following the addition of NaHSe, there is again only a small red shift and broadening of the absorption, making it difficult to confirm the structure as CdS/CdSe/CdS. Nevertheless, it was interesting to observe unusually strong luminescence from these nanocrystals as shown in Figure 8.5. The intensity of the luminescence is unlike that of many samples of CdS nanocrystals prepared by the PVP capping method and is consistent for quite a number of syntheses of (supposed) CdS/CdSe/CdS samples. The shape and position of the emission spectrum (red)

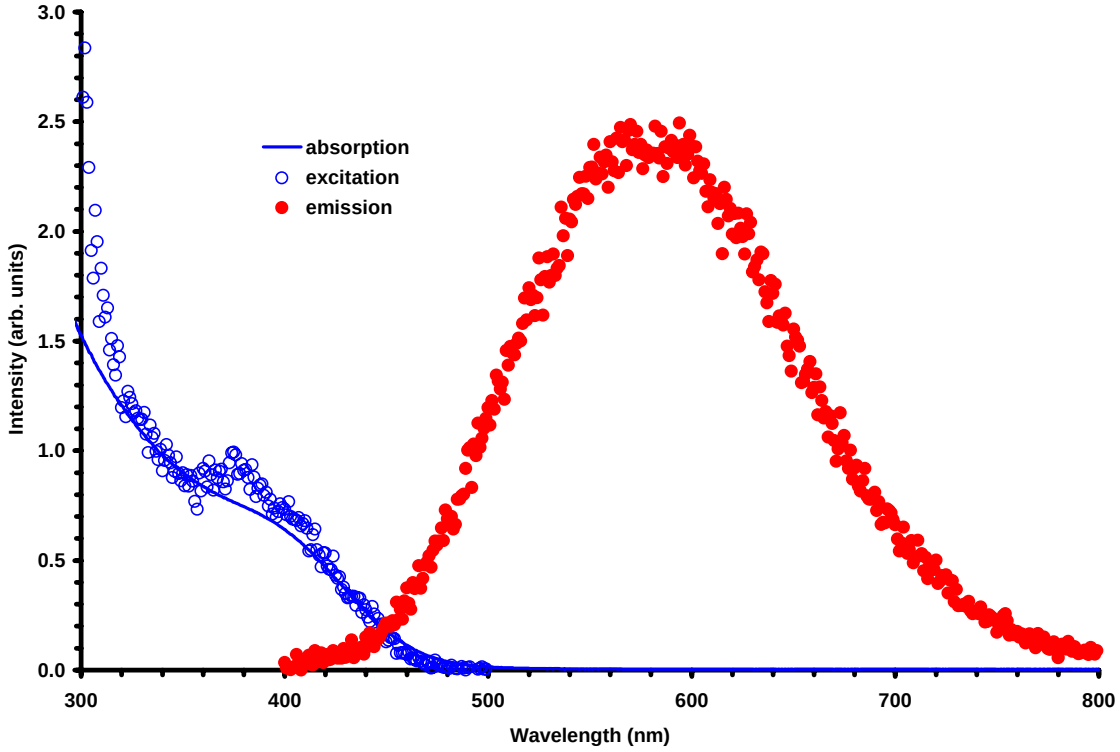

Figure 8.5. Absorption, luminescence and luminescence excitation spectra of CdS/CdSe/CdS nanocrystals.

indicated that the emission is likely trap emission from either surface or internal defect states of the nanocrystal. The excitation spectrum (blue circles) closely follows the absorption spectrum (blue line) and suggests the luminescence is intrinsic and not a result of energy transfer between particles or sensitization by other molecules. Luminescent lifetimes were recorded for samples of large CdS/CdSe nanocrystals and a typical decay profile is shown in Figure 8.6. The luminescence decays with a three-component lifetime: one fast component of 5 ns, a middle component of 37 ns and a long component of 128 ns. Multi-component luminescence lifetimes have been found for a number of

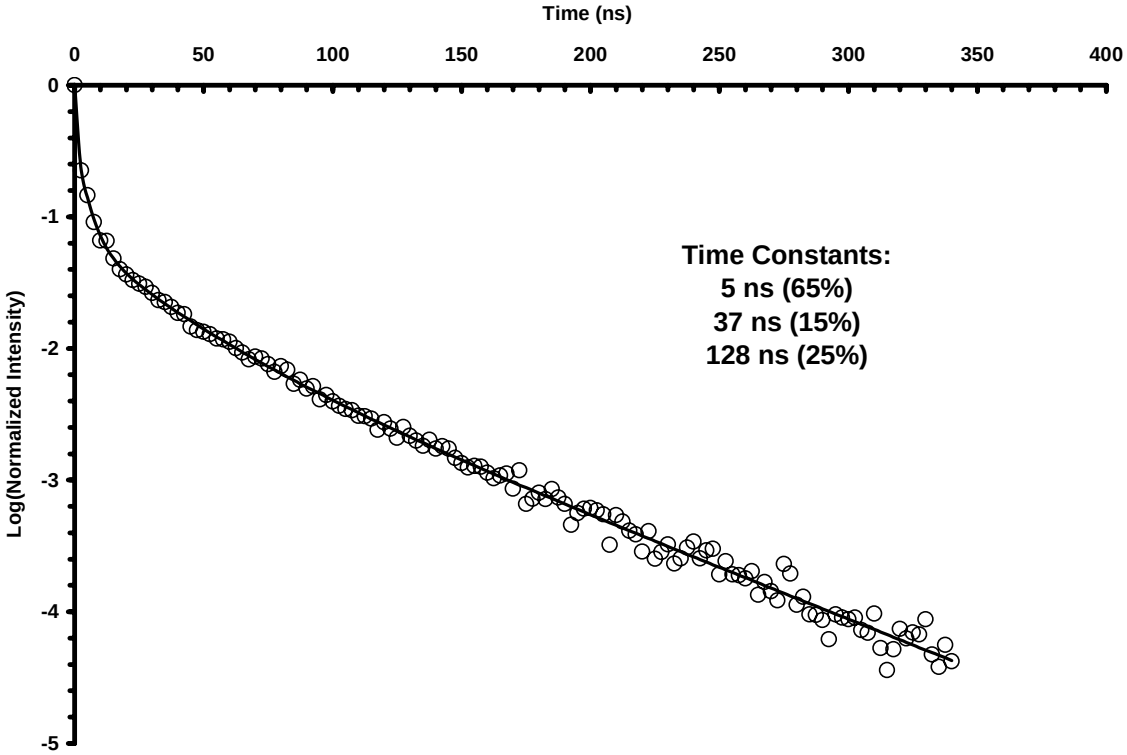

Figure 8.6. Luminescence decay of CdS/CdSe/CdS nanocrystals.

nanocrystals and are likely the result of inhomogeneity in the samples and the existence of numerous excited state relaxation pathways.

CdS/CuS/CdS

Figure 8.7 shows the absorption spectra collected during the preparation of CdS/CuS/CdS nanocrystals. The spectrum in red is that of CdS core nanocrystals prepared at room temperature. Upon addition of $CuSO_4$ the absorption spectrum changes dramatically. The spectra collected after addition of $CuSO_4$ share almost no resemblance to the original CdS spectrum: the absorption spectrum flattens and extends out into the

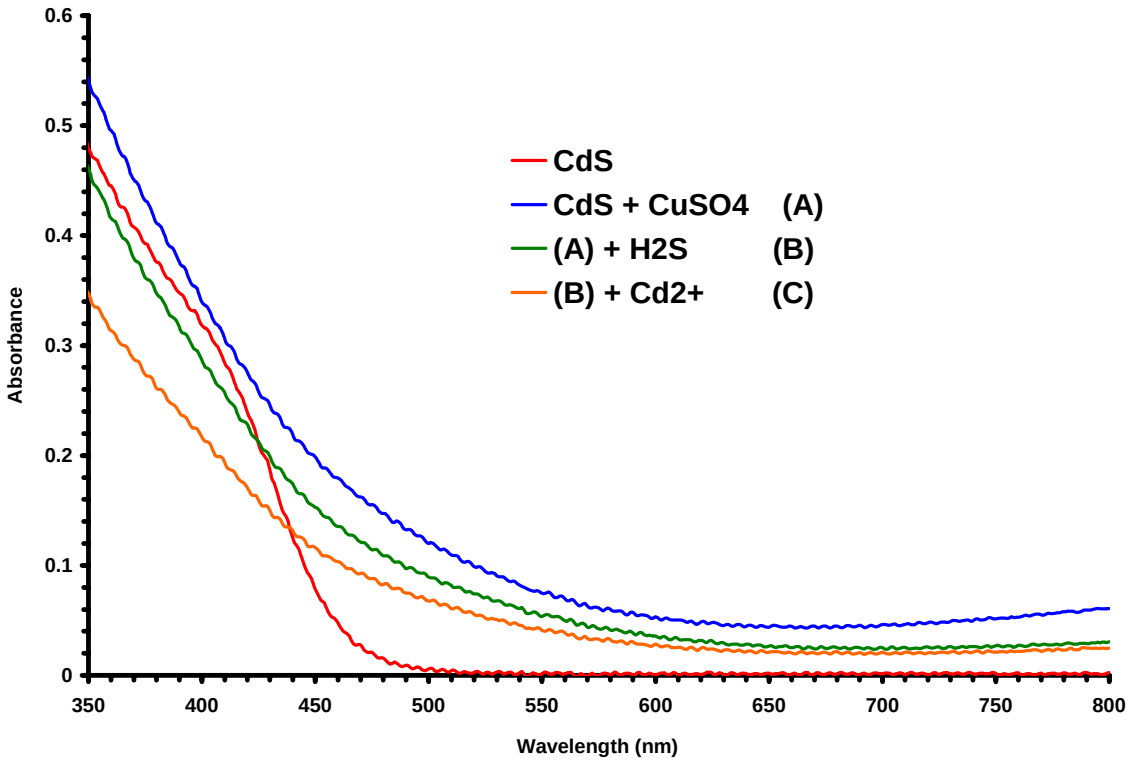

Figure 8.7. Absorption spectra collected during the preparation of CdS/CuS/CdS nanocrystals.

red with the growth of a small hump in the spectrum at around 800 nm. It is clear that the addition of Cu^{2+} had a dramatic effect on the structure of the particle, although it is difficult to determine the structure based on the spectroscopic evidence alone. Since the shift in absorption did not follow the behavior of the CdS/HgS/CdS quantum dot quantum well, a confident assignment of this product as CdS/CuS/CdS is not possible without further results.

References

1. A. Eychmueller, A. Mews. *Ber. Bunsenges. Phys. Chem.,* **1998**. 102, 1343-1357.
2. A. Yeh, G. Cerullo, U. Banin, A. Mews, A. P. Alivisatos, C. V. Shank. *Physical Review B,* **1999**. 59, 7, 4973-4977.
3. M. Braun, S. Link, C. Burda, M. A. El-Sayed. *Physical Review B,* **2002**. 66, 20, 205312-205317.

CHAPTER 9

ULTRAFAST ELECTRONIC RELAXATION AND ELECTRON LOCALIZATION IN CdS/CdSe/CdS COLLIODAL QUANTUM WELL NANOCRYSTALS

The relaxation and localization times of excited electrons in CdS/CdSe/CdS colloidal quantum wells were measured for the first time using sub-picosecond spectroscopy. HRTEM analysis and steady-state PL demonstrate a narrow size distribution of 5-6 nm epitaxial crystallites. By monitoring the rise time of the stimulated emission as a function of pump intensity, the relaxation times of the electron from the CdS core into the CdSe well are assigned. Two-component rise times in the stimulated emission are attributed to intraband relaxation of carriers generated directly within the CdSe well (fast component) and charge transfer of core-localized carriers across the CdS/CdSe interface (slow component). With increasing pump intensity, the charge transfer channel between the CdS core CdSe well contributes less to the stimulated emission signal due to filling and saturation of the CdSe well conduction band making the interfacial charge transfer component less efficient. The interfacial charge transfer time of the excited electron was determined from the slow component of the stimulated emission build-up time and had a value of 1140 fs. Further observations also suggest for the first time that excitation of colloidal quantum wells can produce excitons within the CdS core and CdSe well *simultaneously* under the right pumping conditions.

Introduction

The history of semiconductor research over the past century has been characterized by steadily increasing material heterogeneity [1]. Research began with pure bulk materials, and has progressed towards structures with ever increasing spatial and chemical complexity. While quantum dots have now been studied since the early 1980s [2], only in the past several years has the combination of monolayer accuracy growth with greatly simplified high quality colloidal synthesis been achieved [3]. These developments, along with steady improvement in understanding growth mechanisms, have enabled increasingly sophisticated demonstrations of colloidal semiconductor nanocrystal synthesis. A diversity of 2 and 3 layered quantum dot structures [4], tetrapods [5], and multi-layered nano-wires have recently synthesized. This has led to demonstration of single-tetrapod transistors [6] and QDQW random lasers [7]. There is a considerable interest in using such structures in the development of lasers and optoelectronic applications. Colloidal chemistry methods are cheaper and easier than the epitaxial techniques used to make semiconductor quantum wells and have the additional advantage of tunability in size, shape, quantity and functionality. Photoluminescence of considerable efficiency (30% QY) has been observed in CdS/CdSe/CdS [8] that make them potentially ideal for electro-optical applications. Radiative and non-radiative relaxation dynamics have also been studied using time-resolved spectroscopy [9].

For optoelectronic and electro-optical applications, the dynamics of the electrons and holes in these semiconductor nanocrystal heterostructures must be well understood. Using sub-picosecond spectroscopy, the localization times of electron and holes have been measured in CdS/HgS/CdS quantum dot quantum well nanocrystals [10].

Relaxation times for the charge carriers were determined by monitoring the rise time of the stimulated emission from the colloids excited with different excitation wavelengths. Stimulated emission requires that both an electron and hole be present in the lowest excited state for radiative recombination. The rise time of the emission may therefore be limited by the localization time of the slowest of the two charge carriers. This limitation is reached only if it is assumed that both electron and hole originate within the same layer of the nanocrystal heterostructure. Optically generated electrons and holes generated directly within the quantum well layer can immediately contribute to the emission process without needing to undergo interfacial charge transfer.

An extensive amount of work has been done to characterize the relaxation dynamics in nanometer sized CdSe quantum dots. In particular, the relaxation pathways of electrons and holes have been characterized using femtosecond transient spectroscopy [11, 12]. One of the issues considered in these studies was the association of electrons and holes to particular optical signals in the transient data. Careful analysis of the results suggested that transient optical signals in the visible region were primarily signatures of electron relaxation while transient optical signals in the NIR could be assigned to both electron and hole *intra*-band relaxation. While the transient bleach observed in the visible is an *inter*-band transition between the valence and conduction bands of the CdSe nanocrystal, the high density of valence band hole states and much lower density of conduction band electron states allows the hole to occupy numerous valence band states at room temperature for a corresponding occupation of only one of the accessible conduction band electron states (1S or 1P). This same argument should apply not only to CdSe but also to any semiconductor in which the electron effective mass is smaller than the hole effective mass, i.e. CdS, ZnS, CdTe. In this way the *inter*-band transitions

observed in semiconductor nanocrystals will be dominated by the relaxation of electrons. Experimental support for this hypothesis has been provided through observation of complementary 1P decay/1S buildup dynamics, identical 1S and 2S transient bleach dynamics and conduction band state-filling limited dynamics in CdSe nanocrystals [11, 13].

In this report we will investigate the ultrafast relaxation dynamics of a quantum dot quantum well (or colloidal quantum well) consisting of a CdS core and CdSe well.

Experimental

The following chemicals were purchased from Sigma-Aldrich (Milwaukee, WI): oleic acid (90%), octadecene (90%), trioctylphosphine (TOP, 90%), anhydrous methanol (99.5%), chloroform (99+%), cadmium oxide (99.99%), selenium (99.5+%), mercaptoacetic (99.5%) acid and used without further purification. Sulfur (precipitated, 99+%) was purchased from Fischer, and 2-propanol (99.7%) was purchased from Alfa Aesar. Reactions took place in a three-neck flask, heated and stirred by a laboratory heating mantle and magnetic stirrer. The flask was sealed except when adding reagent in order to minimize ODE evaporation and oxygen contamination. A small 1 mm needle (BD 25G1) was placed in one cap in order to release excess pressure. Stock solutions (0.02M) were made from each precursor by heating S in ODE, CdO in oleic acid/ ODE, and Se in TOP/ODE.

Synthesis

For CdS core synthesis, 1 mmol cadmium stock solution was heated to 300°C, at which point 0.4 mmol sulfur precursor was injected into the rapidly stirred solution. The reaction was allowed to proceed (typically 10 minutes) until the solution color remained constant. Aliquots were taken for optical absorption measurements. Purification was accomplished by extracting free oleic acid and un-reacted Cd precursor with methanol by phase separation induced with methanol. CdS core size was estimated from the wavelength of the resolved exciton peak in the absorption spectrum [14].

The total surface area of all CdS nanocrystals was then calculated using the measured size assuming that S was the limiting reagent. From this information, precursor injection quantities needed to grow additional monolayers of CdSe, and CdS for varying radii core crystals were calculated. After a portion of previously synthesized CdS core solution was heated to 190ºC, Cd and Se precursors were injected sequentially allowing 15 minutes after solution color change ceased between injections. After growing two CdSe monolayers, the temperature was increased to 230ºC at which point an additional two capping layers of CdS were grown by sequentially injecting Cd and S solutions. Removing free oleic acid and any unreacted precursor by washing with methanol purified the resulting colloidal quantum wells. Due to experimental uncertainty in calculating precursor quantities for monolayer growth, small amounts of homogenously nucleated crystals occur as evidenced by a small higher energy peak in the photoluminescence spectrum at 430nm. Size selective precipitation was employed to isolate quantum wells from homogeneously nucleated quantum dots. This was accomplished by adding propanol to the sample drop wise until the onset of turbidity was reached. Colloidal

quantum wells were then isolated by centrifugation at 11,000 rpm for 1-2 minutes. A fraction was re-suspended in hexane for HRTEM analysis, while the remainder was re-suspended in octadecene for steady-state and transient optical analysis.

Structural Analysis

Structural analysis of individual crystallites was accomplished using JEOL 4000EX high-resolution electron microscope. Negatives were scanned using an Epson Perfection 4990 at 4800dpi. Image analysis was accomplished using ImageJ.

Optical Studies

Crystal growth was observed by monitoring the red shift of the band edge by UV-Visible absorption using a Beckman DU-640 spectrophotometer. Steady state luminescence spectra were collected using a scanning spectrofluorimeter (Photon Technology Incorporated). Quantum yield was determined by comparison to Rhodamine B under identical conditions. Sub-picosecond pump-probe transient spectroscopy was carried out using an amplified Ti:Sapphire laser system and a traditional slow-scan pump-probe optical setup. The amplified Ti:Sapphire laser (Clark-MXR CPA-1000) has an output of 0.8 mJ, 100 fs pulses at a fundamental wavelength of 795 nm. A small fraction of the beam (4%) was split and sent to a white-light continuum generator while the remaining 96% was used for harmonic generation (398 and 265 nm) and the pumping of two OPAs (Quantronix TOPAS). Pump beams from either the harmonic generator or OPA were passed down a delay line and overlapped with the white light continuum beam

within the sample. The spot size of the excitation beam at the sample was measured using the razor-edge method and had a diameter of 180 micrometers. Single wavelength kinetics was monitored using a monochromator/photodiode arrangement coupled to a boxcar integrator and a lock-in amplifier. The pump beam was chopped at 492 Hz (f/2) and used as the reference frequency for the lock-in.

Results and Discussion

Structural and Chemical Analysis

Figure 9.1 contains absorption spectra from small aliquots of nanocrystal suspensions obtained at various stages of quantum well synthesis. These aliquots were measured prior to size-selective precipitation of the quantum wells from homogeneously nucleated crystals. The changes in absorption at the band edge demonstrate the salient characteristics of 3D and 1D quantum confinement, namely, a sharp peak and staircase-like structure respectively.

High Resolution Electron Microscopy

High-resolution transmission electron microscopy (HRTEM) was used to determine particle size, morphology and crystal structure. Figure 9.2A contains a cluster of mono-disperse crystallites 5-6 nm in diameter. The particles have quite similar size and shape that is consistent with the sharp band edge absorption and narrow emission features observed optically. The individual crystallites are wurtzite single crystals as

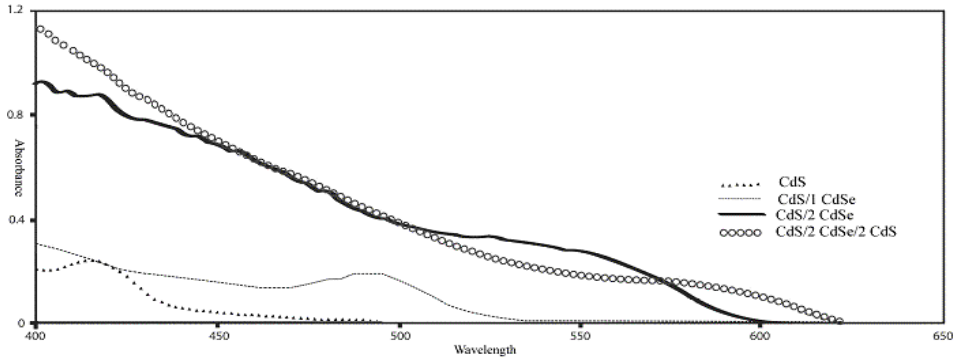

Figure 9.1. Absorption spectra collected during the preparation of CdS/CdSe/CdS colloidal quantum wells.

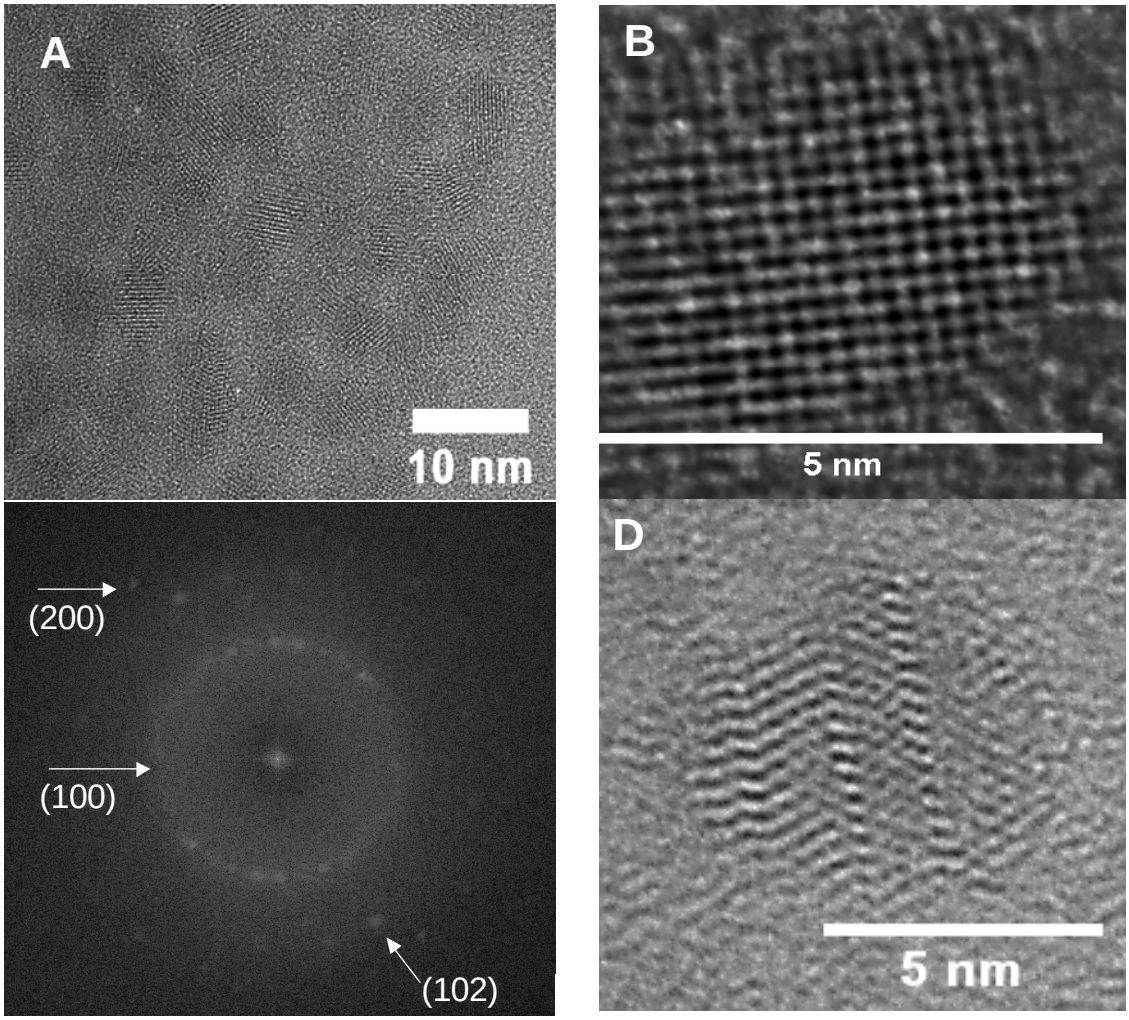

Figure 9.2. TEM images of CdS/CdSe/CdS colloidal quantum wells: (A) Lower magnification image shows the uniformity in size of the 5-6 nm nanocrystals, (B) Atomic resolution image of a single CdS/CdSe/CdS crystal, (C) Fourier transform of a single nanocrystal showing a wurtzite crystal structure, (D) Atomic resolution image of a rare nanocrystal containing a dislocation.

determined from the Fourier transform of Figure 9.2A (Figure 9.2C). Figure 9.2B shows an atomic resolution image of a quantum dot/quantum well nanocrystal. Growth of the CdSe well and CdS cap layers took place epitaxialy in all crystallites examined, as no evidence of grain boundaries or interfaces was observed. Since wurtzite CdSe has lattice parameters 3.67% and 4.14% larger in the a: and c: directions than CdS, it is expected that several monolayers of CdSe inside a CdS quantum dot would create a strained region. However due to the high interfacial curvature inherent to nanocrystals, strain accommodation is possible [15]. Out of the several hundred crystals observed, only one crystal was observed that contained a resolvable dislocation. This rare observation is shown in Figure 9.2D.

Optical Characterization

While first principles are sufficient to calculate precursor injection quantities necessary for monolayer accuracy growth, inevitable broadening of the size, shape, and defect distribution of nanocrystal populations occurs. Homogeneous nucleation during the well and capping layer growth can also occur. By allowing time between precursors injection for absorption and reaction to occur, homogeneous nucleation can be limited to small quantities. We employed a single cycle of size selective precipitation using propanol as a miscible non-solvent to extract the larger colloidal quantum wells of interest from homogeneously nucleated contamination. Additional cycles of size-selective precipitation did not result in significant sharpening of the emission peak indicating that a high degree of uniformity was achieved in the colloidal hetero-structures. Ground state absorption and steady-state photoluminescence spectra of size

selected and purified CdS/CdSe/CdS nanocrystals are shown in Figure 9.3. The absorption spectrum features the "stair-step" progression that is indicative of a 2-D quantum well structure. The band-edge absorption is relatively sharp, reflecting the narrow size distribution of this colloidal sample. The photoluminescence peak shows a slight Stokes shift from the absorption band edge, is quite narrow in line width (30 nm fwhm) with a quantum yield of ~21%

Ultrafast Relaxation Dynamics

Ultrafast relaxation dynamics in CdS/CdSe/CdS nanocrystals were investigated using sub-picosecond transient absorption spectroscopy. Samples were excited at 500 nm and the excited state was monitored at 610 nm – the peak of the steady state emission. A decrease in the transient differential absorption (dA) at 610 nm corresponds to stimulated emission at the band-edge and will be proportional in intensity to the number of charge carriers present in the lowest excited electron (1S) and hole states. The number of excitons (e-h pairs) generated in each particle depends on the pump intensity of the excitation pulse and may be calculated using $N_{eh} = J_p\sigma_a$, where J_p is the pump fluence ($1/cm^2$) and σ_a is the absorption cross section (cm^2) given by $\sigma_a = (4\pi R^3/3) \times \varepsilon(\lambda)$ where R is the nanocrystal radius and $\varepsilon(\lambda)$ is the nanocrystal extinction coefficient at the excitation wavelength (λ). Figure 9.4 shows transient differential absorption traces monitored at 610 nm for CdS/CdSe/CdS nanocrystals with exciton densities (# e-h pairs) of 0.10 (orange crosses), 0.31 (red circles), 0.99 (black triangles), 1.97 (green diamonds) and 4.94 (blue squares). The traces shown are non-linear least squares fits to the experimental data for visual clarity of the kinetics and correct adjustment of "time zero".

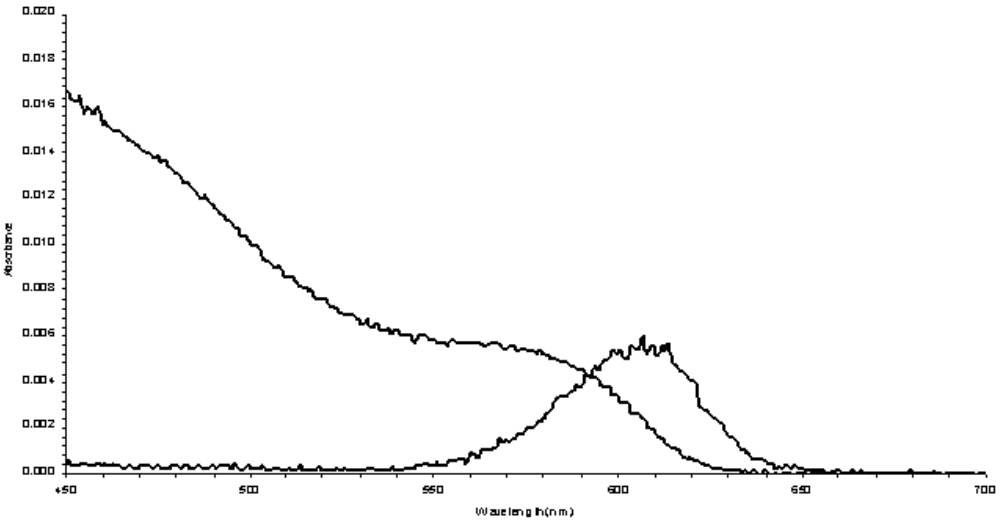

Figure 9.3. Ground state absorption and steady-state photoluminescence spectra of CdS/CdSe/CdS nanocrystals. The emission peak is occurs at 610nm and the quantum yield was estimated to be 21% compared to Rhodamine B under identical collection conditions.

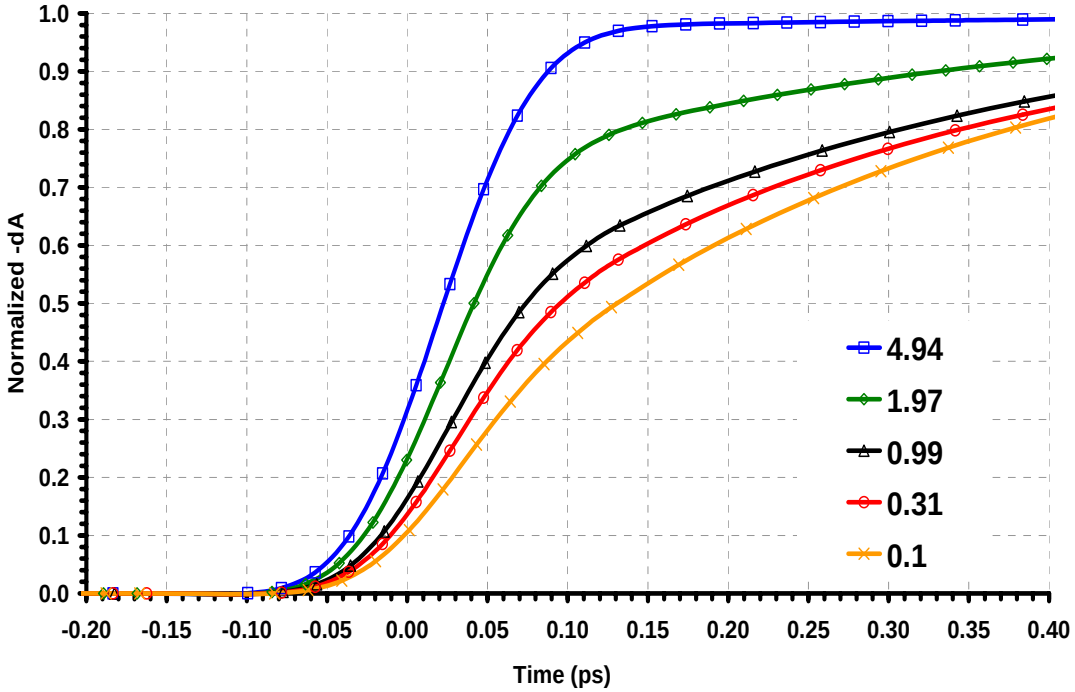

Figure 9.4. Transient differential absorption traces monitored at 610 nm for CdS/CdSe/CdS nanocrystals with exciton densities (# e-h pairs) of 0.10 (orange crosses), 0.31 (red circles), 0.99 (black triangles), 1.97 (green diamonds) and 4.94 (blue squares). The traces shown are non-linear least squares fits to the experimental data for visual clarity of the kinetics and correct adjustment of "time zero".

The analysis of the ultrafast data will focus on the early time (< 1 ps) portion of the kinetics with particular emphasis on the behavior of the rise times of the transient signals. The rise time of the transient signal at 610 nm is proportional to the population rate of the lowest excited electron state of the nanocrystal. Although the electronic energy levels of CdS/CdSe heterostructures are not fully understood at this point and likely composed of mixed CdS/CdSe electronic states, it is reasonable to assume that the lowest electron energy level be a doubly degenerate 1S level strongly localized within the CdSe well. To be sure that dynamics monitored at 610 nm were from electron relaxation alone, measurements were done with excitation above the apparent 1P(e) level using a 400 nm pump pulse. The decay of the 1P(e) state at 450 nm (Figure 9.5, open squares) corresponds very closely to the rise of the 1S(e) state at 610 nm (Figure 9.5, closed circles), suggesting that decay from the 1P(e) state directly feeds the 1S(e) state and that the signal is dependent only on electron dynamics.

If it is the case that monitoring at 610 nm probes the lowest excited 1S(e) state in the CdSe well, it is expected that the intensity of the transient signal at 610 nm should reach a maximum at 2 e-h pairs per particle (i.e. a filled 1S level). The intensity of the measured transient signal at 610 nm as a function of # e-h pairs is shown in Figure 9.6. The intensity of the transient signal increases sharply from 0 to 2 e-h pairs and then stays at a constant value of ~0.1 dA units between 2 and 5 e-h pairs per particle, suggesting a filling of the lowest electron energy level. This is consistent with the assumption that the lowest electron energy level in CdS/CdSe/CdS is a doubly degenerate 1S level since the signal saturates at a value of 2 e-h pairs per particle. From this result we can suppose that monitoring the transient -dA at 610 nm will give information about the rate of population of the lowest 1S electron level in the nanocrystal. Since this energy level is also expected

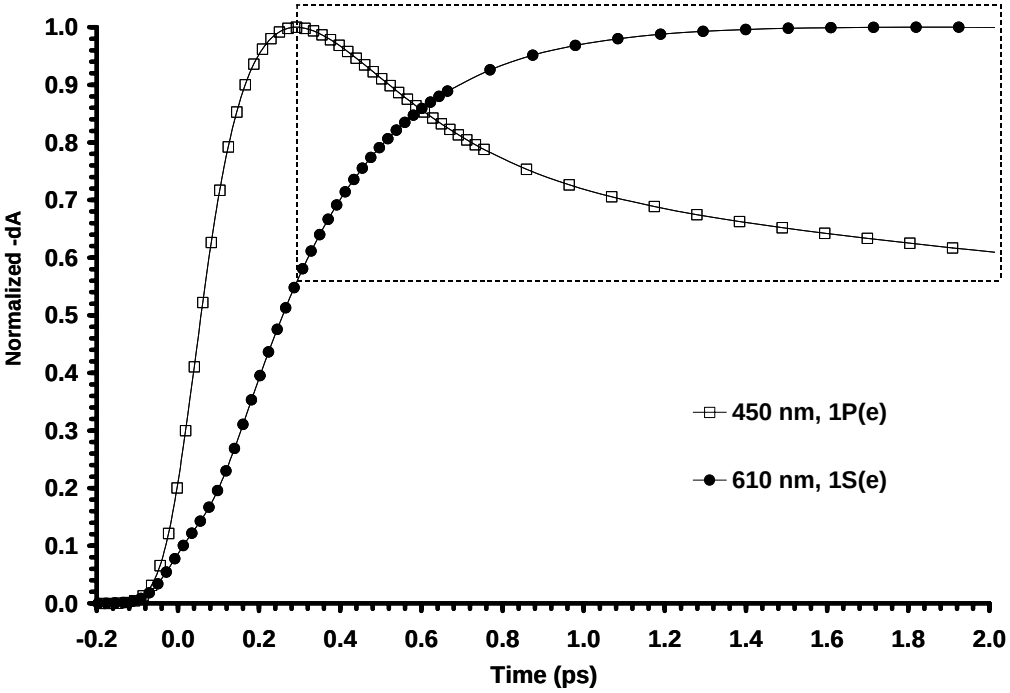

Figure 9.5. Transient differential absorption traces monitored at 450 nm (1P electron state) and 610 nm (1S electron state) for CdS/CdSe/CdS nanocrystals following excitation at 400 nm.

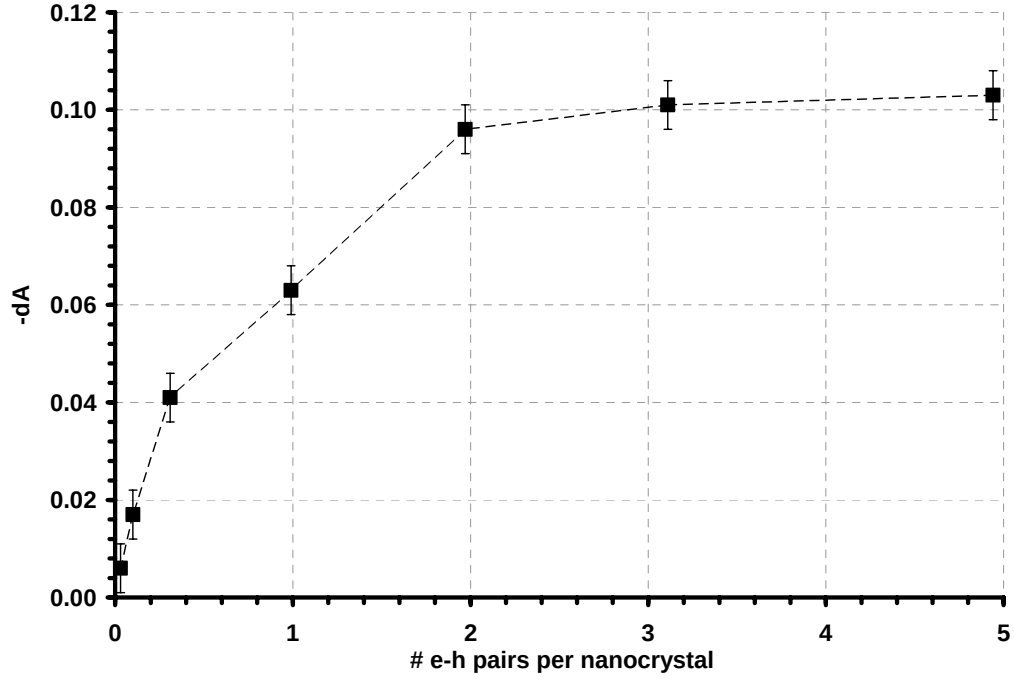

Figure 9.6. Intensity of the negative differential absorbance (-dA) of CdS/CdSe/CdS colloidal quantum wells as a function of exciton density (# electron-hole pairs per particle).

to represent states that are tightly localized to the CdSe well, the interpretation may be extended to consider localization times for electrons into the CdSe well. In order to understand dynamics, the kinetic nature of the transient signal at 610 nm needs to be considered in detail.

From close inspection of the rise traces in Figure 9.4, it is apparent that, for some of the exciton densities, there are two components to the rise time. The distinction is most apparent for 1.97 e-h pairs with an inflection point occurring at about 0.1 ps after "time zero". The origin of this two-component rise time is not immediately apparent, but is likely due to two simultaneous events in the nanocrystal relaxation having different time constants. The relative amplitude of the two components changes with exciton density: the slow component taking a larger fraction at low # e-h pairs and the fast component dominating for high # e-h pairs. This change has been quantified by determining the *amplitude fraction of the fast rise time* as a function of exciton density using the following procedure. First, the second derivatives of the normalized rise time traces are taken to identify the inflection points of the traces in quantitative manner. Then, the value of the normalized –dA at the time of the inflection point is taken as the *amplitude fraction of the fast rise time.* Such a procedure is justified for interpreting rise times that are difficult to analyze by exponential data fitting due to the highly non-exponential (or multi-exponential) behavior of kinetic processes in semiconductor nanocrystals. The results of this procedure are shown in Figure 9.7. As observed qualitatively, the amplitude fraction of the fast rise time becomes larger with increasing exciton density. This suggests that large # e-h pairs cause interference between the two processes responsible for the two-component rise time. It is interesting to point out that the amplitude of the fast rise never reaches zero, even for very low exciton densities (<<1

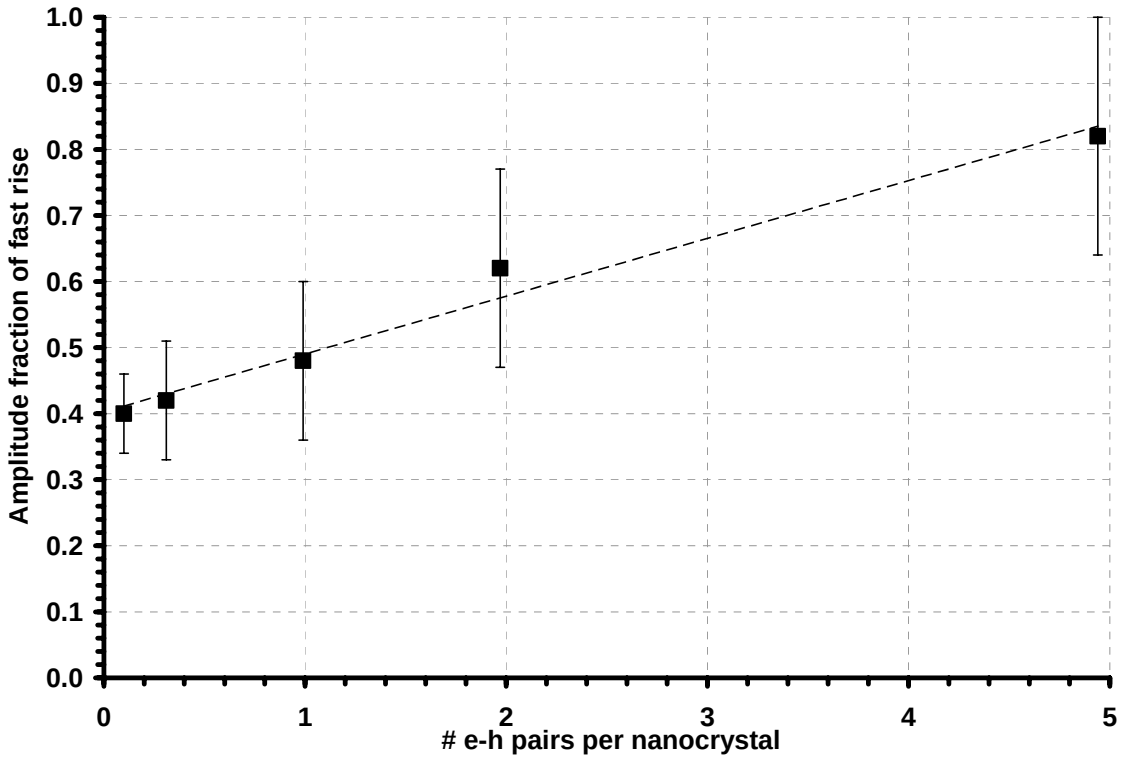

Figure 9.7. Amplitude fraction of the fast rise time (see text for details) of CdS/CdSe/CdS colloidal quantum wells as a function of exciton density (# electron-hole pairs per particle).

e-h pair). Instead, the intercept at # e-h pairs = 0 is 0.40, indicating that the fast component contributes at least 40% to the transient rise at all exciton densities. After identification of the fast and slow components of the rise time, the next step is to determine the value of the time constants associated with these fast and slow processes. Again, the non-exponential nature of the kinetics makes it difficult to reach reasonable values of time constants using exponential data fitting procedures, and instead we implement an *instantaneous rate-of-change* (first derivative) procedure to find the *apparent rise time* of the transient signals. All traces were first converted to a natural logarithm scale so that the slope of the curves would reflect a decay rate as understood for exponential rise and decay processes. For the fast rise time, a value of the

instantaneous rate-of-change was recorded at a point in the trace *before* the inflection point determined previously and the slow rise time was taken at a point *after* the inflection point. Specifically, fast rise times were found from the first derivative of the trace at a value of 20% the signal maximum and slow rise times were taken at 80% the signal maximum. The results of this procedure are shown in Figure 9.8. It is clear that there is a sharp difference between the fast and slow components of the rise time and that the time constant of each changes with exciton density. Although the change in the fast component is only very slight, the slow component drops dramatically above 2 e-h pairs per particle. Below 2 e-h pairs, the slow component has an apparent rise time of ~1.2 ps, which then falls to 276 fs as the slow rise converges to the fast rise at > 2 e-h pairs. The interpretation of this result is clear: filling of the lowest 1S electron level effectively shuts down the slow component of the relaxation process. This interpretation is only valid if the fast and slow processes occur simultaneously. One possible identification is assignment of the fast component to *intra*-band relaxation within the lowest excited energy level, localized within the CdSe well. The slow component would then be assigned to *interfacial charge transfer* from the lowest conduction band level in the CdS core into the lowest energy level of the nanocrystal, localized in the CdSe well. To help justify the assignment of the fast component to *intra*-band relaxation within the CdSe well, ultra-fast measurements were also done using 570 nm excitation to pump directly into the lowest excited energy level of the nanocrystal. The observed signal did not change as a function of pump intensity and showed no indication of a two-component rise process. The result from this experiment is shown in Figure 9.9 overlaid with the data collected using 500 nm, 4.94 e-h pair excitation for comparison. The two traces are identical within experimental error. Since 570 nm excitation pumps directly into the

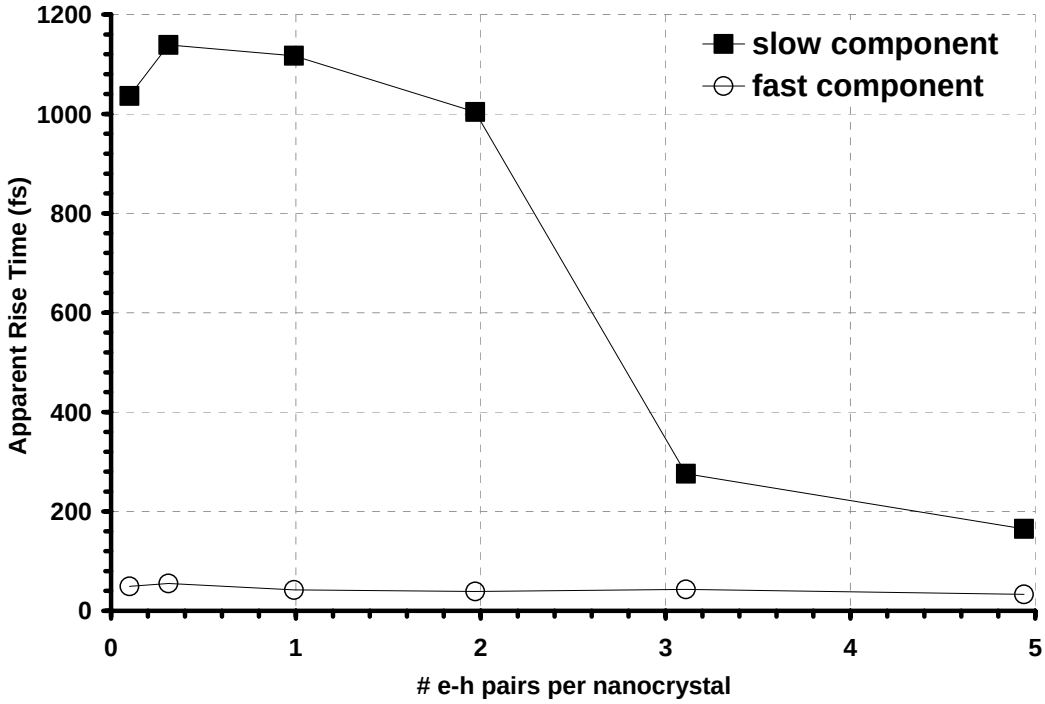

Figure 9.8. Apparent rise times of the slow (filled squares) and fast (open circles) components of the rise time at 610 nm in CdS/CdSe/CdS colloidal quantum wells excited with a 100 fs, 500 nm laser pulse.

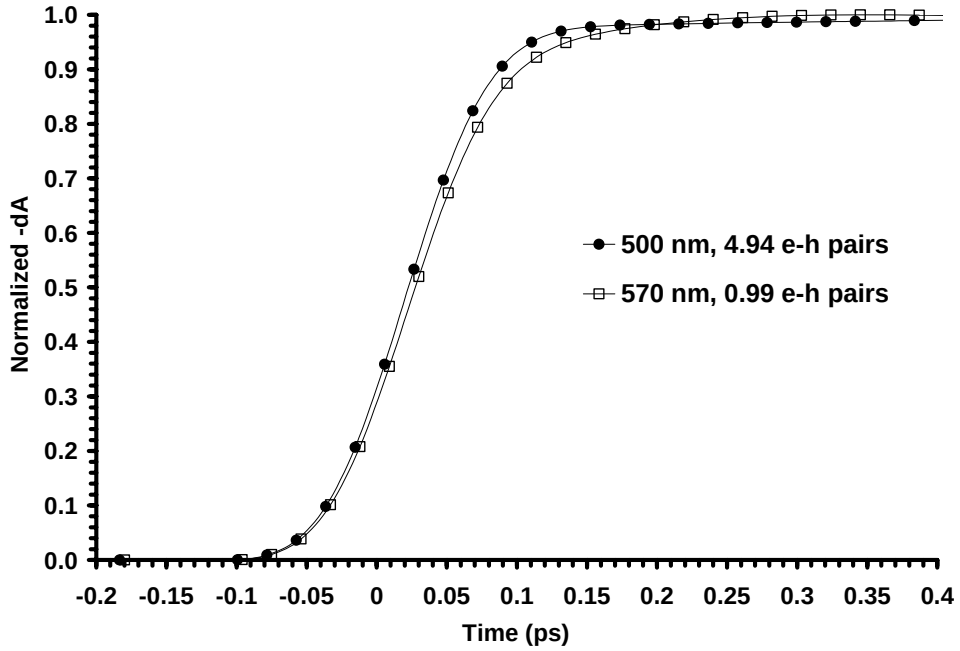

Figure 9.9. Transient differential absorption monitored at 610 nm for CdS/CdSe/CdS nanocrystals with excitation at 500 nm, 4.94 e-h pairs (closed circles) and 570 nm, 0.99 e-h pairs (open squares).

lowest excited energy level localized within the CdSe well, the fast rise process observed can be assigned to rapid *intra*-band relaxation within the CdSe well.

The situation described above is shown schematically in Figure 9.10. Energy level diagrams are shown to depict the expected relaxation pathways in CdS/CdSe/CdS nanocrystals under the two mentioned excitation conditions. As shown in the top panel of Figure 9.10, 500 nm excitation (green arrow) pumps an electron into a core CdS state that is below the 1P electron level of the CdSe well, but above the 1S electron level. The 500 nm pump can also populate the 1S level in the CdSe well. Relaxation from the core CdS state (dark blue arrow) by interfacial charge transfer into the CdSe well is responsible for the slow component of the two-component rise time. Relaxation within the 1S(e) level of the CdSe well (light blue arrow) is responsible for the fast component of the rise time. Once in the 1S level of the CdSe well, the electron recombines with the hole to give the emission (orange arrow) observed at 610 nm in our experiments. A different picture is seen when using 570 nm excitation as shown in the bottom panel of Figure 9.10. A 570 nm photon does not have enough energy to populate the CdS core level as the 500 nm pump did. Therefore the only component to the relaxation is the fast *intra*-band relaxation (light blue arrow) of the electron within the 1S level of the CdSe well. With the described model in place, the remainder of the discussion will be focused on quantitative analysis of the results collected using 500 nm excitation.

At low exciton densities < 2 e-h pairs, both fast and slow processes can occur and contribute to the observed rise time signal since none of the electron levels are filled to maximum Pauli occupancy. At high exciton densities > 2 e-h pairs, the lowest electron energy level in the CdSe well is filled and excess electrons in the CdS core cannot cross into the well until the electrons occupying the well radiatively or non-radiatively

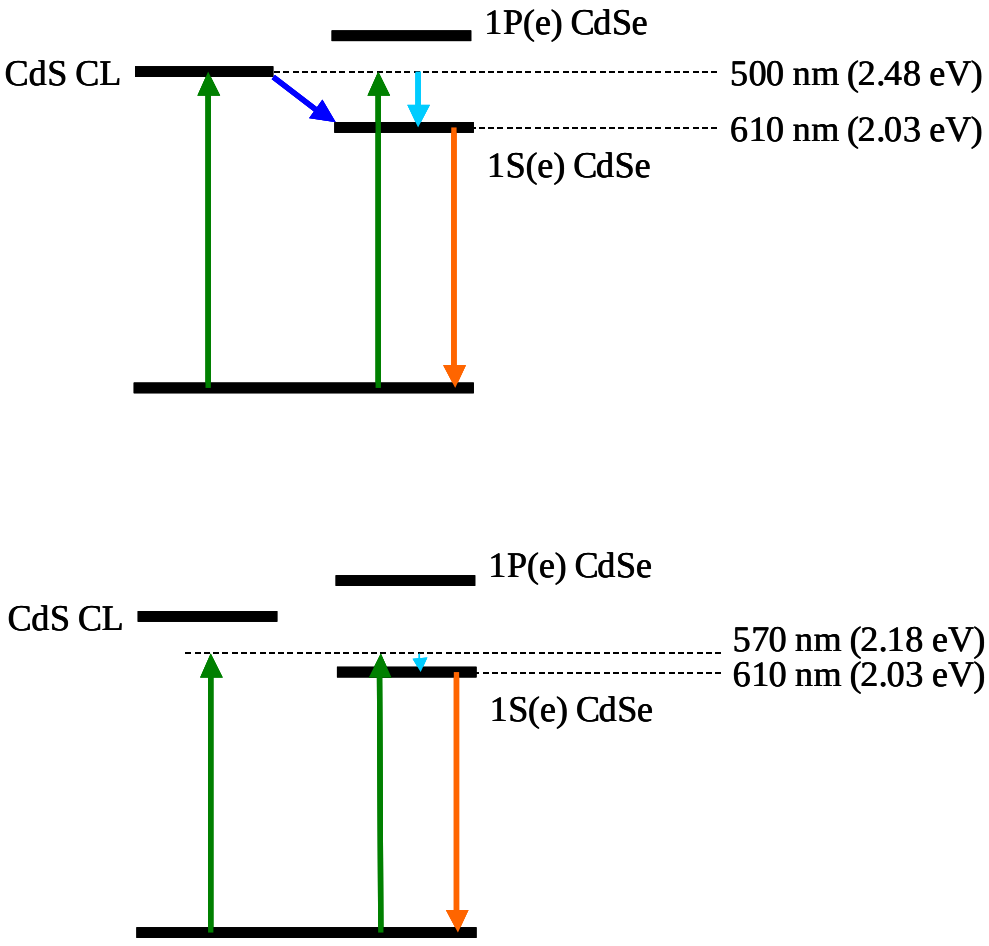

Figure 9.10. Energy level diagrams used for interpretation of the experimental data. Top panel shows the expected relaxation pathways when 500 nm excitation is used. The bottom panel shows the expected relaxation pathways when 570 nm excitation is used. All energy levels and shown to scale.

recombine with holes in the valence band levels. Since recombination times are typically in the 100s of picoseconds or greater, the electrons in the CdS core are effectively trapped and must relax through other mechanisms besides interfacial charge transfer. Underlying this interpretation is also the requirement that excitation of CdS/CdSe/CdS nanocrystals result in population of *both* the core CdS and the CdSe well simultaneously. Such a possibility has not been considered for semiconductor nanocrystal heterostructures up to this point, but may be plausible given the effects of quantum confinement and the relative closeness of the conduction band levels in CdS and CdSe (only 0.5 eV offset in bulk). In fact, some results from our analysis of the ultrafast data indirectly point to the possibility of simultaneous excitation of core and well. Recall the value of 40% amplitude fraction of the fast rise time from the 0 e-h pair intercept in Figure 9.6. In the limit of infinitesimally small # e-h pairs, the amplitudes of the fast and slow components, A_{fast} and A_{slow}, are determined simply by the product of the respective initial populations at t = 0 of the CdSe well and CdS core and the rate constants of *intra*-band relaxation (IB) and interfacial charge transfer (CT).

$$A_{fast} = p_{CdSe} k_{IB}$$
$$A_{slow} = p_{CdS} k_{CT} \qquad (9.1)$$

The sum of these is proportional to the population of the lowest excited 1S(e) state from which emission is observed at 610 nm. Taking into account the absorption coefficients (σ, cm^{-1}) of the CdS core and CdSe well, the population of the lowest 1S(e) state may be written as

$$p_{1S(e)} = \tau_{1s(e)} N_{gs \to es} L \left(\frac{\sigma_{CdS}}{\tau_{slow}^{CT}} + \frac{\sigma_{CdSe}}{\tau_{fast}^{IB}} \right) \qquad (9.2)$$

where $\tau_{1s(e)}$ is the lifetime of the 1S(e) state, $N_{gs \to es}$ is the number of ground state nanocrystals converted to excited state, L is the absorption pathlength (cm) and τ_{slow}^{CT} and τ_{fast}^{IB} are the rise times of the slow and fast components, respectively. From this it may be seen that the amplitude fractions of the fast and slow components are proportional to the absorption coefficients of the CdS core/CdSe well divided by the rise times of the slow and fast components. Using a value of 0.4 for the amplitude fraction of the fast rise and 0.6 as the complimentary amplitude fraction of the slow rise, along with the values of 55 fs and 1140 fs for the fast and slow rise times, we may calculate the relative absorption coefficients for the CdSe well and CdS core. The results are that nearly 97% of the absorption populates the CdS core, while only 3% populates the CdSe well. Despite the small absorption coefficients for the well, the significant amplitude of the fast component comes from the much more rapid relaxation time for *intra*-band relaxation compared to the slow interfacial charge transfer.

Conclusion

Nanocrystal heterostructures consisting of a CdS core, two layer CdSe well and two layer CdS shell have been synthesized and studied using ultra-fast time-resolved spectroscopy. The prepared crystals have a well-defined crystal structure and exhibit high luminescence quantum yield. The relaxation of excited electrons was investigated

using sub-picosecond transient absorption spectroscopy. The rise time of the lowest excited 1S electron level in the CdSe well shows two component which have been identified as *intra*-band relaxation within the CdSe well (fast component) and interfacial charge transfer from the CdS core to the CdSe well (slow component). What is surprising is that these processes occur simultaneously, which suggests that optical excitation of CdS/CdSe/CdS nanocrystals can produce excitons in both the CdS core and CdSe. This is the first time this has been observed and has interesting implications on the electronic structure and application of semiconductor nanocrystal heterostructures.

References

1. M. R. Melloch, J. M. Woodall, E. S. Harmon, N. Otsuka, F. Pollak, D. D. Nolte, R. M. Feenstra, M. A. Lutz. *Annual Review of Materials Science*, **1995**. 25,

2. H. Weller, U. Koch, M. Gutierrez, A. Henglein. *Ber. Bunsenges. Phys. Chem.*, **1984**. 88, 649.

3. D. Battaglia, J. Li, Y. Wang, X. Peng. *Angewante Chemie International Edition*, **2003**. 42, 5035-5039.

4. D. Battaglia, B. Blackman, X. Peng. *J. Am. Chem. Soc.*, **2005**. 127, 10889-10897.

5. L. Mann, E. C. Scher, A. P. Alivisatos. *J. Am. Chem. Soc.*, **2000**. 122, 51, 12700-12706.

6. Y. Cui, U. Banin, M. T. Bjoerk, A. P. Alivisatos. *Nano Letters*, **2005**. 5, 1519-1523.

7. J. Xu, M. Xiao. *Applied Physics Letters*, **2005**. 87, 17, 173117/1 - 173117/3.

8. J. Xu, M. Xiao, D. Battaglia, X. Peng. *J. Opt. Soc. Am. B*, **2005**. 22, 5,

9. J. Xu, M. Xiao, D. Battaglia, X. Peng. *Applied Physics Letters*, **2005**. 87,

10. M. Braun, S. Link, C. Burda, M. A. El-Sayed. *Physical Review B*, **2002**. 66, 20, 205312-205317.

11. Klimov, V. I., D. W. McBranch, C. A. Leatherdale, and M. G. Bawendi. *Physical Review B: Condensed Matter and Materials Physics*, **1999**. 60, 19, 13740-13749.

12. Klimov, V. I., Ch J. Schwarz, D. W. McBranch, C. A. Leatherdale, and M. G. Bawendi. *Physical Review B: Condensed Matter and Materials Physics*, **1999**. 60, 4, R2177-R2180.

13. Klimov, Victor I. *Journal of Physical Chemistry B*, **2000**. 104, 26, 6112-6123.

14. T. Vossmeyer, L. Katsikas, M. Giersig, I. G. Popovic, K. Diesner, A. Chemseddine, A. Eychmueller, H. Weller. *Journal of Physical Chemistry*, **1994**. 98, 7665-7673.

15. R. B. Little, M. A. El-Sayed, G. W. Bryant, S. Burke. *Journal of Chemical Physics*, **2001**. 114, 4, 1813-1822.

16. M. J. Hytch, E. Snoeck, R. Kilaas. *Ultramicroscopy*, **1998**. 74, 3, 131-146.

17. G. Ade, R. Lauer. *Ultramicroscopy*, **1999**. 77, 3, 177-185.

18. A. Yeh, G. Cerullo, U. Banin, A. Mews, A. P. Alivisatos, C. V. Shank. *Physical Review B*, **1999**. 59, 7, 4973-4977.

CHAPTER 10

ORDER OF MAGNITUDE ENHANCEMENT OF LUMINESCENCE IN SILVER CAPPED CdS QUANTUM DOTS

The quantum yield of trap emission in 3 nm CdS quantum dots increases ten-fold when coated with nanometer thin layers of metallic silver. The reduction of silver on the surface of the quantum dot proceeds through reaction with thiol-functionalized ligands on the surface of the quantum dot. The maximum of enhancement is achieved after the suspension of mercaptoacetic acid capped quantum dots is allowed to react with $AgNO_3$ for 48 hours. The increase in quantum yield is coupled with an increase in the luminescence decay time.

Introduction

Semiconductor-metal interfaces are extremely important in modern electronics. Such hetero-junctions serve at the most fundamental level as Schottky diodes, and ohmic or blocking contacts. When a metal-semiconductor junction is formed, electrons flow from one material to the other until the Fermi levels of the two become equal. The band bending and direction of electron flow are determined by the relative chemical potential of the two materials. While such behavior has been understood for over 50 years, the behavior of quantum confined metal-semiconductor junctions has not been previously studied. In this work we report on the effect of a silver shell on colloidal CdS quantum dots.

In recent years semiconductor nanocrystals or quantum dots, (crystals smaller than the Bohr exciton radius) have been the subject of intense research efforts motivated by the promise of their interesting tunable optoelectronic properties in tandem with the availability of low cost colloidal synthesis methods. Early research beginning in the 1980's focused on elucidating the fundamental physics of such quantum-confined structures [1]. More recent work has built upon the knowledge elucidated in the early studies by increasing the diversity of synthetic approaches, compositions (particularly II-IV and III-V), control of size distribution and shape, surface modifications, and device development [2-4]. A particularly important development in quantum dot research was to overcoat the core crystal with another semiconductor of higher band gap as in the prototypical CdSe/ZnS core-shell system [5]. Such semiconductor-semiconductor heterostructures in general are less sensitive to environmental conditions (solvent) and exhibit significantly higher band-edge quantum yield than their organic ligand capped counterparts. The higher band gap semiconductor serves to greatly reduce leakage of the core quantum dot wavefunction into the environment by passivation of surface states and protection from quenching molecules in the environment.

While most efforts at improving the performance of quantum dots has focused on achieving a high quantum efficiency of band gap emission, little attention has been paid to the enhancement of trap emission. Trap luminescence if more often viewed as a defect in the nanocrystals performance and efforts such as the over-coating of CdSe quantum dots with ZnS is aimed at reducing the trap luminescence and increasing the band-gap luminescence. However, the broad emission of trap luminescence (100-150 nm) [6, 7] makes it a nearly ideal for applications in tunable light sources. The problem is that trap

emission is typically much weaker than band-edge emission, even for poorly passivated surfaces and smaller clusters that show trap emission exclusively [8].

We will report the observation of considerable enhancement of the trap emission from CdS quantum dots that are over-coated with metallic silver. Observations of up to ten-fold trap emission enhancement are discussed in terms of radiative and non-radiative factors affecting the trap luminescence.

Experimental Section

Materials

The following chemicals were purchased from Sigma-Aldrich (Milwaukee, WI): Oleic acid (OA), octadecene (ODE), anhydrous methanol, chloroform, cadmium oxide (99.99%), sulfur (99.9%), selenium (99+%), silver nitrate, HEPES buffer, and mercaptoacetic acid.

Synthesis of CdS Quantum Dots

Reactions took place in a three-neck flask, heated and stirred by a heating mantle. Cadmium sulfide core crystals were synthesized by decomposition of organometallic precursors in a non-coordinating solvent [9]. A solution of 1 mmol CdO, 400 μL oleic acid and 4 ml ODE was heated to 300°C, at which point 0.4 mmol sulfur dissolved in 0.6 mL ODE was injected into the rapidly stirred solution. The temperature was reduced to 250°C and held constant for 5 minutes after which the solution was allowed to cool.

Purification was accomplished by extracting free oleic acid and un-reacted Cd precursor with methanol. Ligand exchange was accomplished by addition of chloroform and mercaptoacetic acid (MAA) [10]. Nanocrystals fall out of suspension after several minutes in the solution. Isolation of MAA capped CdS crystals were accomplished by centrifugation. The crystals were then washed twice in chloroform to remove free MAA, collected by centrifugation, washed in methanol, and re-dispersed in a quantity of de-ionized water equal to the volume of the initial synthesis product.

Growth of CdS@Ag heterostructures

Samples were prepared by mixing 100 μL of MAA-capped CdS solution and various amounts (5-20 μL) of silver nitrate solution (2 mmol) in a sufficient volume of HEPES buffer (**M) to make 3 mL of solution. Observing the change in deep-trap emission as a function of time using steady state photoluminescence monitored the growth of the capping layer of silver. The samples were stirred continuously during the experiments to ensure efficient mixing and to encourage homogenous growth. Absorption measurements were made before and after silver growth.

Results

The CdS quantum dots are initially dispersed in organic solvent with oleic acid as a capping material. In order to reduce silver salts onto the nanocrystals, they had to be re-dispersed in water using thiol-functionalized capping ligands. This procedure alone changes the luminescence properties of the quantum dots, as shown in Figure 10.1. The

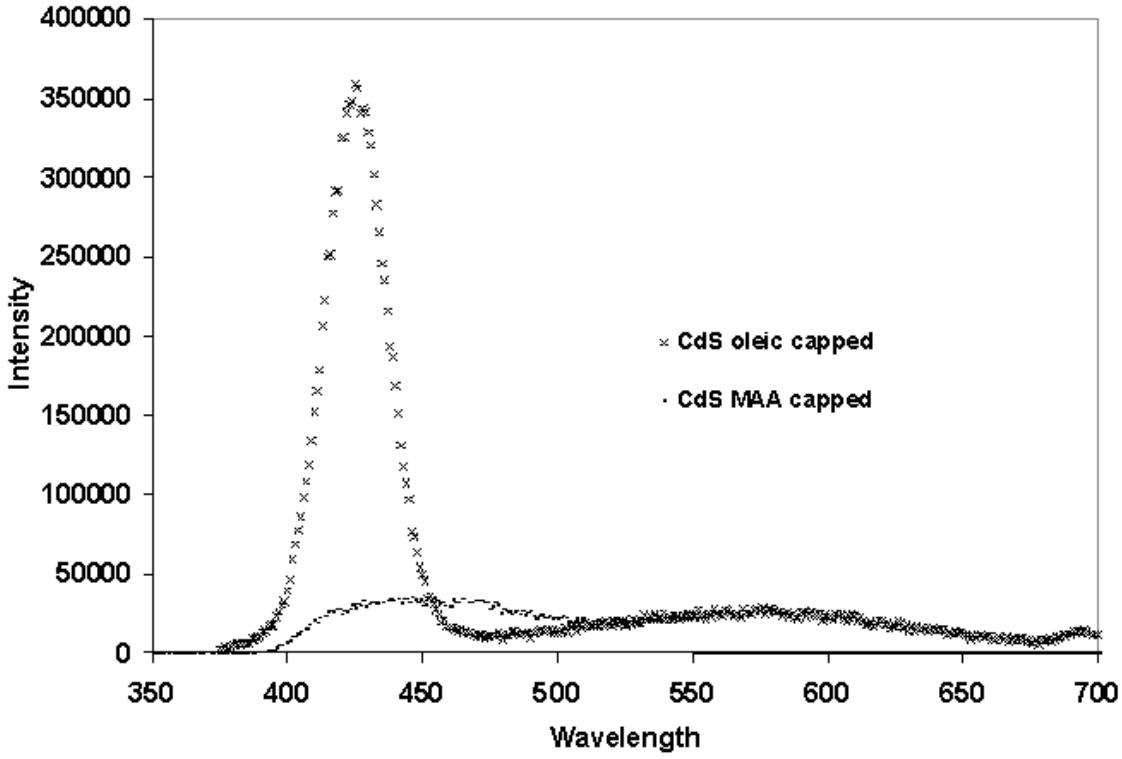

Figure 10.1. Photoluminescence of as-synthesized oleic acid capped CdS crystallites compared to the PL of water-soluble mercaptoacetic acid capped crystals. The ligand exchange results in a large decrease in band edge luminescence while trap emission intensity is unchanged.

emission spectrum of the oleic acid capped sample shows a strong band-edge emission, while in the mercaptoacetic acid (MAA) capped sample, the band-edge emission is quenched and only the residual trap emission remains. The deposition of silver onto the surface of these water soluble, MAA capped quantum dots selectively enhances this trap emission.

The effects of a silver monolayer on CdS nanocrystals were explored by monitoring the change in steady state fluorescence and absorption as well as fluorescence lifetime, and high resolution TEM. The growth of the Ag capping layer was observed by measuring the increase in trap fluorescence intensity as a function of time as shown in

Figure 10.2. Baseline fluorescence intensity from MAA-capped CdS was established prior to injection of $AgNO_3$. The $AgNO_3$ quantity was calculated to produce 1-2 monolayers of Ag on the CdS crystallites. Figure 10.2 demonstrates that upon injection of 25 nmol $AgNO_3$ an exponentially decreasing enhancement rate is observed which reaches a plateau of approximately 3x fluorescence enhancement after 15 minutes incubation time.

The mechanism of silver reduction was explored by closing the fluorimeter shutter repeatedly following a 40 nmol $AgNO_3$ injection to determine if the 350 nm excitation light used for these experiments affected the luminescence enhancement rate. Initially it was believed that the reduction process was photochemical, and doing the experiment with intermittent light exposure would therefore affect the growth kinetics. The inset of Figure 10.2 shows that enhancement is not dependent upon the excitation light as the enhancement curve follows a similar exponentially decreasing rate in the absence of light as observed in the presence of light. This observation strongly indicates that the reduction of Ag^+ ions is due to the displacement of the mercaptoacetic acid ligands and subsequent oxidation-reduction reaction, rather than a photochemical reduction process.

In order to determine if the enhancement of the trap emission was limited by Ag^+ concentration, three smaller injections of 15 nmols each were introduced as shown in Figure 10.3. It is clearly seen that immediately following each injection, a new increase in emission (due to enhancement) is observed. The magnitude of the intensity change decreases from the first injection to the third, which seems to indicate that fluorescence enhancement is directly related to the total amount of Ag added and proportional to the

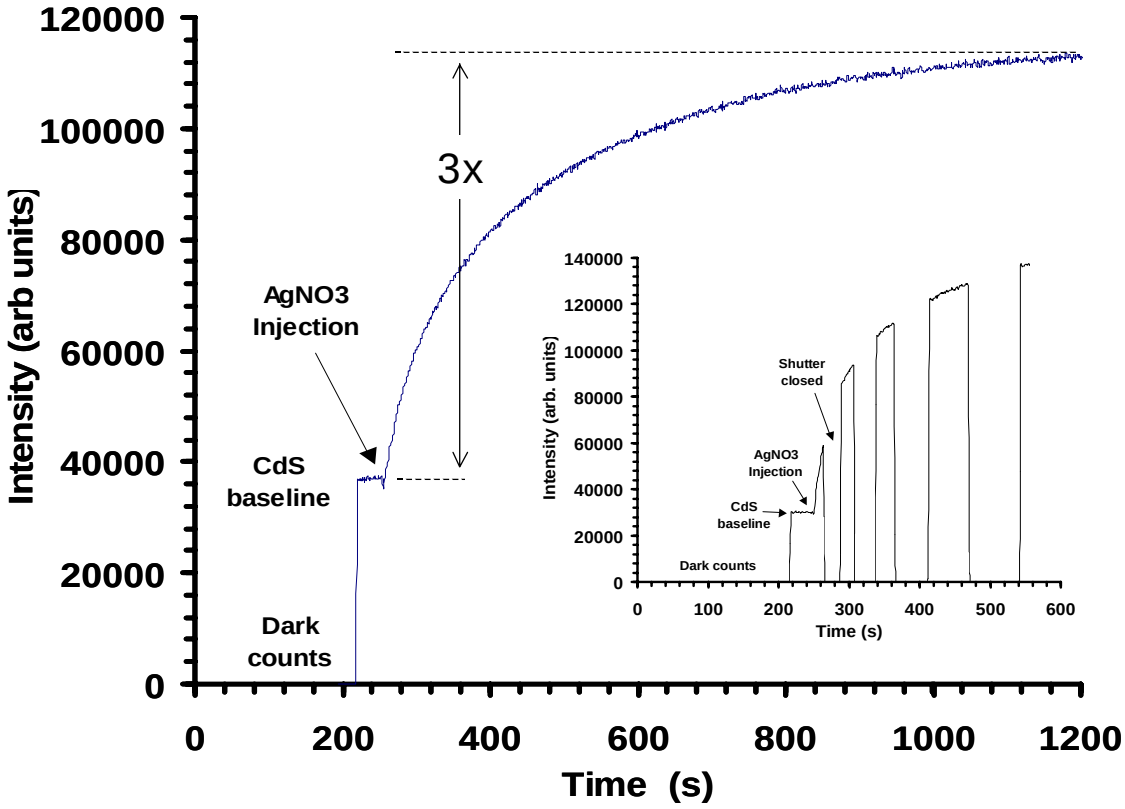

Figure 10.2. Luminescence intensity monitored during the growth of an Ag monolayer on water soluble, mercaptoacetic acid capped CdS quantum dots (3.9 nm average diameter). Emission was monitored near the peak of trap emission. The enhancement rate decreases nearly exponentially, reaching a plateau after 20 minutes. Inset: luminescence intensity at the peak of deep trap emission monitored as a function of time with the excitation shutter opened and closed repeatedly to demonstrate that silver growth and the associated enhancement is not dependent upon illumination.

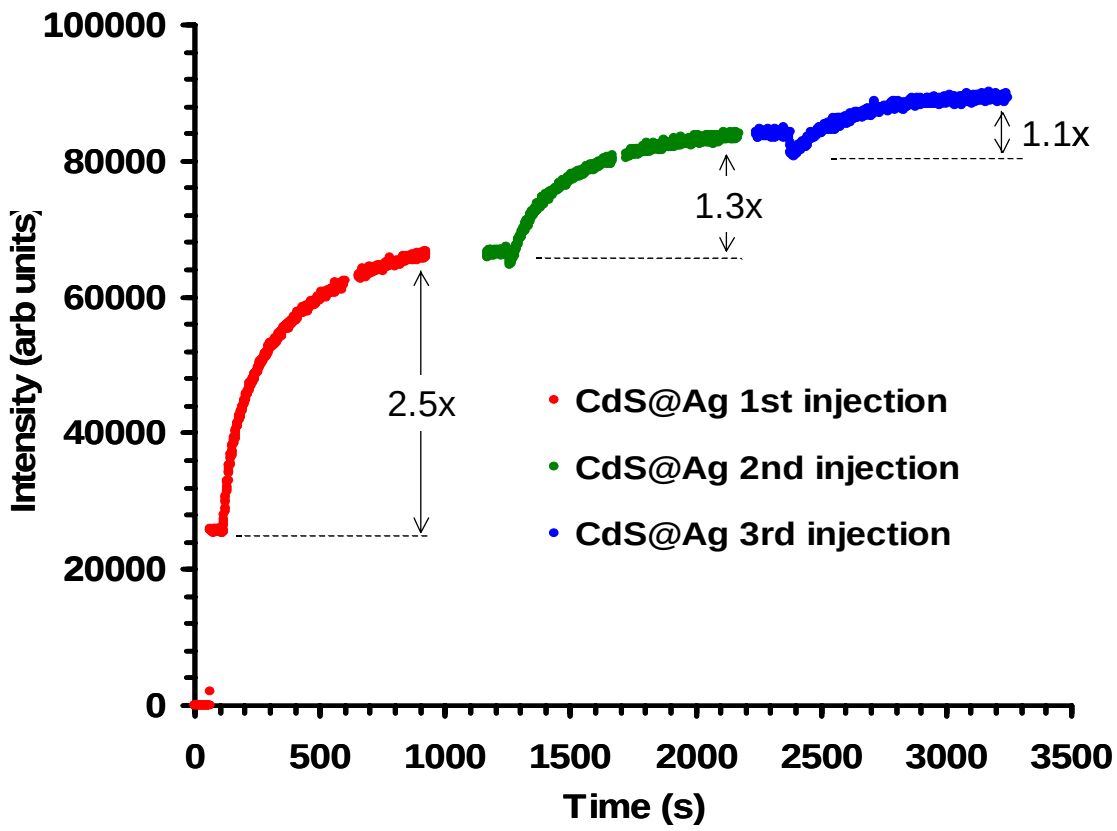

Figure 10.3. Luminescence intensity monitored as a function of time. Three $AgNO_3$ injections of 7.5 μL each were introduced at different times that caused an exponentially decreasing enhancement rate to occur. The magnitude of the emission intensity increase dropped from 2.5x to 1.3x to 1.1x with successive Ag^+ additions.

surface coverage of Ag on the CdS nanocrystals. Furthermore, once a complete monolayer has been formed, significant additional enhancement is not achieved by thickening the silver layer. In fact it was observed that injection of 100 mmol $AgNO_3$ under the same conditions yields similar initial enhancement at first but leads to visible aggregation and quenching of fluorescence within days, whereas samples with 1-2 ML of Ag remain stable in solution for at least several weeks.

Figure 10.4 shows the evolution of the trap emission spectrum as a function of time following injection of silver ion. While significant increases in trap emission yield can be observed on short growth time scales (minute), the full development of the emission does not occur until 48 hours later. This phenomenon may have to do with an annealing process and stabilization of the Ag/quantum dot interface with time, as will be explored in the discussion to follow.

HRTEM images were collected of the crystallites after incubation with $AgNO_3$ in order to determine the morphology of Ag growth. Figure 10.5 shows a high-resolution image of the crystals that appear as dark spots due to contrast or as well-defined lattice fringe images depending upon the orientation of the individual crystallites with respect to the beam. We were not able to observe any discrete silver particles nor were we able to distinguish diffraction spots corresponding to Ag planes in the Fourier transforms of the HRTEM images. These observations are consistent with Ag growth localized only to the surface of crystallites and limited to 1-2 monolayers. Such thin layers would not be expected to produce resolvable lattice fringe.

Photoluminescence Decay Times

Photoluminescence decay times of Ag coated and bare CdS nanocrystals were measured using time resolved PL spectroscopy. Emission was monitored at the peak of the steady state emission (600 nm) with 337 nm light pulses used as the excitation (N_2 laser). The PL decay time increases dramatically with Ag coating as seen in the Figure

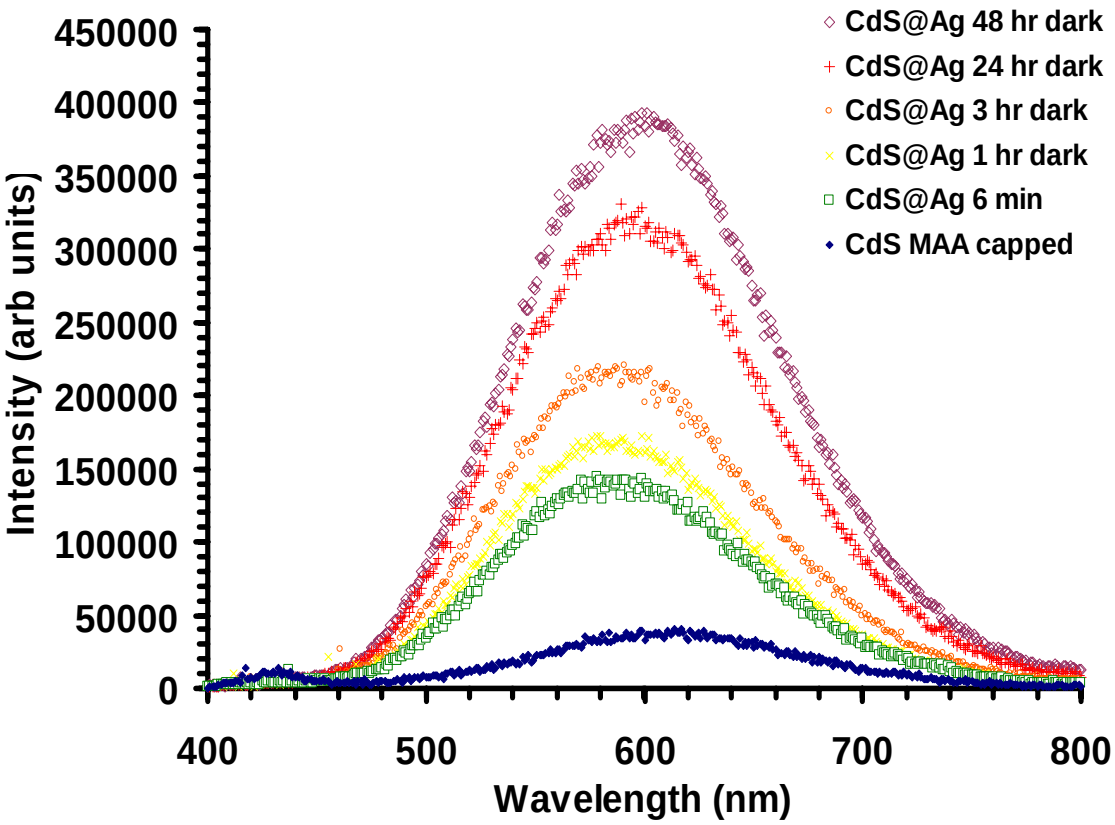

Figure 10.4. Steady-state luminescence of water soluble, mercaptoacetic acid capped CdS nanocrystals after aging in darkness for several time periods.

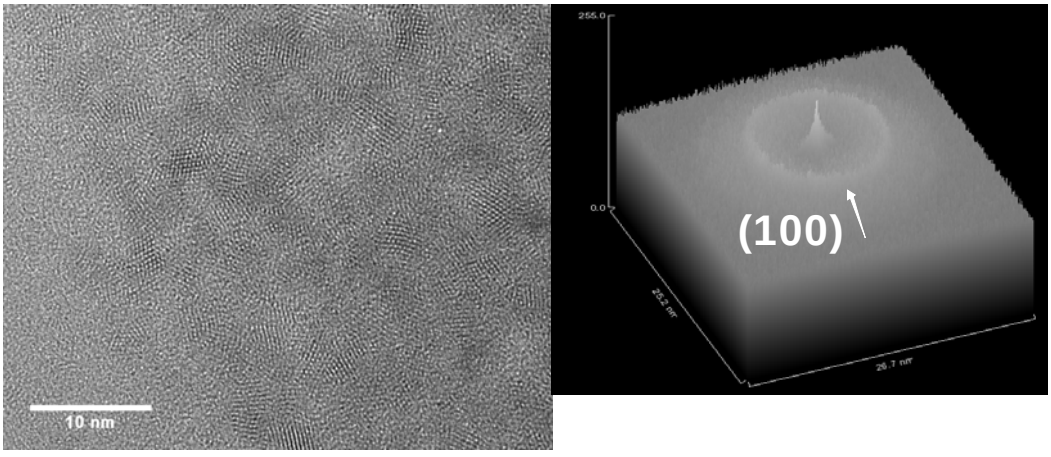

FFT shows diffraction ring corresponding To (100) planes in wurtzite CdS

Figure 10.5. High resolution TEM shows CdS crystallites after growth of an Ag monolayer. The Fourier transform shows a diffraction ring that corresponds to the (100) planes of wurtzite CdS.

10.6. The decay traces in the main frame are plotted on a log scale in order to ease visualization of the difference in decay times. The decay times will be considered here as time needed to decrease intensity to $1/100^{th}$ of its original value (i.e $t_{1/100}$). The PL decay time is multi-exponential and extends as long as 1400 ns in Ag coated CdS nanocrystals. Figure 10.6 demonstrates that luminescence decay in the Ag coated sample is about 2.3 times slower than the uncoated CdS sample.

Discussion

Enhancement Mechanisms

We have shown that a monolayer of Ag on water-soluble CdS quantum dots results in an increase in luminescence quantum yield and luminescence decay time of trap emission. The nature of this luminescence enhancement is presumably due to interaction of the silver layer with trap states localized on the surface of the CdS crystallites. There are numerous possibilities that could explain the observed enhancement. One of these is that the silver acts as a capping layer that isolates the CdS surface from quenching molecules (H_2O and O_2). Another possibility is that the Ag monolayer could increase the intrinsic population of radiative trap sites by inhibiting de-trapping of charge carriers back into the band gap states. The effect of Ag could be to enhance the radiative rate of the trap emitters through electric field mediated mechanisms. Finally, the silver shell could introduce new traps with radiative probabilities higher than the original traps.

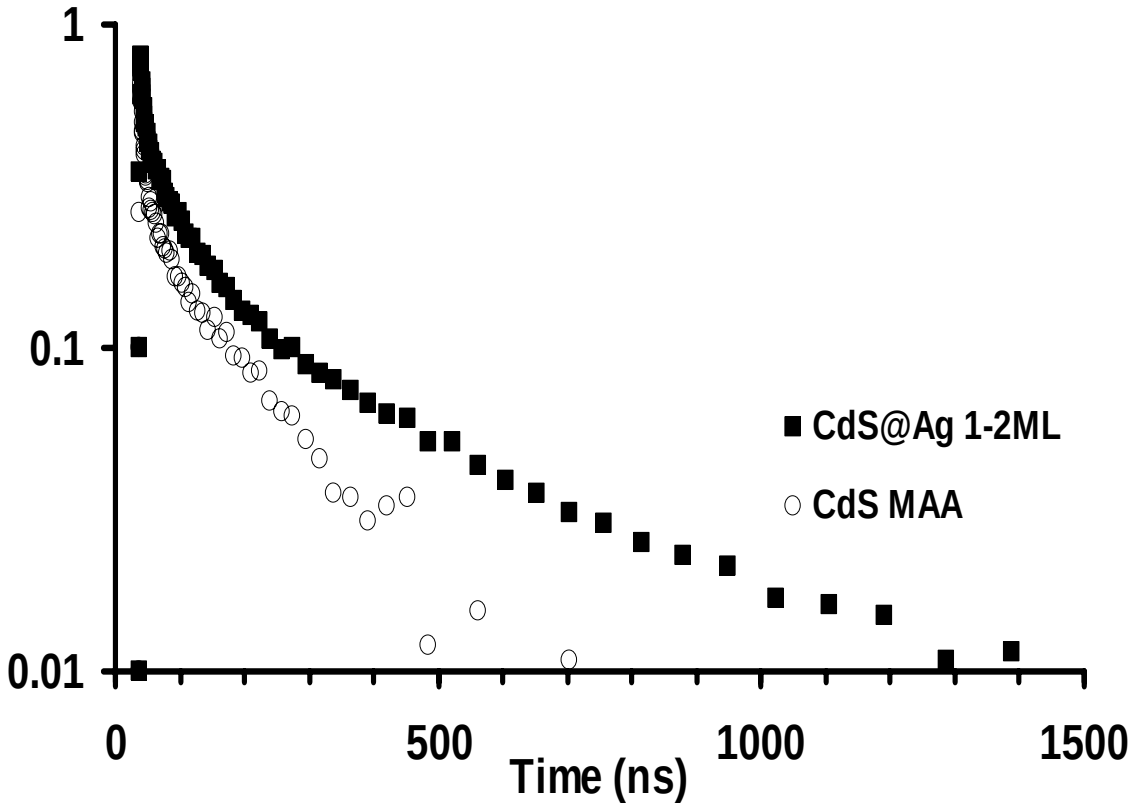

Figure 10.6. Luminescence lifetime data collected for Ag capped and mercaptoacetic acid capped CdS crystallites are plotted. Multi-exponential behavior is observed for both samples. The data shows that the fast component of the Ag capped sample is 2.3 times slower than that of the MAA capped sample.

The role of an Ag monolayer as an isolating shell from quenching molecules can be considered by looking at the nature of the CdS nanocrystal surface before growth of the Ag monolayer. Figure 10.1 shows that both band-gap and trap emission is present in the as-synthesized oleic acid capped samples. The narrow band-gap fluorescence peak, along with the results of TEM seen in Figure 10.5 indicates a monodisperse sample of CdS crystallites. Excitation spectra collected while monitoring emission across the broad trap emission band at 450 nm, 600 nm, and 750 nm yielded identical spectra. This indicates that the broad trap emission originates from a heterogeneous population of traps

within a reasonably homogeneous population of crystallites. This is also observed after the ligand exchange procedure and demonstrates that the monodispersity of the starting sample is not lost when the oleic acid capped nanocrystals are transferred to water. Though most of the intrinsic properties of the CdS nanocrystals remain unchanged, ligand exchange and re-dispersion in aqueous buffer quenches band edge luminescence intensity almost completely, as demonstrated in Figure 10.1. However, the ligand exchange and re-dispersion does not affect the intensity of the trap emission. This seems to indicate that the trap emitters are insensitive to quenching expected by exposure to aqueous solution and potential loss of capping ligands though the ligand exchange procedure. It follows from this observation that the luminescence enhancement seen with monolayer Ag coverage may involve silver playing an active role in suppressing intrinsic non-radiative relaxation mechanisms or enhancing the radiative rate of trap emitters as opposed to simply acting as a passive barrier between aqueous solution/quenchers and the crystallite surfaces.

Spectral Shifts

The time evolution of the trap emission enhancement is accompanied by readily observed shifts in the emission band position (Figure 10.4). During the first 6 minutes of silver growth, the enhancement of trap emission is accompanied by a blue shift in the emission peak from 605 nm to 575 nm. With increased time the additional enhancement is then accompanied by a red shift in the emission peak that after 48 hours reaches 590 nm, close to the initial band maximum at 605 nm. All luminescence changes occur without any change in the absorption spectrum, so no change in the electronic structure

of the nanocrystal is responsible for the shifts seen in the trap emission. Trap emission has commonly been characterized in terms of “deep” and “shallow” traps, depending on the energy of the trap states relative to the band edge of the nanocrystal, i.e. deep traps lower in energy than shallow traps. Given the very broad trap emission observed in our experiments, it is not unreasonable to assume that the emission band is a composition of shallow and deep trap emission bands. The blue shift of the spectrum that is observed during the first stages of Ag growth may then be characterized by preferential enhancement of shallow trap emitters relative to deep trap emitters. At later stages of the Ag growth, the enhancement of the deeper trap emission “catches up” with the shallow trap enhancement, resulting in an apparent shift of the spectrum back to lower energy. The differences in the emitting states of CdS nanocrystals are not only characterized by energy, but also by the associated wavefunctions. It is known that band edge states are delocalized over the bulk of the nanocrystal whereas deep traps are localized at specific surface sites (dangling bonds, unpassivated atoms) [11]. In between these extremes, shallow traps are semi-localized states. Since shallow traps are less localized than deep traps, the initial stages in the growth of the silver layer may roughly passivate large surface areas of the nanocrystal, affecting these states most strongly that would account for the blue shift of the PL enhancement. As the CdS@Ag interface anneals with increasing time to configurations with fewer defects and increasing stability, the relative enhancement of the localized deep trap states may increase which would account for the observed red shift.

Effects of Ag shell on the luminescence decay times and quantum yield

In temperature-dependent luminescence decay time studies on CdS nanoparticles without Ag shells, it has previously been suggested that the fast component of the PL decay time for trap emission is due to de-trapping of charge carriers away from the traps and into band edge states [6]. This de-trapping process serves as an intrinsic non-radiative mechanism for depopulation of trap states and suppression of the trap emission. If de-trapping was effectively depopulating the trap states, it is expected that the luminescence decay times would be faster than the intrinsic radiative lifetime. For CdS crystals coated with a monolayer of Ag, the decay time is longer (Figure 10.6) than the corresponding decay time for uncoated CdS. The longer PL decay time for silver capped samples suggests that the silver layer may be inhibiting the de-trapping mechanism, but perhaps not to a large enough extent to fully explain the 10x increase in trap emission quantum yield for the Ag coated nanocrystals. The decay time increases only by a factor of 2.3. If the increase in steady-state luminescence was solely due to suppression of de-trapping and other non-radiative sources of relaxation, the decay time should increase by a full factor of 10. This observation indicates that either the radiative lifetime decreases (due to radiative enhancement) or that the Ag shell introduces new trap sites altogether with higher radiative probability than the original sites.

Let us now calculate the enhancement of the radiative probability assuming the first enhancement mechanism: the Ag layer inhibits the non-radiative quenching and increases the radiative rate of the original trap sites. The quantum yield for luminescence can be expressed in terms of the rate of radiative and non-radiative relaxation by the following simple equation

$$QY = \frac{k_{rad}}{k_{rad} + k_{non-rad}} = \frac{k_{rad}}{k_{obs}} = k_{rad}\tau_{PL} \qquad (10.1)$$

where k_{rad} and $k_{non\text{-}rad}$ are the rates (s^{-1}) of radiative and non-radiative relaxation from the emitting state, respectively. The sum of these rates is equal to the overall observed luminescence rate k_{obs} - which is simply the inverse of the luminescence lifetime. The increase in quantum yield may either be due to an increase in the radiative rate or a decrease in the non-radiative rate. Our luminescence decay time results show that the lifetime increase, suggesting a decrease in the non-radiative rate. However, this increase in lifetime τ_{PL} only accounts for a factor of 2.3 in the increase in QY, the remaining factor of 4.3 must come from increase in the radiative rate. The addition of the Ag layer must increase the radiative probability by 4.3. Other reports have shown significant enhancement of luminescence of dye molecules imbedded on silver islands on glass substrates [12, 13] which was explained in terms of field enhancement from the intense surface plasmon of the silver islands. The increase in quantum yield was accompanied by a corresponding decrease in the PL lifetime, consistent with a model of radiative enhancement. For the case of thin 1-2 monolayer silver shells grown on CdS, it is impossible to consider plasmon field enhancement since the particle size is too small to support a plasmon resonance in the spectral region of the trap emission.

At this point it is difficult to assign a mechanism of the radiative enhancement in Ag capped CdS quantum dots, however our results show that such enhancement is necessary to account for the observed order-of-magnitude increase in quantum yield. Of course if one considers the second mechanism, which proposes that the presence of the Ag shell introduces entirely new interfacial trap sites with different radiative and non-

radiative properties, the enhanced emission should not be compared to the original emission.

References

1. R. Rossetti, R. Hull, J. M. Gibson, L. E. Brus. *Journal of Physical Chemistry*, **1985**. 82, 1, 552-559.
2. Yu, W. William and Xiaogang Peng. *Angewandte Chemie, International Edition*, **2002**. 41, 13, 2368-2371.
3. Battaglia, David, Jack J. Li, Yunjun Wang, and Xiaogang Peng. *Angewandte Chemie, International Edition*, **2003**. 42, 41, 5035-5039.
4. R. Xie, U. Kolb, J. Li, T. Basche, A. Mews. *Journal of the American Chemical Society*, **2005**. 127, 20, 7480-7488.
5. M. A. Hines, P. Guyot-Sionnest. *J. Phys. Chem.*, **1996**. 100, 468-471.
6. A. Eychmueller, A. Haesselbarth, L. Katsikas, H. Weller. *Ber. Bunsenges. Phys. Chem.*, **1991**. 95, 1, 79-84.
7. B. S. Zou, R. B. Little, J. P. Wang, M. A. El-Sayed. *International Journal of Quantum Chemistry*, **1999**. 72, 439-450.
8. C. Landes, M. Braun, M. A. El-Sayed. *J. Phys. Chem. B*, **2001**. 105, 10554.
9. W. Yu, L. Qu, W. Guo, X. Peng. *Chem. Materials*, **2003**. 15, 2854-2860.
10. W. C. Chan, S. Nie. *Science*, **1998**. 281, 5385, 2016-8.
11. Y. Wang, N. Herron. *J. Phys. Chem.*, **1991**. 95, 525-532.

12. J. Lukomska, J. Malicka, I. Gryczynski, J. R. Lakowicz. *Journal of Fluorescence*, **2004**. 14, 4, 417-423.

13. K. Aslan, Z. Leonenko, J. R. Lakowicz, C. D. Geddes. *Journal of Fluorescence*, **2005**. 15, 5, 643-654.

APPENDICES

Appendix 1 – LabVIEW Program Documentation

Appendix 2 – Exponential Data Fitting Spreadsheet Documentation

APPENDIX 1

LABVIEW PROGRAM DOCUMENTATION

Signal Scan 4.0 LabVIEW™ VI

by

Alexander W. Schill

alexanderschill4@comcast.net

Signal Scan 4.0 is a LabVIEW™ VI (Virtual Instrument) designed to integrate and control the operation of a kilohertz Ti:sapphire laser based femtosecond spectroscopy system using the lock-in technique. Signal Scan 4.0 allows the user to control the data collection parameters in order to obtain a single diagnostic kinetic trace. For accumulation of several traces for statistical analysis, the user is recommended to use the Accumulate 5.4 VI. Page references are with respect to the first page of documentation (this page).

Principles of operation

Signal Scan 4.0 performs the following functions:

-advances the delay line in user designated increments

-records the position of the delay line

-converts the delay line position to time in picoseconds

-records the signal from the lock-in amplifier

-records the phase of the signal from the lock-in

-calculates the transient absorption from the lock-in signal

-plots the transient absorption versus time

-plots phase versus time

-manipulates lock-in parameters such as sensitivity and integration time

-returns the delay line to start after the trace is complete

-writes text files of the signal vs. time and phase vs. time traces

The Front Panel

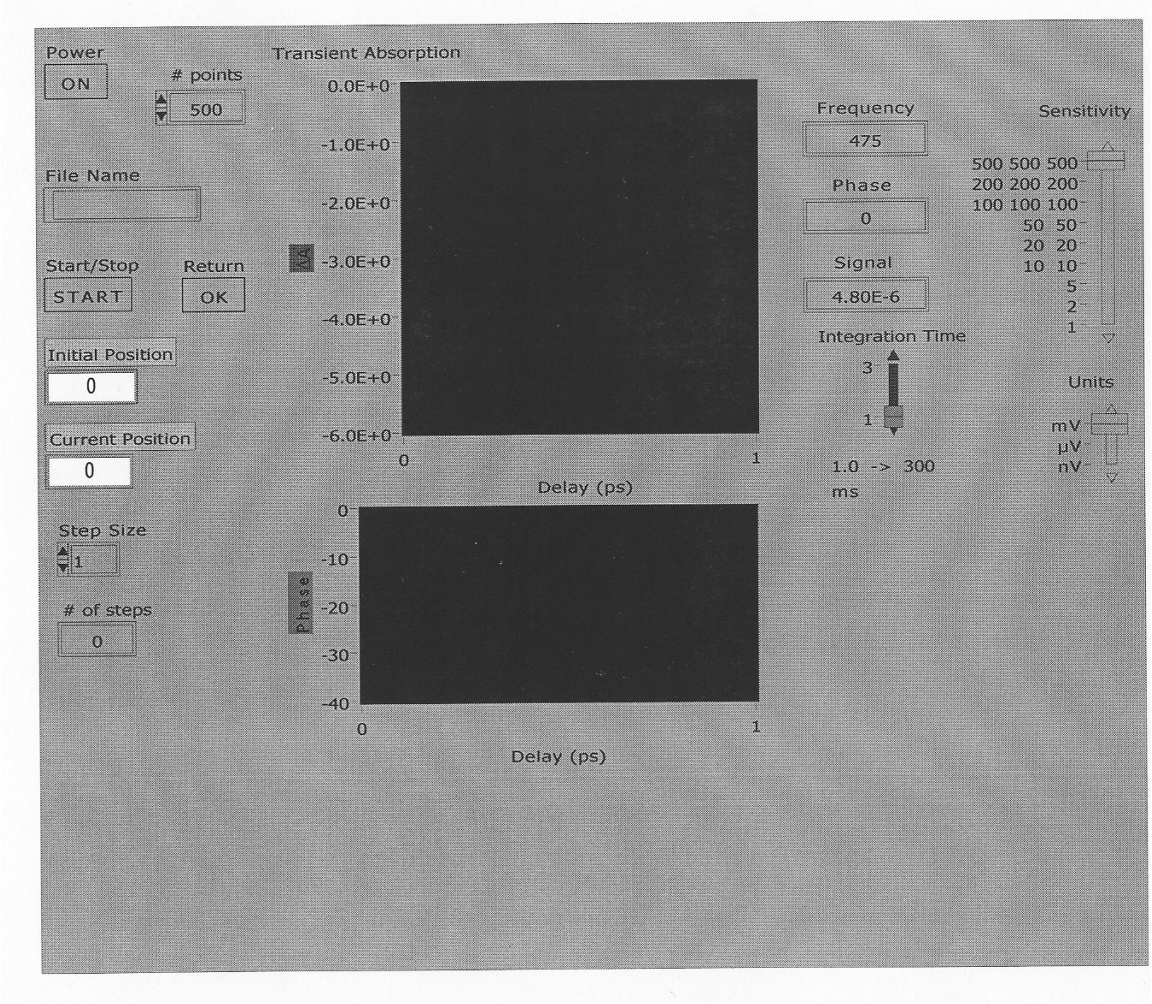

The following controls and indicators are found on the front panel of Signal Scan 4.1:

Power button: must be in the “ON” position for the program to work. Stop the program by switching the power to “OFF”.

points control: determines the number of data points displayed simultaneously on the screen.

File Name input: here the user types the file name he wishes to use. If the file name is not changed between scans, the data collected will append to the file. (i.e. the file will not be overwritten)

Start/Stop button: starts and stops the advancement of the delay line.

Return button: sends the delay line back to the initial position from which it started.

Initial position indicator: displays the initial position of the delay line in steps.

Current position indicator: displays the current position of the delay line in steps.

Step size control: here the user may set the size of step he would like to use for the collection. This value can be changed during a run by simply stopping the delay line (via the STOP button), adjusting the step size and then hitting the START button.

# of steps indicator: displays the number of steps taken for given step size. Note that this is not the total number of steps. The user should note the number of steps taken at each step size to determine input parameters for Accumulate 5.3.

Transient absorption XY graph: displays the transient absorption versus time kinetic trace.

Phase XY graph: displays the phase of the lock-in signal versus time.

Frequency indicator: indicates the frequency in Hz of the locked-in waveform being analyzed by the lock-in amplifier.

Phase indicator: indicates the phase of the locked-in waveform.

Signal indicator: indicates the amplitude of the locked-in waveform in volts.

Integration Time control: allows selection of two integration times indicated by the key below the slider.

Sensitivity control: sets the sensitivity of the lock-in amplifier.

Units control: sets the units of sensitivity setting for the lock-in.

The Block Diagram

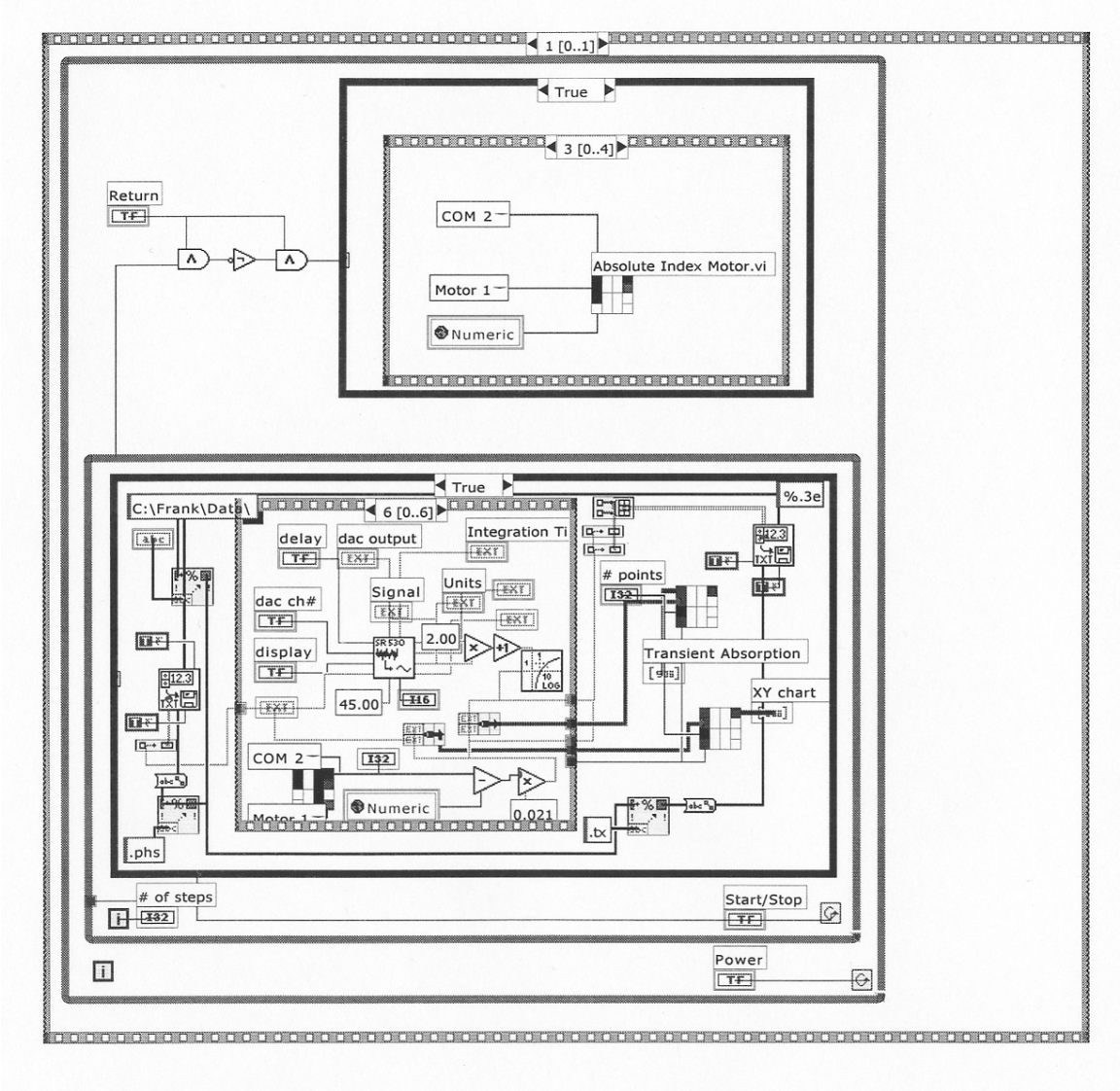

The block diagram determines the function of the VI in LabVIEW™. The symbols and structures in the diagram are compiled into code for execution of the program. The outermost structure is a sequence structure that executes a series of commands in order, one after another. In particular, this structure performs the duties of first recording the initial delay line position (pages 11-12) and then executing the delay line advancement and data recording procedures (frame 1, shown above). Within the sequence structure, but surrounding the remaining parts of the block diagram is a WHILE loop controlled by the power button. The loop continues as long as the power button is in the “ON’ position. The next two structures are a CASE structure and a WHILE loop controlled by the START/STOP button. Within the CASE structure is a sequence structure that controls return of the delay line to the initial position (page 7). The delay line will only return if the START/STOP button and the RETURN button are both pressed. Within the WHILE loop is a CASE structure that either advances the delay line (True) or does nothing (False), depending on the status of the START/STOP button. The sequence for the advancement of the delay line and recording of data is shown on page 9. The two innermost sequence structures are frames 6 and 2 from the sequences responsible for advancing the delay line (right) and returning the delay line to the initial position (left), respectively. Frame 6 controls reading data from the lock-in amplifier, converting the signal to a transient absorbance, reading the delay line position, converting the delay line position to a time in picoseconds and bundling the data for display on the graphs.

Frame 2 sets the speed of the delay line for its return trip and enables a backlash correction for more accurate repositioning of the delay line.

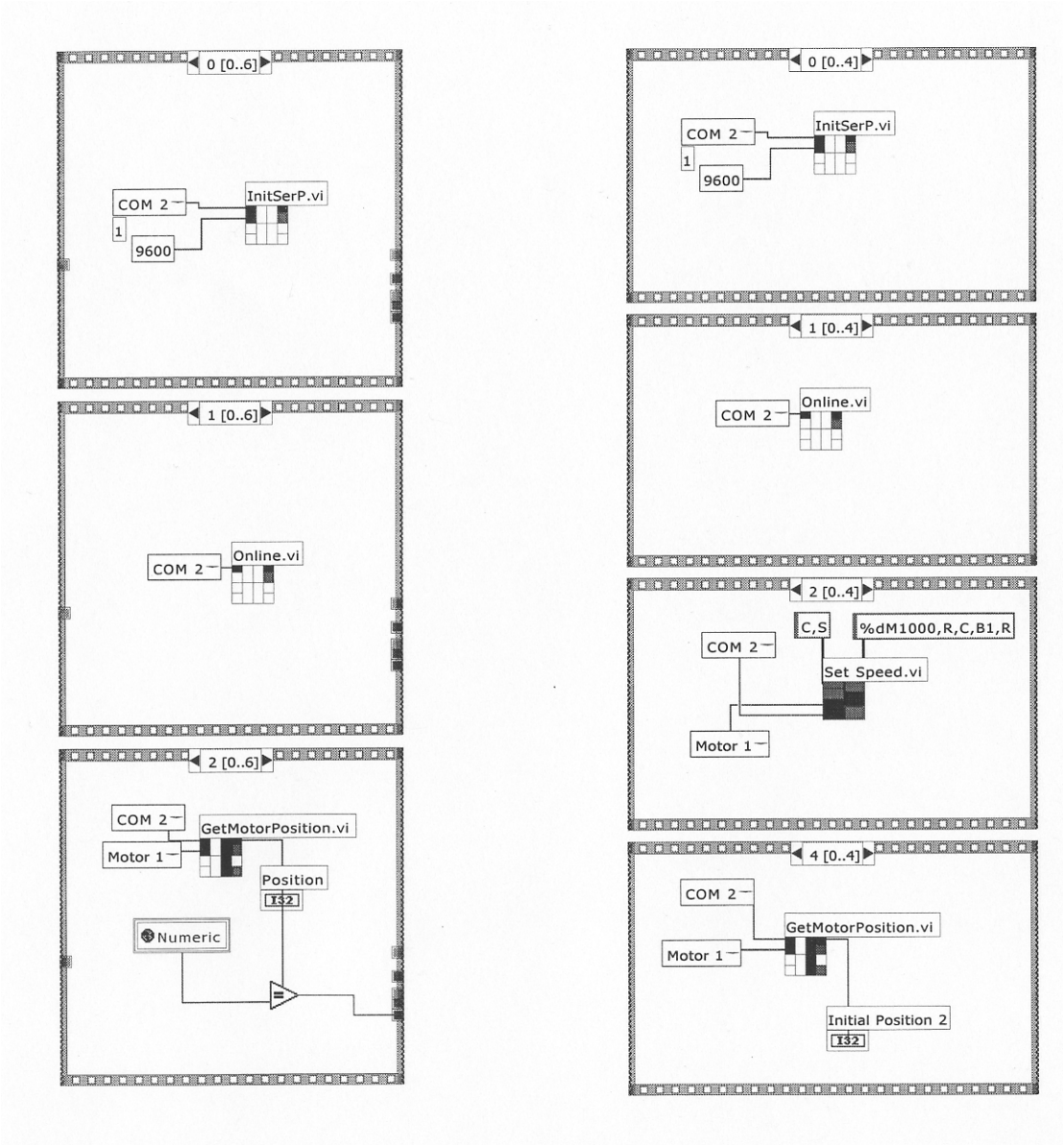

The sequence structures on the above right are frames 0,1, 2 and 4 of the return delay line sequence. The frame 0 opens communication between the computer and the delay line. Frame 1 brings the delay line online to receive

commands. The Frame 2 indexes the motor to the recorded initial position that is stored as a global variable “Numeric”. Frame 4 acquires the position of the delay line after it has returned.

The sequence structures on the above left are frames 0, 1 and 2 of the six frames making up the sequence for advancing the delay line and recording data. The first two frames (0 and 1) are identical to the frames 0 and 1 described for the return delay line sequence. Frame 2 acquires the delay line position and compares it to the initial delay line position.

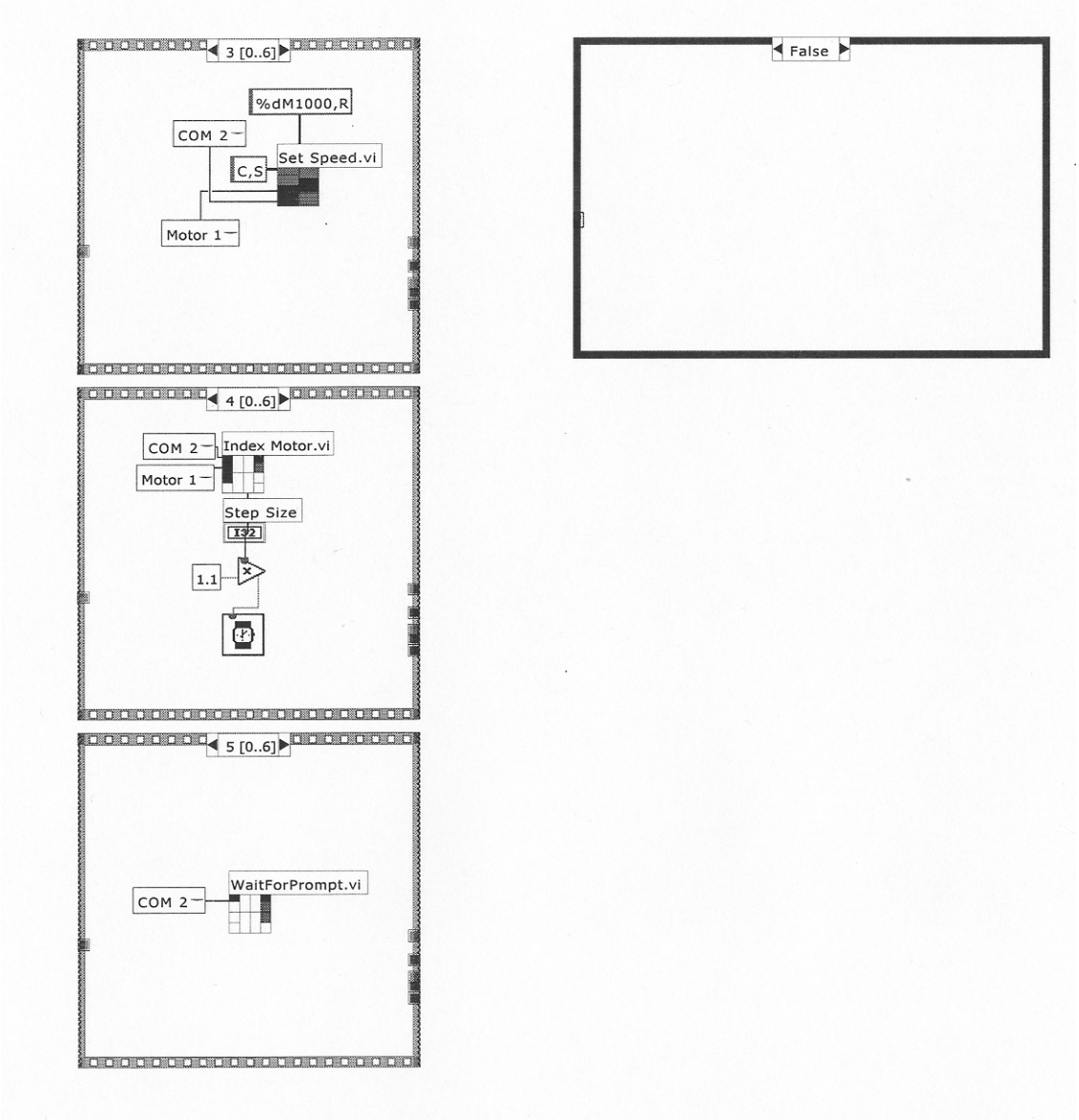

The sequence structures shown here are frames 3, 4 and 5 of the six frames making up the sequence for advancing the delay line and recording data. Frame 3 sets the speed of the motor to 1000 steps/second. Frame 4 advances the delay line by a given step size and waits 110% of the time it takes the delay line to move before proceeding to the next frame. This ensures that the delay line has stopped before any further movement is initiated. Frame 5 is a “wait for

prompt" command that prevents the delay line from performing any actions before it receives an OK from the delay line motor controller.

The case structure on the above right is the complementary CASE to the sequence that returns the delay line to the initial position. Unless the START/STOP button is in the STOP position and the RETURN button is pressed, this frame is accessed and nothing is done (the delay line does not return).

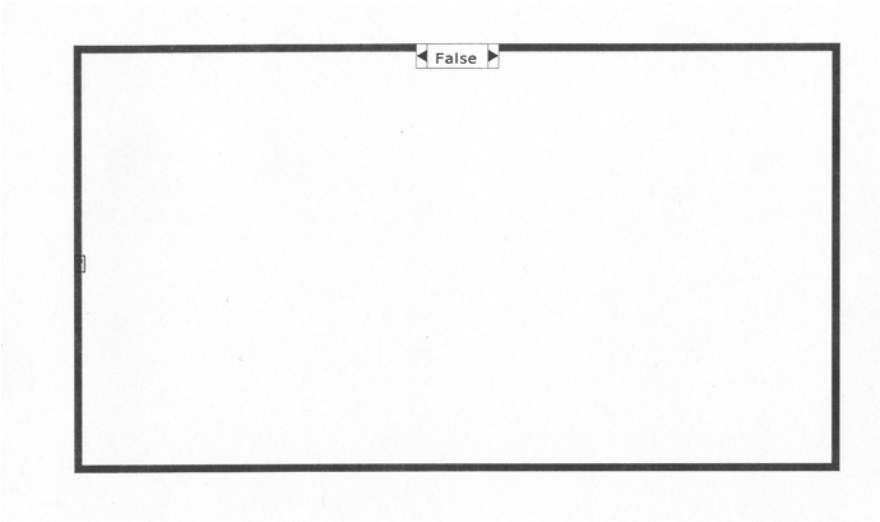

The only structure seen here is the complementary CASE structure to the advance delay line and record data sequence. This frame is accessed when the START/STOP button is in the STOP position and the program does nothing.

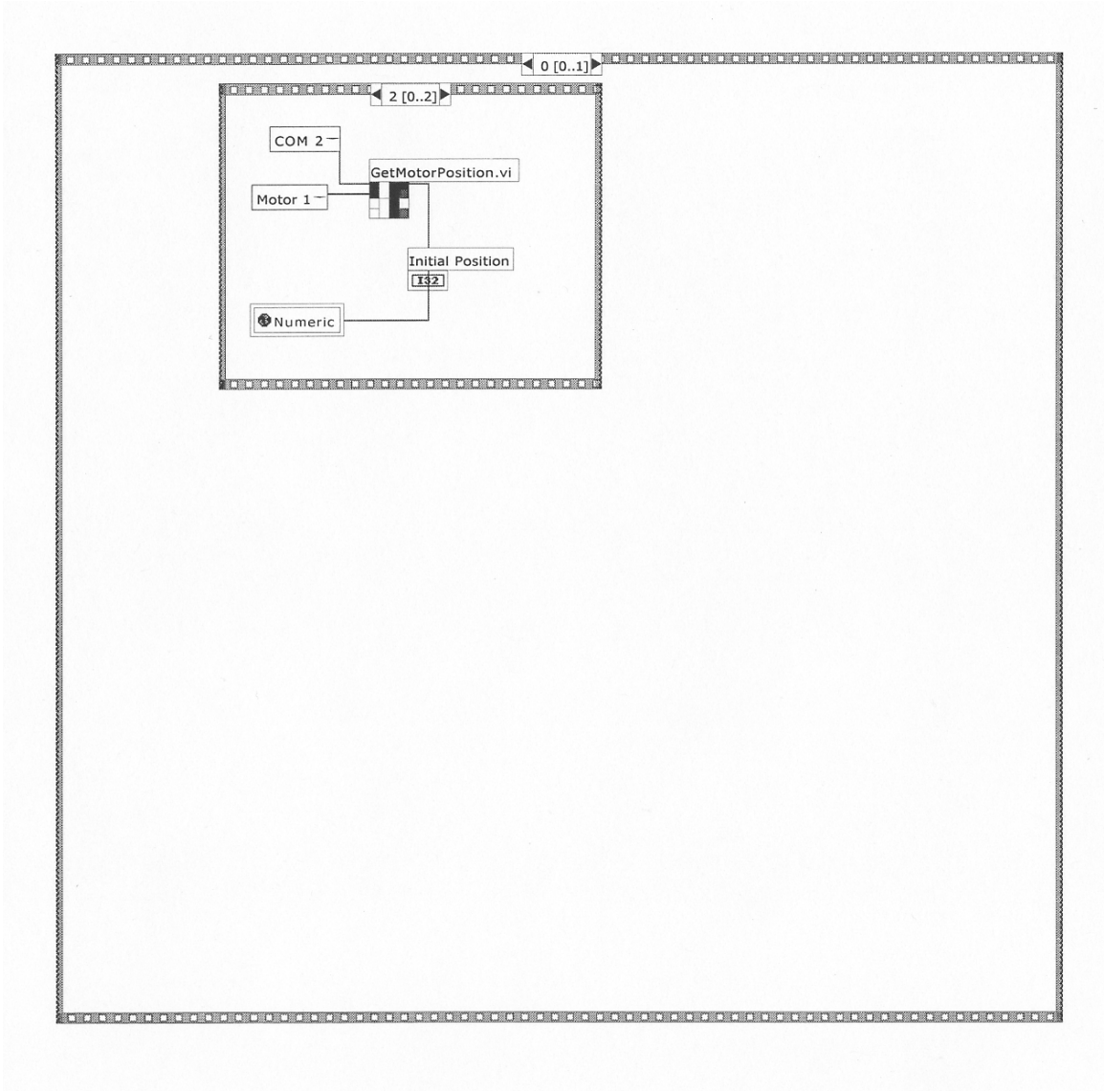

The outer sequence structure shown corresponds to the outer most frame of the block diagram on page 5. This frame is the first step performed by the program and contains a sequence that acquires the initial delay line position and stores it as a global variable. The sequence structure within this frame is frame 2 of the sequence that acquires the initial delay line position. Frames 0 and 1 of this sequence are found on page 12.

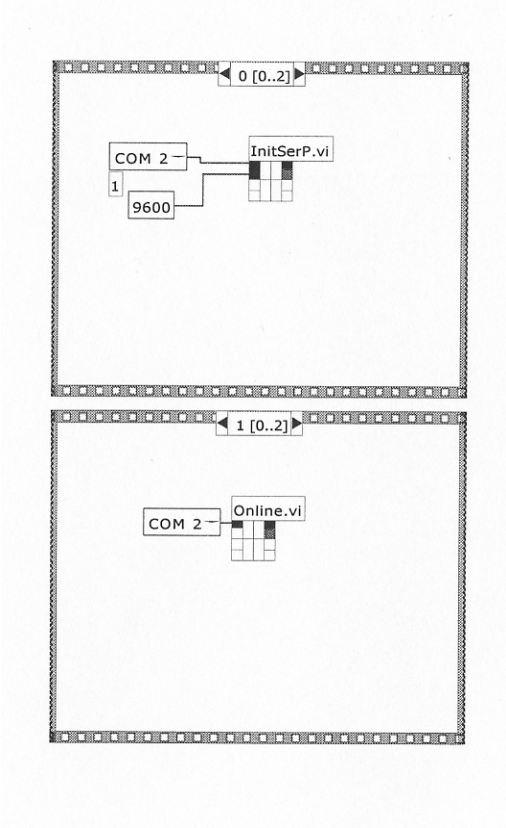

The two sequence structures shown here are frames 0 and 1 of the sequence that acquires the initial position of the delay line. Frame 0 establishes communication between the delay line motor controller and the computer. Frame 1 brings the delay line online in order to receive commands.

SubVIs and Functions

National Instruments™, Velmex™ and Stanford Research™ provided all SubVIs for control of the delay line and lock-in amplifier. For a detailed description of the functions used in this program, use the Help function in the LabVIEW™ editor.

Accumulate 5.4 LabVIEW™ VI

by

Alexander W. Schill

alexanderschill4@comcast.net

Accumulate 5.4 is a LabVIEW™ VI (Virtual Instrument) designed to integrate and control the operation of a kilohertz Ti:sapphire laser based femtosecond spectroscopy system using the lock-in technique. Accumulate 5.4 allows the user to control the data collection parameters in order to accumulate and average a series of kinetic traces. Page references are with respect to the first page of documentation (this page).

Principles of operation

Accumulate 5.4 performs the following functions:

-advances the delay line in user designated increments

-records the position of the delay line

-converts the delay line position to time in picoseconds

-records the signal from the lock-in amplifier

-records the phase of the signal from the lock-in

-calculates the transient absorption (TA) from the lock-in signal

-plots the transient absorption versus time

-plots phase versus time

-manipulates lock-in parameters such as sensitivity and integration time

-returns the delay line to start after the trace is complete

-writes text files of the signal and phase vs. time

-calculates and plots a running average TA trace and writes it to file

-calculates and plots a running average phase trace and writes it to file

The Front Panel

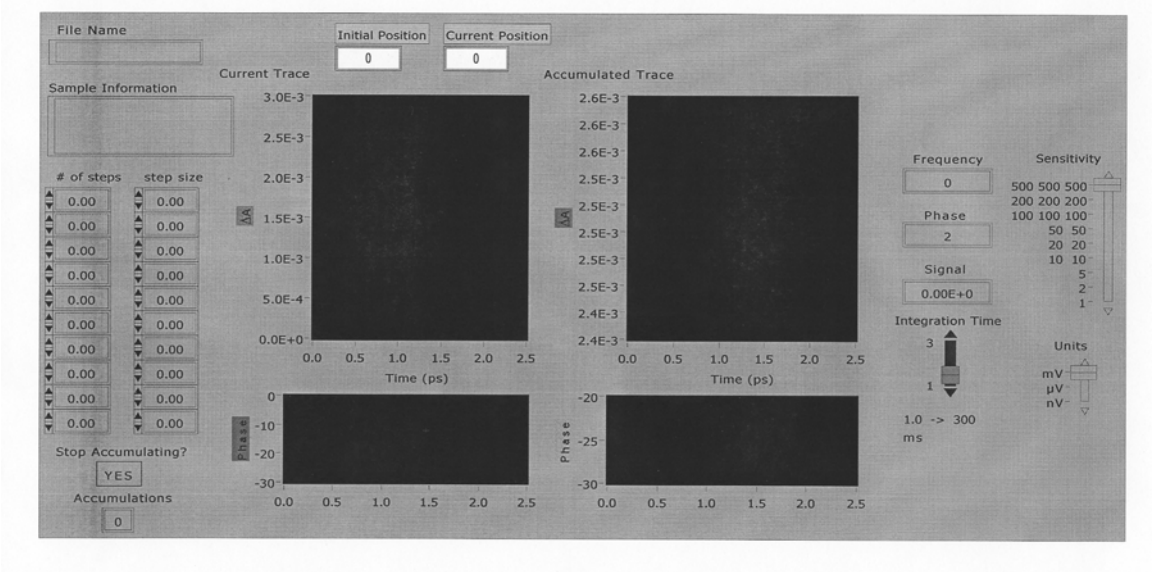

The following controls and indicators are found on the front panel of Accumulate 5.3:

File Name input: here the user inputs the name of the file to be created. The program will append an integer to the name corresponding to the accumulation number of each file. The averaged, accumulated file will have no integer appended to its name. A parameter file (.par extension) will be written that contains the parameters of the experiment.

Sample Information input: here the user enters information relevant to the sample he is studying.

# of steps/step size controls: here the user inputs the collection sequence he wishes to perform. The collection sequence proceeds from top to bottom. Inputs with zeros will not be performed.

Stop Accumulating? button: press to stop the accumulations. The program will run once more after this button is pushed to the “YES” position.

Accumulations indicator: displays the number of accumulations performed.

Initial position indicator: displays the initial position of the delay line in steps.

Current position indicator: displays the current position of the delay line in steps.

Current Trace XY graph: displays the current and previous kinetic traces and phase traces of the accumulation.

Accumulated Trace XY graph: displays accumulated kinetic and phase traces of the accumulation procedure.

Frequency indicator: indicates the frequency in Hz of the locked-in waveform being analyzed by the lock-in amplifier.

Phase indicator: indicates the phase of the locked-in waveform.

Signal indicator: indicates the amplitude of the locked-in waveform in volts.

Integration Time control: allows selection of two integration times indicated by the key below the slider.

Sensitivity control: sets the sensitivity of the lock-in amplifier.

Units control: sets the units of sensitivity setting for the lock-in.

The Block Diagram

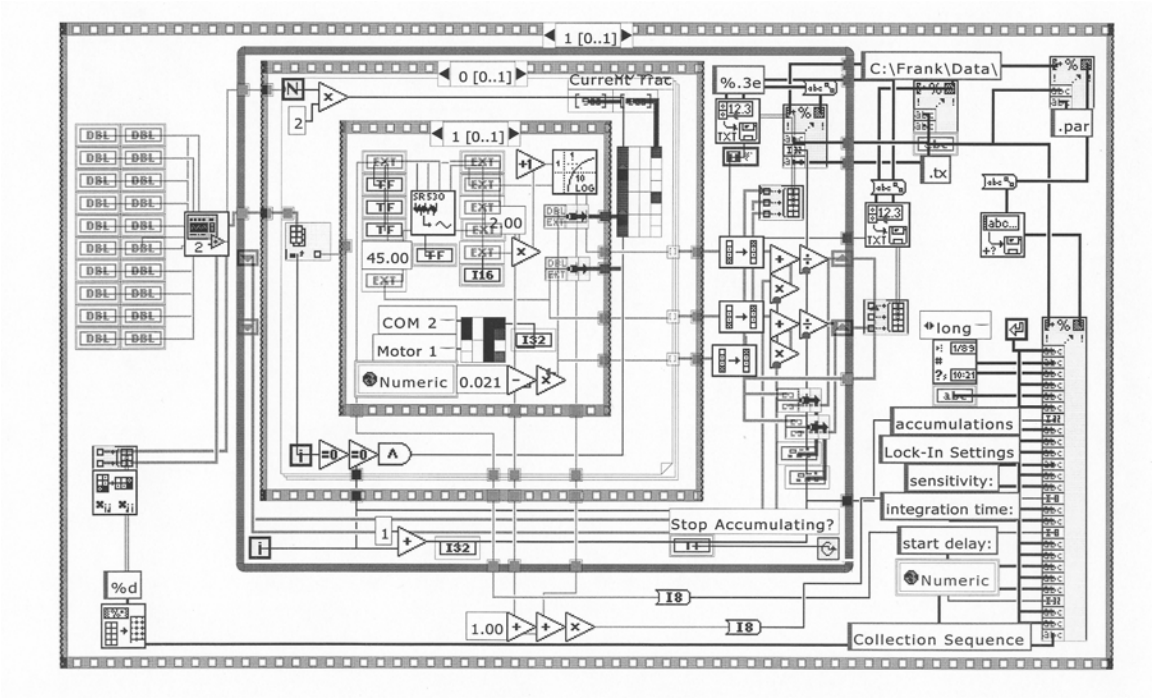

The block diagram determines the function of the VI in LabVIEW™. The symbols and structures in the diagram are compiled into code for execution of the program. The outermost structure is a sequence structure that executes a series of commands in order, one after another. In particular, this structure performs the duties of first recording the initial delay line position (page 11) and then executing the delay line advancement, data recording and accumulation procedures (frame 1, shown above). Within the sequence structure is a WHILE loop that runs the accumulation procedure until the Stop Accumulating? button is

pressed or the program is stopped externally (via the stop button in LabVIEW™). To the left of the WHILE loop is a SubVI that generates a collection sequence array for use within the accumulation loop. To the right of the WHILE loop are the functions that control saving of accumulated data and writing a parameter file. Within the WHILE loop is a sequence structure that performs the delay line advancement and data collection steps (frame 0 shown above) and then returns the delay line to the initial position when finished (frame 1, page 8). Within the sequence structure is a FOR loop that runs the advance delay line and record data sequence for a given number of data points. To the right of the sequence are the mathematical functions that perform the running average and plot the average on the graph. The innermost sequence structure is frame 0 of the advance delay and record data sequence. Frame 0 reads the signal and phase from the lock-in, converts the signal to transient absorbance, acquires the position of the delay line, converts the position to time in picoseconds and bundles the data points for display in the XY graphs.

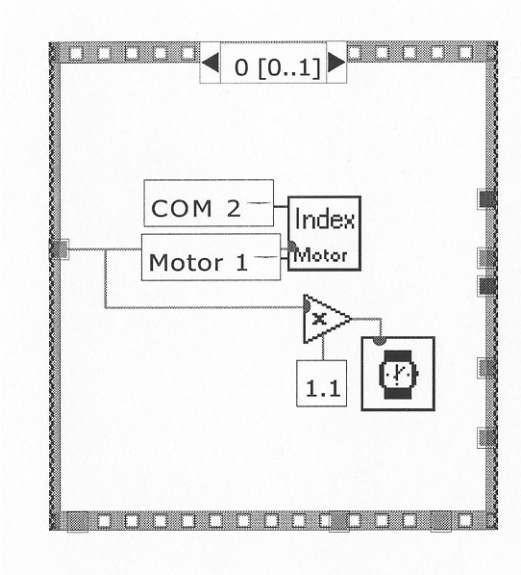

The sequence structure shown here is frame 0 of the sequence that advances the delay line and records the data. Frame 0 indexes the motor a given step size from the collection sequence and waits 110% of the time it takes to move before proceeding to the next frame. This ensures that the delay line has completely stopped before starting any new motion.

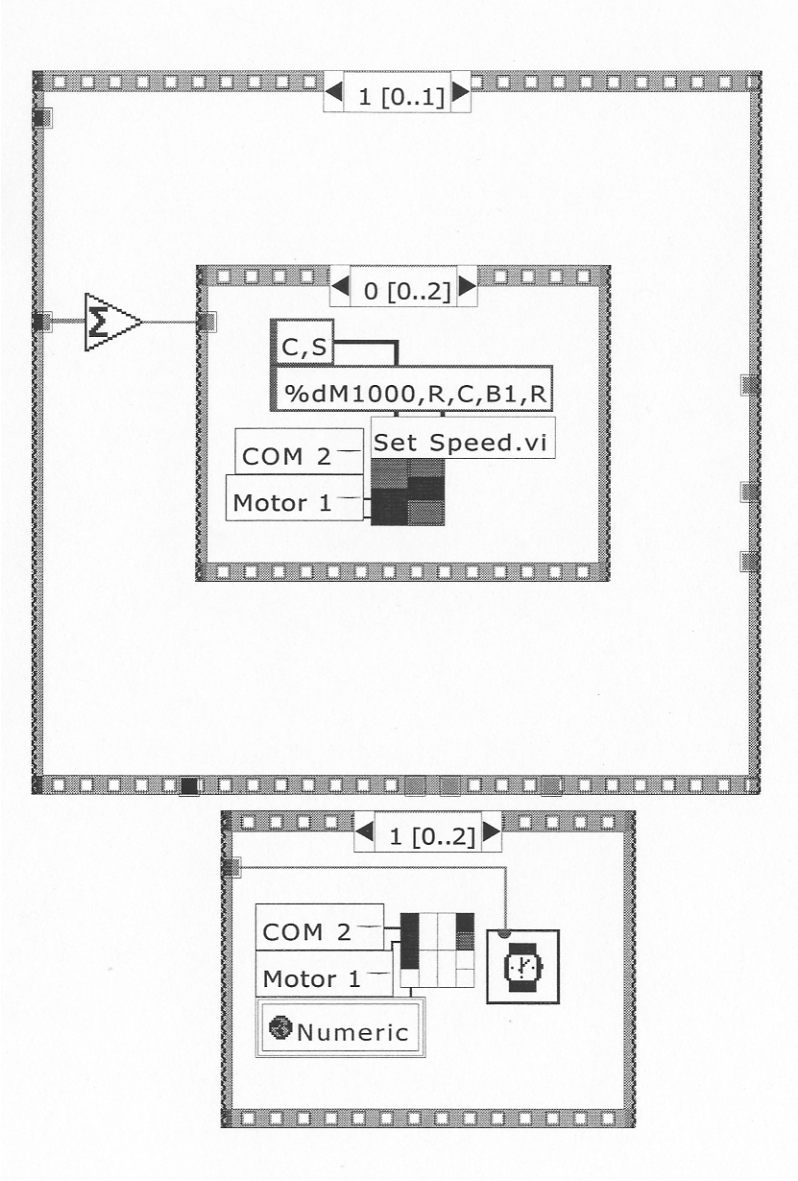

The large sequence structures shown here is frame 1 of the sequence that controls advancement and return of the delay line for an individual scan. The smaller sequence structures are frames 0 and 1 of the sequence that returns the delay line to its initial position. Frame 0 sets the motor speed to 1000 steps/second and enables backlash correction for more accurate repositioning of the delay line. Frame 1 returns the motor to its initial position while waiting the amount of time it takes the delay line to make the return trip. This ensures that

the delay line has made it all the way back to the starting position before beginning the next scan.

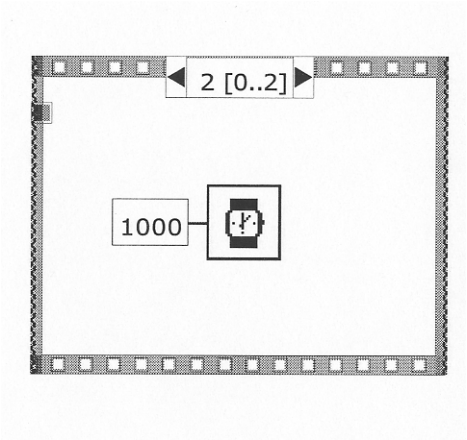

The sequence structure shown here is frame 2 of the sequence that returns the delay line to its initial position before beginning the next scan. Frame 2 causes the program to wait one second before proceeding to the next scan. This ensures that the delay line has come to a complete stop before any new motion begins.

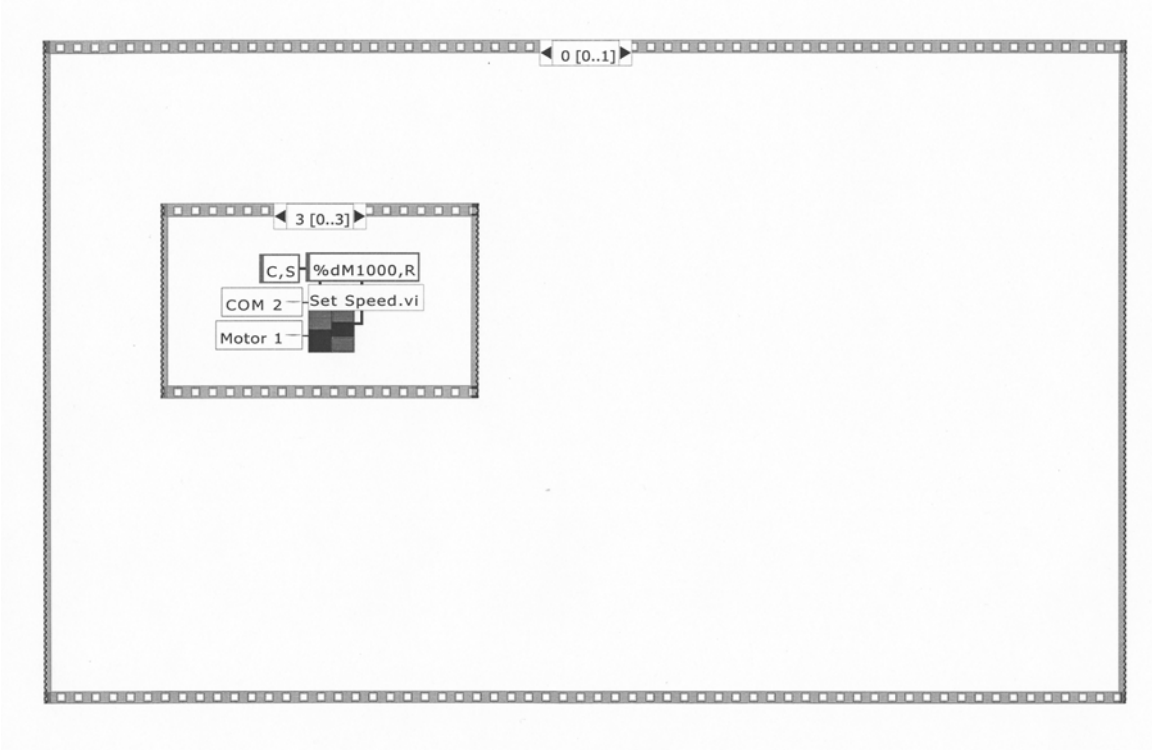

The large sequence structure shown here is frame 0 of the outermost sequence of the block diagram. Frame 0 is the first set of tasks that is performed by the program and involves initialization of the delay line motor controller, setting the speed of the motor to 1000 steps/second and acquiring the initial delay line position. The smaller sequence structure is frame 3 of the sequence just described and is responsible for setting the motor speed to 1000 step/second.

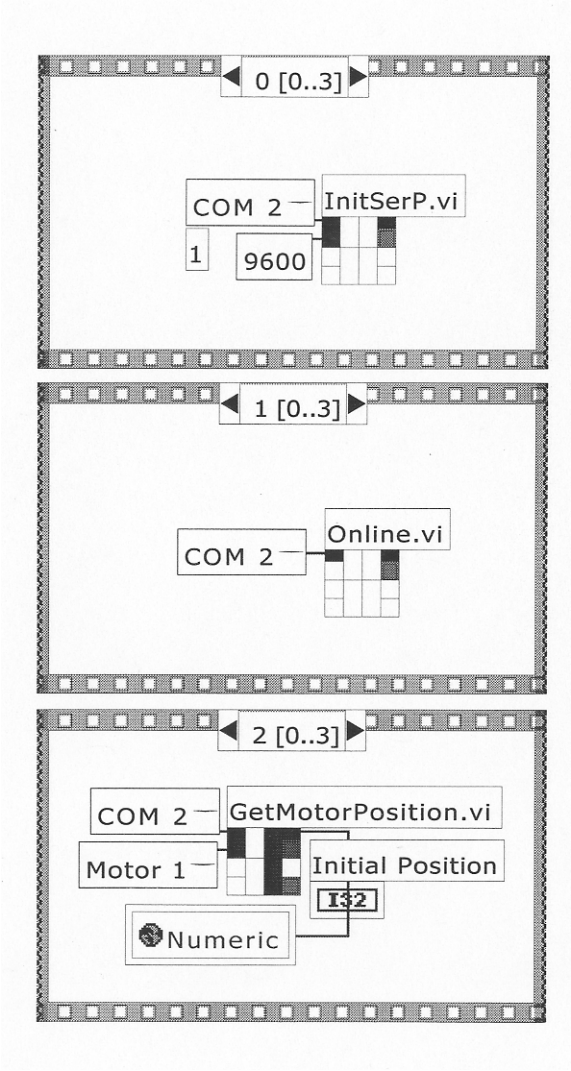

The sequence structures shown here are frames 0,1 and 2 of the sequence that initializes the delay line and acquires the initial delay line position. Frame 0 opens communication between the computer and the delay line motor controller. Frame 1 brings the delay line online in order to receive commands. Frame 2 acquires the initial position of the motor and writes that value to a global variable.

SubVIs and Functions

With the exception of the Collection Sequence Generator SubVI, National Instruments™, Velmex™ and Stanford Research™ provided all SubVIs for control of the delay line and lock-in amplifier. For a detailed description of the functions used in this program, use the Help function in the LabVIEW™ editor.

Spectra 2.7 LabVIEW™ VI

by

Alexander W. Schill

alexanderschill4@comcast.net

Spectra 2.7 is a LabVIEW™ VI (Virtual Instrument) designed to integrate and control the operation of a kilohertz Ti:sapphire laser based femtosecond spectroscopy system using the lock-in technique. Spectra 2.7 allows the user to control the data collection parameters in order to record a chirp-free transient absorption spectrum. Page references are with respect to the first page of documentation (this page).

Principles of operation

Spectra 2.7 performs the following functions:

-scans the monochromator

-advances the delay line to compensate for chirp

-records the position of the delay line

-records the signal from the lock-in amplifier

-records the phase of the signal from the lock-in

-calculates the transient absorption (TA) from the lock-in signal

-plots the transient absorption versus wavelength

-plots phase versus wavelength

-manipulates lock-in parameters such as sensitivity and integration time

-returns the delay line to start after the spectrum is complete

-writes text files of the signal and phase vs. wavelength

-calculates and plots a running average TA spectrum and writes it to file

-calculates and plots a running average phase spectrum

The Front Panel

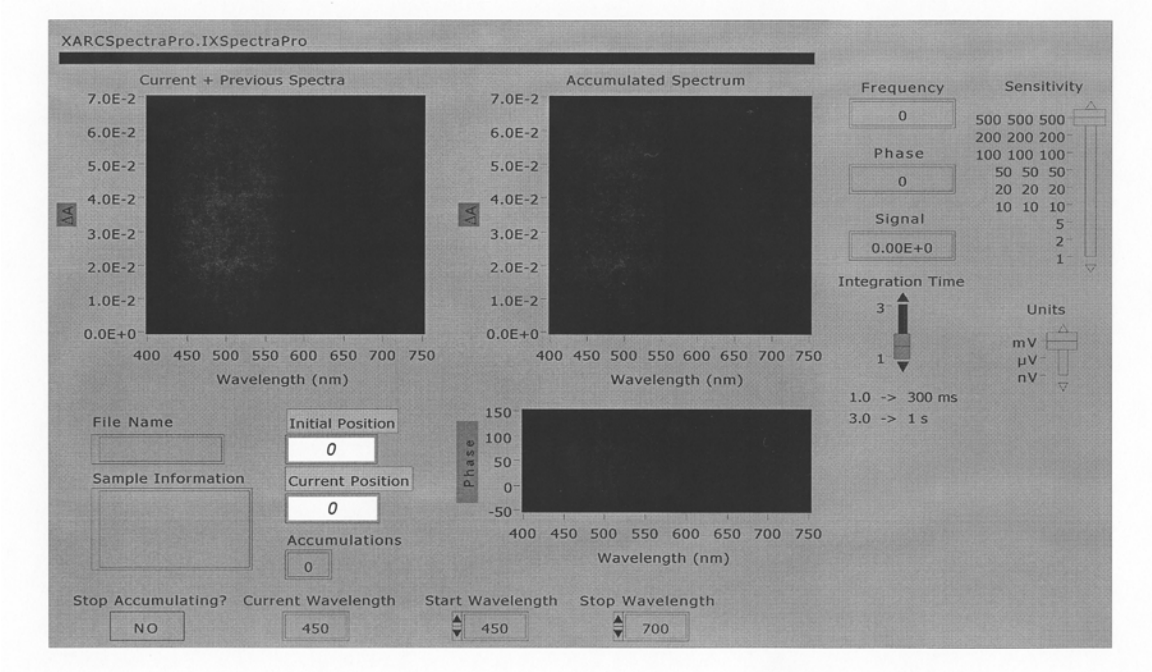

The following controls and indicators are found on the front panel of Spectra 2.7:

File Name input: here the user inputs the name of the file to be created. The program will append an integer to the name corresponding to the accumulation number of each file. The averaged, accumulated file will have no integer appended to its name. A parameter file (.par extension) will be written that contains the parameters of the experiment.

Sample Information input: here the user enters information relevant to the sample he is studying.

Stop Accumulating? button: press to stop the accumulations. The program will run once more after this button is pushed to the “YES” position.

Accumulations indicator: displays the number of accumulations performed.

Initial position indicator: displays the initial position of the delay line in steps.

Current position indicator: displays the current position of the delay line in steps.

Start/Stop Wavelength controls: here the user inputs the starting and ending wavelengths over which the monochromator will scan.

Current Wavelength indicator: displays the current position of the monochromator as a wavelength in nanometers.

Current + Previous Spectra XY graph: displays the current and previous spectra of the accumulation.

Accumulated Spectrum XY graphs: displays accumulated transient absorbance and phase spectra of the accumulation procedure.

Frequency indicator: indicates the frequency in Hz of the locked-in waveform being analyzed by the lock-in amplifier.

Phase indicator: indicates the phase of the locked-in waveform.

Signal indicator: indicates the amplitude of the locked-in waveform in volts.

Integration Time control: allows selection of two integration times indicated by the key below the slider.

Sensitivity control: sets the sensitivity of the lock-in amplifier.

Units control: sets the units of sensitivity setting for the lock-in.

The Block Diagram

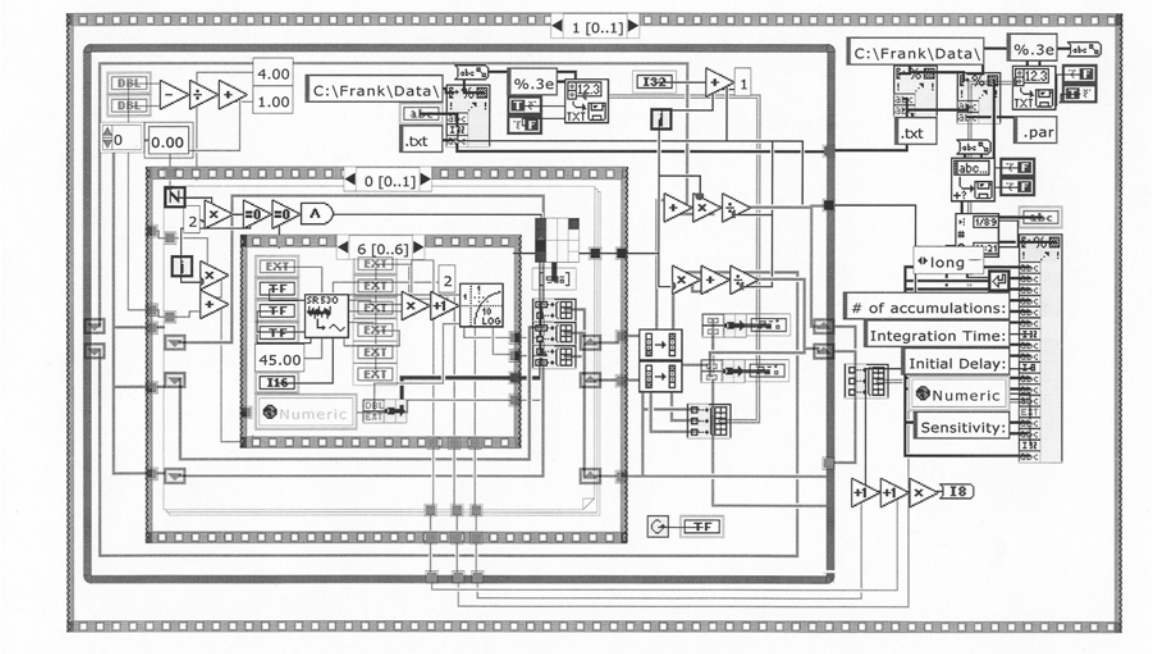

The block diagram determines the function of the VI in LabVIEW™. The symbols and structures in the diagram are compiled into code for execution of the program. The outermost structure is a sequence structure that executes a series of commands in order, one after another. In particular, this structure performs the duties of first recording the initial delay line position (page 12) and then executing the monochromator scan, delay line advancement, data recording and accumulation procedures (frame 1, shown above). Within the sequence structure is a WHILE loop that runs the accumulation procedure until the Stop Accumulating? button is pressed or the program is stopped externally (via the stop button in LabVIEW™). To the right of the WHILE loop are the functions that

control saving of accumulated data and writing a parameter file. Within the WHILE loop is a sequence structure that performs the monochromator scan, delay line advancement and data collection steps (frame 0, shown above) and then returns the delay line and monochromator to the initial position when finished (frame 1, page 11). Within the sequence structure is a FOR loop that runs the monochromator scan, advance delay line and record data sequence for a calculated number of data points. To the right of the sequence are the mathematical functions that perform the running average and plot the average on the graph. The innermost sequence structure is frame 6 of the advance delay and record data sequence. Frame 6 reads the signal and phase from the lock-in, converts the signal to transient absorbance, acquires the wavelength of the monochromator and bundles the data points for display in the XY graphs.

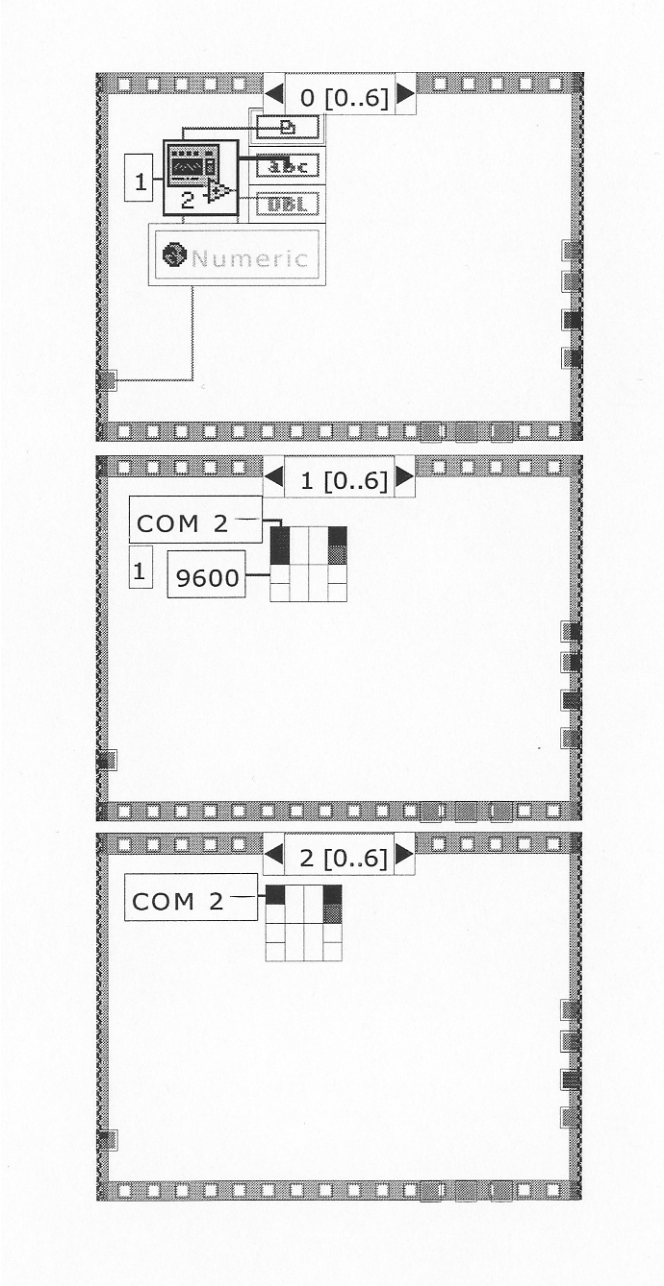

The sequence structures shown here are frames 0-2 of the sequence that scans the monochromator, advances the delay line and records the data. Frame 0 moves the monochromator four nanometers and writes the position of the monochromator to a global variable “Numeric”. Frame 1 opens communication

between the computer and the delay line motor controller. Frame 2 brings the delay line online in order to receive commands.

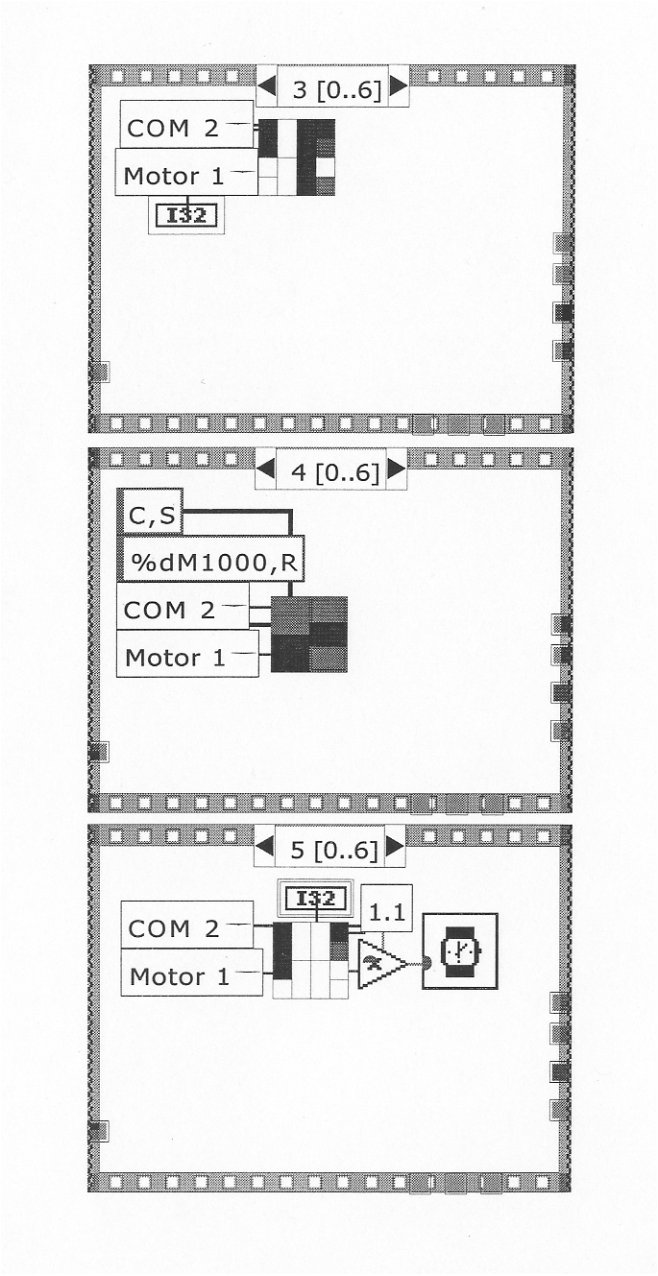

The sequence structures shown here are frames 3-5 of the sequence that scans the monochromator, advances the delay and records the data for an

individual spectrum. Frame 3 acquires the position of the delay line. Frame 4 sets the speed of the delay line motor to 1000 steps/second. Frame 5 advances the delay line while waiting 110% of the time it takes the delay line to move before proceeding to the next frame.

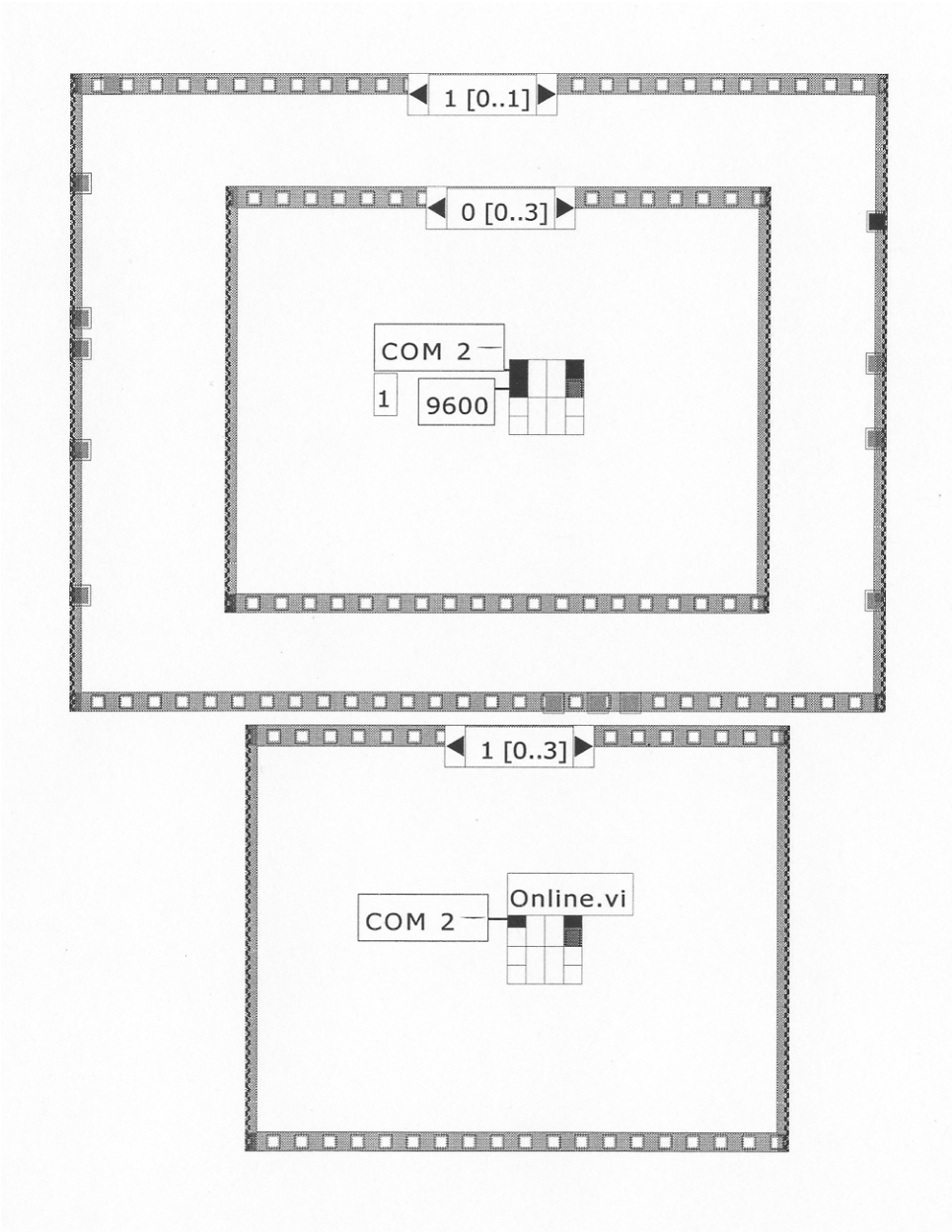

The large sequence structure shown above is frame 1 of the sequence that scans the monochromator, advances the delay, records the data and returns the delay line to its initial position before beginning the next spectrum. The small sequence structures are frames 0 and 1 of the sequence that returns the delay line to its initial position before starting the next spectral scan. Frame 0 opens communication between the computer and the delay line motor controller. Frame 1 brings the delay line online in order to receive commands.

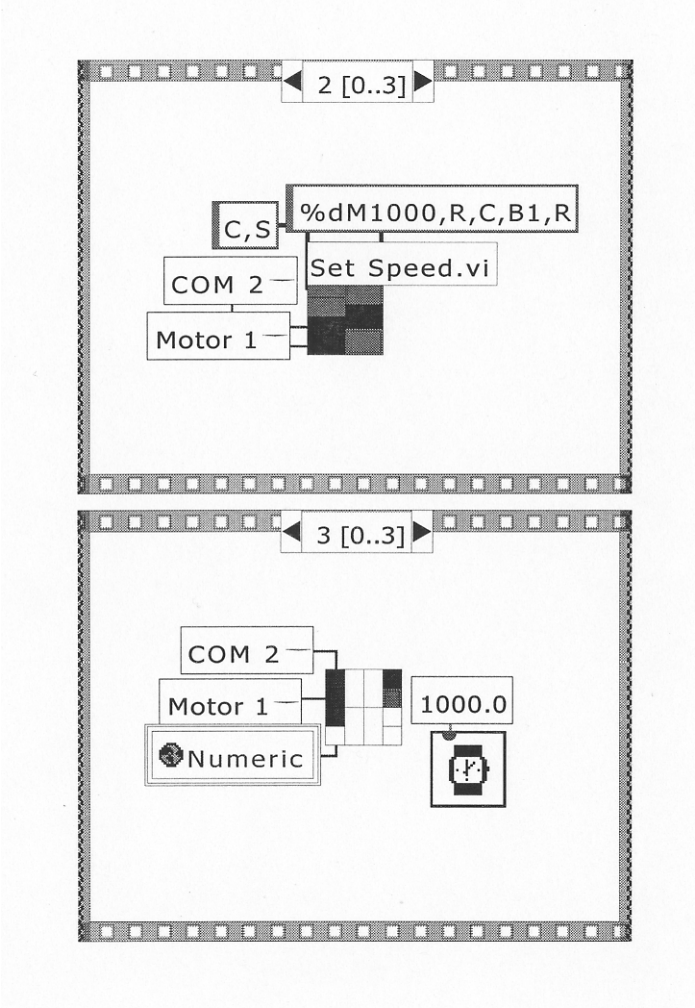

The sequence structures shown above are frames 2 and 3 of the sequence that returns the delay line to its initial position before beginning the next spectral scan. Frame 2 sets the speed of the delay line to 1000 steps/second and enables a backlash correction for more accurate positioning of the delay line. Frame 3 returns the delay line while waiting one second to ensure that the delay line completes the trip before beginning any new motion.

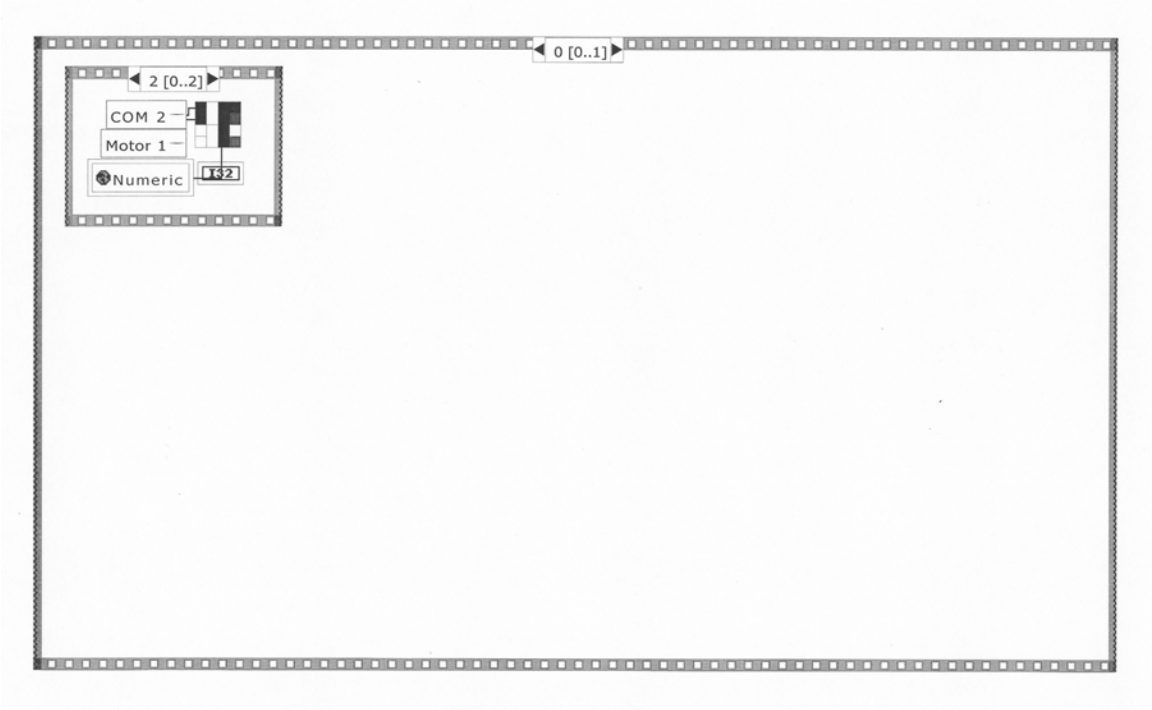

The large sequence structure is frame 0 of the outermost sequence of the block diagram. Frame 0 is the first set of tasks that is performed by the program and involves initialization of the delay line motor controller, setting the speed of the motor to 1000 steps/second and acquiring the initial delay line position. The smaller sequence structure is frame 2 of the sequence just described and is

responsible for acquiring the initial position of the delay line and writing it to a global variable “Numeric”.

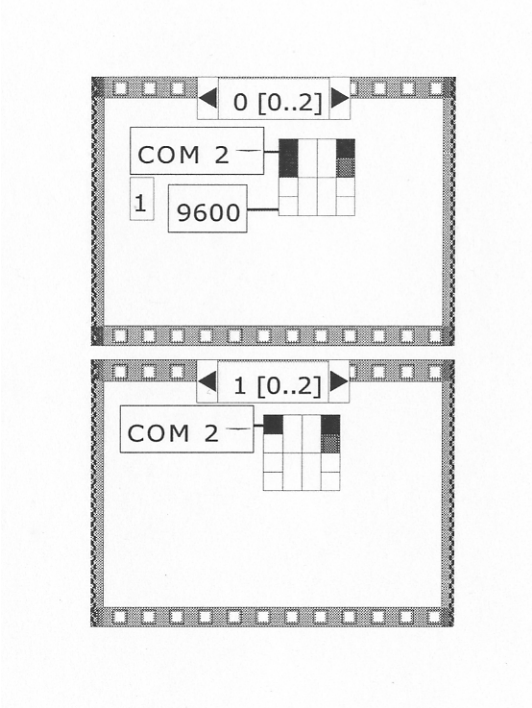

The sequence structures shown here are frames 0 and 1 of the sequence that initializes the delay line and acquires the initial delay line position. Frame 0 opens communication between the computer and the delay line motor controller. Frame 1 brings the delay line online in order to receive commands.

SubVIs and Functions

National Instruments™, Velmex™ and Stanford Research™ provided all SubVIs for control of the delay line and lock-in amplifier. For a detailed

description of the functions used in this program, use the Help function in the LabVIEW™ editor.

APPENDIX 2

EXPONENTIAL DATA FITTING DOCUMENTATION

EXPONENTIAL DATA FITTING.xls

MICROSOFT EXCEL™ SPREADSHEET DOCUMENTATION

by Alexander W. Schill

alexanderschill4@comcast.net

The Exponential Data Fitting.xls Excel Spreadsheet is designed to quantitatively fit exponential rise and decay kinetic data obtained from time-resolved spectroscopy experiments. The spreadsheet uses the weighted non-linear least squares fitting methodology and includes the necessary parameters for determining goodness-of-fit and evaluation of fit functions.

Features

Exponential Data Fitting.xls performs the following functions:

- Numerically simulates kinetic data using exponential functions convoluted with a Gaussian response function.
- Finds the nonlinear least squares fit to experimental data
- Plots the fit function along with the weighted residuals
- Calculates the normal probability plot for evaluation of goodness of fit and evaluation of the fit function

The Workbook

The Exponential Data Fitting.xls workbook consists of five (5) worksheets:

(1) Simulated Data (single)

(2) Fitting Simulation (single)

(3) Simulated Data (multiple)

(4) Fitting Simulation (multiple)

(5) Simulation Trials

Simulated Data (single) Worksheet

This worksheet may be used to simulated single exponential decay traces with randomly distributed standard errors. This sheet was initially used to develop the simulation model that would be used in the fitting worksheets. The components of this worksheet are as follows:

<u>IRF Parameters (cells B2 and B3)</u>

Shift (cell B2) – the offset in the temporal direction for the center of the Gaussian instrument response function (IRF)

Width (cell B3) – the width of the Gaussian instrument response function. Related to the pulsewidth of the excitation source used for the kinetic measurement.

Decay Parameters (cells E2 and E3)

Pre-Exp Factor (cell E2) – parameter in the single exponential decay function y = A*exp(-t /T) where A is the pre-exponential factor, t is the time displacement from time zero, T is the time constant for the decay.

Time Constant (cell E3) – parameter in the single exponential decay function y = A*exp(-t /T) where A is the pre-exponential factor, t is the time displacement from time zero, T is the time constant for the decay.

Data Parameters (cell B7 through E207)

Time (cells B7 through B207) – user designated time (any units)

IRF (cells C7 through C207) – calculated instrument response function based on the IRF parameters input in cells B2 and B3.

B7 = NORMDIST(A7,$B$2,$B$3,FALSE)

Signal (cells D7 through D207) – simulated kinetic signal from the IRF and decay parameters input in cells E2 and E3.

C7 = B7*$E$2

C8 = B8*$E$2+C7*EXP(-(A8-A7)/$E$3)

C9 = B9*$E$2+C8*EXP(-(A9-A8)/$E$3)

Noisy Signal (cells E7 through E207) – simulated kinetic data adjusted with random errors to simulate noisy data traces

D7 = $D$5*RANDBETWEEN(-100,100)+C7

Residuals (cells F7 through F207) – difference between noisy and noise-free simulated data.

E7 = D7-C7

Noise Factor (cell D5) – determines the magnitude of the error in the noisy signal simulation

Graphs

The top graph in the worksheet shows the simulated data: noise free data shown as a line and noisy data indicated with open circles. The instrument response function is also plotted for comparison of the simulated pulsewidth to the simulated decay curve.

Below the top graph is a plot of the residuals (cells F7 through F207) to show the scatter of the simulated noisy signal.

Fitting Simulation (single) Worksheet

This worksheet is used to fit experimental or simulated single exponential decays using a nonlinear least squares fitting routine. The components of this worksheet are as follows:

IRF Parameters (cells B3 and B4)

Shift (cell B3) – the offset in the temporal direction for the center of the Gaussian instrument response function (IRF)

Width (cell B4) – the width of the Gaussian instrument response function. Related to the pulsewidth of the excitation source used for the kinetic measurement.

Decay Parameters

Pre-Exp Factor (cell E3) – parameter in the single exponential decay function y = A*exp(-t /T) where A is the pre-exponential factor, t is the time displacement from time zero, T is the time constant for the decay.

Time Constant (cell E4) – parameter in the single exponential decay function y = A*exp(-t /T) where A is the pre-exponential factor, t is the time displacement from time zero, T is the time constant for the decay.

Fit Parameters (cells H2, H3, H4)

SSR (cell H2) – Sum of Squares of the Residuals (SSR)

Reduced SSR (cell H3) – Reduced Sum of Squares of the Residuals equal to the SSR divided by the number of data points. Appropriately weighted residuals should give a value close to 1.00 for the Reduced SSR.

F Statistic (cell H4) – value for the F Statistic determined from the Reduced SSR. Used to evaluate confidence intervals for the fitting parameters.

Upper Limit RSSR (cell H5) – value for the upper limit of RSSR such that the value of the F Statistic falls within the 95% confidence interval.

Experimental Data (cells C6, C7, A11-C211)

Avg SD (cell C6) – average of the standard deviations given in cells C11-C211

Avg Sd adj (cell C7) – user applied offset to the value of the average SD. Used if the estimated avg SD is not the correct magnitude for the experiment.

Time (cells A11-A211) – time axis of the data

Signal (cells B11-B211) – value of the signal at each time

SD (cells C11-C211) – user estimated or measured standard deviation in the value of the signal at each time.

Fitting Functions (cells D11-F211)

Adj. Time (cells D11-D211) – time in cells A11-A211 minus the IRF shift in cell B3.

D11 = A11-$B$3

IRF (cells E11-E211) – calculated instrument response function based on the IRF parameters input in cells B3 and B4.

E11 = NORMDIST(A11,$B$3,$B$4,FALSE)

Fit Function (cells F11-F211) - simulated kinetic signal from the IRF and decay parameters input in cells E3 and E4.

F11 = E11*$E$3

F12 = E12*$E$3+F11*EXP(-(A12-A11)/$E$4)

F13 = E13*$E$3+F12*EXP(-(A13-A12)/$E$4)

Analysis Functions (cells G11-J211)

Residuals (cells G11-G211) – difference between the value of the experimental signal and the fit function at each time.

G11 = B11-F11

Weighted Residuals (cells H11-H211) – the residuals in cells G11-G211 divided by the averages adjusted standard deviation (avg SD adj, cell C7)

H11 = G11/$C$6

Res. Sqr. (cells I11-I211) – the residuals squared.

I11 = G11*G11

Wght. Res. Sqr. (cells J11-J211) – the weighted residuals squared. Sum to give SSR.

J11 = H11*H11

Graphs

The graph located in L29 through Q41 shows a plot of the experimental data (open circles), the fit function (line) and the instrument response (dashed line).

The graph located in L42 through Q55 shows the plot of the residuals

The graph located in L56 through Q67 shoes the plot of the weighted residuals

The graph shown in N1 through Q27 shows the support plane analysis plot used to determine confidence intervals for the decay constant. See Lakowicz, J. R. *Principles of Fluorescence Spectroscopy, Second Edition* Section 4.9.C for details of this analysis procedure.

The graph shown in W11-AC26 is the normal probability plot. The procedure for determining the normal probability plot can be found in almost any undergraduate statistics textbook. Consult such materials for details.

Simulated Data (multi) Worksheet

This worksheet may be used to simulate multiple exponential decay traces with randomly distributed standard errors. This sheet was initially used to develop the simulation model that would be used in the fitting worksheets. The components of this worksheet are as follows:

<u>IRF Parameters (cells B12 and B13)</u>

Shift (cell B12) – the offset in the temporal direction for the center of the Gaussian instrument response function (IRF)

Width (cell B13) – the width of the Gaussian instrument response function. Related to the pulsewidth of the excitation source used for the kinetic measurement.

Decay Parameters (cells B16 through F17)

Pre-Exp Factor (cells B16 through F16) – parameters in the multiple exponential decay function y = A*exp(-t /T1)+B*exp(-t /T2)+C*exp(-t /T3)+D*exp(-t /T4)+E*exp(-t /T5) where A-E are the pre-exponential factor, t is the time displacement from time zero, T1-T5 are the time constants for the decay.

Time Constant (cells C16 through F16) – parameters in the single exponential decay function y = A*exp(-t /T1)+B*exp(-t /T2)+C*exp(-t /T3)+D*exp(-t /T4)+E*exp(-t /T5) where A-E are the pre-exponential factor, t is the time displacement from time zero, T1-T5 are the time constants for the decay.

Data Parameters (cell B7 through J207)

Time (cells A21 through A521) – user designated time (any units)

IRF (cells B21 through B521) – calculated instrument response function based on the IRF parameters input in cells B2 and B3.

B21 = NORMDIST(A21,$B$12,$B$13,FALSE)

Signal Components (cells C21 through G521) – components of the exponential decay determined from the input values of the time constants and pre-exponential factors in cells B16 through F17.

C21 = $B21*B$16

C22 = $B22*B$16+C21*EXP(-($A22-$A21)/B$17)

D21 = $B21*C$16

D22 = $B22*C$16+D21*EXP(-($A22-$A21)/C$17)

Etc.

Total Signal (cells H21 through H521) – sum of signal components A through E in cells C21 through E521.

H21 = SUM(C21:G21)

Noisy Signal (cells I21 through I521) – simulated kinetic data adjusted with random errors to simulate noisy data traces.

I21 = $I$18*RANDBETWEEN(-100,100)+H21

Residuals (cells F7 through F207) – difference between noisy and noise-free simulated data.

J21 = I21-H21

Noise Adjustment (cell I18) – enters into the calculation of the noisy signal as a factor that increases or decreases the magnitude of the noise.

Graphs

The two graphs shown at the top of the worksheet are plots of the simulated data (left) and the residuals in the noise (right).

Fitting Simulation (multi) Worksheet

This worksheet is used to fit experimental or simulated multiple exponential decays using a nonlinear least squares fitting routine. The components of this worksheet are as follows:

Data Range (cells B2 through B4)

Starting Cell (cell B2) – cell selected from the Experimental Data and Weights column 'Cell' to mark the beginning of the data set to be fit.

Ending Cell (cell B3) – cell selected from the Experimental Data and Weights column 'Cell' to mark the ending of the data set to be fit.

# of Data Points (cell B4) – simply calculates the number of points used in the fit based on the Starting and Ending Cell numbers.

B4 = $B$3-$B$2+1

Analysis Parameters (cells B7 though B11)

SSR (cell B7) – Sum of Squares of the Residuals (SSR)

Reduced SSR (cell B8) – Reduced Sum of Squares of the Residuals equal to the SSR divided by the number of data points. Appropriately weighted residuals should give a value close to 1.00 for the Reduced SSR.

Limiting F Lower (cell B9) – lower value for the F Statistic determined from the number of data points and a 95% confidence level.

Limiting F Upper (cell B10) – upper value for the F Statistic determined from the number of data points and a 95% confidence level.

Limiting RSSR (cell B11) – largest value of the RSSR such that the parameters for the fit fall within the 95% confidence interval of the optimized fit parameters.

IRF Parameters

Shift (cell B14) – the offset in the temporal direction for the center of the Gaussian instrument response function (IRF)

Height (cell B15) – adjustable height of the instrument response function

Width (cell B16) – the width of the Gaussian instrument response function. Related to the pulsewidth of the excitation source used for the kinetic measurement.

Weighting Options (cells B19 through B23)

Ind.? (1 for “yes”), cell B19 – asks the user if he would like to use independent weights (enter a 1) for each data point or used an average standard deviation instead (enter a 0).

Ind. Adj. Factor (cell B20) – adjustment coefficient applied to the individual standard deviations to increase or decrease the magnitude of the standard error.

Avg. SD (cell B21) – average of the standard deviations in the data for the experiment from cells D31 through D531.

B21 = AVERAGE(D31:D531)

Adj. Factor (cell B22) - adjustment coefficient applied to the average standard deviations to increase or decrease the magnitude of the standard error.

Decay Parameters (cells B26 through F27)

Pre-Exp Factor (cells B26 through F26) – parameters in the multiple exponential decay function y = A*exp(-t /T1)+B*exp(-t /T2)+C*exp(-t /T3)+D*exp(-t /T4)+E*exp(-t /T5) where A-E are the pre-exponential factor, t is the time displacement from time zero, T1-T5 are the time constants for the decay.

Time Constant (cells B27 through F27) – parameters in the single exponential decay function y = A*exp(-t /T1)+B*exp(-t /T2)+C*exp(-t /T3)+D*exp(-t /T4)+E*exp(-t /T5) where A-E are the pre-exponential factor, t is the time displacement from time zero, T1-T5 are the time constants for the decay.

Experimental Data and Weights (cells A31 through E531)

Cell (cells A31 through A531) – assigns the number of the cell for use in determining the starting and ending cells of the data to be fit.

Time (cells B31 through B531) – time axis of the data

Signal (cells C31 through C531) – signal at each point in time

SD (cells D31 through D531) – experimentally determined standard deviation in the signal at each point in time

Weight (cells E31 through E531) – inverse of the SD multiplied by the individual adjustment factor in cell B20

E31 = $B$20/D31

Fitting Functions

Adj. Time (cells F31 through F531) – time in cells B31 through B531 minus the IRF shift in cell B16.

F31 = B31-$B$16

IRF (cells G31 through G531) – calculated instrument response function based on the IRF parameters input in cells B14 through B16

G31 = $B$15*NORMDIST(B31,$B$14,$B$16,FALSE)

Signal Components A-E (cells H31 through L531) – components of the exponential decay determined from the input values of the time constants and pre-exponential factors in cells B26 through F27.

H31 = $G31*B$26

H32 = $G32*B$26+H31*EXP(-($B32-$B31)/B$27)

I31 = $G31*C$26

I32 = $G32*C$26+G31*EXP(-($B32-$B31)/C$27)

Etc.

Total Function (cells M31 through M531) – sum of the individual components of the fit in cells H31 through L531.

M31 = SUM(H31:L31)

Analysis Functions (cells N31 through P531)

Residuals (cells N31 through N531) – differences between the experimental data and the fit function at each data point

N31 = C31-M31

Weighted Residuals (cells O31 through O531) – product of the residual at each data point times the individual weighting factor for that data point. Used only if a '1' is entered under Ind.? in the weighting options section.

IF($B$19=1,E31*N31,N31/$B$23)

Selected W Residuals (cells P31 through P531) – chooses only those residuals from data points to be included in the least squares fit as indicated in the Data Range

section. Multiplies a 1 times the value for the weighted residual at that point if it falls within the Data Range, otherwise multiplies by 0.

P31 = O31*IF(AND(IF($A31>=$B$2,1,0),IF($A31<=$B$3,1,0)),1,0)

Normal Probability Plot (Q31 through S531)

Sorted W Residuals (cells Q31 through Q531) – this column contains the results from the sorting macro NormProbSort which sorts the selected weighted residuals in order from most negative to most positive.

%ile (cells R31 through R531) – calculates the percentile (%ile) of each entry in the sorted residuals column for the assignment of a Z statistic.

R31 = 100*(A31-$A$31+1-0.5)/$B$4

Z (cells S31 through S531) – calculates the value of the Z statistic based on the percentile determined in cells R31 through R531.

S31 = NORMSINV(R31/100)

Graphs

The graph shown in cells C1 through G16 is a plot of the experimental data vs. cell number for estimating the useful portion of the decay curve to be fit.

The graph shown in cells H1 through L16 is a plot of the experimental data (open circles), the fit function (line) and the IRF (dashed line).

The graph shown in cells H17 through L27 is a plot of the weighted residuals.

The graph shown in cells M1 through P28 is the normal probability plot determined automatically with the help of the NormProbSort macro, the Visual Basic script of which is given below. Normal probability plots are discussed in most undergraduate statistics textbooks. Consult such materials for details.

NormProbSort Visual Basic Script

```
Sub NormProbSort()
'
' Macro3 Macro
' Macro recorded 2/16/2003 by Alexander W. Schill
'

'
    Range("Q32:Q5012").Select
    Selection.ClearContents
    StartCell = Range("B2")
    EndCell = Range("B3")
    Range(Cells(StartCell, 16), Cells(EndCell, 16)).Select
    Selection.Copy
    Range("Q32").Select
    Selection.PasteSpecial Paste:=xlValues, Operation:=xlNone, SkipBlanks:= _
        False, Transpose:=False
    Range("Q31:Q5012").Select
    Application.CutCopyMode = False
    Selection.Sort Key1:=Range("Q32"), Order1:=xlAscending, Header:=xlGuess, _
        OrderCustom:=1, MatchCase:=False, Orientation:=xlTopToBottom
End Sub
```